UC Irvine

UC Irvine Electronic Theses and Dissertations

Title

Neural circuit reorganization and functional plasticity following traumatic brain injury

Permalink

https://escholarship.org/uc/item/3v2583zw

ISBN

9798173723697

Author

Tierno, Alexa Marie

Publication Date

2026-11-03

Copyright Information

This work is made available under the terms of a Creative Commons Attribution License, available at https://creativecommons.org/licenses/by/4.0/

Peer reviewed|Thesis/dissertation

eScholarship.org Powered by the California Digital Library
University of California

UNIVERSITY OF CALIFORNIA,
IRVINE

Neural circuit reorganization and functional plasticity following traumatic brain injury

DISSERTATION

submitted in partial satisfaction of the requirements
for the degree of

DOCTOR OF PHILOSOPHY

in Biomedical Sciences

by

Alexa Marie Tierno

Dissertation Committee:
Associate Professor Robert F. Hunt, Chair
Professor David C. Lyon
Professor Oswald Steward
Assistant Professor Katherine Thompson-Peer

2026

Chapter 2 © 2026 Tierno et al.
Chapter 3 © 2022 Frankowski et al.
All other materials © 2026 Alexa Marie Tierno

DEDICATION

To my grandfather

Donde estes, Tata, espero que estes orgulloso

TABLE OF CONTENTS

LIST OF FIGURES.....iv

ACKNOWLEDGEMENTS vi

VITA.....viii

ABSTRACT OF THE DISSERTATION xi

INTRODUCTION 1

CHAPTER TWO: Cortex-wide neuron activation after traumatic brain injury in mice 25

CHAPTER THREE: Brain-wide reconstruction of inhibitory circuits after traumatic brain injury .39

CHAPTER FOUR: Brain injury degrades the precision of hippocampal spatial representations 94

CONCLUSIONS.....116

REFERENCES 127

APPENDIX A: Miniscope surgery protocol 151

APPENDIX B: Calcium Imaging and Behavior Analysis 163

LIST OF FIGURES

Page

Figure 1.1: Hippocampal CA1 principal cell inputs. 4

Figure 1.2: Schematic of TRAP2 transgenic mouse model....8

Figure 1.3: Place cell schematic....10

Figure 1.4: Timeline of traumatic brain injury....19

Figure 2.1: Hemisphere-wide cell activation following TBI....32

Figure 2.2: Buprenorphine activates a small number of cells....33

Figure 2.3: Cell activation extends beyond the glia scar.....34

Figure 2.4: Ai14^{+} cells are putative neurons. 35

Figure 3.1: SST interneuron loss after focal TBI.....50

Figure 3.2: Input neurons to hilar SST interneurons 51

Figure 3.3: Virus specificity in hippocampus....52

Figure 3.4: Reorganization of brain-wide input to hippocampal SST interneurons after TBI. 55

Figure 3.5: Optimization of enhanced iDISCO+ protocol 56

Figure 3.6: Protocol for image registration and analysis. 57

Figure 3.7: Individual animal plots of input to hilar SST interneurons 59

Figure 3.8: Input neurons innervating hilar SST interneurons in hippocampus 60

Figure 3.9: Retrograde circuit tracing data represented as a convergence index. 61

Figure 3.10: Distant brain regions remain structurally intact 65

Figure 3.11: Replication of CHAT immunostaining with conventional immunostaining in a separate cohort of animals....65

Figure 3.12: Identification of CA1 input neurons....66

Figure 3.13: TBI produces highly focal neurodegeneration 68

Figure 3.14: SST interneurons are not reduced in PFC after TBI 69

Figure 3.15: Distribution of starter neurons in PFC....70
Figure 3.16: Virus specificity in PFC....72
Figure 3.17: Input to SST interneurons in PFC is reorganized after TBI. 75
Figure 3.18: Individual animal plots of input to PFC SST interneurons. 76
Figure 3.19: Input neurons innervating PFC SST interneurons. 79
Figure 3.20: Retrograde circuit tracing data in PFC represented as a convergence index....80
Figure 3.21: Transplanted SST interneurons integrate into brain-injured hippocampus....82
Figure 3.22: Distribution of transplanted MGE-SST cells....83
Figure 3.23: Transplanted SST interneurons receive local and long-range input....85
Figure 3.24: Individual animal plots of input to transplanted SST interneurons....86
Figure 3.25: Input to transplanted interneurons....87
Figure 4.1: Verification of CA1 targeting and cell type specificity of jGCaMP8m expression....102
Figure 4.2: Track layout and running speed 102
Figure 4.3: Pipeline for calcium signal extraction and analysis from miniscope recordings....103
Figure 4.4: Field of view (FOV) and calcium traces from all recorded mice 104
Figure 4.5: CA1 activity is preserved after brain injury....106
Figure 4.6: Chronic brain injury alters the recruitment and spatial precision of CA1 representations. 109
Figure 4.7: Firing rate maps of CA1 neurons....110
Figure 4.8: Place cell stability, firing rates and nonspatial cell properties....112
Figure 4.9: Novelty discrimination is impaired after brain injury 113

ACKNOWLEDGEMENTS

I would like to thank my mentor, Dr. Robert Hunt, for the opportunity to work in his lab and continued support throughout the years. I have learned an enormous amount about science and how to conduct research. I carry with me the lessons I learned these past 6 years, always asking "Why am I doing this? And how do I know?" Your high standards and expectations have made me a better scientist, and I am grateful for that.

Thank you to my wonderful committee members: Drs. Oswald Steward, David Lyon, Katherine Thompson-Peer and Lulu Chen. Your insight at every committee meeting made my research stronger. Thank you for your guidance, patience, and support. Thank you to my rotation mentor, Dr. Gyuri Lur, for introducing me to *in vivo* imaging and teaching me how to code.

Thank you to my friends, those that have known me before UCI and the friendships I've made during grad school. Special thanks to Gerardo: Thank you for sitting next to me on the bus at interview weekend. I didn't know I was meeting my best friend and that we would go through PhD together – long days in the lab, matcha runs, and paint nights. And to Brittney, thanks for taking care of me, being an amazing travel and conference partner, and a lifelong friend. To my beer Friday crew, Gergely, Gautam, Matt, Madeleine, Leticia, thank you for being the light at the end of the tunnel every week.

To my family, thank you for always being my number one supporters, those here and those in Mexico. Especially to my grandma who has been through all my major life events by my side.

As I was looking ahead to the next step in my career, I wondered whether moving somewhere outside of California would be something I could do. But I kept thinking, how could I just leave my friends and family behind and go someplace where I don't know anyone and have to start fresh? Then I thought, that's what my parents did when they moved to the US, they left family and friends behind and started from zero, so that I could have more opportunities and a better life. Your unwavering love and support never goes unnoticed and I hope I've made you proud.

To my second parents, my amazing in-laws and brother-in-law: thank you for your love, support and understanding. I know I can always count on you guys for anything, especially a good time.

And to my husband, my rock. Thank you for your unconditional love, for listening to me talk about my failed experiments day after day, for bringing me coffee after I already had 3 that day, for coming with me to the lab late at night, and for sacrificing things because of my lab work. Thank you for keeping me sane these past 6 years and lifting me up when I felt like I just couldn't do it.

The text and figures of Chapter 2 of this dissertation are a reprint of the material as it appears in Tierno A, Baraban A, Hunt RF (2026). Cortex-wide neuron activation after traumatic brain injury in mice. *eNeuro*. 13(5), used with permission from Society for Neuroscience (CC BY 4.0). The coauthors listed in this publication are Aidan Baraban and Robert Hunt. Aidan Baraban performed immunohistochemistry experiments and data analysis. Robert Hunt contributed to writing, editing, analyses, and making figures.

The text and figures of Chapter 3 of this dissertation are a reprint of the material as it appears in Frankowski JC, Tierno A, Pavani S, Cao Q, Lyon DC, Hunt RF (2022). Brain-wide reconstruction of inhibitory circuits after traumatic brain injury. *Nature communications*, 13(3417), 1-16, used with permission from Springer Nature (CC BY 4.0). The coauthors listed in this publication are Jan Frankowski, Shreya Pavani, Quincy Cao, David Lyon and Robert Hunt. Jan Frankowski performed CCI surgeries, virus and transplant surgeries, immunostaining, iDISCO+ brain clearing, light-sheet imaging, wrote initial Python code, performed cell count quantifications and initial data analyses. Shreya Pavani performed immunohistochemistry experiments. Quincy Cao performed data analysis. David Lyon provided rabies virus. Robert Hunt contributed to writing, editing, analyses, and making figures.

I would like to thank Di Wu for manual inspection of automated spike inferences and Daniel Aharoni for recommendations on analysis pipelines used in Chapter 4.

Financial support was provided by the National Institutes of Health Grants R01-NS096012, R01-EY024890, F31-NS106806, and F31-NS132447.

VITA

Alexa Marie Tierno

2017	B.S. in Neuroscience, University of California, Los Angeles
2017-2018	Laboratory Technician, University of California, Los Angeles
2020	M.S. in Integrative Biology and Physiology, University of California, Los Angeles
2026	Ph.D. in Biomedical Sciences, University of California, Irvine

FIELD OF STUDY

In vivo physiology and circuits after traumatic brain injury

PUBLICATIONS

Tierno A, Hunt RF. (2026). Brain injury degrades the precision of hippocampal spatial representations. ***bioRxiv****.*

Ingraham Dixie KL, Tierno A, Thornton MA, Mekonnen MA, Dale EA, Zhong H, Edgerton VR, Phelps PE (2026). Olfactory ensheathing cell transplantation combined with electrical epidural stimulation as a long-term treatment for severe spinal cord injury in female Fischer 344 rats. ***European Journal of Neuroscience,*** 64(4): e70648. PMID: 42604866

Tierno A, Baraban A, Hunt RF (2026). Cortex-wide neuron activation after traumatic brain injury in mice. ***eNeuro.*** 13(5). PMID: 42140701.

Stokes EG, Vasquez JJ, Azouz G, Nguyen M, Tierno A, Zhuang Y, Galinato VM, Hui M, Toledano M, Tyler I, Shi X, Hunt RF, Aoto J, KT Beier (2025). Cationic peptides cause memory loss through endophilin-mediated endocytosis. ***Nature*****,** 1-11. PMID: 39814881.

Phelps PE, Tierno A (2023) Cholinergic spinal interneurons in ***Spinal Interneurons*** [Lane MA and Zholudeva LV] Invited book chapter, Academic Press***,*** 159-170*.*

Frankowski JC*, Tierno A*, Pavani S, Cao Q, Lyon DC, Hunt RF (2022). Brain-wide reconstruction of inhibitory circuits after traumatic brain injury. ***Nature communications***, 13(3417), 1-16. PMID: 35701434. *co-first authors

Frankowski JC*, Foik AT*, Tierno A, Machhor JR, Lyon DC, Hunt RF (2021). Traumatic brain injury to primary visual cortex produces long-lasting circuit dysfunction. ***Communications biology***, 4(1), 1-12. PMID: 34789835. *co-first authors

Jin B*, Alam M*, Tierno A, Zhong H, Roy RR, Gerasimenko Y, Lu DC, Edgerton VR (2020) Serotonergic facilitation of forelimb functional recovery in rats with cervical spinal cord injury. ***Neurotherapeutics***, 18(2)1226-1243. PMID: 33420588. *co-first authors

Invited talks

Investigator Workshop, American Epilepsy Society Meeting, Los Angeles, CA 2024

AMPA receptor synaptic plasticity and post-traumatic amnesia

A&N Grad Day Symposium, UC Irvine 2024

Blocking AMPA receptor endocytosis prevents post-traumatic memory loss

A&N Grad Day Symposium, UC Irvine 2023

Transplantation of human-derived interneurons into the injured brain

Investigator Workshop, American Epilepsy Society Meeting, Nashville, TN 2022

Large-scale 3D reconstruction of inhibitory circuits in an injured brain

Gordon Research Conference: Mechanisms of Epilepsy and Neural Synchronization 2022

Barcelona, Spain *Large-scale 3D reconstruction of inhibitory circuits in an injured brain*

Quantum Photonics: Academic Paper Seminar, Clubhouse 2022

Brain-wide reconstruction of inhibitory circuits after traumatic brain injury

Neuroblitz, UC Irvine 2021

Traumatic brain injury to primary visual cortex produces long-lasting circuit dysfunction

ABSTRACT OF THE DISSERTATION

Neural circuit reorganization and functional plasticity following traumatic brain injury

by

Alexa Marie Tierno

Doctor of Philosophy in Biomedical Sciences

University of California, Irvine, 2026

Associate Professor Robert F. Hunt, Chair

Traumatic brain injury produces lasting cognitive impairments that can persist long after the initial insult. Although the primary injury may be spatially restricted, its effects on neural circuits can be widespread, beyond the site of tissue damage and evolve over time. In this dissertation, I investigated the effects of brain injury across multiple levels of neural circuit organization, from early patterns of neuronal activation to the functional integrity of hippocampal spatial representations. First, I examined the spatial extent of neuronal activation during the initial response to focal injury using a targeted recombination in active populations (TRAP) reporter mouse model. I found widespread activation of neurons that extended well beyond the glial response to injury. Second, using rabies virus whole-brain tracing, I found that brain injury reorganized inhibitory circuits in the hippocampus, converting interneurons into hyperconnected hubs while reducing their long-range inputs. Interestingly, this same pattern of reorganization was seen in a distant brain region, the prefrontal cortex, that is not directly damaged by the injury. Finally, I examined the functional consequences of chronic circuit disruption within the hippocampus, a structure critical for learning and spatial memory. Using longitudinal *in vivo* calcium imaging of CA1 neurons in freely behaving mice, I evaluated how brain injury alters the activity and spatial coding of individual neurons. Despite relatively preserved overall neuronal activity and the continued presence of place cells, brain injury degraded the precision of spatial

representations in the hippocampus. Place cells exhibited broader tuning and the population of cells capable of participating in spatial representations was diminished after injury. These alterations were accompanied by impaired spatial novelty discrimination, linking disrupted spatial coding and cognitive impairment. Together, these findings support a model in which chronic dysfunction after injury emerges not only from neuronal loss but from widespread and lasting changes in the organization and function of surviving circuits.

INTRODUCTION

The complexity of the brain arises not only from the activity of individual neurons, but from their organization into interconnected networks. Within these networks, patterns of activity are continuously shaped by the integration of sensory input, internal brain states and prior experiences, allowing neural populations to encode and retain information that ultimately translate into behavior. The integrity of neurons and their connections is therefore fundamental to brain function, and perturbations to these relationships can alter information processing across these interconnected circuits. The hippocampus provides an example of this relationship between circuit and function given its anatomical organization, defined pathways and diverse neuronal populations supporting learning and memory. Importantly, organization can be disrupted by neurological disorders, such as traumatic brain injury (TBI), which initiates acute and chronic changes in neuronal activity and circuit connectivity. Examining hippocampal anatomy and physiology alongside the mechanisms and consequences of TBI aids in our understanding of circuit reorganization, neural function, and behavior after injury.

Anatomical organization of the hippocampus

A critical hub for learning and memory through its convergence of a variety of cortical and subcortical inputs is the hippocampus (Squire, 1992). The hippocampus contains not only a diversity of cellular subtypes but each division within the structure has a role in shaping memory processing. As first described by Lorente de No (1934), the main regions of the hippocampus include CA1, CA2, CA3, along with the dentate gyrus, each with a layered structure that allows for inputs and outputs to be distributed. Much of what we know about the hippocampus is through studying the classical cortico-hippocampal circuit, or trisynaptic path. Information from the entorhinal cortex enters the hippocampus through the perforant path and synapses onto the granule cells of the dentate gyrus (Steward and Scoville, 1976). These granule cells send mossy

fiber projections to CA3 pyramidal neurons, which in turn send excitatory input to CA1 neurons through Schaffer collaterals. CA1 neurons comprise the main output of the hippocampus, projecting to subiculum, entorhinal cortex, and other cortical regions (Amaral et al., 1991). The information flow through the circuit depends on the coordinated activity of excitatory principal neurons and the diverse populations of inhibitory neurons. The principal excitatory neurons of CA1, CA2, and CA3 are classified as glutamatergic, pyramidal cells, whose highly organized morphology and laminar arrangement allow integration of activity and hippocampal output (Amaral and Witter, 1989). The pyramidal layer (stratum pyramidale, SP) contains somas of principal neurons whose dendrites extend apically, into the stratum radiatum (SR) and stratum lacunosum-moleculare (SLM), and basally into the stratum oriens (SO). Although hippocampal pyramidal neurons share many similarities, their location within the circuit dictates their connectivity and function. Of relevance, CA1 pyramidal neurons integrate pathways locally and from cortical regions, serving as the major processing center and output of the hippocampus.

CA1 pyramidal neurons

Pyramidal neurons in CA1 are organized in a laminar fashion, with their somas arranged in the pyramidal layer and their dendrites extending into superficial and deep layers (Spruston, 2008). The dendrites are comprised of two domains: the apical and basal dendrites. The apical dendrite extends from the apex of the soma into stratum radiatum and stratum lacunosum-moleculare, while the basal dendrite extends from the base of the soma and into stratum oriens. The dendrites play a pivotal role in synaptic integration that ultimately leads to an action potential, exciting the neuron’s postsynaptic targets.

Pyramidal neurons receive inputs at various locations along the dendritic tree and soma. One of the major excitatory inputs comes from CA3, which arrives at the proximal apical dendrite or sometimes the soma of CA1 neurons through the Schaffer collaterals. CA2 pyramidal neurons

also make excitatory synapses with CA1 neurons, providing an additional source of modulation (Chevaleyre and Siegelbaum, 2010). The most distal part of the apical dendrite receives input from the temporoammonic pathway that originates from the entorhinal cortex. Inputs from the entorhinal cortex come from both the medial and lateral regions. Neurons from layer II/III of the medial entorhinal cortex (MEC) synapse on the proximal end of CA1 while neurons from the lateral entorhinal cortex (LEC) mostly synapse on the distal end. The integration of inputs depends not only on excitatory drive but on the convergence of inhibitory interneuron inputs as well.

Interneurons

Intermingled within each layer are important modulators of the network, the interneurons (Pelkey et al., 2017). This diverse group of cells can be divided into several subtypes, characterized by morphology, projection type, firing patterns, or neurochemical expression profile. Over the years, studies find that even within interneuron subtypes, there are developmental differences that shape the gene expression profiles and thereby how they interact with the hippocampal network. Nearly all interneurons share a common theme which is the use of gamma-aminobutyric acid, or GABA, as their neurotransmitter (Pelkey et al., 2017). GABA neurons have been localized in the brain using immunohistochemistry or in situ hybridization for the enzyme that synthesizes GABA, which is glutamate decarboxylase (GAD) (Erlander et al., 1991). GAD65 and GAD67 have been extensively used to label interneurons, although other markers exist including but not limited to somatostatin (SST), parvalbumin (PV), calretinin (CR), neuronal nitric oxide synthase (nNOS), reelin, neuropeptide Y (NPY), cholecystokinin (CCK), and vasoactive intestinal peptide (VIP) (Freund and Buzsaki, 1996; Klausberger and Somogyi, 2008; Rudy et al., 2011). Developmentally, interneurons are born in the ganglionic eminence, which is subdivided into the medial, lateral, and caudal ganglionic eminences (Wonders and Anderson, 2006). Each of these structures gives rise to different interneuron subtypes. The medial ganglionic eminence (MGE) gives rise to SST and PV cells. These migrate tangentially and populate the neocortex and

hippocampus (Wichterle et al., 1999; Butt et al., 2005). VIP and CCK interneurons are born in the caudal ganglionic eminence (Anderson et al., 2001) while medium spiny neurons that ultimately reside in the basal ganglia migrate from the lateral ganglionic eminence (Stenman et al., 2003). MGE-derived neurons have been studied extensively, especially through their use in cell transplantation studies (Wichterle et al., 1999; Alvarez-Dolado et al., 2006; Baraban et al., 2009; Hunt et al., 2013b; Zhu et al., 2019).

Interneurons innervate specific subcellular compartments of pyramidal neurons and provide precise control over their excitability, synaptic integration and output. For example, SST neurons synapse on the distal parts of the basal dendrites while PV interneurons provide axo-somatic inputs. CCK interneurons also provide somatic inhibition onto CA1 neurons (**Figure 1.1**). In this way, interneurons regulate glutamatergic input and control network activity. This unique ability to control shape synaptic plasticity and downstream behaviors is exemplified by SST interneurons.

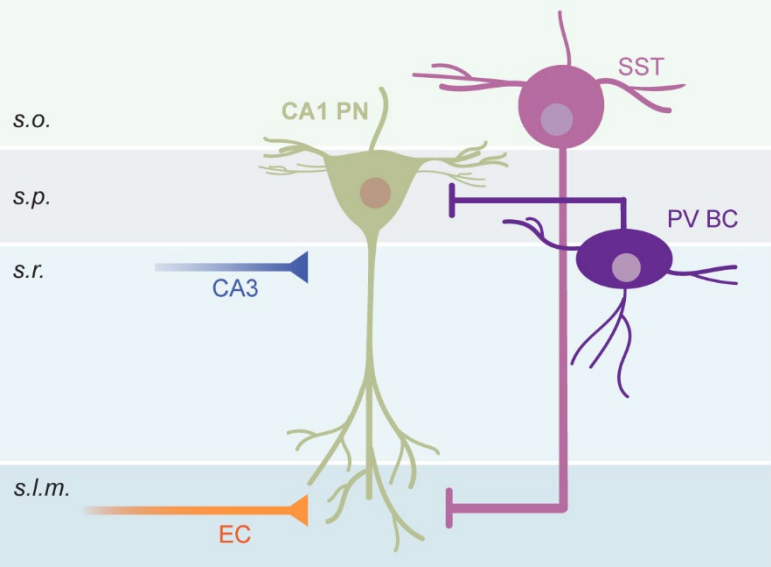


Figure 1.1: Hippocampal CA1 principal cell inputs. CA1 principal neurons (green) receive excitatory input through Schaffer collaterals from CA3 (blue) more proximally on their dendrites, while inputs from the entorhinal cortex (EC; orange) synapse on the most distal dendrites of CA1 neurons (shown on the left side). Interneurons provide different types of inhibitory inputs onto principal cells (shown on the right). PV basket cells provide perisomatic inhibition (purple) while SST interneurons (pink) provide dendritic inhibition.

SST interneurons are found in the neocortex and in the hippocampus (Pelkey et al., 2017). Hippocampal SST neurons are mainly located in stratum oriens of CA1 and the hilus of the dentate gyrus (Katona et al., 1999). CA1 SST neurons extend their processes across several layers and ultimately synapse on the distal dendrites of pyramidal neurons. This allows for modulation of signals coming from the entorhinal cortex, for example (Leão et al., 2012). SST neurons comprise a majority of inhibitory neurons in the hilus and mainly send their projections onto local granule cells and to the septal nucleus (Yuan et al., 2017). They are considered non-fast-spiking cells based on their electrophysiological properties (Pelkey et al., 2017; Klausberger and Somogyi, 2008). Inputs onto SST interneurons are not restricted to the hippocampus, but can arise from the medial septum, diagonal band, and entorhinal cortex. A more in-depth discussion of SST interneuron inputs using rabies tracing and brain clearing experiments that demonstrate brain-wide inputs in the context of brain injury is described in Chapter 3.

Immediate early genes

Anatomical connectivity ultimately shapes when and where neurons become active. One way to identify populations of neurons active by a particular experience is through activity-dependent gene expression. This can be modulated by neurotransmitters, electrical activity, and growth factors, all which play a role in mediating communication and plasticity in the nervous system. A class of genes that are rapidly and transiently transcribed within minutes of a stimulus are called immediate early genes (IEG). These genes were first discovered as proto-oncogenes (Curran and Teich, 1982) but have since been used to study active populations of neurons after stimulation. These include but are not limited to: c-fos, c-jun, Krox24, and Arc (Sheng and Greenberg, 1990).

One of the most commonly studied IEGs is *c-fos*, whose gene expression was first studied in fibroblasts and differentiated PC13 cell lines (Greenberg and Ziff, 1984; Curran and Morgan,

1985). C-fos protein levels are relatively low in neurons at basal levels (Sagar et al., 1988; Hughes et al., 1992). However, within minutes of application of nerve growth factor (NGF), c-fos transcription levels increase. Other stimuli such as activation of voltage-gated calcium channels and neurotransmitter release can also elicit c-fos expression (Greenberg et al., 1986; Morgan and Curran, 1986). Specifically, extracellular calcium entry through NMDA receptor activation leads to increases in c-fos mRNA, which can be blocked using a calcium chelator (Gissel et al., 1997). Additionally, depolarizing stimuli like high potassium concentrations can also lead to the transient expression of c-fos (Didier et al., 1989). This leads to the idea that expression of c-fos can be used as a marker, or correlate, of neuronal activity.

Early studies performed to understand the time dynamics of c-fos were done in models of hyperactivity (Dragunow and Robertson, 1987). In these initial studies, hippocampal seizures were induced and the time course of c-fos immunoreactivity was recorded. Granule cells in the dentate gyrus expressed c-fos at high levels between 30 minutes and 8 hours after seizure activity. In addition to other areas of the hippocampus such as CA1 and CA3 displaying c-fos expression, deeper cortical regions like the amygdala and striatum were also labeled. Given this information, the authors also sought to study c-fos expression in the context of brain injury (Dragunow and Robertson, 1988). Again, a time course of c-fos expression was performed after penetrating injury to the brain and showed that between 1 and 72 hours after injury, there was a massive increase in c-fos expression after injury. Interestingly, this study showed both neurons and glia-like cells expressed c-fos after injury.

In a rat model of TBI, specifically fluid percussion injury, c-fos expression increased within 2 hours and up to 24 hours after injury throughout the ipsilateral cortex, with bilateral expression in areas of the hippocampus (Raghupathi et al., 1995b). CA1 neurons are also intensely labeled by 15 minutes post-injury, returning to baseline by 24 hours (Phillips and Belardo, 1992). Together these

data show that c-fos expression is reliably elevated after injury but the spatial brain-wide extent of this activation has not been carefully characterized. Given the transient nature of IEG expression, injury methodology, and differences in immunohistochemistry antibodies and methods, there are conflicting results on the expression pattern of c-fos following a brain injury and what the implications of this labeling could be.

In the past decade, technological advances have been made to overcome the challenge of transient IEG protein expression. The approach called targeted recombination in active populations (TRAP) was engineered to permanently label neurons that were transiently activated by a stimulus (Guenthner et al., 2013). Mice are genetically engineered to express two important components: a drug-dependent recombinase and a transgene that expresses an effector protein in a recombination-dependent manner. Specifically, a tamoxifen-inducible Cre-recombinase ($CreER^{T2}$) mouse is crossed to reporter mouse that expresses the red fluorescent protein, tdTomato, given excision of the floxed STOP codon. Only upon delivery of tamoxifen, or its active metabolite, 4-hydroxytamoxifen (4-OHT), is a neuron labeled with tdTomato if it was "active," or expressing c-fos during the recombination window (**Figure 1.2**). Throughout Chapter 2, the term "active" is used to describe Ai14-labeled neurons. Given what we know about c-fos expression, "activity" is most likely due to the influx of calcium upon NMDA receptor activation. Improvements to this mouse model have been made (TRAP2), such that endogenous fos expression is preserved, more brain regions are reliably labeled, and the original Cre is codon-optimized (DeNardo et al., 2019). This technique has been extensively used in modern neuroscience to study learning and memory, stress, and neurological disorders (Roy et al., 2022; Lesuis et al., 2025; Brodovskaya et al., 2021, 2025). The spatial extent of a focal injury in mice during the early phase of TBI is described in Chapter 2 using this transgenic model.

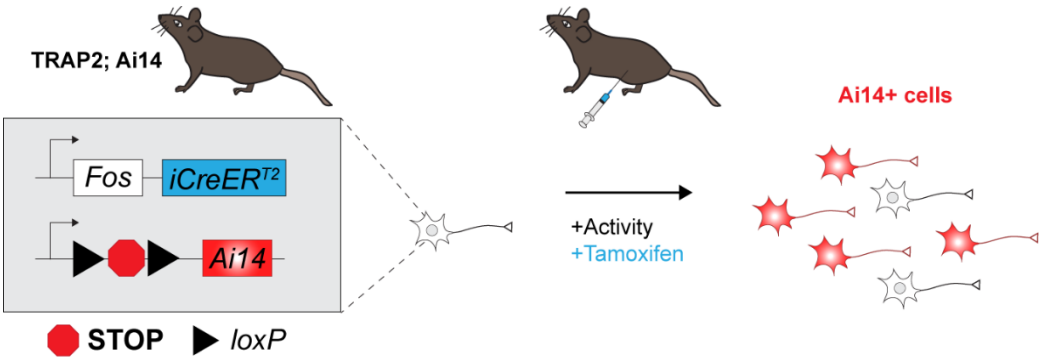


Figure 1.2: Schematic of TRAP2 transgenic mouse model. Upon tamoxifen delivery, Cre is activated, excising the STOP codon, and Ai14 is thereby expressed in neurons where Fos was transcribed

Correlation of spatial representations and place cells

Spatial representations of the external world are critical for survival, navigation and problem-solving. The hippocampus has become the center for studying memory and navigation since the surgical removal of significant portions of patient H.M.'s temporal lobe bilaterally after years of suffering from epilepsy (Scoville and Milner, 1957). One key symptom that was noted in patient H.M. following the surgery, apart from the well-documented retrograde amnesia, was his inability to navigate his way around the hospital, for example to locate the bathroom. This set up a series of fundamental studies for understanding how the hippocampus functions to create and store memories (Squire, 1992).

The development of methods to record hippocampal neuron activity was necessary for our understanding of brain function in awake, behaving mice. Using electrodes capable of recording the activity of single neurons, the relationship between hippocampal cell activity and an animal's location in space could be directly tested and thus the discovery of "place cells" emerged (O'Keefe and Dostrovsky, 1971). Place fields emerge when a place cell will preferentially fire as an animal enters a specific location in their environment (O'Keefe and Conway, 1978). Collectively, the activity of hippocampal place cells forms a neural representation, or cognitive map, of the environment (O'Keefe, 1976).

Place cell dynamics

A defining characteristic of place cells is their ability to consistently fire in specific patterns across repeated experiences of the same environment. When an animal repeatedly explores a familiar environment, individual place cells exhibit increased firing within specific regions in space, referred to as place fields (O'Keefe, 1976) (**Figure 1.3**). These spatial firing patterns can remain remarkably consistent, with neurons maintaining similar place field locations and activity patterns over time (Thompson and Best, 1990). This suggests that hippocampal networks can maintain reliable representations of familiar environments allowing spatial information to be represented across experiences. This is an important feature of hippocampal function and spatial memory.

Stability of place cells can be characterized by looking at a single neuron or a population of neurons. At the single-cell level, the stability of a place cell can be assessed by features such as location, size and firing rate similarity across repeated exposure to an environment. A common approach is to compare the spatial firing rates across two exposures to the same environment using a spatial correlation. Higher correlation values reflect similar patterns of activity, suggesting more stable representations. At the population level, stability can be assessed by determining whether the firing pattern of all neurons remains consistent across experiences. Examining stability at different levels of organization can provide insight into how reliable the hippocampal network represents a specific environment.

Although place cells can maintain consistent spatial firing patterns in familiar environments, their activity is also dynamic, updating rapidly with changes in the environment (Leutgeb et al., 2005). Changes to the shape of the enclosure in which animals are tested alters the activity of place cells, causing them to start firing, stop firing or completely change their firing location (Muller and Kubie, 1987). When an animal is placed in a novel environment, initially the population of place

cells fire less robustly, but with exploration, a place cell code emerges that differs from the familiar environment one (Wilson and McNaughton, 1993). Together, the ability for the population of place cells to change their firing patterns, creating new cognitive maps (remapping), allows animals to distinguish between environments. Importantly, this suggests that place cells participate in multiple representations, allowing the hippocampus to store memories based on different patterns of neural activity. Additionally, the balance between stability and flexibility of the hippocampal network is critical for understanding how disease or injury can alter the dynamics of spatial representations.

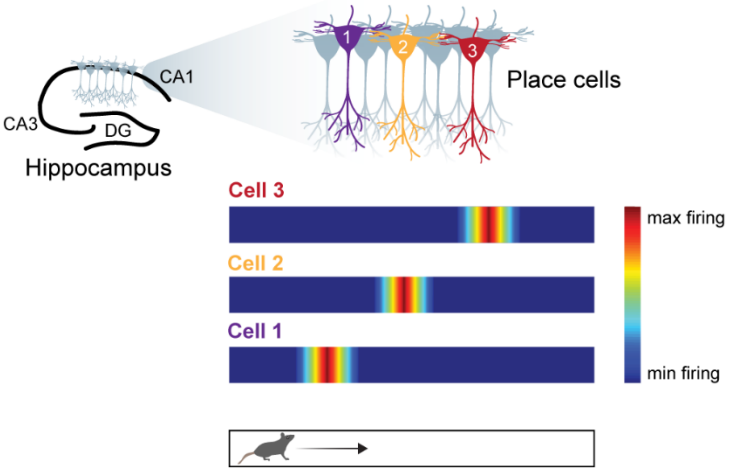


Figure 1.3: Place cell schematic. CA1 pyramidal neurons in the hippocampus that fire preferentially when an animal enters an environment, such as when an animal traverses a linear track are called place cells. Their distinct firing patterns create place fields, which correspond to areas of the track where a neuron will maximally fire (red). Together, these place fields create a cognitive map of the animal's environment.

The dynamic nature of place cells relies heavily on network activity and the ability of pyramidal neurons to integrate inputs locally and from extrahippocampal brain regions. Interneurons play a crucial role in the firing patterns of CA1 pyramidal neurons and hence, spatially modulated cells. Inhibition allows for spatial selectivity in place cells by suppressing out-of-field firing (Grienberger et al., 2017). SST interneurons, providing dendritic inhibition, can regulate the bursting patterns of place cells (Royer et al., 2012). On the other hand, perisomatic inhibition by PV interneurons

regulates pyramidal neuron spiking and oscillation patterns. Local inhibition can therefore constrain the activity of pyramidal neurons into a sparce spatial code needed for processing of spatial representations (Jeong and Singer, 2022).

Using miniaturized calcium imaging to study neuronal population activity

In vivo recording of neurons using electrophysiology paved the way for functional studies and expanded our understanding of neuronal activity at the single-cell level. However, the need to record populations of neurons in a single animal became more important as a way to study network activity. This is particularly important when studying spatial coding given the need to assess spatial responsiveness, tuning and stability at the population-level. Therefore, calcium imaging emerged as a way to simultaneously record hundreds of neurons in a single animal.

Genetically encoded calcium indicators, such as GCaMP, are used to image activity in defined neuronal populations, specifically translating activity-dependent changes in intracellular calcium into changes in fluorescence (Tian et al., 2009; Zhang et al., 2023). In combination with GCaMP, two-photon imaging allows for structural and functional imaging of neurons at cellular resolution (Denk et al., 1990). Although powerful, this technique often requires animals to be head-fixed, which limits the types of behaviors that can be tested. Electrophysiological methods allow for freely moving behaviors but lack the cell-type specificity of calcium imaging. Thus, miniaturized microscopes, or miniscopes, overcome these limitations by allowing optical recordings from fluorescently labeled neurons in freely moving animals that can be longitudinally tracked (Ghosh et al., 2011). UCLA miniscopes have become a popular option for *in vivo* studies given their open-source documentation and relative ease of use (Shuman et al., 2020). For hippocampal preparations, a gradient refractive index (GRIN) lens is implanted into the brain by carefully aspirating the overlying cortex to allow access to hippocampal structures, such as CA1. The

combination of cellular resolution and unrestricted movement make miniscopes an optimal tool for studying hippocampal neuronal activity as it relates to spatial navigation and memory.

The ability to repeatedly record CA1 neuronal activity during freely moving behavior provides a unique opportunity to examine spatial representations over time (Ziv et al., 2013). Individual neurons can be identified as having spatially selective firing patterns. Furthermore, their spatial tuning can be characterized through place field size and stability. The distribution of populations of spatially responsive neurons can also be examined to determine how spatial representations change or reorganize. Thus, using miniscopes to study the hippocampus and other subcortical regions has emerged as a popular and useful tool, especially in disease contexts (Cai et al., 2016; Shuman et al., 2020; Guo et al., 2023; Antonoudiou et al., 2024; de Sousa et al., 2026).

Place cells and disease

Stable and spatially precise place cell activity depends on the coordinated activity of local hippocampal circuits and their afferent inputs. Consequently, disruptions to any part of these circuits can have damaging results on spatial representation, even when place cells remain present. Pathological changes may manifest as more subtle alterations in spatial tuning, place field stability, or remapping. These changes have been observed across several neurological conditions and experimental models of hippocampal dysfunction, suggesting the integrity of the hippocampal place code is sensitive to disturbances in the cellular and network mechanisms supporting normal hippocampal function.

Alterations in place cell dysfunction have been well characterized in conditions related to hippocampal-dependent cognitive impairment. In models of epilepsy, characterized by cell loss in hippocampal regions together with circuit reorganization, place cells have been shown to be dysfunctional. Following status epilepticus, place cells display disorganized place fields that are

less stable, leading to deficits in spatial memory tasks (Liu et al., 2003). In contrast, an acute seizure produces transient suppression of place cell activity and memory performance, which recovers by 24 hours. In epileptic mice, place cells display reduced firing rates and decreased in spatial information, while previously inactive neurons displayed spatially modulated firing patterns (Lenck-Santini and Holmes, 2008). These observations suggest that seizure activity can induce remapping of hippocampal representations, potentially disrupting the fidelity of neural representation of familiar environments.

Impaired spatial coding can arise not only from neuronal loss but from disruption of the temporal coordination of hippocampal circuits. In a model of temporal lobe epilepsy, the pattern of interneuron firing was desynchronized between CA1 and the dentate gyrus (Shuman et al., 2020). Rodents also display profound reductions in place cells numbers and their information content, accompanied by progressive deterioration of stability across repeated sessions shown through remapping. Together, these findings suggest that precise coordination of inhibitory and network activity is crucial for maintaining spatial representations and disruptions to this coordination may contribute to cognitive impairment in epilepsy.

Alzheimer's disease provides another well-characterized model of how pathological disruption of hippocampal circuitry can affect spatial representations without complete elimination of place cell activity. The Tg2576 model of Alzheimer's disease, animals exhibited larger place fields and reduces spatial information in conjunction with spatial memory deficits (Cacucci et al., 2008). Whereas repeated exposure to a familiar environment increases stability of spatial representations, in the case of APP transgenic mice, spatial firing maps were less reliable and precise (Zhao et al., 2014). Hippocampal disruption of spatial representations extends beyond the single neuron level deficit. In the 3xTg model, not only were CA1 place cell representations less stable, but the coordination of place cell firing with theta and slow-gamma oscillations was

reduced (Mably et al., 2017). Importantly, the effects of Alzheimer's-related pathology on spatial deficits are not uniform. Grid cells of the entorhinal cortex from young APP knock-in mice displayed spatial coding impairments while their CA1 place cells showed no deficits in their ability to code for space (Jun et al., 2020). This points to the idea that different components of the entorhinal-hippocampal circuit may exhibit distinct temporal vulnerabilities to pathological disruption.

The relationship between hippocampal circuit integrity and spatial coding is particularly relevant in the context of brain injury. TBI can produce persistent alterations in hippocampal cellular and circuit dysfunction and is frequently associated with deficits in learning and memory. Few electrophysiological studies, however, have demonstrated alterations in hippocampal neuronal representations following a mild brain injury. Following a mild fluid percussion injury, rats demonstrated a reduction in the number of neurons exhibiting task-related spatial activity (Eakin and Miller, 2012). More direct examination of hippocampal CA1 place cells has shown that a mild fluid percussion injury reduces the spatial information context of CA1 neurons and produces larger, less stable place fields (Broussard et al., 2020). Additionally, place cells failed to exhibit the normal increase in firing rate associated with novelty, coinciding with poor performance on an object location memory task. Notably, these alterations occur in the absence of overt neuronal loss. Determining whether these circuit-level alterations are accompanied by changes in the development, maintenance and precision of hippocampal place cell representations may provide insight into mechanisms of cognitive dysfunction after brain injury.

Traumatic brain injury (TBI) – epidemiology and classification

TBI is defined as an external force, such as a forceful bump, blow, or jolt to the head that disrupts normal brain function (Center for Disease Control and Prevention, 2025; Menon et al., 2010). TBI is a heterogeneous brain disorder with considerable variability in presentation. Brain injuries can

be penetrating, nonpenetrating or both depending on the cause of the injury. Nonpenetrating injuries commonly occur as a result of a fall, motor vehicle accident, sports-related injury, or assault. A penetrating injury occurs when an object, such as a bullet or bone fragment, enters the brain tissue. Immediately after a brain injury, patients report dizziness, headache, or confusion. Depending on the injury severity, symptoms can evolve to loss of consciousness, coma or even death.

Over 60,000 deaths in the United States can be attributed to TBIs (Center for Disease Control and Prevention, 2021). This brain disorder affects people of all ages but is more common in males than in females (Maas et al., 2022). Although mild TBIs, such as concussions, can resolve on their own, patients with severe brain injuries typically live with long-lasting disabilities that affect their independence and daily activities (Thornhill et al., 2000; Corrigan and Hammond, 2013).

The difficulty of diagnosing and treating brain injuries stems from the heterogeneity of TBI. Clinicians commonly use the Glasgow Coma Scale (GCS) to diagnose patients who have sustained a brain injury based on their level of consciousness by testing eye, motor and verbal function (Teasdale and Jennett, 1974). Broadly, mild TBI occurs when the patient has suffered only a transient alteration in their mental state, while a severe TBI involves an extended period of time when the patient lost consciousness or has suffered amnesia (Obasa et al., 2024). Injury severity is rated on a 15-point scale, with 13-15 being a mild TBI, 9-12 being a moderate TBI, and <9 being a severe TBI. The GCS, however, does not consider the pathophysiology, anatomy, or mechanism of the injury. It is also difficult to diagnose different age populations using the GCS alone, especially in mild TBI cases that may not present with overt symptoms.

Anatomical location of the injury can also aid in classifying the injury type and severity (Saatman et al., 2008). Paired with computed tomography (CT) scans or magnetic resonance imaging

(MRI), this classification helps reveal more about the structural damage to the brain and insights on how to proceed with treatment (Maas et al., 2008). Advances in imaging resolution, including diffusion tensor imaging, can identify more mild damage to small white matter tracts and small brain bleeds. In addition, the mechanisms of injury can lead to reasonable predictions about the severity of the injury. For example, contusion or epidural hematomas can result from focal injuries, such as when the head is struck or strikes an object (contact injury). In contrast, noncontact injuries where the brain moves within the skull, can cause more diffuse injuries like concussion, subdural hematomas, or diffuse axonal injury (Saatman et al., 2008).

Whereas clinical TBI can be classified using GCS, loss of consciousness and imaging, experimental TBI is defined according to model or mechanism of injury, injury severity, focal versus diffuse pathology, single versus repetitive injury, and post-injury timepoint. These distinctions are important because different experimental TBI methods reproduce different components of the heterogeneous pathology observed in human TBI patients, especially related to memory dysfunction and seizure occurrence.

Memory after TBI

The initial presentation and characteristics of brain injury are not always necessarily a predictor of the neurological consequences that emerge post-injury. TBI patients commonly report persistent cognitive, behavioral, and neurological impairments. Of these, memory impairments and post-traumatic epilepsy are the most related to hippocampal dysfunction after TBI.

Memory problems constitute a common and potentially long-lasting consequence of brain injury. Deficits in learning and memory are frequently reported after TBI and can persist beyond the acute stages of injury, particularly following moderate to severe injuries (Vakil, 2005). These impairments are not restricted to a single memory process but can affect encoding, acquisition

and retrieval of information, such as in episodic memory (Paterno et al., 2017). The persistence of cognitive impairment varies across patients, typically influenced by severity and characteristics of the injury. Although severe TBI is strongly associated with long-term cognitive dysfunction, the location of injury can also factor in determining long-term impairment. The hippocampus is particularly relevant to memory dysfunction after TBI. Hippocampal atrophy is commonly observed in TBI patients, accompanied by memory problems (Bigler et al., 2002; Himanen et al., 2005; Ariza et al., 2006). Damage, however, is not restricted to the hippocampus. Diffuse axonal injury and disruption of white matter pathways can interfere with communication between brain regions that are involved in memory processing, and the severity and type of impairment can depend on the specific pathway damaged (Kinnunen et al., 2011).

Greater injury severity and the extent of structural damage are associated with poorer cognitive outcomes (Dikmen et al., 2009). Structural changes to the brain can continue well beyond the acute injury period, including progressive tissue loss and alterations in white matter (Farbota et al., 2012). This suggests that memory dysfunction cannot be attributed solely to damage sustained at the time of injury, but the progressive cellular and circuit-level changes that develop following injury.

Post-traumatic epilepsy (PTE)

In addition to persistent cognitive impairment, TBI can produce long-term alterations in neuronal excitability that increase the risk of recurrent seizures and development of PTE. PTE refers to the development of recurrent unprovoked seizures attributable to the TBI and is highly prevalent after TBI (Frey, 2003; Pease et al., 2024). Seizures occurring within the first 7 days of injury are referred to as post-traumatic seizures, whereas seizures occurring after that are considered late post-traumatic seizures (Agrawal et al., 2006).

The incidence of PTE varies across patient populations and is strongly influenced by characteristics and severity of TBI (Annegers et al., 1998; Zhong et al., 2025). The risk of PTE is particularly high following severe TBI and can persist for many years. Importantly, PTE can emerge in the latent period after injury, ranging from 8 days to 20 years (Yu et al., 2021). The delayed onset is also indicative of the progressive changes of neural circuits within the injured brain, not simply as a direct consequence of the mechanical insult. Greater injury severity, prolonged loss of consciousness, post-traumatic amnesia, intracranial hemorrhage, subdural hematoma, contusions, and skull fracture are all risk factors for developing PTE (Hunt et al., 2013a). The occurrence of post-traumatic seizures can also predict whether a patient will develop PTE (Ferguson et al., 2010; Ritter et al., 2016).

The persistence of cognitive dysfunction and increased susceptibility to epilepsy demonstrates that the consequences of TBI extend well beyond the initial insult. Therefore, it is necessary to understand the progression of cellular and circuit-level changes that arise after TBI to link the acute injury to long-lasting neurological dysfunction and alterations in network excitability.

TBI – cellular and circuit plasticity

TBI is a dynamic process in which the primary injury initiates a series of secondary cellular responses that continue to alter neural circuits throughout the post-injury timeline. These processes occur across overlapping timescales, starting with immediate structural damage and cell death, followed by secondary biochemical and inflammatory responses and ultimately long-term circuit reorganization (Pearn et al., 2017). Thus, understanding TBI disease progression is critical for determining how acute injury affects cognitive outcomes (**Figure 1.4**).

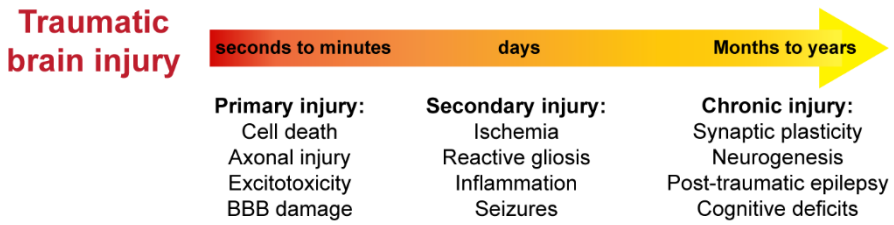


Figure 1.4: Timeline of traumatic brain injury.

Primary injury refers to the immediate and largely irreversible damage to brain tissue caused by the biomechanics of the initial insult (Ray et al., 2002). Depending on the mechanisms of injury, compression, tension and shear forces all contribute to the disruption of neuronal membranes, axons, blood vessels and surrounding tissue. Within the first minutes to hours after injury, mechanical deformation of the plasma membrane can lead to a dysregulation of ion flow with detrimental effects. With higher shear forces, blood vessels can rupture, leading to intracranial hemorrhage. At the tissue level, these processes can result in contusion, edema, diffuse axonal injury and direct neuronal loss (Werner and Engelhard, 2007; Maas et al., 2008). Primary injuries initiate a cascade of events that lead to secondary injury mechanisms.

Although tissue damage is greatest focally, at the site of injury, neuronal degeneration is not necessarily restricted to the region directly damaged by the mechanical insult. Brain regions anatomically connected to the injured tissue can undergo degeneration. One such structure that is particularly susceptible to neuronal loss after TBI is the hippocampus (Hunt et al., 2013a). Damage within hippocampal subregions is especially relevant given the role of the hippocampus in learning and memory. The initial loss of neurons following TBI removed cells from the circuit in addition to setting the stage for subsequent circuit reorganization.

In response to primary injury, secondary injury evolves over minutes to days after TBI and involves cellular and physiological mechanisms that can lead to progressive tissue damage (Werner and

Engelhard, 2007). Ionic homeostasis is disrupted and increases in intracellular calcium can activate proteases that degrade the cytoskeleton (Wolf et al., 2001; Saatman et al., 2010). Excessive glutamate release and the activation of NMDA receptors, as a consequence of elevated calcium levels, can further increase calcium influx. This cycle of excitotoxicity continues and exacerbates ion leakage, compromising neuronal function and survival. Delayed cell death occurs during this phase of injury, leading to the release of toxins into the extracellular space. Ionic imbalance creates substantial energetic demands as neurons attempt to maintain membrane potential, contributing to mitochondrial dysfunction and free radical and reactive oxygen species buildup (Hunt et al., 2013a). Excitotoxicity is accompanied by blood-brain-barrier disruption, edema, and a robust and rapid inflammatory response which involves microglia, astrocytes and infiltrating immune cells, peaking within the first days after injury (Morganti-Kossmann et al., 2002). Secondary injury responses create an environment in which surviving neurons and circuits attempt to retain function.

While neuronal loss is a prominent consequence of both primary and secondary injury, the long-term functional outcome of TBI is also determined by how surviving neurons respond to the post-injury environment. Loss of neurons and their synaptic connections disrupts patterns of excitation and inhibition, which requires circuits to adapt to changes in local and long-range inputs. This is particularly important in the hippocampus, as it undergoes substantial circuit reorganization after TBI. In addition to loss of principal neurons, injury can disrupt inhibitory interneuron populations (Lowenstein et al., 1992; Toth et al., 1997; Santhakumar et al., 2000; Buritica et al., 2009; Swartz et al., 2006; Cantu et al., 2015; Almeida-Suhett et al., 2015; Frankowski et al., 2019). Changes in GABAergic signaling, including reductions in $GABA_A$ receptor expression and inhibitory synaptic transmission, can shift the balance between excitation and inhibition within CA1 and dentate gyrus of the hippocampus (Almeida-Suhett et al., 2015; Raible et al., 2015; Becerra et al., 2021). At the same time, surviving neurons undergo a number of electrophysiological changes after TBI that

can ultimately affect function. These changes are not necessarily uniform across neuronal populations. For example, following experimental TBI, dentate granule cells receive more excitatory inputs, accompanied by a decrease in inhibitory inputs (Hunt et al., 2010, 2011). On the other hand, inhibitory neurons in the hilus have increases in excitatory inputs after injury (Hunt et al., 2011).

Chronic injury is characterized by the emergence of neural circuit reorganization in response to the neuronal loss, inflammation, and disrupted connectivity. As acute cellular responses subside, structural and functional alterations can persist for months to years following TBI. Commonly seen in temporal lobe epilepsy models, dentate granule cells of the hippocampus sprout collaterals and form recurrent networks, also known as mossy fiber sprouting (Cronin and Dudek, 1988; Swartz et al., 2006). This mossy fiber sprouting is also present after TBI and is more robust in cases of severe TBI compared to mild TBI (Hunt et al., 2009). These anatomical changes can be associated with network dysfunction as these newly formed, functional recurrent networks could be contributing to synchronous activity seen after brain injury (Hunt et al., 2009, 2010). Persistent changes can lead to hippocampal excitability and subsequently PTE (Gupta et al., 2014; Agrawal et al., 2006). Additionally, post-traumatic plasticity can also disrupt the precise organization of hippocampal circuits, changing the way information, such as memory, is processed.

Chronic functional deficits despite the survival of neuronal populations suggest that neuronal loss alone cannot account for chronic neurological dysfunction after brain injury. To better understand the mechanisms by which brain injury affects circuit function and behavior over time, a variety of pre-clinical models of TBI have been established.

In vivo modeling of TBI using rodent models

Several preclinical models of brain injury have been proposed in an attempt to understand how cellular and physiological changes after TBI contribute to the long-term neurological outcomes. The advantage of using these models is the ability to investigate injury processes under controlled conditions, changing the biomechanics, severity and timing of injury. No experimental model captures the full heterogeneity of human TBI, thus model selection depends on the biological question.

Closed head injury models, where the skull remains intact prior to impact, can lead to blood-brain-barrier disruptions, edema, and neurological function deficits (Shapira et al., 1993). Weight drop TBI induces injury through the impact of a falling mass and depending on the experimental preparation, can produce focal and diffuse pathology (Feeney et al., 1981; Marmarou et al., 1994). Blast injury models, mimicking the type of injuries military personnel sustain, use a compression-driven shock tube to simulate blast effects, resulting in diffuse axonal injury, cerebral edema and neurological dysfunction (Cheng et al., 2010; Reneer et al., 2011). Recently, a Closed-Head Impact Model of Engineered Rotational Acceleration (CHIMERA) was developed, causing damage to major white matter tracts along with inflammation and neurodegeneration, without causing obvious tissue deformation (Namjoshi et al., 2014; McNamara et al., 2020).

On the other hand, open head injury models create an injury through a craniotomy, or open skull, and impact the dura directly. The lateral fluid percussion model inflicts an insult by a pendulum striking a piston of a reservoir of fluid to generate a fluid pressure pulse to the intact dura (McIntosh et al., 1987, 1989; Dixon et al., 1987). This model can replicate the intracranial hemorrhage, edema and progressive grey matter damage seen in human TBI patients (Graham et al., 2000; Xiong et al., 2013). The controlled cortical impact (CCI) is another commonly used model for open head injury, where the rigid impactor will directly strike the intact dura, creating a TBI. The work described in subsequent chapters utilizes the CCI model, described below.

Developed over 30 years ago to study brain injury in ferrets, the controlled cortical impact (CCI) model is one of the most widely used experimental closed head TBI models that has since been refined (Lighthall 1988). The biomechanics of the injury can be studied well using this model (Dixon et al., 1991). Not only are the experimental parameters tightly controlled but CCI can model contusive injuries that are restricted to particular brain regions. The CCI device is composed of a steel small-bore impactor with a pneumatically-driven piston that is electronically controlled. The impactor is mounted on a crossbar with adjustable height that allows the impactor tip to contact and compress the brain surface through a craniotomy to a predetermined depth. The velocity of the impactor can also be adjusted by controlling the air pressure. Since its development, it has been adapted to study TBI in other species such as rats (Dixon et al., 1991), mice (Smith et al., 1995), swine (Alessandri et al., 2003; Manley et al., 2006), and non-human primates (King et al., 2010).

An important advantage of CCI is its ability to reproduce several pathological and functional consequences observed following TBI. One common feature in humans after TBI is neuron loss that occurs rapidly in neocortex and hippocampus (Buritica et al., 2009; Swartz et al., 2006). CCI also reproduces this, with cell death reported as early as 1 hour after impact in the CA3 region of the hippocampus (Baldwin et al., 1997). Neuronal loss remains prevalent at 48 hours after CCI in mice, with degenerating neurons present near the injury site (Smith et al., 1995). Fluorojade and silver staining reveal similar patterns of neurodegeneration in the hippocampus that peak at 48 hours post-TBI and largely subside by 7 days (Anderson et al., 2005; Hall et al., 2005, 2008). These changes are accompanied by a robust microglial and astrocytic response (Smith et al., 1995, Zhu et al., 2019; Frankowski et al., 2021) and by structural pathology extending beyond the focal site of impact (Hall et al., 2008). Although CCI causes an initial spatially restricted injury, the

downstream consequences are not restricted to the immediate lesion. Brain-wide effects after CCI will be discussed further in Chapters 2 and 3.

CCI is a widely used model for studying the evolution of brain injury and its long-term consequences relevant to human TBI. Experimental TBI can produce alterations in neuronal excitability and spontaneous seizure activity which make CCI useful for investigating the mechanisms contributing to the development of PTE. The incidence of seizure activity is influenced by injury severity, with more severe injuries resulting in a higher likelihood of spontaneous seizures. In addition, memory deficits can be experimentally replicated using the CCI model. For example, latency to find a hidden platform on a Morris Water Maze is significantly increased in mice with TBI suggesting deficits in spatial navigation (Hamm et al., 1992; Smith et al., 1995). Additionally, CCI can disrupt the ability for a mouse to discern between a moved object in an object location memory task (Zhu et al., 2019). More specifically, spatial memory deficits are evident in CCI mice, where they display a lack of discrimination between a novel environment in a fear conditioning paradigm (Zhu et al., 2019).

To understand how neural circuit function and network activity is affected after TBI, a brain-wide to cellular-level approach is necessary. In the next chapters, I will be discussing the brain-wide extent of neuronal activation (Chapter 2), circuit reorganization (Chapter 3), and how hippocampal place cell activity is disrupted following TBI (Chapter 4). Finally, I will conclude with final remarks related to my work and describe potential future experiments.

CHAPTER TWO

Cortex-wide neuron activation after traumatic brain injury in mice

Abstract

Following a traumatic brain injury (TBI), the neocortex undergoes time-dependent cellular responses including immediate tissue deformation, enhanced excitability, and elevated expression of immediate early genes. However, the spatial extent of early neuronal activity after a focal injury remains unclear. Here we use targeted recombination in active populations reporter mice of both sexes to identify neurons activated in the acute phase following a controlled cortical impact injury applied to the somatosensory neocortex. We find widespread cell activation across large portions of the cortex that extends beyond the astrocytic and microglial responses marking the injury site. Activated cells are predominantly neurons, and few cells co-label with GFAP or IBA1. Our findings reveal that even focal injury engages cortical circuits across large portions of the injured brain, highlighting the importance of considering cortex-wide neuronal dynamics in the early postinjury period and their potential impact on network excitability, remodeling, and recovery.

Introduction

Traumatic brain injury (TBI) can lead to life-long physical, emotional, and cognitive disabilities. The initial response to injury involves a wide range of modifications to brain structure and function, including tissue deformation, excitotoxicity, cell death, neuroinflammation, metabolic dysfunction, and progressive neural circuit remodeling (Hunt et al., 2013). One of the most robust indicators of acute brain damage is the activation of immediate early genes (IEGs; Herrera and Robertson, 1996). IEGs, such as *fos* and *Arc*, are genes that are expressed at low levels in quiescent cells but become rapidly activated by cellular stimulation (Sheng and Greenberg, 1990; Lanahan and

Worley, 1998). As a result, IEG expression is frequently used as a marker of neuronal activity in studies attempting to link brain circuit function to behavior (Guzowski et al., 2005; DeNardo and Luo, 2017; Nambu et al., 2022) and in experimental models of epilepsy (Dragunow and Robertson, 1987; Lauterborn et al., 1996), ischemia (Kiessling and Gass, 1993), or TBI in rodent and human (Dragunow and Robertson, 1988; Raghupathi et al., 1995b; Dutcher et al., 1999).

In experimental models, TBI is almost immediately followed by increased expression of IEGs in the neocortex and hippocampus, as determined by histological analysis. Among studies of comparable injury severities, some have shown IEG activation focally restricted to areas near the lesion (Dragunow and Robertson, 1988; Dragunow et al., 1990; Förstner and Knöll, 2020) whereas other studies have documented more widespread patterns of IEG activation involving c-*fos* expression in one or both hemispheres (Phillips and Belardo, 1992; Yang et al., 1994, 1995; Belluardo et al., 1995; Raghupathi et al., 1995a; Abrous et al., 1999). Although more commonly used as an activity marker, IEGs have been repeatedly shown to participate in molecular mechanisms of plasticity underlying behavior, such as memory (Nambu et al., 2022). This raises the possibility that acute IEG expression may mark sites of future circuit remodeling, which could involve areas across the brain beyond the site of injury (Harris et al., 2016; Frankowski et al., 2022). Therefore, a deeper understanding of acute neuron activation in response to TBI is important, because it has the potential to reveal the earliest evidence that a neuron will undergo synaptic changes. Here we used a transgenic mouse line, called targeted recombination in active populations (TRAP), to label all of the cell populations that were activated by a controlled cortical impact (CCI) injury. This approach revealed extensive neuron activation across the neocortex, hippocampus, and select subcortical brain areas.

Materials and methods

Animals

All animal procedures were performed under Institutional Animal Care and Use Committee (IACUC) approval by the University Laboratory Animal Resources and adhered to National Institutes of Health Guidelines for the Care and Use of Laboratory Animals. Experiments were performed on adult mice of both sexes maintained in standard housing conditions on a 12 h light/dark cycle with food and water provided *ad libitum*. Homozygous Fos$^{tm2.1(icre/ERT2)Luo/J}$ (or TRAP2) mice (Jax Stock No: 030323) were crossed with homozygous Cg-Gt(ROSA)26Sor$^{tm14(CAG-tdTomato)Hze/J}$ (or Ai14) reporter mice (Jax Stock No: 007914) to produce hemizygous offspring, as done previously (DeNardo et al., 2019).

Brain injury

CCI injury was performed on male and female mice at Postnatal Day(P)60 (Frankowski et al., 2022). Briefly, mice were anesthetized by 2% isoflurane inhalation and placed on a custom stereotaxic frame. The skull was exposed by a midline incision, and a 4–5 mm craniotomy was made ~1 mm from the sagittal suture and centered between the lambda and bregma. The skull cap was removed using fine forceps. The CCI device consisted of a computer-controlled, pneumatically driven impactor fitted with a beveled stainless-steel tip 3 mm in diameter (Precision Systems and Instrumentation; TBI-0310). Brain injury was delivered to the neocortex using the following parameters: depth, 1.0 mm; velocity, 3.5 m/s; and dwell time, 500 ms. The incision was sutured without replacing the skull cap, and animals were allowed to recover on a heating pad. All animals, except a portion of controls, received buprenorphine hydrochloride (Buprenex; 0.05 mg/kg, i.p.) at the time of surgery and 12 h later. Control mice were anesthetized by 2% isoflurane and remained anesthetized for ~30 min (or about the duration of a CCI surgery) and allowed to recover on a heating pad.

Tamoxifen preparation and delivery

Tamoxifen (Sigma-Aldrich, catalog #5648) was dissolved at 20 mg/ml in corn oil (Sigma-Aldrich, catalog #C8267) by shaking at 37°C overnight. Immediately prior to CCI surgery, all mice were injected intraperitoneally with 75 mg/kg of tamoxifen. Similar studies using tamoxifen injections have been performed in a contusion model of spinal cord injury (Brown et al., 2022).

Immunohistochemistry

Mice were transcardially perfused with 4% paraformaldehyde (v/v), and free-floating vibratome sections (50 µm) were processed using standard immunostaining procedures. Primary antibodies were chicken anti-NEUN (1:1,000; Millipore, catalog #Abn91, RRID:AB_11205760), rabbit anti-DsRed (1:1,000; Takara Bio, catalog #632496, RRID:AB_10013483), mouse anti-GFAP (1:500; Millipore, catalog #MAB3402, RRID:AB_94844), and rabbit anti-IBA1 (1:1,000; FUJIFILM Wako Pure Chemical, catalog #019-19741, RRID:AB_839504). For secondary antibodies (1:1,000; Life Technologies), we used Alexa Fluor 488-conjugated goat antibody to mouse IgG (catalog #A-11029, RRID:AB_2534088), goat anti-chicken (catalog #A-11039, RRID:AB_2534096), Alexa Fluor 546-conjugated goat antibody to rabbit (catalog #A-11035, RRID:AB_2534093), and Alexa Fluor 647-conjugated goat antibody to rabbit (catalog #A-21244, RRID:AB_2535812). Blocking buffer consisted of 10% normal goat serum, 1% BSA, and 0.1% Triton X-100 in PBS; primary antibodies were incubated overnight at 4°C and secondary antibodies incubated at room temperature for 2 h. As expression of tdTomato was already strong in activated cells, we did not perform immunostaining against tdTomato in most experiments. Sections were then mounted on charged slides (Superfrost plus, Thermo Fisher Scientific) with Fluoromount-G that contained DAPI. Epifluorescent images were obtained using a Leica DM6 microscope with the Leica LAS X software. Confocal images were obtained with an Olympus FV3000 laser scanning microscope. Brightness and contrast were adjusted manually using FIJI (ImageJ) and applied to the entire image.

Volumetric analysis

Coronal brain sections (50 µm thick, 300 µm apart) that comprised the entire rostral to caudal extent of the lesion were mounted on slides and coverslipped with Fluoromount-G containing DAPI. Sections were imaged at 5× magnification using a Leica DM6 microscope. Eight sections were analyzed per animal, and the percentage of the ipsilateral cortex remaining was calculated by outlining the borders of the neocortex in both hemispheres using FIJI (ImageJ) and calculating the ratio of ipsilateral to contralateral cortex volume (Frankowski et al., 2019; Zhu et al., 2019). The neocortex was defined as the region between the dorsal aspect of the corpus callosum and the pial surface. Regions of the cortical subplate (e.g., amygdala, endopiriform nucleus) were excluded from analysis.

Immunostaining analysis

Fluorescently labeled sections (50 µm, 300 µm apart) were imaged at 5–40× using a Leica DM6 microscope or Olympus FV3000 confocal microscope and quantified using FIJI (ImageJ). For quantification of the percentage area, the ipsilateral and contralateral cortical area was outlined, and the percentage area above the fluorescence threshold was measured using ImageJ according to a previous protocol (Jensen, 2013; Frankowski et al., 2021). The same settings were used for all sections. For measurements of the dorsal neocortex, a region of interest was drawn 2 mm lateral to the edge of the cavity in the ipsilateral neocortex, and 16 consecutive sections (every sixth coronal section, 300 µm apart) were quantified and averaged per animal. For paraventricular nucleus of the thalamus (PVT) and somatosensory neocortex analyses, three consecutive brain sections 300 µm apart were analyzed through the PVT or somatosensory cortex per animal. For colocalization analysis, a region of interest was randomly selected lateral to the contusion cavity in the ipsilateral neocortex. All cells that expressed Ai14 and/or NEUN, GFAP, and IBA1 were counted at the lesion epicenter and ±300 µm from the lesion epicenter, and the values were averaged to obtain a mean percent cell colocalization per animal.

Statistical analysis

All statistical tests were performed with GraphPad Prism 10. Data were compared by two-tailed Student's *t* test, two-way ANOVA followed by a Tukey post hoc test for multiple comparisons, two-way repeated–measures ANOVA followed by Bonferroni's post hoc test or Fisher's exact test. Normality was assessed in GraphPad at the time of analysis. Data are expressed as mean ± SEM, N = animals, and significance was set at $p < 0.05$.

Results

To visualize early neuron activation in response to TBI, we used TRAP, which allows for permanent genetic labeling by a specific experience (DeNardo et al., 2019). We crossed a TRAP2 Cre-driver mouse line with mice expressing Ai14 as a reporter and delivered a 1.0 mm depth CCI injury over the somatosensory cortex at P60 (**Figure 2.1A**). Control mice were anesthetized but did not receive a brain injury. Mice were administered tamoxifen immediately prior to brain injury to label cells activated within a recombination window up to 36 h after the time of brain injury (Guenthner et al., 2013; Onishi et al., 2024). Upon visual inspection of the lesion site after impact, the dura was found to be intact in the brain-injured animals.

At 7 d after TBI, the lesion consisted of a cavity extending through the thickness of the neocortex and included substantial distortion of the hippocampus ($N = 3$ mice). Uninjured controls showed no overt cortical lesion in any animal examined (**Figure 2.1**). Brain-injured animals had ~20% decrease in cortical volume ipsilateral to the injury, as compared with uninjured controls (**Figure 2.1B**; control, 100 ± 0.3%; TBI, 83 ± 1.1%; $p = 0.002$; two-tailed *t* test). This is nearly identical to prior observations using similar impact parameters (Frankowski et al., 2019; Zhu et al., 2019). Next, we examined neuronal activation after TBI by quantifying Ai14 reporter expression, which labels cells that were active around the time of injury, in the ipsilateral and contralateral neocortex.

In uninjured controls, Ai14 expression was very low, as expected (DeNardo et al., 2019), with Ai14-labeled cells found sparsely distributed throughout the brain (**Figure 2.1C,D**). We found a significant increase in the percentage of Ai14 area in the ipsilateral, but not contralateral, hemisphere in mice that received a TBI, as compared with controls (**Figure 2.1C,D**). In brain-injured animals, Ai14+ cells were found throughout the ipsilateral neocortex. We also noted substantial Ai14+ expression in the amygdala, internal capsule, cerebral peduncle, and lateral thalamic nuclei known to interact with the somatosensory neocortex, including the reticular thalamus and ventrobasal complex. In the hippocampus, moderate Ai14+ expression was observed in dentate gyrus granule cells of the contralateral hemisphere at the injury epicenter of all brain-injured animals. Ai14 expression was sparse or absent in these brain areas of control animals. These results suggest brain injury produces an early, but selective, activation of multiple cortical and subcortical brain areas.

Having previously observed brain-wide reorganization of interneuron circuitry in the prefrontal cortex (PFC) (Frankowski et al., 2022), which interacts with the dorsal hippocampus but is not directly damaged by CCI injury (Hall et al., 2005, 2008; Frankowski et al., 2022), we asked whether PFC is activated by the acute injury. Quantification of Ai14+ cells in the prelimbic area of PFC revealed a significant increase in cell activation in the injured hemisphere (**Figure 2.1E,F**).

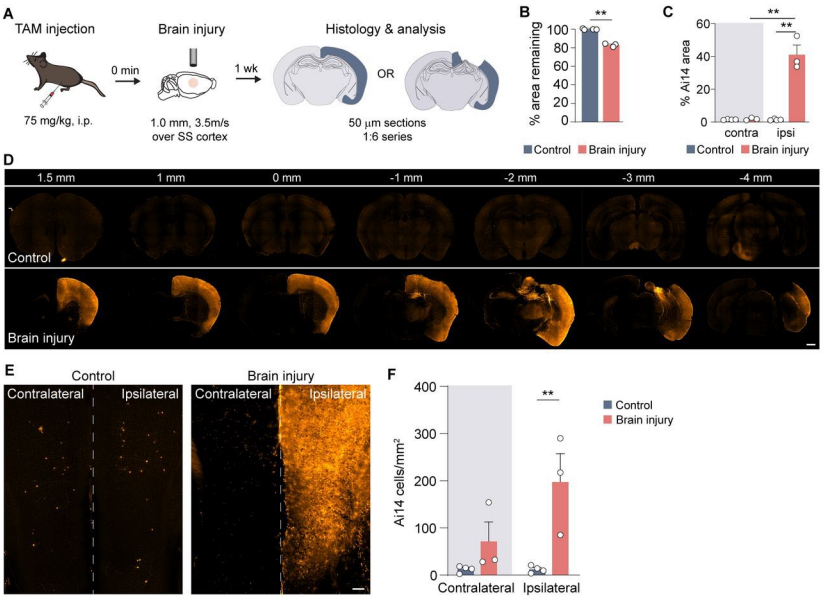


Figure 2.1: Hemisphere-wide cell activation following TBI. A. Experimental design schematic. **B.** Quantification of the percentage tissue remaining ipsilateral to the injury in control and brain-injured mice. $^{**}p = 2.3 \times 10^{-3}$, control versus TBI; two-tailed *t* test, $N = 3–4$ mice per group. **C**. Quantification of the percentage area of Ai14 expression in contralateral or ipsilateral hemispheres. $^{**}p = 2.27 \times 10^{-6}$, control versus brain injury; $^{**}p = 4.59 \times 10^{-6}$, brain injury ipsilateral versus contralateral; two-way ANOVA with Tukey's post hoc analysis, $N = 3–4$ mice per group. **D**. Coronal brain sections of Ai14 reporter expression every 300 µm through the brain of representative control and brain-injured animals. Scale bar, 1 mm. **E**. Ai14 reporter expression in the prelimbic area of PFC. Scale bar, 100 µm. **F**. Quantification of Ai14 + cell density in contralateral and ipsilateral hemisphere of PFC in control and brain-injured animals. $^{**}p = 7.3 \times 10^{-3}$, ipsilateral control versus brain injury; two-way ANOVA with Tukey's post hoc analysis, $N = 3–4$ mice per group.

During surgery, animals were administered buprenorphine, a synthetic opioid analgesic that acts as a partial mixed opioid agonist at the µ-receptor (Kumar et al., 2024) and has potential to activate neurons independent from TBI. To test the effect of buprenorphine on neuron activation, we examined Ai14 expression in the somatosensory neocortex and PVT, a brain area that exhibits opioid receptor-dependent modulation of firing (Hou et al., 2023), in mice with and without a buprenorphine injection. These experiments were only performed in uninjured control animals, because it is not ethical to withhold analgesics from brain-injured animals. In both brain areas, we observed a significant increase in Ai14-labeled cells following buprenorphine administration, as compared with animals that did not receive buprenorphine (**Figure 2.2**). However, the increase in Ai14 expression was modest. We conclude that the increase in cell activation after TBI is much more likely to be driven by TBI than a heightened response to analgesics.

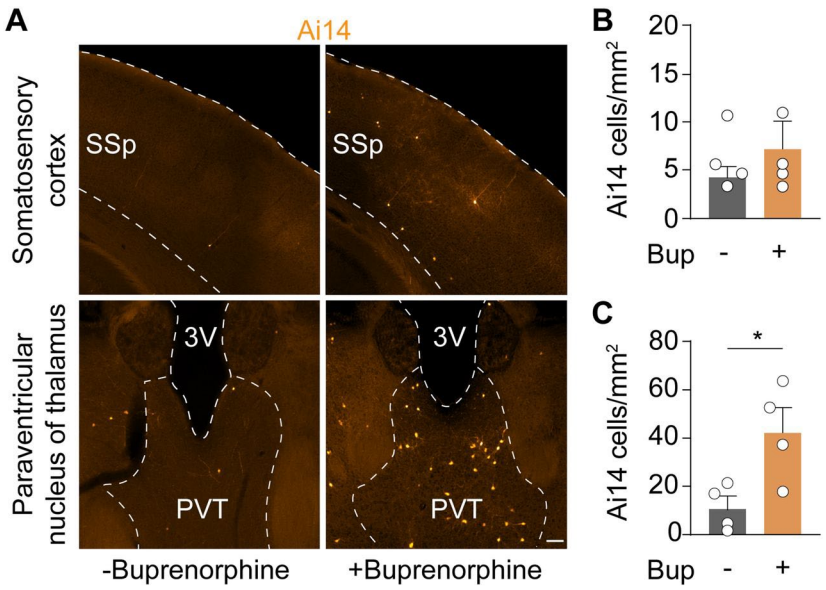


Figure 2.2: Buprenorphine activates a small number of cells. **A**. Ai14 expression in the somatosensory neocortex (top) and PVT (bottom) of mice with and without a single administration of 0.05 mg/kg buprenorphine. Scale bar, 100 µm. **B**, **C**. Quantification of Ai14 expression in the somatosensory cortex (B) and PVT (C). PVT: $*p = 4.2 \times 10^{-2}$; −Bup versus + Bup; $N = 4$ mice per group; two-tailed t test. SSp, primary somatosensory cortex; 3V, third ventricle.

To label the extent of the lesion, we examined glial responses in the neocortex (**Figure 2.3A**). To do this, we performed an immunostaining analysis at 7 d after injury for glial fibrillary acidic protein (GFAP), a marker of astrocytes, and ionized calcium-binding adaptor molecule 1 (IBA1), a marker of activated microglia. Comparisons were made between age-matched uninjured controls and brain-injured animals. In all brain-injured animals, the impact site could be clearly identified by a dense pattern of GFAP and IBA1 staining ipsilateral to the injury. No overt neocortical lesion was observed in any uninjured control animal. Analysis of the glial responses every 300 µm along the anterior–posterior axis revealed GFAP and IBA1 immunostaining was most robust at the lesion site, decreased with distance from the injury epicenter and was significantly higher in brain-injured mice compared with controls (**Figure 2.3B,C**). In contralateral hemisphere, we did not observe a difference between groups, consistent with the relatively focal lesion produced by CCI injury. This pattern of neuroinflammation is qualitatively similar with prior studies demonstrating increases in glial responses following 1.0 mm impact depths (Zhu et al., 2019).

Analysis of Ai14 expression every 300 µm along the anterior–posterior axis revealed intense immunostaining throughout the ipsilateral hemisphere that did not decrease with distance from the injury epicenter (**Figure 2.3D**). In these animals, the area of cell activation did not peak at the lesion area and taper with distance from the injury epicenter, as seen with GFAP and IBA1 expression. Instead, we observed elevated Ai14 immunostaining throughout most of the ipsilateral neocortex. Taken together, these results suggest there is broad cell activation in the ipsilateral hemisphere in the early period after a contusion injury that extends beyond the area directly damaged by the injury.

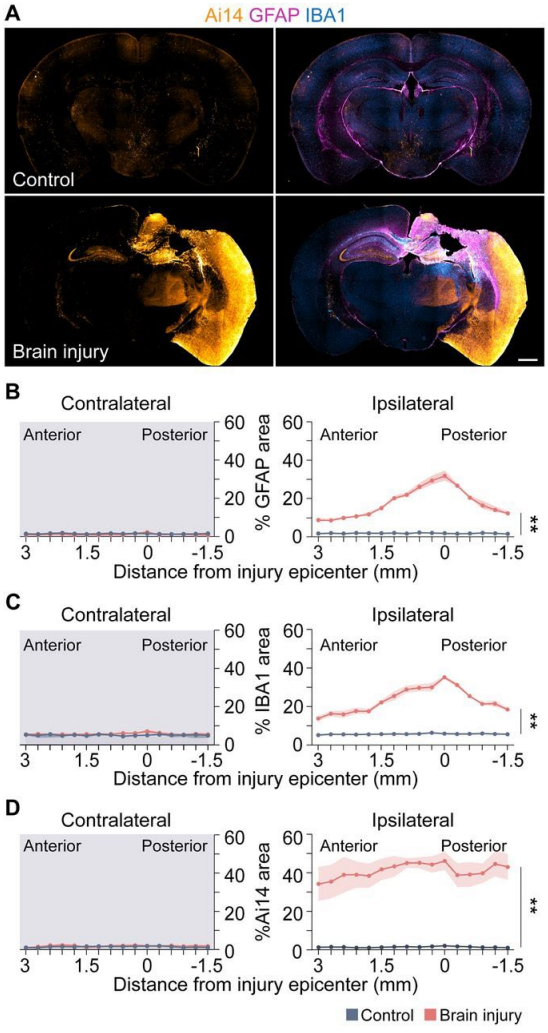


Figure 2.3: Cell activation extends beyond the glia scar. A. Coronal brain sections of Ai14 (orange), GFAP (magenta), and IBA1 (blue) at the injury epicenter of a control and brain-injured mouse. Representative animals are

from $N = 4$ controls and 3 TBI animals. Scale bar, 100 µm. **B–D**. Quantification of GFAP (B), IBA1 (C), or Ai14 (D) expression in 16 sequential brain sections of the neocortex along the anterior–posterior (AP) axis contralateral (left) and ipsilateral (right) to the injury (GFAP, $^{**}p = 3.7 \times 10^{-9}$, control vs brain injury; IBA1, $^{**}p = 3.3 \times 10^{-6}$, control vs brain injury; Ai14, $^{**}p = 4.6 \times 10^{-4}$, control vs brain injury; two-way rmANOVA with Bonferroni's post hoc analysis).

Nearly all Ai14+ cells were morphologically identified as neurons, consistent with prior studies reporting that TRAP preferentially labels neurons (Guenthner et al., 2013). This was confirmed by colabeling with NEUN, and no difference was detected between groups (control, 92 ± 3%; TBI, 90 ± 1%; p = 0.49; two-tailed *t* test; $N = 3$–4 mice per group; **Figure 2.4A,C**). To test whether glia were also labeled after TBI, we quantified Ai14+ cell colocalization with GFAP and IBA1 in the neocortex just lateral to the injury site. In controls, none of the Ai14+ cells expressed GFAP or IBA1 (**Figure 2.4B,C**). In brain-injured animals, only ~2% of Ai14+ cells expressed GFAP or IBA1. No differences were detected in the proportion of cells labeled for either marker ($p = 0.99$; $N = 3$–4 mice per group, Fisher's exact test). This result suggests the increase in Ai14 expression observed ipsilateral to the injury was not driven by Ai14+ activated glia.

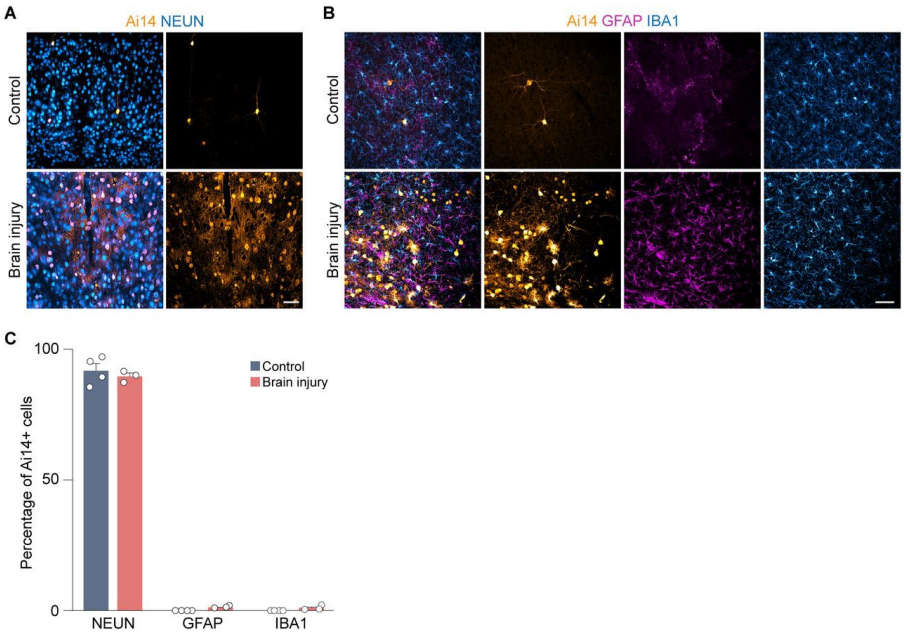


Figure 2.4: Ai14^{+} cells are putative neurons. A. Coronal brain sections of Ai14 (orange) and NEUN (blue) near the injury site in the neocortex of a control and brain-injured mouse. **B**. Coronal brain sections of Ai14 (orange), GFAP (magenta), and IBA1 (blue) at the injury site in the neocortex of a control and brain-injured mouse. Scale bar, 50 µm. **C**. Quantification of Ai14^{+} cells that colabel for NEUN, GFAP, or IBA1.

Discussion

There is little question that neurons rapidly become activated in response to brain damage. Here, we applied a focal contusion injury to the somatosensory neocortex and evaluated brain cell activation around the time of injury. Consistent with prior IEG labeling studies (Dragunow and Robertson, 1988; Dragunow et al., 1990; Phillips and Belardo, 1992; Yang et al., 1994, 1995; Belluardo et al., 1995; Raghupathi et al., 1995a; Abrous et al., 1999; Förstner and Knöll, 2020), our results show focal contusion injury leads to early activation of neurons across the neocortex. Ai14+ neurons were observed broadly throughout the ipsilateral hemisphere, including ventral and subcortical brain areas. The area of neuron activation extended well beyond the lesion area, as determined by the presence of cortical cavity and GFAP immunostaining and remained elevated in all tissue sections examined. These observations highlight the importance of considering brain-wide effects of acute injury in neurotrauma studies.

Prior studies have reported wide variation in IEG expression after experimental brain injuries, with some studies showing IEG activation primarily near the lesion site (Dragunow and Robertson, 1988; Dragunow et al., 1990; Förstner and Knöll, 2020) and other studies reporting more widespread IEG activation (Phillips and Belardo, 1992; Yang et al., 1994, 1995; Belluardo et al., 1995; Raghupathi et al., 1995a; Abrous et al., 1999). Using a TRAP2 reporter line, which consistently labels c-fos–activated neurons throughout the brain, we observed broad, hemisphere-wide c-fos expression in a widely used focal cortical contusion model. Many cortical areas had noticeable increases in Ai14+ neurons, including the piriform cortex, hippocampus, entorhinal cortex, PFC, auditory cortex, and cortical amygdala; the basolateral amygdala also had overt increases in Ai14+ cells but was not quantified here. Therefore, a focal nonpenetrating contusion injury has potential to broadly affect the brain in the early postinjury period, even in brain areas that are not directly damaged by the mechanical insult. Support for this idea is

provided by fMRI studies in rodents and humans showing broad activation of dispersed brain regions after brain injury compared with healthy controls (McAllister et al., 1999; Christodoulou et al., 2001; Harris et al., 2016).

One possibility for widespread neuron activation after TBI is the presence of injury-induced seizures, which have been reported immediately after CCI in mice (Hunt et al., 2010). However, seizures in these animals are often generalized events that would likely produce bilateral Ai14 expression (Naik et al., 2022), and seizures are only observed in a small minority of animals during the time window immediately following TBI in which neurons would be tagged by TRAP (Hunt et al., 2010). Another possibility is cortical spreading depolarization, which has long been suspected to contribute to the hemisphere-wide pattern of neuron activation after injury (Herrera and Robertson, 1996). Spreading depolarization occurs in >50% of people with TBI (Hartings et al., 2011) and in animal models (Aboghazleh et al., 2021). However, these events are rare in animal models, often involve only a single depolarization wave, and only occasionally involve the entire hemisphere in human patients (Taş et al., 2019). It is currently unknown precisely how far a spreading depolarization event might extend from the injury site in an animal model of TBI. Nonetheless, widespread network activity spanning anterior to posterior cortex has been documented in brain slices of a genetic model of epilepsy (Hou et al., 2021).

Following TBI, injured brain circuits undergo time-dependent structural and functional reorganization. This includes cell-type–specific changes in neuron morphology, intrinsic properties, and synaptic and circuit function (Hunt et al., 2013). While the cellular trigger for these plasticity responses is unknown, an emerging literature provides broad support for synaptic circuit reorganization at the level of cell ensembles. At a behavioral level, post-traumatic retrograde amnesia can be rescued by activating neurons that were tagged during the memory-forming experience prior to injury, suggesting the ensemble representing the lost memory physically exists

after TBI but may be more difficult to access (Chapman et al., 2024). At a structural level, synaptic inputs are selectively gained or removed in a cell-type–specific manner (Hunt et al., 2009, 2010, 2011; Frankowski et al., 2022), and grafted inhibitory neurons are capable of reestablishing long-range connections lost to TBI (Frankowski et al., 2022), which likely underlies the prevention of epilepsy and improved memory precision after TBI (Zhu et al., 2019). While speculative, it is enticing to hypothesize that neurons activated at the time of injury may participate in an “injury cell ensemble” and function differently later in life, as compared with neurons not acutely activated by the initial injury.

Our results show there is broad neuron activation across large portions of the cortex early after a contusion injury in mice, but it is largely restricted to the ipsilateral hemisphere. These results highlight the importance of considering injury dynamics in the initial response to injury and may explain why brain areas distant from the injury become rewired even when not directly damaged by the mechanical insult.

CHAPTER THREE

Brain-wide reconstruction of inhibitory circuits after traumatic brain injury

Abstract

Despite the fundamental importance of understanding the brain's wiring diagram, our knowledge of how neuronal connectivity is rewired by traumatic brain injury remains remarkably incomplete. Here we use cellular resolution whole-brain imaging to generate brain-wide maps of the input to inhibitory neurons in a mouse model of traumatic brain injury. We find that somatostatin interneurons are converted into hyperconnected hubs in multiple brain regions, with rich local network connections but diminished long-range inputs, even at areas not directly damaged. The loss of long-range input does not correlate with cell loss in distant brain regions. Interneurons transplanted into the injury site receive orthotopic local and long-range input, suggesting the machinery for establishing distant connections remains intact even after a severe injury. Our results uncover a potential strategy to sustain and optimize inhibition after traumatic brain injury that involves spatial reorganization of the direct inputs to inhibitory neurons across the brain.

Introduction

Brain function relies on an extremely diverse group of inhibitory interneurons that control the input and output of local networks (Klausberger and Somogyi 2008; Kepecs and Fishell, 2014; Tremblay et al., 2016). In the cerebral cortex, one of the largest populations of interneurons expresses the neuropeptide, somatostatin (SST) (Freund and Buzsaki, 1996; Ascoli et al., 2008; Pelkey et al., 2017). These cells inhibit dendrites and thereby regulate the integration of glutamatergic input to local principal neurons. This endows them with unique roles in shaping synaptic plasticity, learning, and memory (Larkum et al., 1999; Spruston, 2008; Royer et al., 2012; Lovett-Barron et al., 2014; Stefanelli et al., 2016; Cummings and Clem, 2020; Udakis et al., 2020;

Morales et al., 2021). However, SST interneurons are among the most vulnerable to cell death following a brain injury, and their loss has been well documented in experimental models of epilepsy, traumatic brain injury (TBI), and Alzheimer's disease (Lowenstein et al., 1992; Cantu et al., 2015; Butler et al., 2016; Frankowski et al., 2019; Xu et al., 2020), and in humans (de Lanerolle et al., 1989; Beal et al., 1986). In the hippocampus, surviving SST interneurons receive more excitatory drive, form new inhibitory synapses onto glutamatergic neurons and even grow into territories they normally do not occupy (Zhang et al., 2009; Halabisky et al., 2010; Hunt et al., 2011; Peng et al., 2013). This pattern of local circuit rewiring raises the question of whether brain damage reorganizes interneuron connectivity on a much larger scale.

To address this possibility in an unbiased manner, we took advantage of a retrograde monosynaptic rabies virus system and enhanced whole-brain tissue clearing techniques to create brain-wide maps of the direct input to SST interneurons in a mouse model of focal TBI. We found dramatic quantitative differences in both the local and long-range input to hippocampal SST interneurons at the injury site. However, there was no neuron loss within the distant input regions themselves, and the proportion of neuron subtypes targeting starter neurons was stable. To our surprise, we uncovered a similar pattern of circuit reorganization far away from the injury in the prefrontal cortex (PFC), which interacts with the hippocampus bidirectionally (Jin and Maren, 2015) but was not directly damaged by the initial insult. Interneuron progenitors grafted into the lesioned hippocampus successfully established appropriate long-range connections; however, graft-derived interneurons retained the enhanced local input seen after TBI. Thus, our experiments provide new insights about large-scale circuit remodeling following brain injury and suggest that brain damage, even when focally restricted, has a far broader impact on neural circuit function across the entire brain than previously appreciated.

Methods

Animals

All animal procedures were performed under Institutional Animal Care and Use Committee (IACUC) approval by the University Laboratory Animal Resources at the University of California, Irvine and adhered to National Institutes of Health Guidelines for the Care and Use of Laboratory Animals. Experiments were performed on adult mice of both sexes maintained in standard housing conditions on a 12 h light/dark cycle with food and water provided *ad libitum*. For SST cell quantifications, we used GIN mice maintained on a FVB background (Jax Stock No: 003718). For rabies circuit tracing, we used Sst-IRES-Cre mice maintained on a C57BL/6 J background (Jax Stock No: 018973). We used C57BL/6 J mice (Jax Stock No: 000664) for fluoro-jade C experiments. For cell transplantations, embryonic donor tissue was produced by crossing Sst-IRES-Cre J mice with C57BL/6 J mice (Jax Stock No: 000664) or Ai6-ZsGreen reporter mice (Jax Stock No: 007906); host mice were C57BL/6 J mice (Jax Stock No: 000664).

Experimental Design

Experiments were performed on male and female littermates between P55 and P139. Upon weaning, animals were coded and randomly assigned into uninjured (naïve control), TBI or MGE-injected treatment groups. Brain injured mice and age-matched controls were housed together (2–5 animals per cage) within a temperature- (21–22 °C), humidity- (40–51%), and light- (12 h light:dark cycle) controlled vivarium. The order of injury, virus injection and cell transplantation was also randomized. Blinding was not possible due to the presence of an injury in TBI treatment group. CHAT immunostaining experiments were replicated using a separate, independent cohort of control and brain-injured animals. No other replication studies were performed.

Brain injury

CCI injury was performed on adult male and female mice at P55 (Frankowski et al., 2019). Briefly, mice were anesthetized by 2% isoflurane inhalation and placed in a custom stereotaxic frame.

The skull was exposed by midline incision, and a 4–5 mm craniotomy was made ~1 mm lateral to the sagittal suture and centered between bregma and lambda. The skull cap was removed without damaging the underlying dura. The contusion device consisted of a computer-controlled, pneumatically driven impactor fitted with a beveled stainless-steel tip 3 mm in diameter (Precision Systems and Instrumentation; TBI-0310). Brain injury was delivered using this device to compress the cortex to a depth of 1.0 mm at a velocity of 3.5 m s^{-1} and 500 ms duration. The incision was sutured without replacing the skull cap, and the animal was allowed to recover on a heating pad. A qualitative postoperative health assessment was performed daily for 7 d after TBI and periodically thereafter. All animals that received surgery were treated with buprenorphine hydrochloride (Buprenex; 0.05 mg/kg, delivered i.p.) at the time of surgery and 24 h later. All brain-injured mice survived and remained otherwise healthy until the day of experimentation.

Virus injections

AAV8-hSyn-FLEX-TVA-P2A-GFP-2A-oG with a titer of 1.2×10^{13} genome copies/mL was obtained from the GT3 Core Facility of the Salk Institute and diluted to a titer of 2.4×10^{11} genome copies/mL in sterile 0.9% NaCl prior to use, to prevent impairments in tracing performance (Lavin et al., 2020). RVΔG-mCherry was produced as previously described (Wickersham et al., 2007) with a titer of 5×10^{9} infectious units/mL. Virus was front loaded into beveled glass micropipettes (40 µm tip diameter, Wiretol 5 µl, Drummond Scientific) and injected into the brains of adult uninjured control and brain injured mice at a rate of 15 nL min^{-1} and the needle was left in place for 5 min before retraction. Target coordinates were first verified in a series of preliminary injection studies into control and brain injured mice to determine ideal target locations (e.g., hilus) and the titer and volume of virus that could be delivered into hilus or PFC without leakage into nearby regions. AAV injections (200 nL) were made into hilus of dentate gyrus at the following stereotaxic coordinates: anterior-posterior (AP) −2.0 mm, medial-lateral (ML) 1.30 mm, dorsal-ventral (DV) −1.9 mm. In separate cohort of animals, injections were made into prelimbic cortex: AP 1.8 mm,

ML 0.35 mm and DV −1.4 mm. RVΔG-mCherry (100nL) was injected 3 weeks later at the same location.

Tissue clearing and whole-brain immunostaining

Mice were transcardially perfused with 0.1 M PBS containing 1uL/mL of 10 mg/mL heparin sodium (Serva cat no. 24590.01) followed by 4% PFA in 0.1 M PBS. Samples were postfixed overnight in 4% PFA in 0.1 M PBS. Subsequent steps were performed in 5 mL centrifuge tubes (Eppendorf cat. No 0030119401) with 0.01% sodium azide added to each solution. First, samples were decolorized in 10% 3-[(3-Cholamidopropyl)dimethylammonio]-1-propanesulfonate (CHAPS, Anatrace cat. no. C316S) and 25% N-methyl diethanolamine (MDEA, Alfa-Aesar cat. no. L15712) in 0.1 M PBS for 48 h at 37 °C with nutation. Samples were then washed in 0.1 M PBS for 24 h, dehydrated in a methanol/water gradient (20%, 40%, 60%, 80%, 100%, 100%) for 1 h each and delipidated in 2:1 DCM:MeOH overnight. The next day, samples were washed twice in 100% MeOH for 4 h to remove DCM:MeOH and bleached in 5% H2O2 in 80% MeOH overnight at 4 °C without shaking. Samples were then rehydrated in 60% MeOH, 40% MeOH, 20% MeOH, 0.1 M PBS and PTx.2 for 1 h, incubated in 4 M guanidine hydrochloride (Alfa-Aesar cat. no. A13543-30) and 1% CHAPS in 0.1 M PBS for 24 h and washed overnight in 0.1 M PBS with three solution changes. Next, samples were permeabilized in 10% CHAPS/25% MDEA in 0.1 M PBS overnight at 37 °C with nutation, incubated in 3% NDS/10% DMSO in PTx.2 with nutation at 37 °C overnight. Primary antibody incubations were performed in heparinized 0.1 M PBS containing 0.2% Tween-20 (PTwH) containing 0.25% CHAPS, 3% NDS and rabbit anti-DsRed (1:1000) and chicken anti-GFP antibodies (1:1000) for 7 days at 37 °C with nutation. Samples were then washed in PTwH overnight on an orbital shaker (115 RPM) at room temperature with five solution changes. Secondary antibody diluent was prepared in PTwH containing 0.25% CHAPS, donkey anti-rabbit 546 (1:1000) and goat anti-chicken 647 (1:1000), syringe filtered at 0.2 µm and incubated for 7 days at 37 °C with nutation before washing in PTwH overnight with five solution changes and

shaking at room temperature. The next day, samples were dehydrated in increasing methanol/water gradients (20%, 40%, 60%, 80%, 100% for 1 h each) and allowed to sit in 100% MeOH overnight at 4 °C. Samples were then washed in 2:1 DCM/MeOH for 3 h, followed by two 100% DCM washes for 15 min each and cleared in dibenzyl ether (DBE) overnight at 4 °C. DBE was changed four additional times before imaging for refractive index matching. A step-by-step protocol for whole-brain immunostaining can be found at: https://github.com/roberthuntlab/clearedbrainanalysis.

Light-sheet imaging

Cleared samples were mounted in a 3D-printed sample holder in a custom-built imaging chamber with the same lot of DBE solution used for refractive index matching and imaged using a Zeiss Z1 light-sheet microscope with Zeiss Zen software. Samples were imaged in the sagittal orientation with single-sided illumination using a x5/0.1 illumination objective and a x5/0.16 detection objective at 0.91 µm/pixel resolution with 4.97 µm step size. mCherry-labeled input neurons were imaged using a 561 nm laser coupled to a 575–625 nm BP filter. GFP and auto-fluorescence channels were acquired simultaneously with 488 nm and 638 nm laser lines coupled to 505–545 nm BP and 660 nm LP filters. Laser power was set to 40% intensity for all laser lines with 200 ms exposure. Tile overlap was set to 8%.

Whole-brain 3D image registration and annotation

Raw data (.czi) were converted into hierarchical format (.ims) using Imaris File Converter 9.1 (Bitplane). The 561 nm channel data was downsampled by a factor of two in each dimension and exported as numpy arrays (.npy) using custom Python scripts. Individual tiles were stitched non-rigidly using WobblyStitcher (Kirst et al., 2020). Stitched arrays were exported as .tif series with a background subtraction value determined for each animal. Individual cell positions were manually annotated using cellfinder (Tyson et al., 2021). Image stacks were downsampled to 10 µm

resolution and registered to the Allen Reference Atlas (Wang et al., 2020) using brainreg, a Python port of aMAP (Niedworok et al., 2016). Atlas boundaries were upsampled to the original high-resolution image in ImageJ, and image planes containing cells were inspected for accuracy. To correct for whole-brain registration error, pairs of correspondence points were manually marked where atlas boundaries diverged from anatomical landmarks. Average vector length was calculated, and annotated cell positions were linearly transformed based on the correspondence point vector length. Schematics of the anatomical position of starter cells and input neurons were plotted using brainrender (Claudi et al., 2021). Coronal atlas plates were rendered at selected positions along the anterior/posterior axis and individual cells positions ± 125 µm (hippocampus tracing) or ± 50 µm (PFC tracing) to the selected atlas plate.

Whole-brain quantification

Registered cell positions for each animal were summarized using cellfinder (Tyson et al., 2021). Cell counts were combined for laminated cortical structures. Ipsilateral and contralateral cell counts were analyzed as separate regions. In one uninjured control (hippocampus injection), a small number of rabies-labeled cells were found near the injection tract in overlying neocortex. These cells were excluded from analysis as they were labeled by the needle injection, not trans-synaptic spread of virus. For Euclidian distance calculation, the starter cell centroid was calculated by averaging the atlas coordinates of each registered starter cell and rounding the result to the nearest integer. Three-dimensional Euclidian distance was calculated between the starter cell centroid and each pre-synaptic input neuron position using the following formula:

$$d = \sqrt{(x_2 - x_1) + (y_2 - y_1) + (z_2 - z_1)}$$

where (x_2, y_2, z_2) represents AP, ML and DV of the starter cell centriod, (x_1, y_1, z_1) represents AP, ML and DV of each registered pre-synaptic cell position and *d* represents the length of the calculated distance vector. For analysis of AP and DV distances, cell counts were binned at

200 µm intervals and normalized to the total number of cells for each animal. For analysis of ML distance, cell counts were binned at 100 µm to produce an even number of bins for each hemisphere. Gaussian kernel density estimates were computed using seaborn python script, and bandwidth was set at 0.5.

Reverse clearing

Cleared samples were removed from DBE and washed in DCM twice for 15 min followed by overnight incubation in 2:1 DCM/MeOH. Samples were then rehydrated in 100%, 80%, 60%, 40%, 20% MeOH/water and 0.1 M PBS for 1 h each on an orbital shaker (115 RPM) at room temperature. Free-floating vibratome sections (50 µm) were cut using a vibratome at room temperature in 0.1 M PBS containing 0.05% Triton-X. A step-by-step protocol for reverse clearing can be found at: https://github.com/roberthuntlab/clearedbrainanalysis.

Immunostaining

Mice were transcardially perfused with 4% PFA (v/v) and free-floating vibratome sections (50 µm) were processed using standard immunostaining procedures (Zhu et al., 2019). Primary antibodies were as follows: chicken anti-green fluorescent protein (GFP; 1:1000; Aves, cat no. GFP1020), chicken anti-mCherry (1:1000; Abcam, cat no. ab205402), goat anti-choline acetyltransferase (CHAT; 1:500; Millipore, cat no. AB144P), mouse anti-reelin (1:500; Millipore, cat no. MAB5364, clone G10), rabbit anti-DsRed (1:1000; Clontech, cat no. 632496), rabbit anti-somatostatin (SST; 1:200; Santa Cruz, cat no. SC-7819) and rabbit anti-WFS1 (1:1000; Proteintech, cat no. 11558-1-AP). All antibodies have been previously used for immunostaining analysis in brain. For secondary antibodies (1:1000, Life Technologies), we used Alexa 488–conjugated goat antibody to chicken IgG (cat. no. A11039), goat antibody to mouse IgG (cat. no. A11029), donkey antibody to goat IgG (cat. no. A11055); Alexa 546-conjugated goat antibody to rabbit IgG (cat. no. A11035), donkey antibody to rabbit IgG (cat. no. A10040), Alexa 594–donkey antibody to goat IgG (cat. no.

A11058) and Alexa 647–conjugated goat antibody to chicken IgG (cat. no. A32933). Sections were then mounted on charged slides (Superfrost plus, Fisher Scientific) with Fluoromount-G containing DAPI. Confocal images were obtained with an Olympus FV3000 laser scanning microscope. Epifluorescent images were obtained using a Leica DM6 microscope with Leica LAS X software. Brightness and contrast were adjusted manually using ImageJ, as needed.

Cell quantification in brain sections

Fluorescently labeled sections (50 µm) were imaged using a Leica DM6 microscope with a ×10 or ×20 objective or Olympus FV3000 confocal microscope with a ×20 or ×40 objective and counted using FIJI (ImageJ) (Zhu et al., 2019). All cells that expressed a fluorescent marker were counted in every sixth section through the entire brain (that is, 300 µm apart). All sections containing labeled cells were analyzed per animal and the values averaged to obtain a mean cell density (cells/mm^2).

Fluoro-jade C staining

Mice were transcardially perfused with 4% PFA (v/v) and free-floating vibratome sections (50 µm) were processed for fluoro-jade C staining according to manufacturer instructions (Schmued et al., 2005). Briefly, brain sections were dried on gelatin-coated slides for 30 min at 50 °C. Slides were immersed in 1% NaOH in 80% ethanol for 5 min, 70% ethanol for 2 min, dH2O for 2 min, 0.06% potassium permanganate for 10 min, dH2O for 2 min, 0.00015% fluoro-jade C (Histo-Chem Inc., cat no. 1FJC) and 0.0001% DAPI in 0.1% acetic acid for 10 min, followed by three washes in dH2O for 1 min each. Slides were then dried at 50 °C for 5 min and cleared in xylenes before coverslipping with Eukitt mounting medium (Sigma, cat. no 03989).

Tissue dissection and transplantation

Ventricular and subventricular layers of the MGE were harvested from E13.5 embryos. The time point at which the sperm plug was detected was considered E0.5. Embryonic MGE explants were dissected in Leibovitz L-15 medium, mechanically dissociated by repeated pipetting in L-15 medium and concentrated by centrifugation (3 min at 600 × g). Concentrated cell suspensions were front loaded into beveled glass micropipettes (50 µm tip diameter, Wiretol 5 µl, Drummond Scientific) and injected (3×10^4 cells per injection) into the hippocampus of adult brain-injured mice 7 d after CCI injury. Cell injections were made into stratum radiatum of the CA3 subfield at the following stereotaxic coordinates: AP −2.0 mm, ML 2.45 mm, DV −1.8 mm.

Statistical analysis

All statistical tests were performed with Graphpad Prism 9, R and Microsoft Excel. Sample sizes were based on previous publications (Sun et al., 2014; Ährlund-Richter et al., 2019; Liu et al., 2013). For whole-brain quantitative analyses, the number of input neurons in each distinct brain area was normalized to the total number of input neurons detected in the whole brain (% input) or to the total number of starter cells (convergence index). Data were compared by two-tailed student's *t*-test, one-way ANOVA followed by a Tukey's post hoc test for multiple comparisons, two-way ANOVA followed by a Tukey's post hoc test for multiple comparisons, two-way repeated-measures ANOVA followed by a Bonferroni's post hoc test, Chi-Square analysis or Fisher's exact test. UMAP analysis and Pearson correlation was computed in R. Data are expressed as mean±SEM, *n* = animals unless otherwise specified and significance was set at $P < 0.05$.

Results

Long-term loss of SST interneurons after TBI

Despite their important role in shaping local network activity and memory (Stefanelli et al., 2016; Morales et al., 2021), the precise brain-wide input to SST interneurons in the dentate gyrus has not been systematically defined. We first quantified SST+ neuron density during the chronic period

after TBI using reporter mice that label nearly all SST interneurons with GFP (Oliva et al., 2000). A unilateral controlled cortical impact (CCI) injury was delivered to young-adult mice at P60 (1.0 mm impact depth, 3.5 m s^{-1} and 500 ms duration), and animals were processed for immunostaining eight weeks later. This period corresponds to a time when long-term neuropathology and behavioral phenotypes are well established. In all brain-injured mice, the lesion consisted of a cavity extending through the thickness of the neocortex and included substantial distortion and thinning of the principal cell layers in the hippocampus (**Figure 3.1a**). We observed ~65% reduction in GFP+ cells in the hilus (**Figure 3.1b**), consistent with short-term loss of SST interneurons reported in previous studies (Butler et al., 2016; Frankowski et al., 2019).

Visualization of input neurons to hippocampal SST+ interneurons

To label monosynaptic input to SST interneurons in the chronically injured brain, we used a genetically restricted two-virus approach to anatomically reveal their putative inputs (**Figure 3.1c-e**). We first injected a Cre-dependent helper virus (AAV8-hSyn-FLEX-TVA-P2A-eGFP-2A-oG) into the dentate gyrus of adult SST-Cre mice 4 weeks after TBI. This helper virus provides the receptor that allows EnvA-coated rabies virus to enter only Cre-positive neurons and glycoprotein for rabies virus to transfer retrogradely to monosynaptic input neurons. Three weeks later, we injected a G-deleted and EnvA-pseudotyped rabies virus coding mCherry into the same location (RVΔG-mCherry). Because SST+ interneurons in the dentate gyrus are exclusively located in the hilus, we targeted this region for virus injection. After 7 days, we identified neurons that were positive for both fluorescent reporters at the injection site (starter cells) and neurons infected with the rabies virus were tagged with mCherry (pre-synaptic input neurons). Substantial numbers of neurons in different brain areas were labeled by rabies virus (**Figure 3.2**).

To confirm the specificity of virus labeling, we performed immunostaining against SST at the injection site. We found 97% of the GFP-labeled neurons were SST+ (152 of 156 cells, *n* = 3

mice) (**Figure 3.1f, g**). To evaluate the potential leakage expression of the virus, we performed a series of control experiments. To confirm the dependence of Cre recombination, we injected AAV8-hSyn-FLEX-TVA-P2A-eGFP-2A-oG helper and RVΔG-mCherry virus into Cre- littermates. No neurons were labeled anywhere in the brain (**Figure 3.3a**). In Cre+ animals, GFP+ neurons were only labeled at the injection site and no GFP+ neurons were found outside the injection site (**Figure 3.3**). In both control and brain-injured animals, starter cells were almost exclusively confined to the hilus (**Figure 3.1h**). Only occasional starter cells were found in the adjacent CA3 region; no GFP+ cells were found in CA1, CA2, neocortex, or any other brain region.

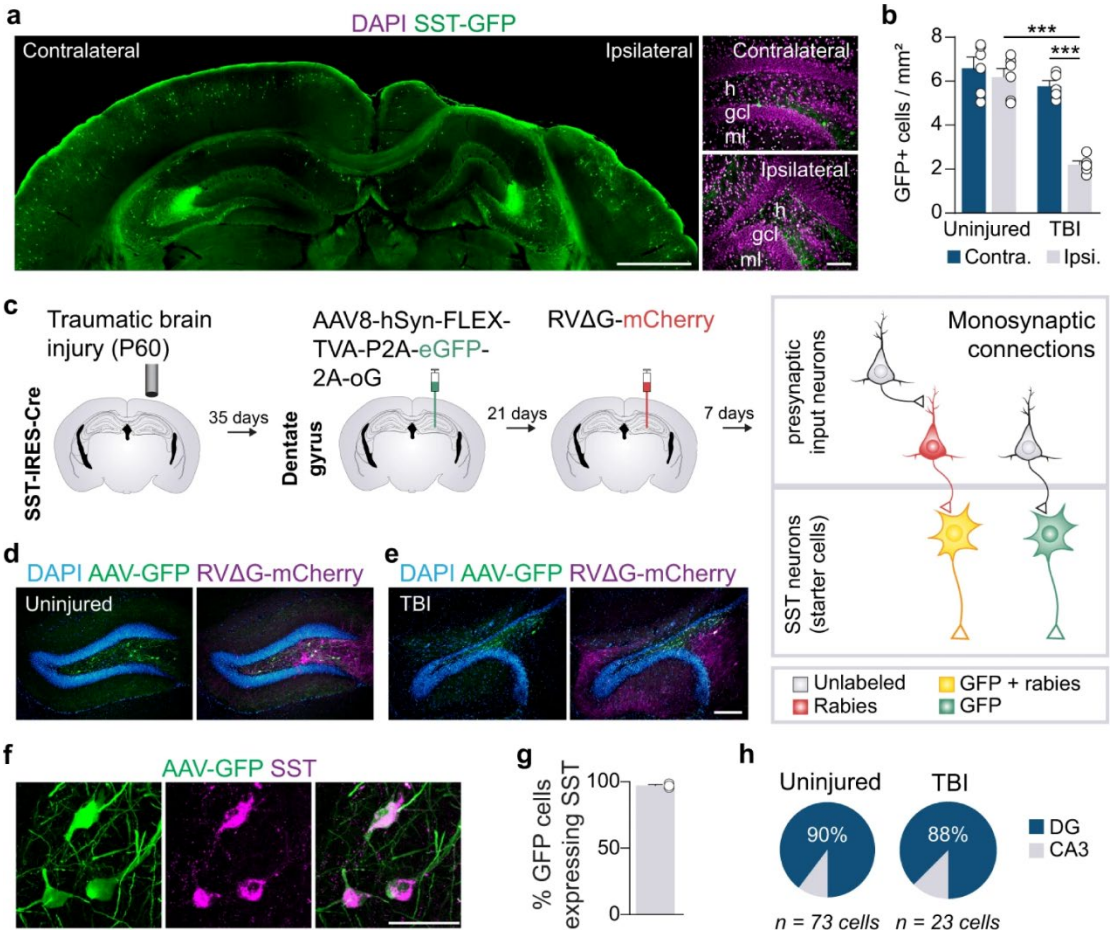


Figure 3.1: SST interneuron loss after focal TBI. a. Coronal section 8 wks after TBI labeled for SST-GFP (green) and DAPI (magenta). h, hilus; gcl, granule cell layer; ml, molecular layer. Representative animal from *n* = 5 TBI mice **b.** Quantification of SST-GFP interneurons in uninjured control and brain-injured animals. ****P* = 1.62E-06, ipsilateral uninjured control versus ipsilateral TBI, ****P* = 1.31E-05, contralateral TBI versus ipsilateral TBI; two-way ANOVA with Tukey's post hoc test, *n* = 6 uninjured and 5 TBI mice. **c.** Schematic showing the two-virus experimental retrograde tracing strategy. **d, e.** Dentate gyrus of an uninjured control (d) and CCI injured animal (e) labeled for DAPI (blue), AAV helper virus (green) and RVΔG-mCherry (magenta). Representative animals from *n* = 4 uninjured and 2 TBI mice. **f.** Coronal section of dentate gyrus labeled for AAV helper virus (green) and somatostatin (magenta). Representative

animal from *n* = 3 uninjured mice. **g.** Quantification of SST expression in neurons labeled with AAV helper virus; *n* = 3 mice. **h.** Distribution of dual color-labeled starter cells in hippocampus; *n* = 73 cells from 4 uninjured controls, *n* = 23 cells from 2 animals with TBI. Error bars, s.e.m.; scale bars, 1 mm (a, left), 100 µm (a, right; d and e) and 50 µm (f).

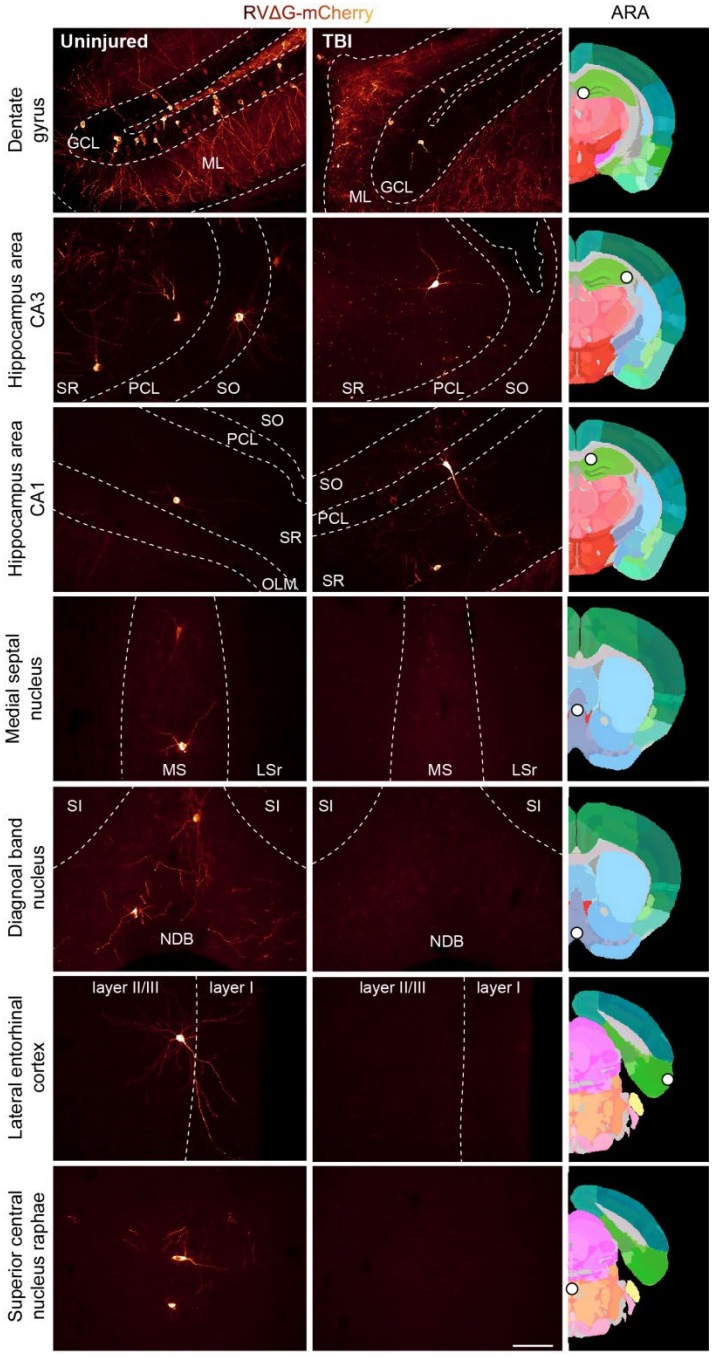


Figure 3.2: Input neurons to hilar SST interneurons. Coronal sections labeled for input neurons (red) in an uninjured control (left) and 8 wks after TBI (right). Representative animals from *n* = 4 uninjured and 2 TBI mice. Image location is indicated by a white dot overlaid onto the corresponding atlas plate from the Allen Reference Atlas (ARA). GCL, granule cell layer; ML, molecular layer; SR, stratum radiatum; PCL, pyramidal cell layer; SO, stratum oriens; OLM, oriens lacunosum moleculare; MS, medial septal nucleus; LSr, lateral septal nucleus, rostroventral part; NDB, diagonal band nucleus; SI, substantia innominata. Scale bar, 100 µm.

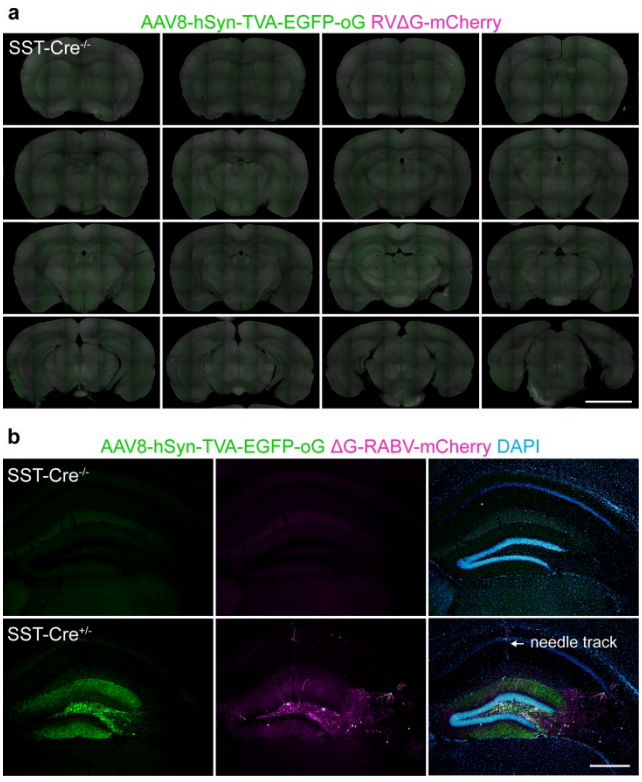


Figure 3.3: Virus specificity in hippocampus. a. Serial coronal sections every 300 µm through the entire brain of an adult SST-Cre-negative mouse labeled for AAV helper virus (green) and RVΔG-mCherry (magenta). Representative animal from *n* = 3. **b.** Coronal section of hippocampus labeled for helper virus (green) and rabies (magenta) in SST-Cre-negative mouse (top) and SST-Cre-positive mouse (bottom). Representative animal from *n* = 3 SST-Cre- and 4 SST-Cre+ mice. Scale bar, 2 mm (a); 500 µm (b).

Whole-brain input to SST-positive neurons is reorganized by TBI

Next, we generated whole-brain maps of neurons sending monosynaptic input to SST interneurons using iDISCO+ brain clearing and whole-brain light-sheet imaging (**Figure 3.4a**). One of the major challenges to these techniques has been accessing input neurons deep within the tissue (Ueda et al., 2020). Building on existing iDISCO+ protocols and recent advances in permeabilization chemistry (Renier et al., 2016; Zhao et al., 2020), we therefore modified the clearing conditions to achieve deep tissue immunolabeling in a traumatically injured brain. We made three key improvements in iDISCO+ sample preparation and imaging procedures (**Figure 3.5**). First, we incorporated an initial wash using N-methyl diethanolamine (MDEA) to decolorize residual unperfused blood, which absorbs light (Faber et al., 2003). Second, we denatured the extracellular matrix using a concentrated guanidine hydrochloride solution prior to

immunolabeling. Third, we incorporated an additional detergent (3-[(3-cholamidopropyl)dimethylammonio]-1-propanesulfonate, CHAPS) to the antibody diluent to enhance the penetration of antibodies deeper into the tissue. These optimizations enabled whole-brain immunolabeling without need for separating the brains into two separate hemispheres, as is commonly done. The raw data acquired from imaging were registered to the Allen Common Coordinate Framework (CCF) and cell positions were annotated and analyzed using tools from the BrainGlobe suite (Claudi et al., 2021; Tyson et al., 2021) (**Figure 3.6**). As expected, the number of starter neurons was reduced in brain-injured animals (control: 48.0 ± 3.7 cells, TBI: 9.4 ± 0.9 cells, $P = 9.45E-06$, two-tailed *t*-test), consistent with the loss of SST interneurons. Starter cells were almost exclusively confined to the hilus (control: 92.8 ± 0.96% starter cells in dentate gyrus, TBI: 89.8 ± 3.2% starter cells in dentate gyrus; $P = 0.3$, Fisher exact test). Although the number of labeled neurons varied from animal to animal, there was a correlation between the number of input neurons and starter cells (**Figure 3.4b**).

Whole-brain mapping of rabies-labeled neurons revealed input from 15 distinct brain regions (**Figures 3.4c**, **3.7, 3.8**). The majority of input came from the dentate gyrus and CA3, as expected (Hunt et al., 2011, Katona et al., 1999; Wittner et al., 2006) followed by the medial entorhinal cortex (ENTm), diagonal band nucleus (NDB) and lateral entorhinal cortex (ENTl). Of note, this pattern of input is different from previous retrograde tracing results in dentate granule cells, which receive considerably weaker projections from ENTm than ENTl and prominent input from mammillary nuclei (Vivar et al., 2012; Li et al., 2020), as well as SST interneurons in CA1, which receive very little input from entorhinal cortex (Sun et al., 2014). After TBI, there was a shift in the Euclidian distance of rabies-labeled neurons to the starter cell centroid (**Figures 3.3d, 3.7**), suggesting input neurons were substantially closer to starter cells after brain injury.

A higher proportion of local connections was confirmed when we analyzed the input to SST interneurons in greater detail. In control animals, approximately 40% of the input neurons were detected outside the hippocampus, and 8% of input neurons were located in the contralateral hemisphere. The proportions of these long-range inputs were significantly reduced in animals with TBI (**Figure 3.4e, f**). Furthermore, we analyzed the probability of input neurons in 200 µm bins along the entire anterior-posterior (AP) axis, from 0 mm (olfactory bulb) to 13 mm (cerebellum) (**Figure 3.4g**). This revealed significant increases in the percentage of input neurons between 6.8 mm to 7.4 mm at the level of hippocampus (6.8–7 mm, uninjured: 6.79 ± 0.79%, TBI: 18.12 ± 5.03%, P = 1.42E-11; 7–7.2 mm, uninjured: 7.15 ± 0.83%, TBI: 18.31 ± 4.01%, P = 3.02E-11; 7.2–7.4 mm, uninjured: 8.67 ± 1.70%, TBI: 16.72 ± 4.55%, P = 7.64E-06; two-way repeated-measures ANOVA with Bonferroni's post-hoc test) and decreases at 10 mm to 10.2 mm at the level of ENTm (control: 7.48 ± 2.04%, TBI: 1.90 ± 1.03%, P = 1.33E-02; two-way repeated-measures ANOVA with Bonferroni's post-hoc test). After TBI, massive input labeling was detected within the ipsilateral hippocampus, with a significantly higher proportion of input from area CA1 (**Figure 3.4h**). However, distant brain areas providing the greatest proportion of input to SST interneurons in controls, such as ENTm and NDB, were found to have a significant reduction in input after TBI (**Figure 3.4h**). To directly compare changes in the number of input neurons rather than the proportion of input, we calculated the convergence index for each animal, defined as the number of mCherry-labeled input neurons divided by the number of GFP- and mCherry-labeled starter cells. This analysis also revealed a significant increase in CA1 input, and decreases in long-range input from ENTm and NDB (**Figure 3.9**). Thus, there is a dramatic shift in both the number and relative proportion of local and long-distance input to hippocampal SST interneurons after TBI.

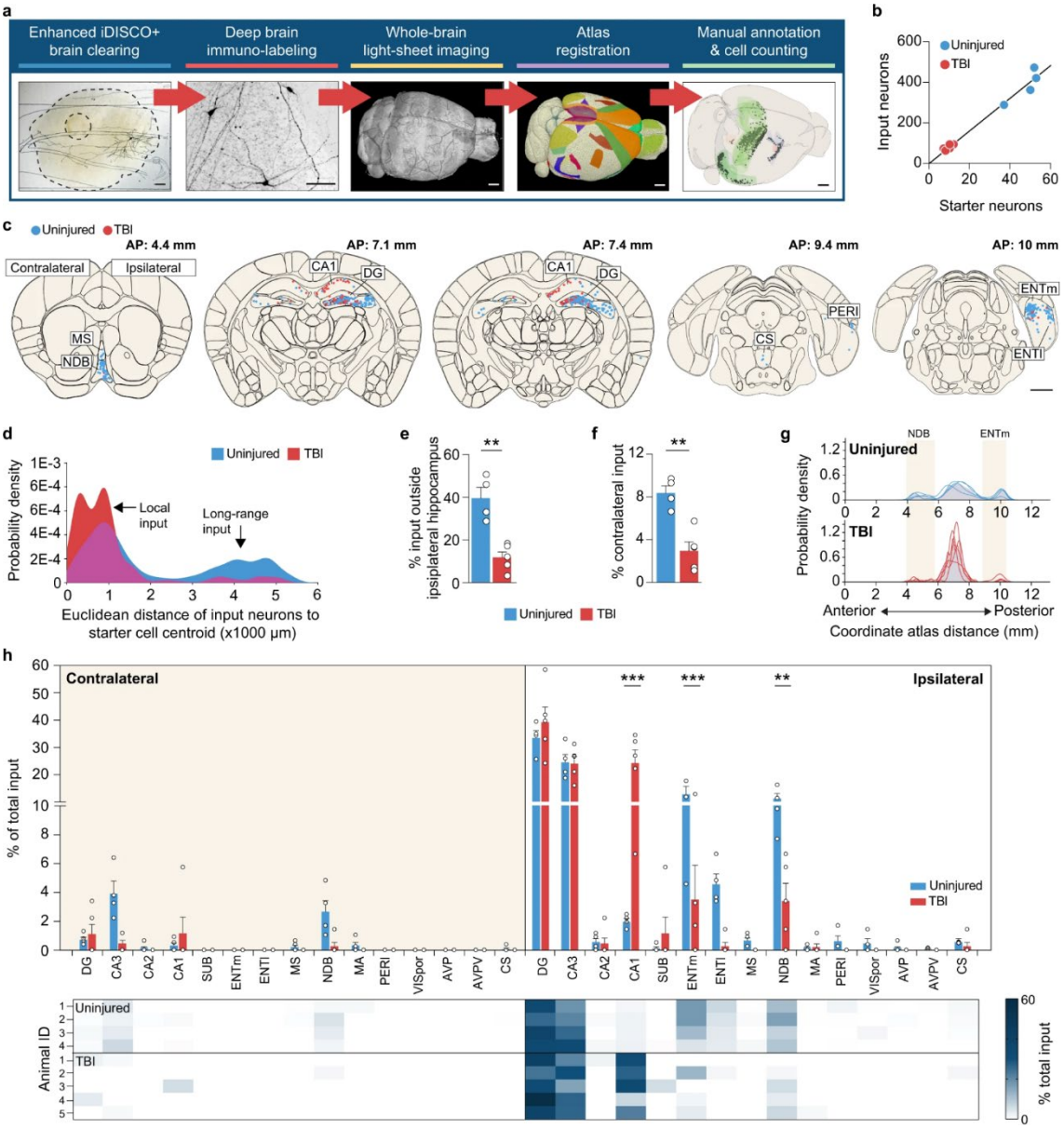


Figure 3.4: Reorganization of brain-wide input to hippocampal SST interneurons after TBI. a. Experimental design for enhanced iDISCO+ brain clearing and whole-brain light-sheet imaging. **b.** Linear regression analysis for number of starter cells and pre-synaptic input neurons in the whole brain (n = 4 uninjured controls, 5 TBI mice; R^2 = 0.98). **c.** Schematic coronal sections (250 µm) showing individual rabies-labeled cells registered in standardized atlas space for uninjured controls (blue) and brain-injured animals (red). One dot represents one neuron. n = 4 uninjured control and 5 TBI animals. **d.** Gaussian kernel cell density plots showing pooled Euclidian distances of input neurons to nearest starter neuron centroid. **e.** Proportion of input neurons found outside ipsilateral hippocampus (DG, CA3, CA2, CA1). Uninjured: 39.6 ± 5.2%, n = 4 mice; TBI: 11.8 ± 2.7 %, n = 5 mice; $^{**}P$ = 1.5E-3; two-tailed t-test. **f.** Proportion of input neurons found in the contralateral hemisphere. Uninjured: 8.4 ± 0.7%, n = 4 mice; TBI: 3.0 ± 0.8 %, n = 5 mice; $^{**}P$ = 2.0E-3; two-tailed t-test. **g.** Gaussian kernel cell density plot of the whole-brain distribution of input neurons along the anterior-posterior axis. Grey shading represents the pooled population with individual lines representing each animal. **h.** Proportion of input neurons found in each discrete brain area. $^{***}P < 1.0E-15$, uninjured versus TBI (CA1), $^{***}P$ = 2.25E-04, uninjured versus TBI (ENTm), $^{**}P$ = 4.69E-03, uninjured versus TBI (NDB); two-way repeated-measures ANOVA with Bonferroni's post-hoc test; n = 4 uninjured and 5 TBI mice. Error bars, s.e.m.; scale bars, 1 mm (except deep immunolabeling in a, 100 µm).

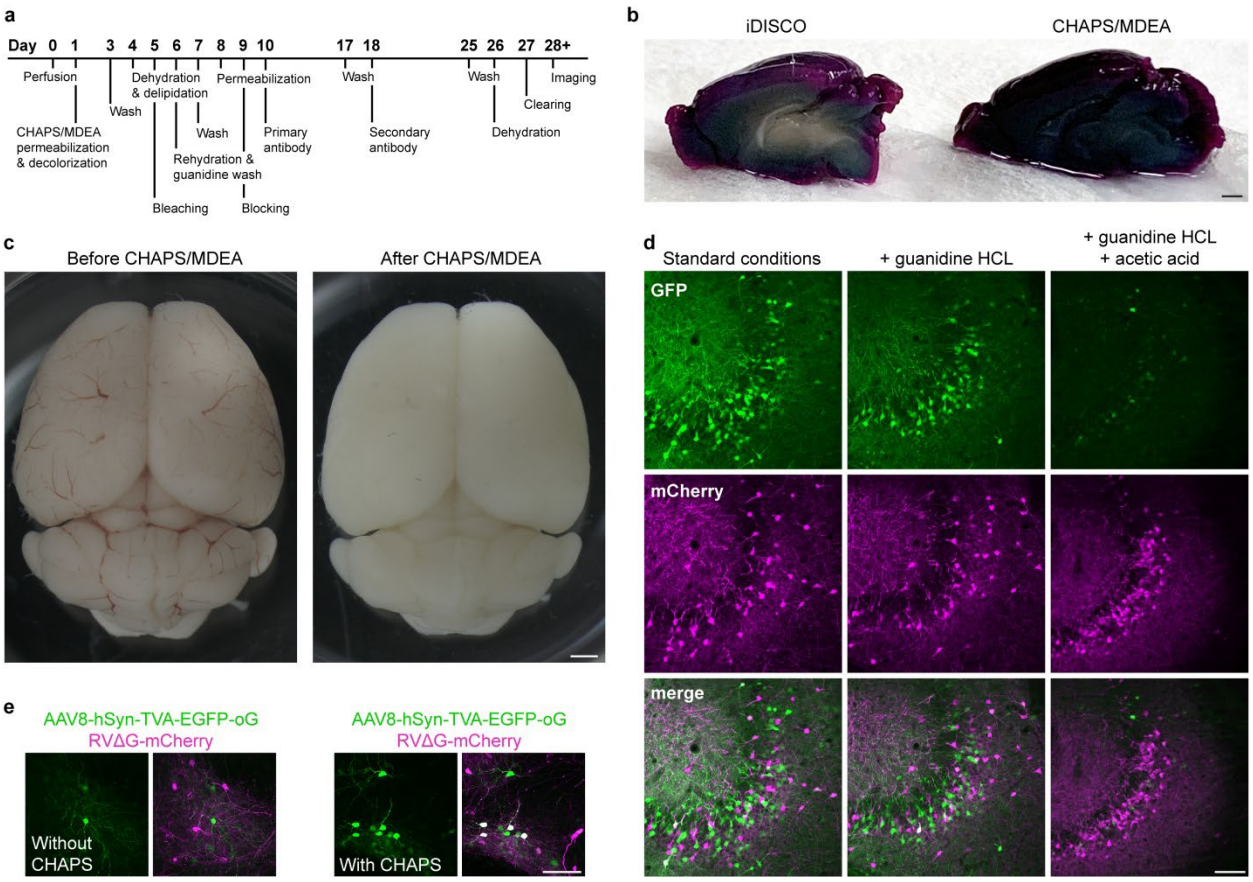


Figure 3.5: Optimization of enhanced iDISCO+ protocol. a. Timeline of brain clearing and immunolabeling. **b.** Whole mouse brains incubated with purple food coloring overnight after permeabilization with iDISCO+ buffer or CHAPS/MDEA buffer for 48 h. **c.** Unperfused mouse brain drop-fixed in 4% PFA overnight (left) and the same brain after 48 h of decolorization in 10% CHAPS/25% MDEA in PBS (right). **d.** Coronal section of hippocampus labeled for AAV helper virus (green) and input neurons (magenta) using standard immunostaining conditions, immunostaining with 4M guanidine HCl treatment or with 4M guanidine HCl and acetic acid treatment. **e.** Coronal section of hippocampus labeled for AAV helper virus (green) and input neurons (magenta) with standard antibody diluent (left) and diluent containing 0.25% CHAPS (right). Scale bar, 1mm (b, c); 100 μm (d, e).

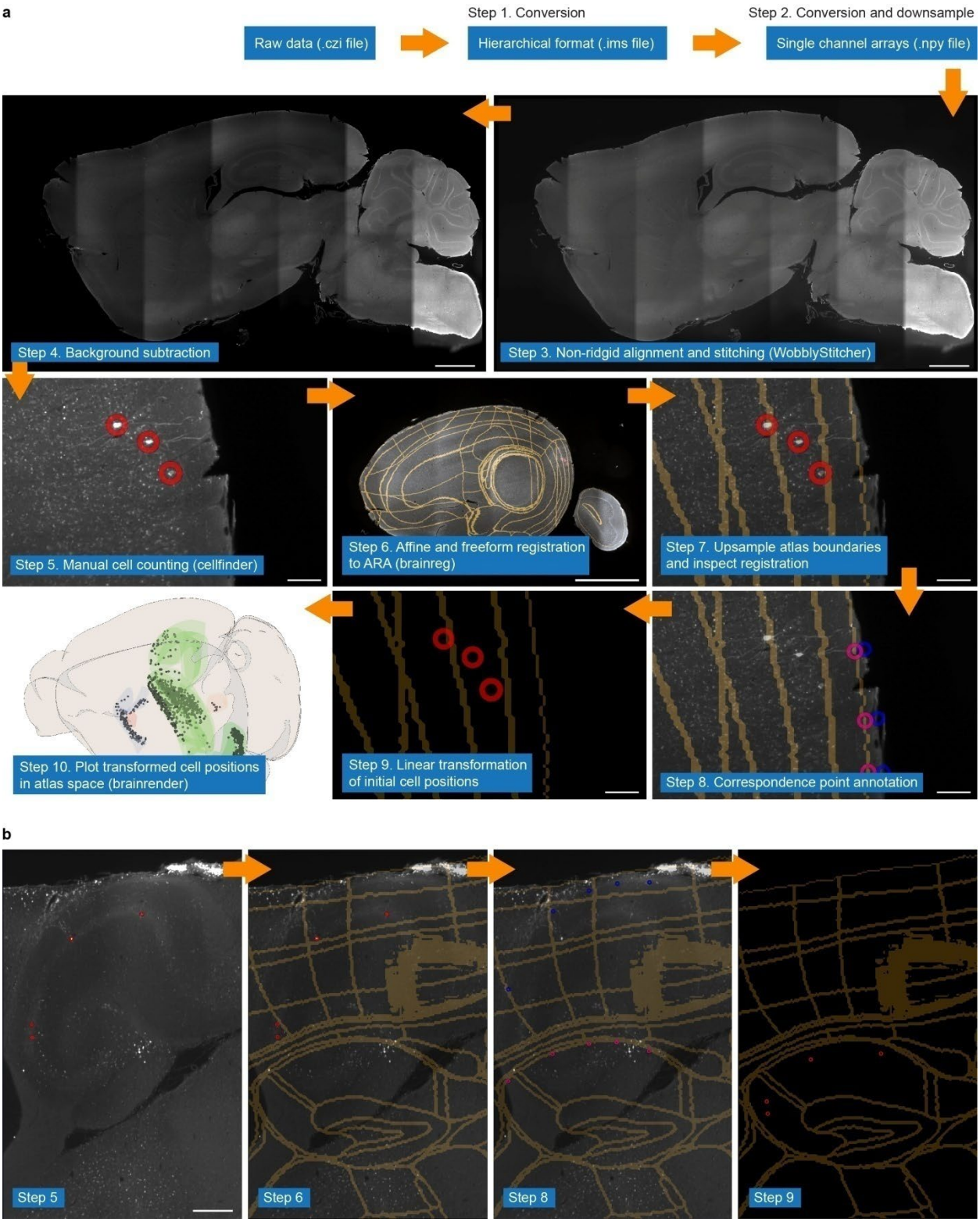


Figure 3.6: Protocol for image registration and analysis. a. Raw data were initially converted from .czi to .ims file format. For each channel, data were downsampled by a factor of two in each dimension and converted to .npy format. 561 nm channel data was stitched using WobblyStitcher and exported as a stack of .tif files. For each animal, background intensity was measured and subtracted from all images in the stack. Individual cell positions were annotated using the graphical interface in cellfinder. 561 nm channel data were then down sampled to 10 μm isotropic

resolution and registered to the Allen Reference Atlas. Atlas boundaries were upsampled to the original imaging resolution and overlaid over 561 nm channel data. For each image plane containing cells, atlas boundaries were manually inspected for accuracy. Registration error was corrected by annotating pairs of points corresponding to region boundaries (blue) and the respective atlas location to correct (magenta) to calculate transformation vector length. Representative animal from *n* = 9 uninjured mice. **b.** Atlas registration at the injury epicenter in a brain injured animal. Representative animal from *n* = 15 TBI mice. Scale bars, 1mm (a, Steps 3, 4 and 6), 100 μm (a, Steps 5, 7-9) and 250 μm (b).

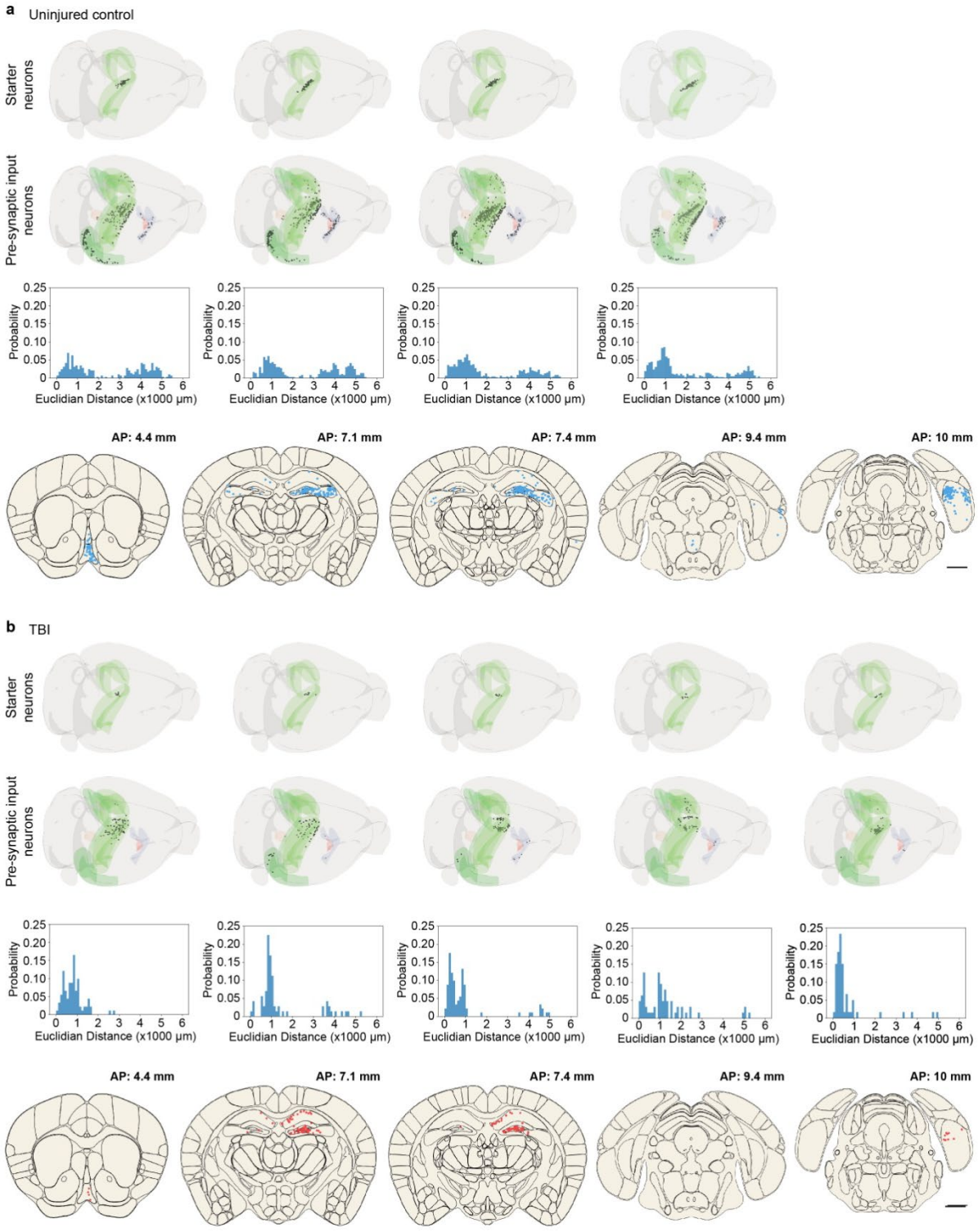


Figure 3.7: Individual animal plots of input to hilar SST interneurons. a, b. Cell counts for each uninjured control (a) and brain injured animal (b). Top: whole-brain plots of starter cells and pre-synaptic input neurons annotated in standardized atlas space. Middle: histograms showing Euclidian distances at 100 µm bins. Black dots represent individual cells registered in standardized atlas space. Shading indicates hippocampal formation (green), pallial regions (blue) and hypothalamus (red). Bottom: Schematic coronal sections (250 µm) showing individual rabies-labeled cells registered in standardized atlas space. Scale bar, 1 mm

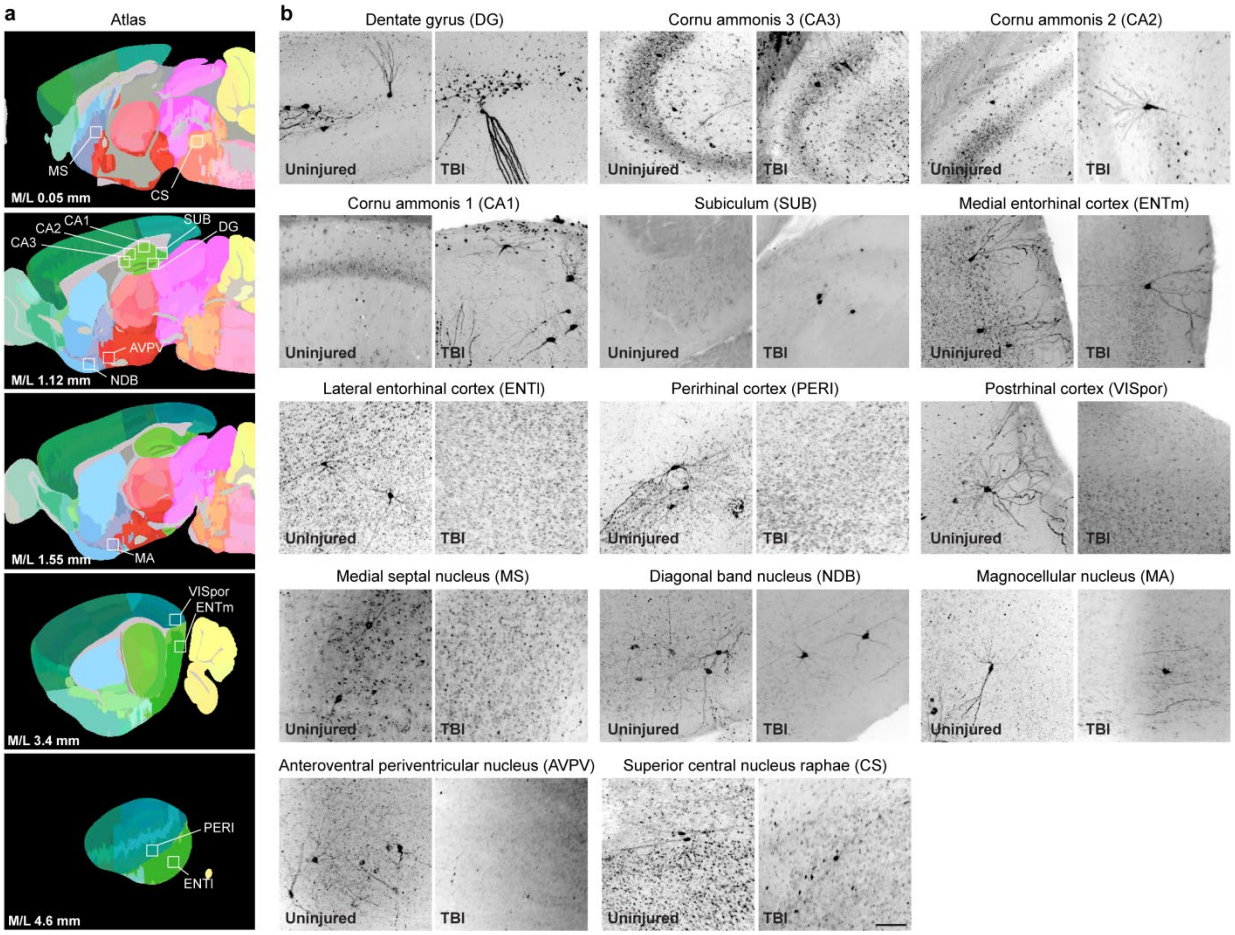


Figure 3.8: Input neurons innervating hilar SST interneurons in hippocampus. a. Sagittal sections obtained from the ARA indicating brain regions where rabies-labeled cells were found. **b.** Maximum intensity projections (100μm) of neurons in whole brains providing direct input to hilar SST interneurons in the intact and damaged brain. Representative animals from *n* = 4 uninjured controls and 5 TBI mice. Scale bar, 100 μm.

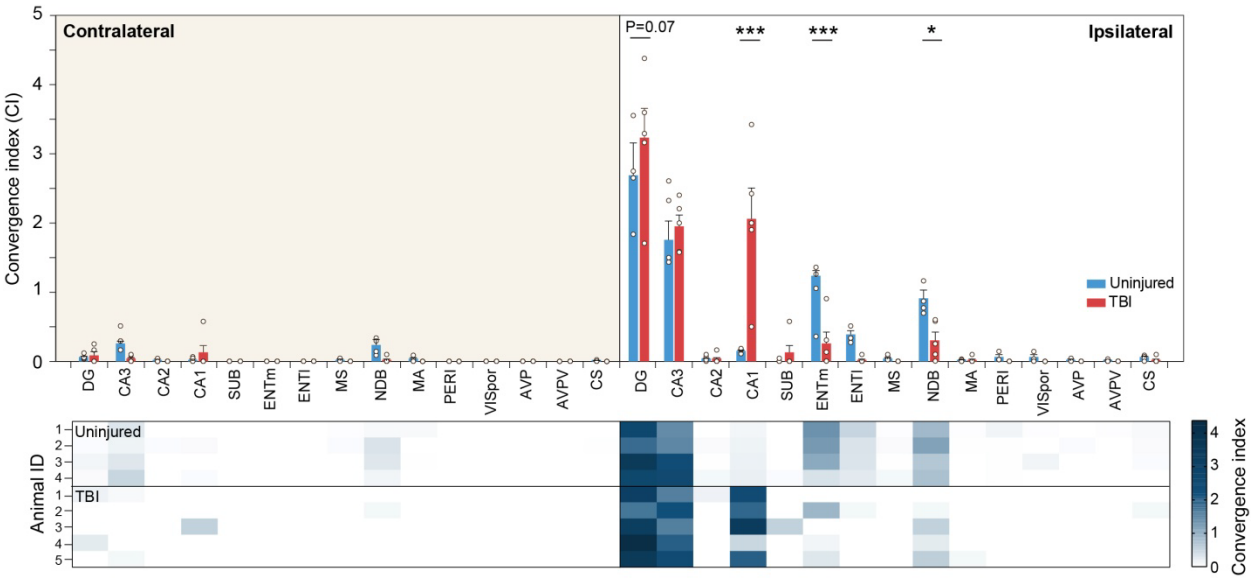


Figure 3.9: Retrograde circuit tracing data represented as a convergence index. The number of rabies-labeled input neurons in each brain area were divided by the total number of starter cells counted for each animal to derive a convergence index for each brain area. Top: Average convergence index for each brain area. Bottom: individual values for each animal represented by a heat-map. ****P* < 1.00E-15, CA1 (ipsilateral), ****P* = 7.19E-04, ENTm (ipsilateral), **P* = 3.29E-02, NDB (ipsilateral); two-way repeated-measures ANOVA with Bonferroni's post-hoc test; *n* = 4 uninjured and 5 TBI mice. Error bars, s.e.m.

Long-range input is proportionally stable, but local input is not

The loss of long-range input after TBI could result from a loss of neurons at distant sites or a loss of anatomical connections. To test this, and to characterize the neurochemical identities of the input to hilar SST interneurons, we developed a method for rehydrating the same brains used for light-sheet imaging and processing them for traditional double-immunofluorescence immunostaining (**Figure 3.10a-c**). Because long-range input to hilar SST interneurons arrives primarily from basal forebrain and ENTm, we quantified neuron populations in these areas.

The basal forebrain contains multiple cell types that project long distances via the fimbria/fornix pathway to the hippocampus, including cholinergic, glutamatergic and GABAergic neurons (Do et al., 2016). In both control and injured animals, the absolute majority of NDB input neurons to hilar SST interneurons expressed choline acetyltransferase (CHAT) (control: 67.1 ± 6.8%, *n* = 3 mice; TBI: 79.2 ± 12.5%, *n* = 4 mice; *P* = 0.99, Fisher's exact test; **Figure 3.10d, e**). This is different from inhibitory interneurons in CA1, which primarily receive GABAergic input from the basal forebrain

(Sun et al., 2014). We did not find a difference in the density of CHAT+ neurons in NDB between control and brain injured animals (**Figure 3.10f**), suggesting CHAT+ neurons were not reduced in the basal forebrain after focal TBI.

Because neurons in NDB and ENTm project directly into the hippocampus, their axons are almost surely damaged by TBI. Therefore, we next examined whether the density of cholinergic projections in the hippocampus were affected by TBI. In both control and injured animals, there was a dense plexus of CHAT+ axonal processes innervating every layer of hippocampus, even at the injury epicenter (**Figure 3.10g, h**). We did not detect a difference in CHAT expression between groups (control, ipsilateral: 20.8 ± 1.9%, control, contralateral: 20.8 ± 1.7%, $n = 3$ mice; TBI, ipsilateral: 22.9 ± 0.6%, TBI, contralateral: 22.0 ± 1.2%, $n = 4$ mice; $P = 0.96$, two-way ANOVA). These results demonstrate the reduction in CHAT+ input neurons was not accompanied by a general loss of CHAT+ afferents in the hippocampus after TBI.

This result was unexpected, because a loss of CHAT immunoreactive neurons has been reported in basal forebrain of diffuse injury models (Leonard et al., 1994; Schmidt and Grady, 1995). To rule out the possibility that cell quantifications were influenced by rabies circuit mapping or brain clearing procedures, we examined a second, independent cohort of control and brain injured animals that did not undergo these procedures ($n = 6$ controls, $n = 4$ TBI animals). In this replication experiment, we also found similar numbers of CHAT+ neurons in NDB of age-matched control and TBI mice (**Figure 3.11**).

In both control and brain injured animals, input neurons in ENTm were found almost exclusively in layer II (**Figure 3.10i**). Approximately 90% of these cells co-expressed reelin and had large multipolar stellate cell morphologies (control: 86.8 ± 0.34%, $n = 3$ mice; TBI: 95.2 ± 4.8%, $n = 3$ mice; $P = 0.99$, Fisher's exact test; **Figure 3.10j**). These results are consistent with prior studies

showing that reelin-expressing stellate cells in ENTm give rise to the main associational glutamatergic pathway known as the perforant path that projects to the dentate gyrus, CA3 and CA2 regions of hippocampus (Steward and Scoville 1976; Pesold et al., 1998; Varga et al., 2010). We did not find a difference in the density of reelin+ neurons in ENTm between control and brain injured animals (**Figure 3.10k**), similar to our results in basal forebrain. Together, our results demonstrate there is a reduction in the amount of input to hilar SST interneurons from both of the major distant brain regions innervating dentate gyrus after focal TBI, but these distant areas remain structurally intact.

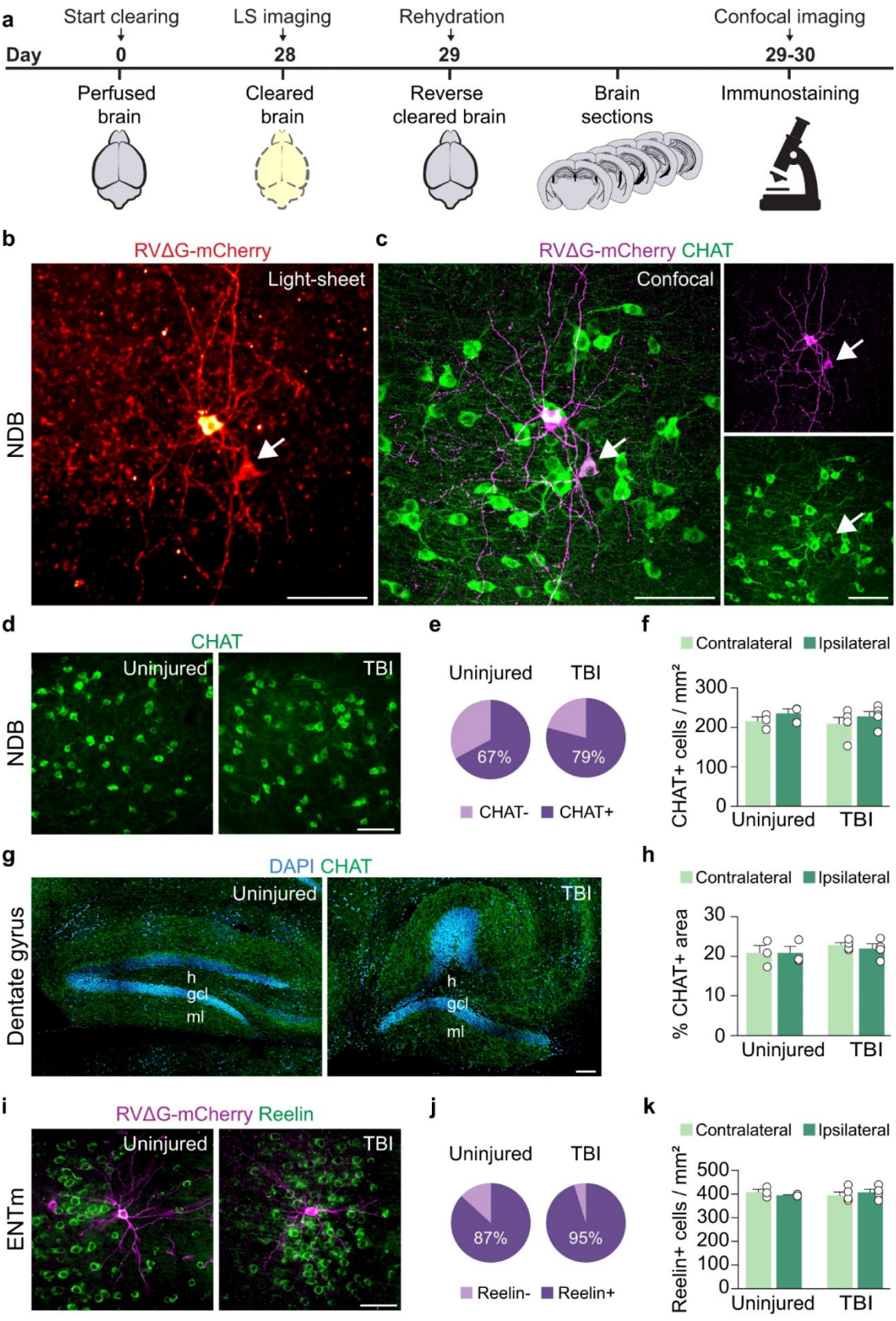

a
Start clearing
LS imaging
Rehydration
Confocal imaging
Day
0
28
29
29-30
Perfused brain
Cleared brain
Reverse cleared brain
Brain sections
Immunostaining
b
RVΔG-mCherry
Light-sheet
NDB
c
RVΔG-mCherry CHAT
Confocal
d
CHAT
Uninjured
TBI
NDB
e
Uninjured
TBI
67%
79%
CHAT-
CHAT+
f
Contralateral
Ipsilateral
CHAT+ cells / mm²
300
200
100
0
Uninjured
TBI
g
DAPI CHAT
Uninjured
TBI
Dentate gyrus
h
gcl
ml
h
Contralateral
Ipsilateral
% CHAT+ area
30
20
10
0
Uninjured
TBI
i
RVΔG-mCherry Reelin
Uninjured
TBI
ENTm
j
Uninjured
TBI
87%
95%
Reelin-
Reelin+
k
Contralateral
Ipsilateral
Reelin+ cells / mm²
500
400
300
200
100
0
Uninjured
TBI

Figure 3.10: Distant brain regions remain structurally intact. a. Schematic showing the experimental protocol for reverse brain clearing and immunolabeling. **b.** Two rabies-labeled input neurons (red) identified in a sagittal optical section of NDB in an intact control brain. Representative animal from *n* = 3 uninjured controls. 50 µm maximum intensity projection obtained by whole-brain light-sheet imaging. **c.** Sagittal section containing the same input neurons (magenta) labeled for CHAT (green) after processing for traditional immunostaining and confocal imaging. Representative animal from *n* = 3 uninjured controls. Arrow indicates co-labeled cell. **d.** NDB of uninjured control (left) and brain-injured animal (right) labeled for CHAT (green). Representative animals from *n* = 3 uninjured and 4 TBI mice. **e.** Proportion of mCherry+ rabies-labeled input neurons that expressed CHAT. **f.** Quantification of CHAT+ neuron density in ipsilateral and contralateral NDB in uninjured controls and brain-injured animals. *n* = 3 uninjured and 5 TBI animals. **g.** Sagittal section of dentate gyrus in uninjured control (left) and brain injured animal (right) labeled for CHAT (green) and DAPI (blue). Representative animals from *n* = 3 uninjured and 4 TBI mice. h, hilus; gcl, granule cell layer; ml, molecular layer. **h.** Quantification of CHAT+ axon density in ipsilateral and contralateral dentate gyrus in uninjured controls and brain-injured animals. *n* = 3 uninjured and 4 TBI animals. **i.** ENTm of uninjured control (left) and brain-injured animal (right) labeled for reelin (green) and mCherry (magenta). Representative animals from *n* = 3 uninjured and 5 TBI animals. **j.** Proportion of mCherry+ rabies-labeled input neurons that expressed reelin. **k.** Quantification of reelin+ cell density in ipsilateral and contralateral ENTm. *n* = 3 uninjured and 5 TBI animals. Error bars, s.e.m.; scale bars, 100 µm.

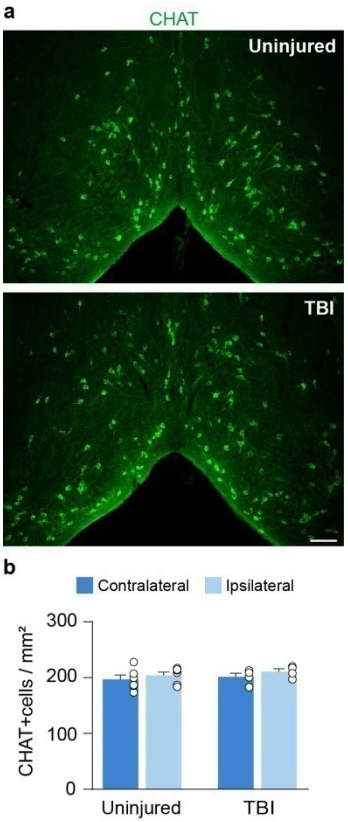


Figure 3.11: Replication of CHAT immunostaining with conventional immunostaining in a separate cohort of animals. a. Coronal sections of NDB labeled for CHAT in an uninjured control and a brain injured animal. Scale bar, 100 µm. **b.** Quantification of CHAT+ cell density. Error bars, s.e.m.

Input from CA1 increased more than 10-fold after TBI. To identify which CA1 neuron types provide input to hilar SST interneurons, we assessed the laminar position of CA1 input neurons in the same reverse-cleared tissue (**Figure 3.12**). In controls, ~65% of CA1 input neurons were

positioned in the pyramidal cell layer. These neurons had morphological features of pyramidal neurons and expressed WFS1, a marker of CA1 pyramidal neurons (**Figure 3.12a**). A smaller portion of CA1 input neurons were found outside the pyramidal layer and did not express WFS1; these are putative interneurons. In brain injured animals, there was a significant increase in the proportion of input neurons positioned in the pyramidal cell layer (control: 64.5 ± 14.0%, $n = 3$ mice; TBI: 92.1 ± 5.1%, $n = 4$ mice; $P = 1.29E-07$, Chi-square test; **Figure 3.12b**). Robust projections from these neurons could be clearly seen entering dentate gyrus (**Figure 3.12a**). Therefore, there is an increase in local CA1 input to hilar SST interneurons after TBI, and CA1 pyramidal neurons are the primary source of this new input.

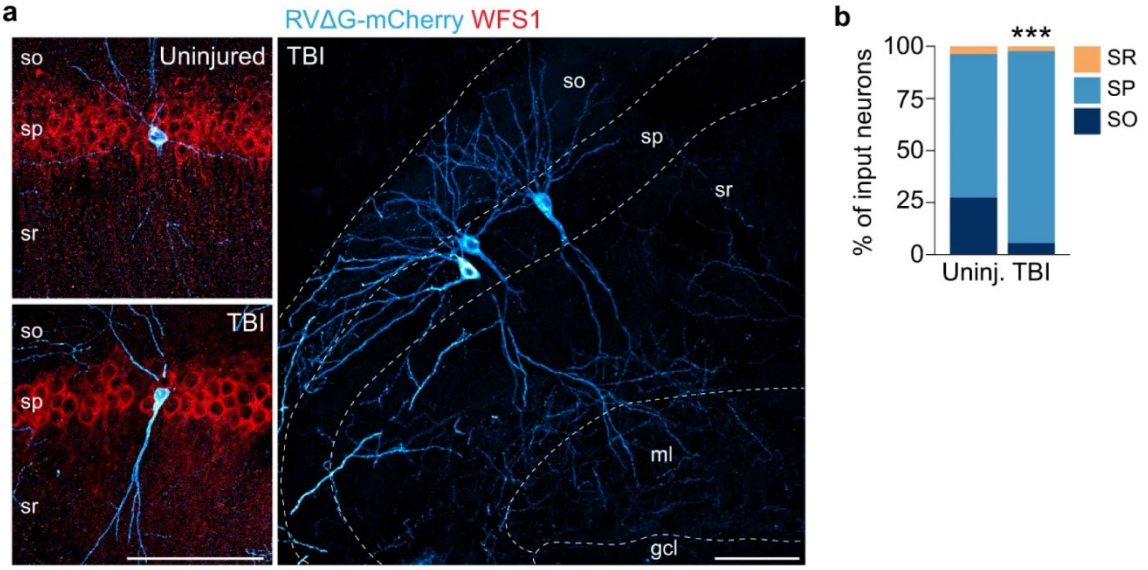


Figure 3.12: Identification of CA1 input neurons. a. CA1 in uninjured control (top) and brain injured animal (bottom) labeled for rabies (blue) and WFS1 (red). Representative animals from $n = 3$ uninjured and 4 TBI mice. so, stratum oriens; sp, stratum pyramidale; sr, stratum radiatum; ml, molecular layer; gcl, granule cell layer. **b.** Proportion of input neurons found in each layer of CA1. ***$P = 1.29E-07$, uninjured versus TBI, two-sided Chi-squared test. $n = 45$ cells from 3 uninjured controls, 183 cells from 4 TBI mice. Scale bars, 100 µm.

Whole-brain connectivity is reorganized in PFC

Having observed dramatic brain-wide reorganization of hippocampal SST interneuron circuitry, we next asked whether the input to SST neurons was also rewired far away from the injury. The PFC is a critical higher-order limbic site that is central to memory retrieval and decision making

and receives a highly diverse pattern of inputs spanning the entire brain, including direct input from hippocampus (Le Merre et al., 2021). At 24 hrs after injury, fluoro-jade C staining revealed degenerating neurons in the hippocampus and neocortex at the injury epicenter, but no labeled cells were detected at distant sites, such as PFC, entorhinal cortex, basal forebrain or thalamus (**Figure 3.13**). This result is nearly identical to previous reports in this model (Hall et al., 2008). We also did not find a difference in SST+ neuron density in PFC eight weeks after TBI (**Figure 3.14**). These results are consistent with producing a highly focal contusive brain injury.

To generate whole-brain maps of the input to SST interneurons in PFC, we used the same two-virus rabies-based approach to label dual-color starter cells and mCherry-labeled input neurons in SST-Cre mice (**Figure 3.15a, b**). For these studies, PFC was defined as including the following subregions based on a consensus drawn from the literature (Le Merre et al., 2021): secondary motor area (MOs), anterior cingulate areas dorsal and ventral (ACAd and ACAv), prelimbic area (PL), infralimbic area (ILA), orbital cortex medial, lateral and ventrolateral (ORBm, ORBl, and ORBvl). Injections were made into the ipsilateral hemisphere (that is, the injured side of the brain). We found 96.5% of the GFP-labeled neurons were SST+, and no neurons were labeled anywhere in the brain after injecting AAV8-hSyn-FLEX-TVA-P2A-eGFP-2A-oG helper and RVΔG-mCherry virus into Cre- animals (**Figure 3.16**). In both control and brain-injured animals, starter cells were almost exclusively located inside the PFC (**Figure 3.15c-f**). Regional distributions of the starter cells were similar to what has previously been published for PFC (Ährlund-Richter et al., 2019), and no differences were detected between groups in the dorsal-ventral location of the starter neurons (**Figure 3.15d**) or layer distribution (**Figure 3.15e**), indicating there was no major bias in the location of the starter cells. As expected, there was a correlation between the number of input neurons and starter neurons, but unlike hippocampus, the number of starter neurons were not reduced in brain-injured animals (control: $n = 283.6 \pm 69.5$ cells; TBI: $n = 178.8 \pm 18.2$ cells, $P = 0.2$, two-tailed *t*-test, $n = 5$ animals per group; **Figure 3.15g**).

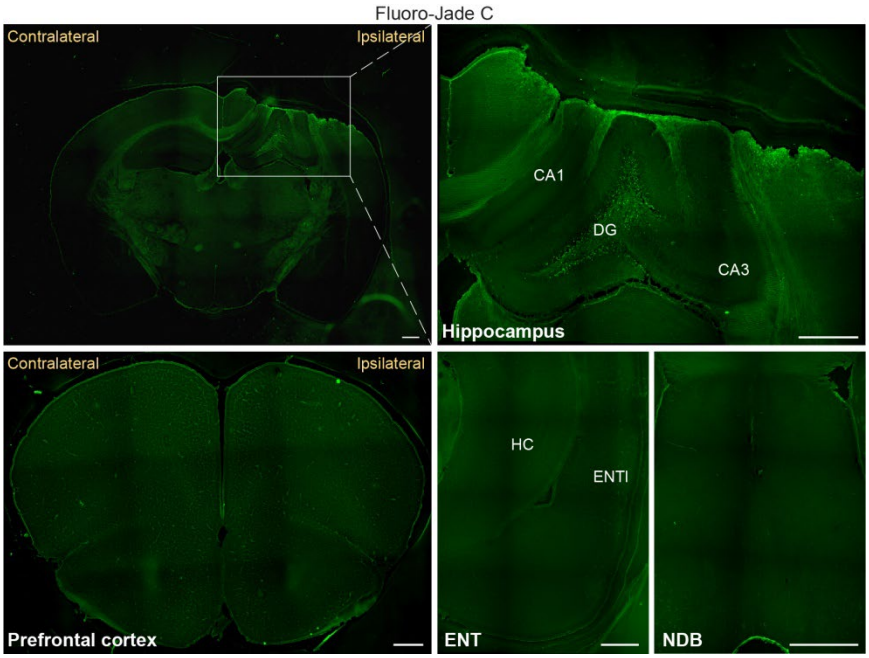


Figure 3.13: TBI produces highly focal neurodegeneration. Coronal sections through dorsal hippocampus (HC), prefrontal cortex, entorhinal cortex (ENT) and diagonal band nucleus (NDB) labeled for fluoro-jade C 24 h after TBI. Representative animal from *n* = 3 TBI mice. Scale bar, 500 µm.

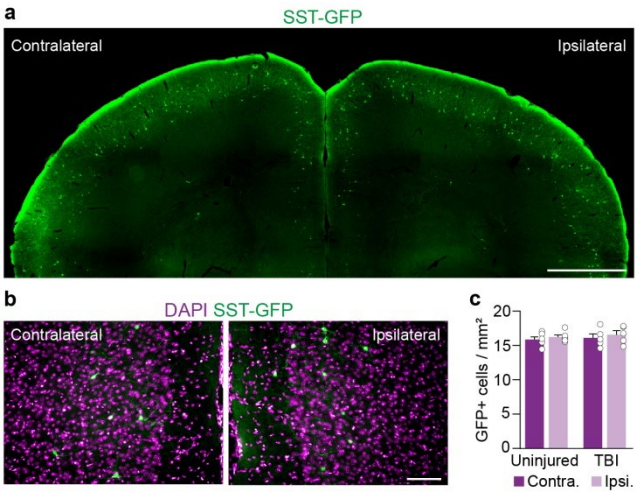


Figure 3.14: SST interneurons are not reduced in PFC after TBI. a, b. Coronal section 8 wks after TBI labeled for SST-GFP (green) and DAPI (magenta). Representative animals from *n* = 5 TBI mice. **c.** Quantification of SST-GFP interneurons in uninjured and brain injured animals. *n* = 6 uninjured controls and 5 TBI mice. Error bars, s.e.m.; scale bars, 1 mm (a), 100 μm (b).

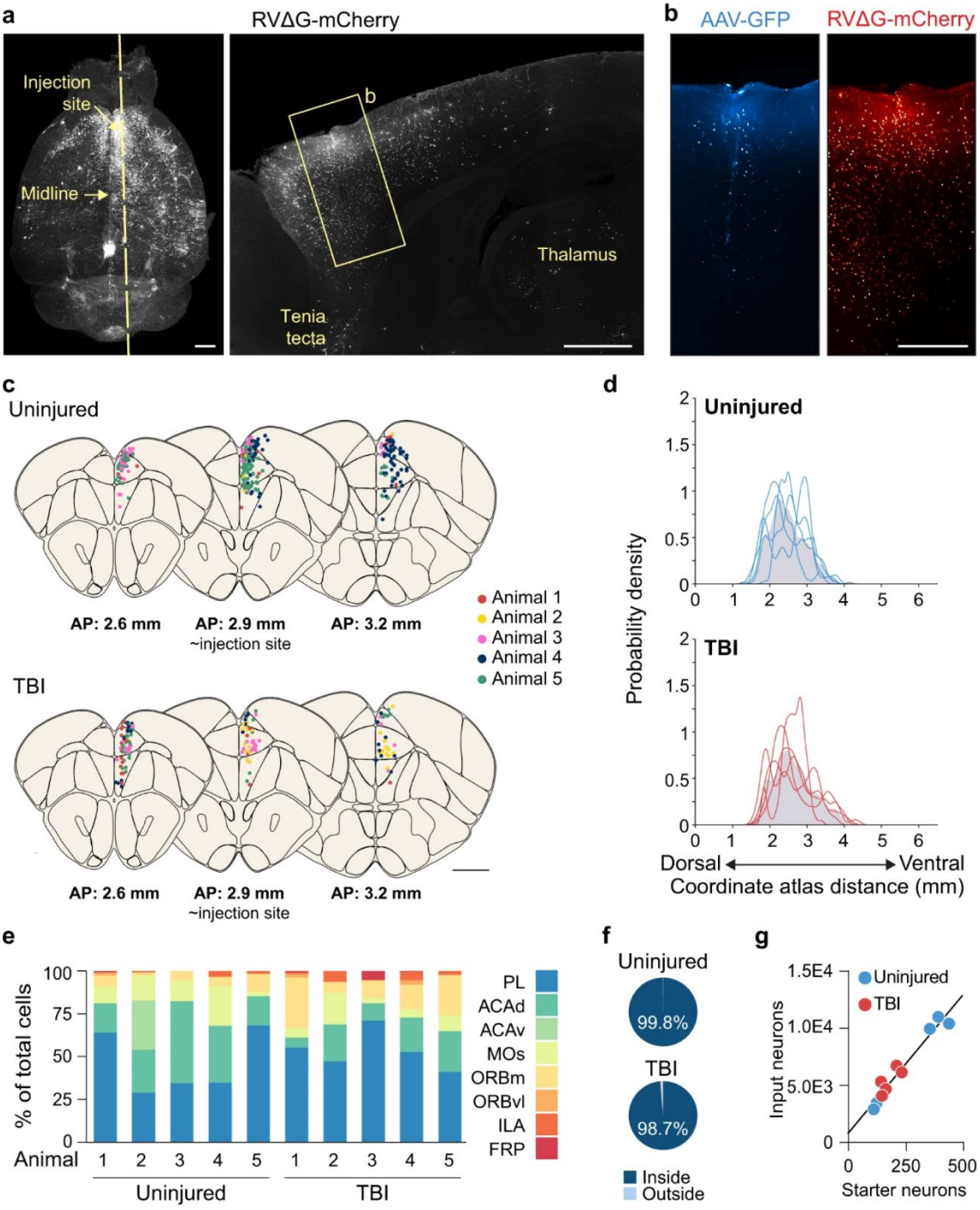


Figure 3.15: Distribution of starter neurons in PFC. a. Left: Whole brain cleared using iDISCO+ and labeled for neurons providing input to PFC SST interneurons (white). Right: 100 µm sagittal optical section of the same brain showing rabies-labeled input neurons at the injection site. **b.** Boxed region shown in (a) labeled for starter cells (blue) and input neurons (red). **c.** Schematic coronal sections (100 µm) showing individual starter cells registered in standardized atlas space for uninjured controls and brain injured animals. Each color corresponds to a different animal. One dot represents one neuron. *n* = 5 animals per group. **d.** Gaussian kernel cell density plots of the whole-brain distribution of starter neurons along the dorsal-ventral axis. Grey shading represents the pooled population with individual lines representing each animal. **e.** Regional distribution of starter cells in uninjured controls and brain injured animals. **f.** Proportion of starter cells identified within PFC (PL, ACAd, ACAv, MOs, ORBm, ORBvl, ILA). **g.** Linear

regression analysis for number of starter cells and pre-synaptic input neurons (n = 5 mice per group; R^2 = 0.95). Scale bars, 1 mm (a and c), 500 μm (b).

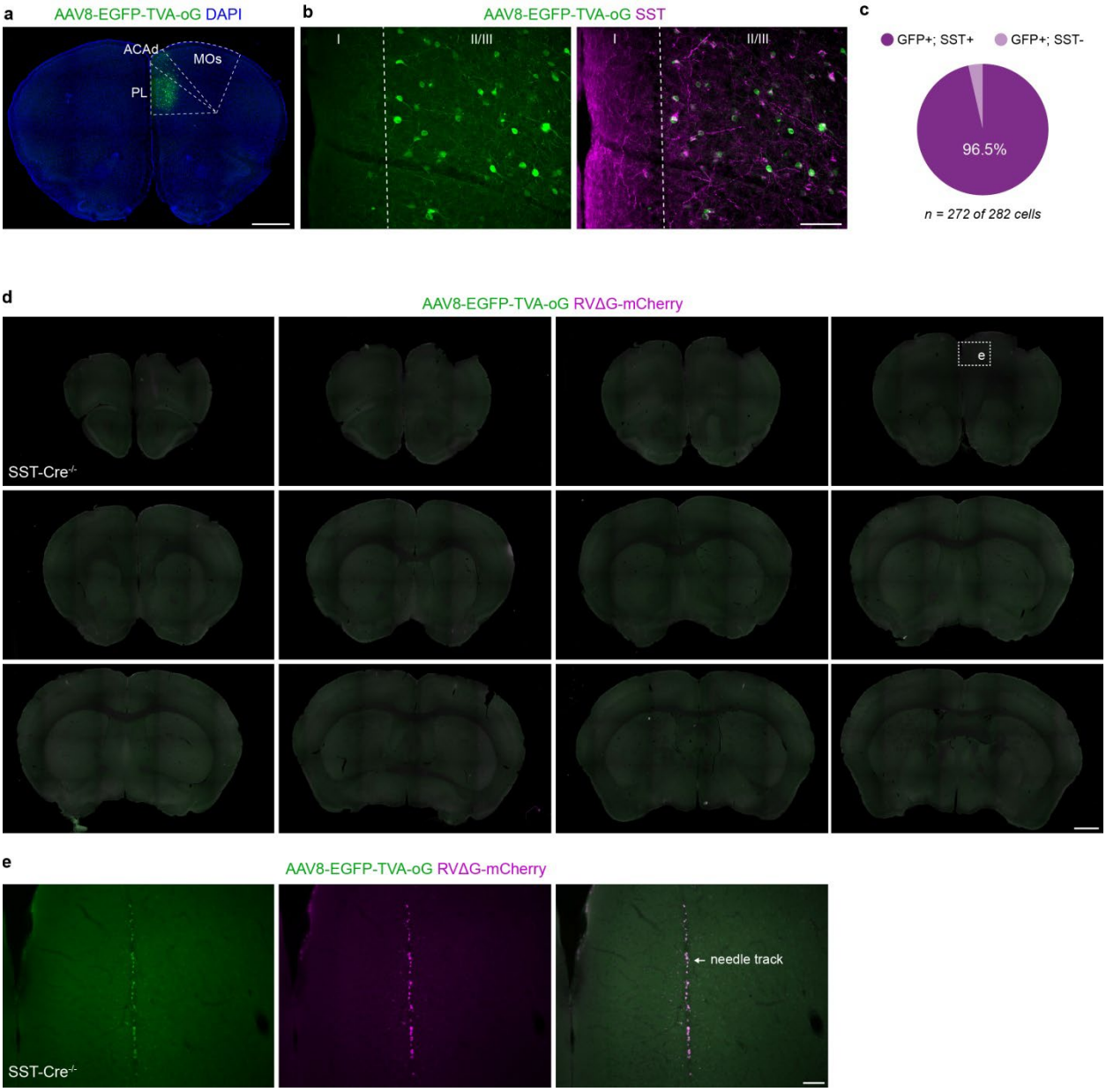


Figure 3.16: Virus specificity in PFC. a, b. Coronal section of a control animal labeled for AAV-GFP helper virus (green), SST (magenta) or DAPI (blue) 3 wks after AAV injection into PFC. **c.** Proportion of GFP+ cells that express SST. **d.** Serial coronal sections every 300 µm through the entire brain of an adult SST-Cre-negative mouse labeled for AAV helper virus (green) and rabies (magenta). **e.** High magnification image of the injection site in PFC of the same SST-Cre-negative mouse shown in d. Scale bars, 1 mm (a, d), 100 µm (b, e).

Next, we quantified the input to SST interneurons in PFC. Whole-brain retrograde tracing revealed input from 178 distinct brain regions (**Figures 3.17a, 3.18, 3.19**). The majority of input was detected within the isocortex, especially in the ipsilateral hemisphere, followed by thalamus,

hippocampus, and pallidum. These results are comparable to previous retrograde tracing results in control animals (Ährlund-Richter et al., 2019; Sun et al., 2019). Within isocortex, PFC subregions provided the most prominent input; the agranular insular area and hippocampus area CA1 also provided prominent input. Analysis of the probability of input along the AP axis showed significant increases in the percentage of input neurons between 3.2 and 3.4 mm at the level of PFC in brain-injured animals (uninjured: 9.14 ± 1.14%, TBI: 12.06 ± 1.41%, P = 4.82E-03; two-way repeated measures ANOVA with Bonferroni's post hoc test). Along the medial-lateral (ML) axis, we detected significantly higher proportion of input neurons between 0.2 and 0.5 mm lateral to midline in the ipsilateral hemisphere (5.9–6.0 mm, uninjured: 8.37 ± 1.38%, TBI: 11.38 ± 1.69%, P = 9.09E-07; 6.0–6.1 mm, uninjured: 10.20 ± 1.12%, TBI: 13.35 ± 0.81%, P = 2.08E-07; 6.1–6.2 mm, uninjured: 8.94 ± 0.61%, TBI: 11.90 ± 1.24%, P = 1.68E-06; two-way repeated-measures ANOVA with Bonferroni's post-hoc test), and a significantly lower proportion of input neurons were found between 0.4 and 0.5 mm lateral to midline in the contralateral hemisphere (5.2 to 5.3 mm, uninjured: 3.22 ± 0.34%, TBI: 1.35 ± 0.32%, P = 3.51E-02; two-way repeated-measures ANOVA with Bonferroni's post-hoc test; **Figure 3.17b**). There was a significant decrease in the overall percentage of contralateral input to SST interneurons after TBI (**Figure 3.17c**), similar to what we observed in the hippocampus. However, no differences were detected in the mean distance of input neurons to the starter cell centroid (**Figure 3.17d**) or the overall percentage of input neurons located outside ipsilateral PFC (**Figure 3.17e**).

Input neurons were initially grouped according to large functional divisions, i.e. isocortex, olfactory areas, hippocampal formation, cortical subplate, striatum, pallidum, thalamus, hypothalamus, midbrain and hindbrain. In brain injured animals, we found that SST interneurons in PFC received significantly greater percentage of total input from the ipsilateral isocortex as compared to controls, but the percentage of input neurons in the contralateral isocortex and ipsilateral thalamus were both reduced (**Figure 3.17f**). In thalamus, anterior thalamic nuclei (ATN) and the ventral

group of dorsal thalamus (VENT) showed a significantly lower proportion of input neurons after TBI (**Figure 3.17g**). Whole-brain analysis of the input neurons in all discrete brain areas revealed that six of the seven areas with altered input after TBI were in the isocortex (**Figure 3.17h**). Notably, not all PFC regions in the ipsilateral hemisphere had a significantly higher proportion of input neurons; input from ACAd and ORBvl were both significantly reduced after TBI. The proportion of input from contralateral PL was also reduced after TBI. Similar results were obtained by analyzing the convergence index for each animal (**Figure 3.20**). This pattern of enhanced local connectivity and reduced long-range input is similar to what we observed in brain injured hippocampus, suggesting that even in brain regions very far away from the injury site, the topographic organization of inhibitory neurons is dramatically rewired after a focal brain injury.

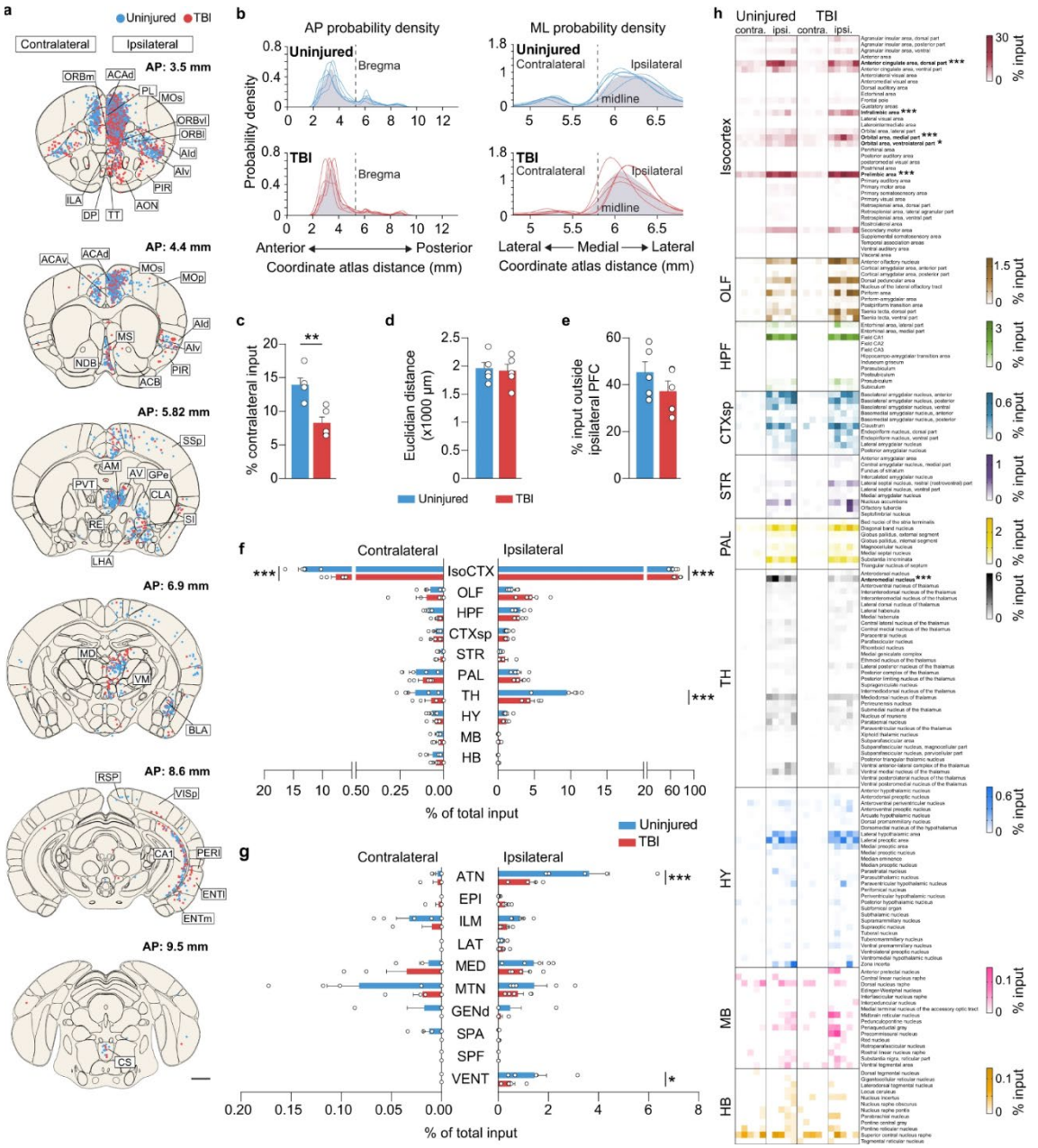


Figure 3.17: Input to SST interneurons in PFC is reorganized after TBI. a. Schematic coronal sections (100 µm) showing individual input neurons registered in standardized atlas space for uninjured controls (blue) and brain injured animals (red). One dot represents one neuron. n = 5 animals per group. **b.** Gaussian kernel cell density plots of the whole-brain distribution of input neurons along the anterior-posterior (AP) and medial-lateral (ML) axis. Grey shading represents the pooled population with individual lines representing each animal. Bregma, 5.3 mm; midline, 5.7 mm. **c.** Proportion of input neurons found in contralateral hemisphere. Uninjured: 14.00 ± 1.02%; TBI: 8.22 ± 0.98%; *n* = 5 mice per group; ***P* = 3.41E-03; two-tailed *t*-test. **d.** Quantification of average Euclidian distance between starter cell centroid and input neuron positions. *n* = 5 animals per group. **e.** Proportion of input neurons found outside ipsilateral PFC. *n* = 5 animals per group. **f.** Proportion of total input arising from high-level brain regions. ****P* = 2.84E-06, uninjured versus TBI (IsoCTX, contralateral), ****P* = 4.46E-10, uninjured versus TBI (IsoCTX, ipsilateral), ****P* = 4.12E-05, uninjured versus TBI (TH, ipsilateral); *n* = 5 mice per group; two-way repeated measures ANOVA with Bonferroni's post hoc test. **g.** Proportion of total presynaptic input arising from thalamic areas. ****P* = 1.16E-11, uninjured versus TBI (ATN, ipsilateral), **P* = 4.46E-02, uninjured versus TBI (VENT, ipsilateral); *n* = 5 mice per group; two-way repeated measures ANOVA with Bonferroni's post hoc test. **h.** Heatmap showing the proportion of input neurons identified in all discrete brain regions innervating PFC. ****P* = 1.00E-15, uninjured versus TBI (ACAd, ipsilateral), ****P* = 1.00E-15, uninjured

versus TBI (ILA, ipsilateral), ***P = 1.00E-15, uninjured versus TBI (ORBm, ipsilateral), *P = 1.25E-02, uninjured versus TBI (ORBvl, ipsilateral), ***P = 1.00E-15, uninjured versus TBI (PL, ipsilateral), ***P = 1.18E-04, uninjured versus TBI (PL, contralateral), ***P = 1.07E-05, uninjured versus TBI (AM, ipsilateral); n = 5 mice per group; two-way repeated measures ANOVA with Bonferroni's post-hoc test. Error bars, s.e.m.; scale bar, 1 mm.

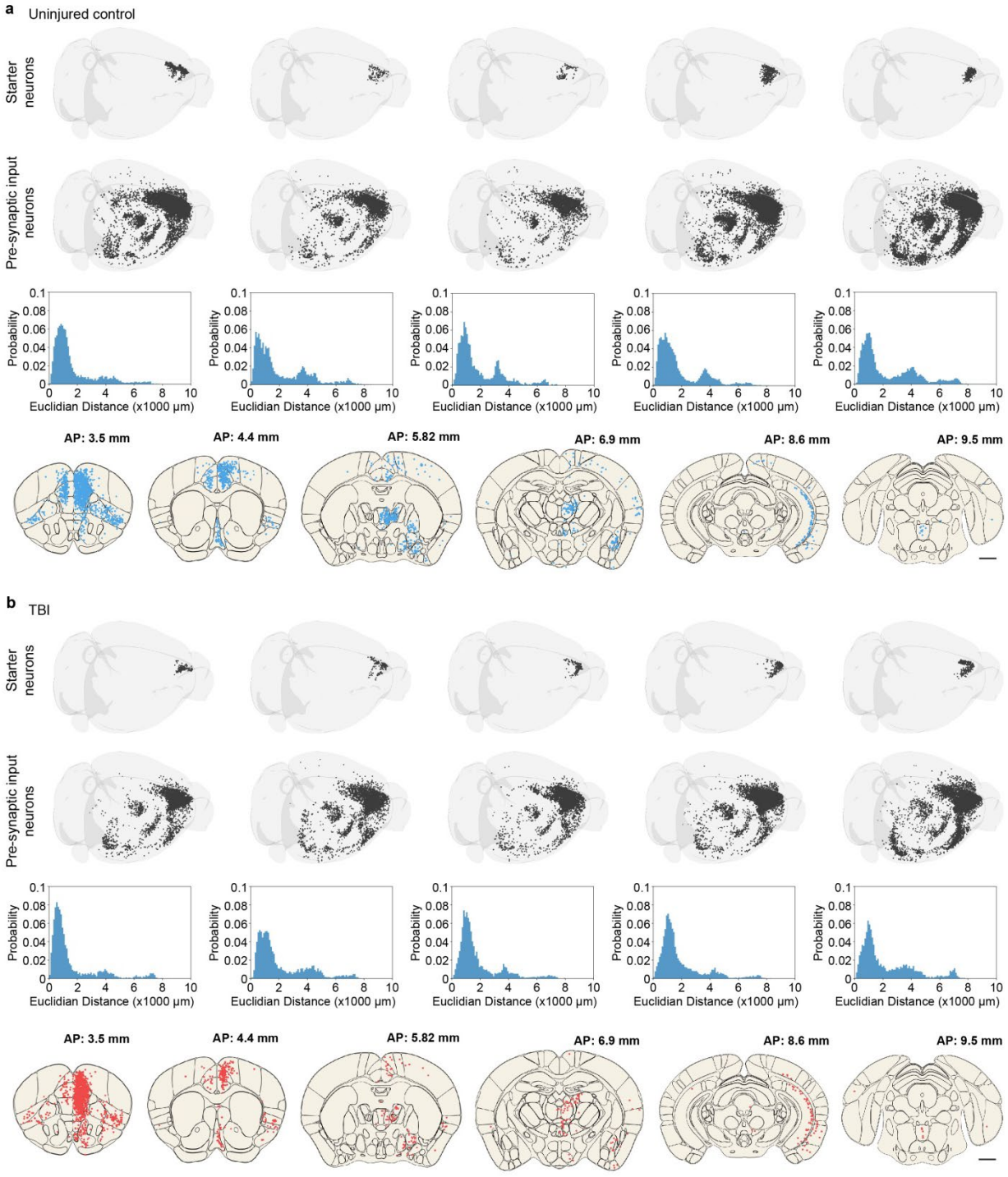


Figure 3.18: Individual animal plots of input to PFC SST interneurons. a, b. Cell counts for each uninjured control (a) and brain injured animal (b). Top: whole-brain plots of starter cells and pre-synaptic input neurons annotated in

standardized atlas space. Middle: histograms showing Euclidian distances at 100 μm bins. Black dots represent individual cells registered in standardized atlas space. Bottom: Schematic coronal sections (250 μm) showing individual rabies-labeled cells registered in standardized atlas space. Scale bar, 1 mm.

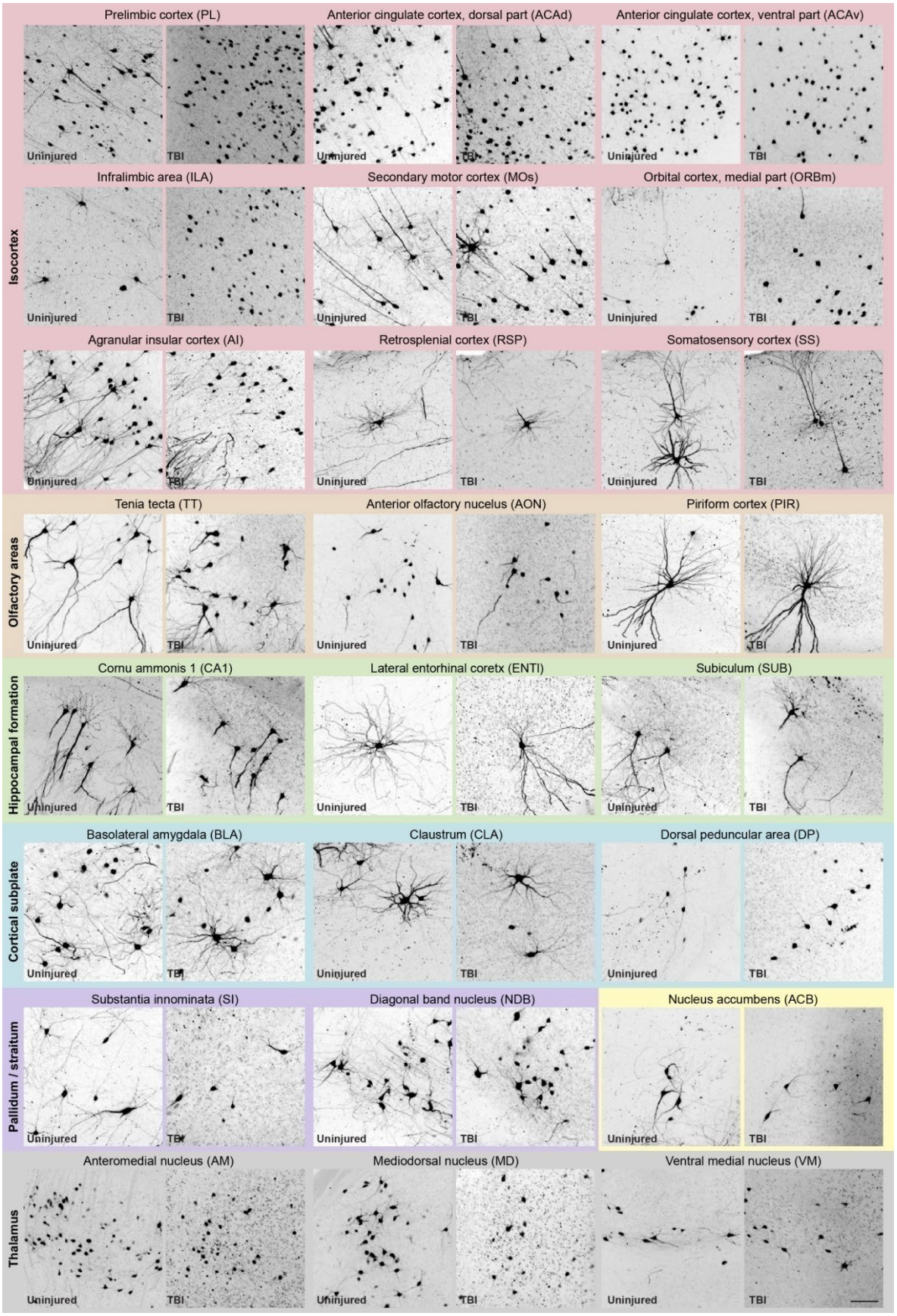

Isocortex
Prelimbic cortex (PL)
Anterior cingulate cortex, dorsal part (ACAd)
Anterior cingulate cortex, ventral part (ACAv)
Infralimbic area (ILA)
Secondary motor cortex (MOs)
Orbital cortex, medial part (ORBm)
Agranular insular cortex (AI)
Retrosplenial cortex (RSP)
Somatosensory cortex (SS)
Olfactory areas
Tenia tecta (TT)
Anterior olfactory nucelus (AON)
Piriform cortex (PIR)
Hippocampal formation
Cornu ammonis 1 (CA1)
Lateral entorhinal coretx (ENTl)
Subiculum (SUB)
Cortical subplate
Basolateral amygdala (BLA)
Claustrum (CLA)
Dorsal peduncular area (DP)
Pallidum / straitum
Substantia innominata (SI)
Diagonal band nucleus (NDB)
Nucleus accumbens (ACB)
Thalamus
Anteromedial nucleus (AM)
Mediodorsal nucleus (MD)
Ventral medial nucleus (VM)
Uninjured
TBI

Figure 3.19: Input neurons innervating PFC SST interneurons. Maximum intensity projections (100 μm) of neurons providing direct input to PFC SST interneurons in the intact and damaged brain. Representative animal from *n* = 5 animals per group. Scale bar, 100 μm.

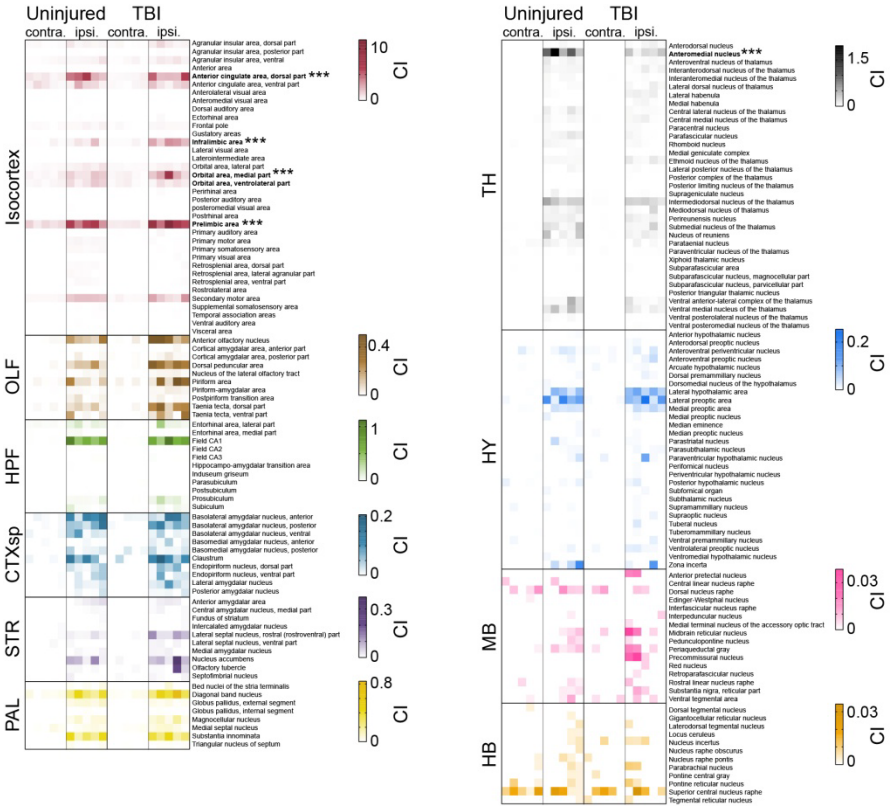


Figure 3.20: Retrograde circuit tracing data in PFC represented as a convergence index. Heatmap showing convergence index for all 178 discrete brain areas providing input to SST interneurons in PFC. ***P = 4.17E-4, uninjured versus TBI (ACAd, ipsilateral), ***P < 1.00E-15, uninjured versus TBI (ILA, ipsilateral), ***P < 1.00E-15, uninjured versus TBI (ORBm, ipsilateral), ***P < 1.00E-15, uninjured versus TBI (PL, ipsilateral), ***P = 1.73E-04, uninjured versus TBI (AM, ipsilateral). Each box represents one animal.

Transplanted SST interneurons establish orthotopic brain-wide connections

Grafts of embryonic-derived interneuron progenitors enable robust restoration of inhibition and are therapeutic in a wide range of acquired brain disorders, including epilepsy (Hunt et al., 2013), Alzheimer's disease (Martinez-Losa et al., 2018) and TBI (Zhu et al., 2019). However, the circuit basis for this regeneration is unknown. Therefore, we tested whether interneuron progenitors are capable of establishing appropriate local and long-range connections in a damaged brain. For this purpose, we harvested GABA progenitors from the medial ganglionic eminence (MGE), the developmental origin of nearly all SST-expressing cortical interneurons (Pelkey et al., 2017).

Then, 7 days after TBI, we transplanted 3×10^4 MGE cells into the ipsilateral hippocampus of C57BL/6 J mice at the injury epicenter. This corresponds to the period of maximal deafferentation after TBI (Scheff et al., 2005). We first examined grafts of SST interneurons harvested from E13.5 SST-Cre donor mice crossed with Ai6 reporter to allow for their visualization after transplantation. At 35 days after transplantation (DAT), transplanted interneurons were found throughout hippocampal subfields (n = 3 animals) (**Figures 3.21a-b, 3.22**). The majority of Ai6-labeled cells expressed SST (83 ± 2.1%, **Figure 3.21c**), confirming selective Cre expression in the SST population of transplanted MGE cells.

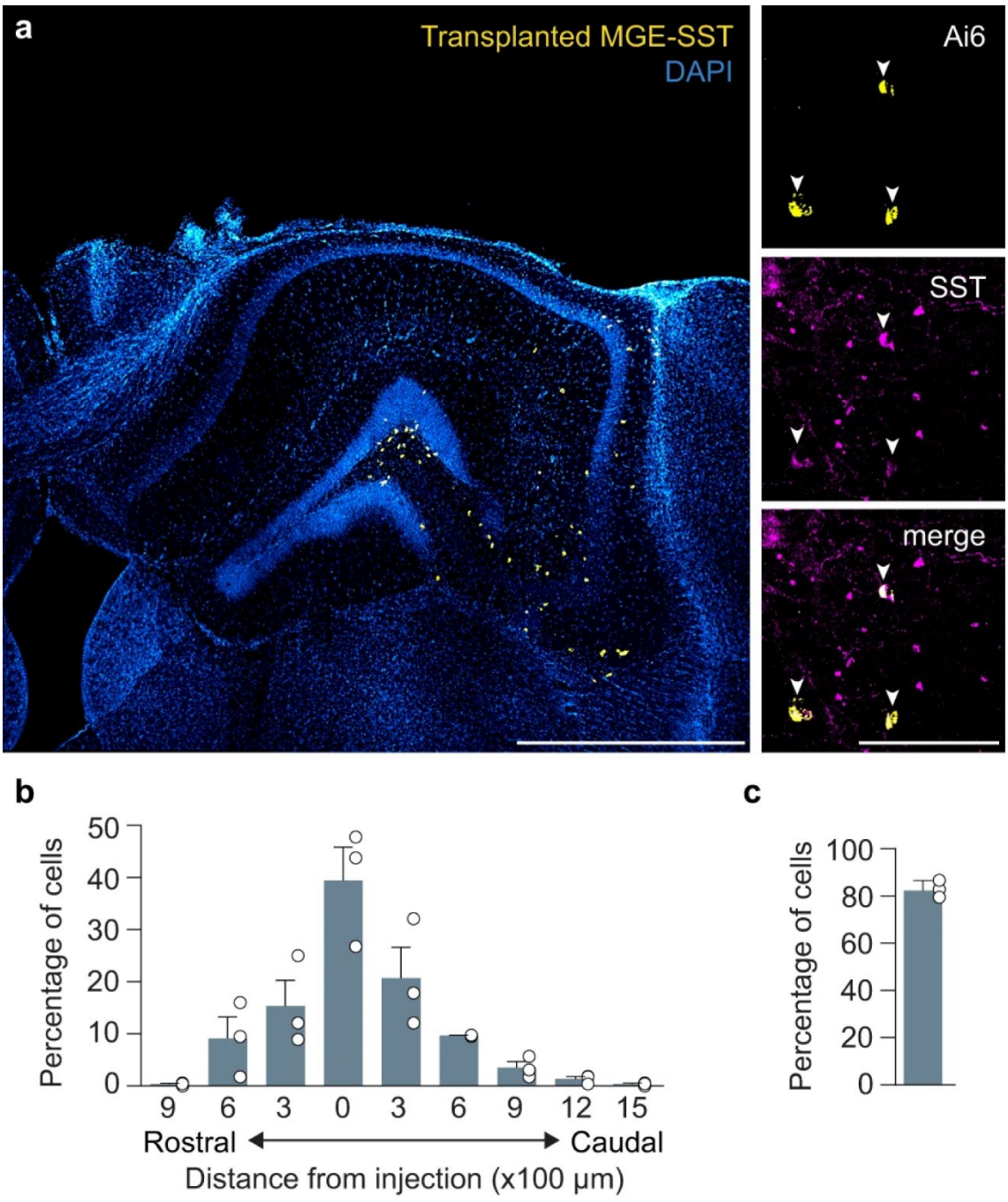


Figure 3.21: Transplanted SST interneurons integrate into brain-injured hippocampus. a. Left: Coronal section of dorsal hippocampus five weeks after transplantation labeled for Ai6-expressing transplanted interneurons (yellow) and DAPI (blue). Representative animal from *n* = 3 mice. Scale bar, 1 mm. Right: Ai6-expressing neurons (yellow) co-labeled for somatostatin (magenta). Scale bar, 100 µm. **b.** Distribution of transplanted SST interneurons 35 DAT, *n* = 3 mice. **c.** Proportion of Ai6-expressing cells that expressed somatostatin, *n* = 3 mice. Error bars, s.e.m.

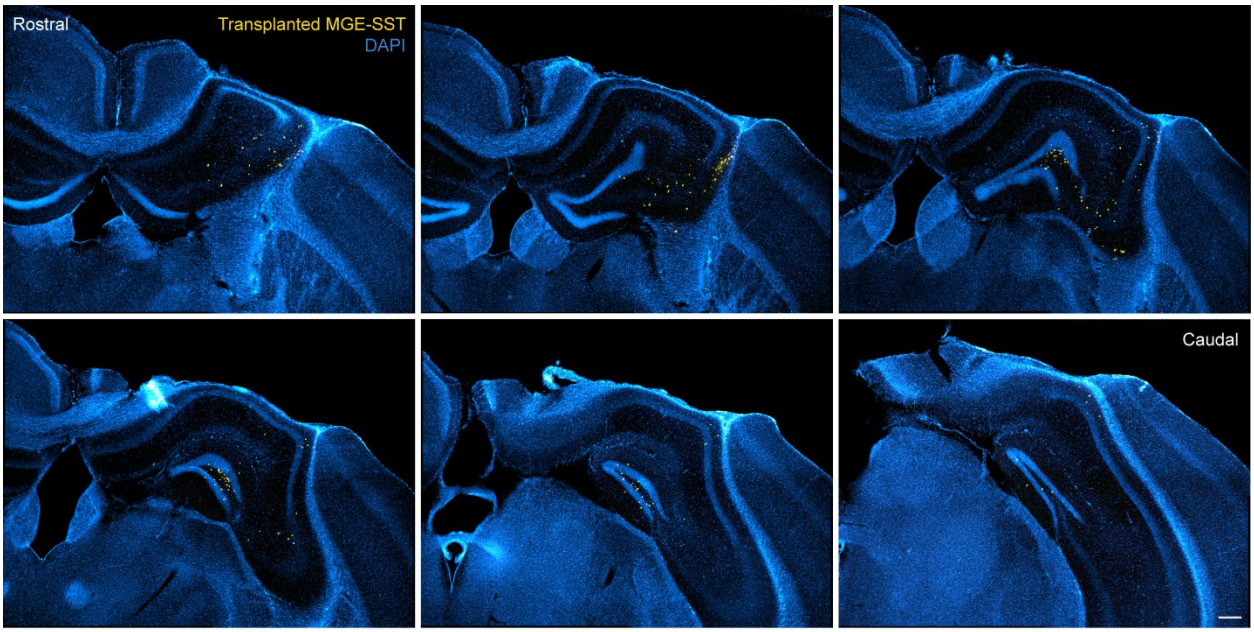


Figure 3.22: Distribution of transplanted MGE-SST cells. Coronal sections spaced 300 µm apart showing the distribution of SST::Ai6-expressing interneurons 35 DAT into a mouse with TBI. Representative animal from *n* = 3 mice. Scale bar, 250 µm.

Next, we performed whole-brain mapping to identify local and long-range inputs to transplanted SST interneurons in the injured brain. For these experiments, donor cells were obtained from SST-Cre+ embryos that did not contain the Ai6 reporter. Transplants were performed 7 days after TBI, virus injections were made into the hippocampus at 8 weeks (AAV8-hSyn-FLEX-TVA-P2A-eGFP-2A-oG) and 11 weeks (RVΔG-mCherry) after injury, and animals were processed for brain clearing and analysis 7 days after the final virus injection. This period corresponds to a time when MGE transplantation shows robust therapeutic effects on memory and seizures in brain injured animals (Zhu et al., 2019). We found substantial numbers of input neurons across the brain labeled by rabies virus (**Figure 3.23a-c**). Notably, input neurons were identified in 14 distinct brain areas, including all regions of the hippocampus, ENTm, ENTl, medial septum and NDB (**Figures 3.23c-f, 3.24**). The majority of input came from the hippocampus, including robust input from area CA3 and CA1. This pattern of local input was similar to what we observed in brain injured animals that did not receive transplants rather than controls (**Figure 3.25**). To determine whether regional

inputs co-vary, we calculated Pearson's correlation coefficients for each pair of input regions. This showed a significant positive correlation between several input regions including CA1, CA2, magnocellular nucleus (MA), prosubiculum (ProS), subiculum (SUB), and perirhinal cortex (PERI), indicating that when transplanted neurons receive input from one region, they generally received input from the other correlated regions (**Figure 3.23g**). Thus, transplanted SST interneurons received orthotopic input patterns, but transplanted cells showed enhanced local input seen after TBI.

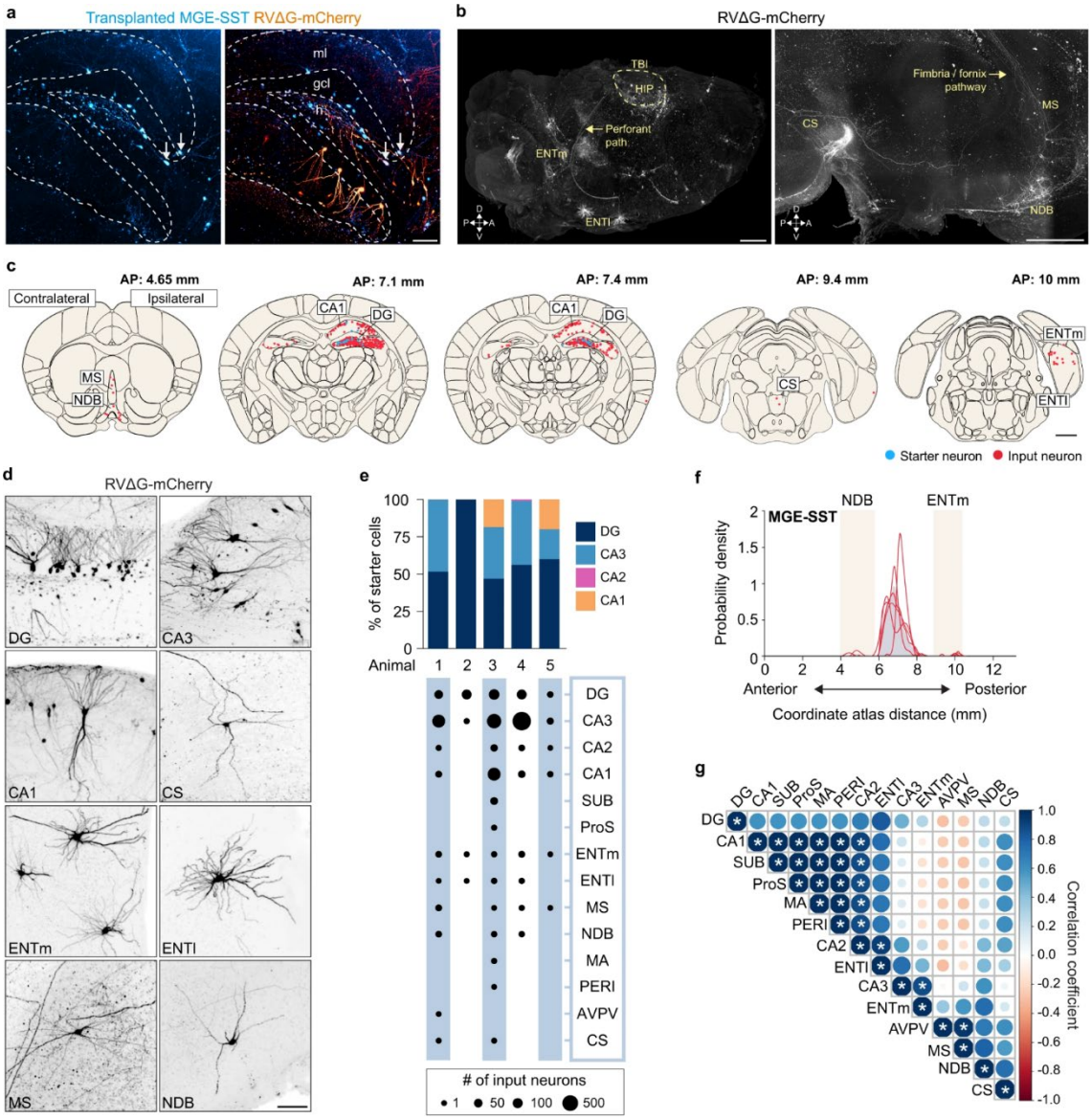


Figure 3.23: Transplanted SST interneurons receive local and long-range input. a. A 100 µm sagittal optical section of dentate gyrus labeled for transplanted cells (blue) and input neurons (orange). White arrows, starter cells. h, hilus; gcl, granule cell layer; ml, molecular layer. **b.** Left: whole-brain render of the entire ipsilateral hemisphere of the same animal shown in (a) labeled for input neurons (white). Dotted circle outlines the injury border overlying hippocampus (HIP). Right: Whole-brain render showing input neurons in superior central nucleus raphae (CS), medial septum (MS), and diagonal band nucleus (NDB). Representative animal from *n* = 5 mice. **c.** Schematic coronal sections (250 µm) showing individual starter cells (red) and input neurons (blue) registered in standardized atlas space. One dot represents one neuron. *n* = 5 animals. **d.** Maximum intensity projections (100 µm) of neurons providing input to transplanted SST interneurons in the intact injured brain. Representative animals from *n* = 5 mice. **e.** Top: proportion of transplanted starter cells found in each layer of hippocampus. Bottom: bubble plot of brain areas containing rabies-labeled input neurons. **f.** Gaussian kernel cell density plot of the whole-brain distribution of input neurons along the anterior-posterior axis. Grey shading represents the pooled population with individual lines representing each animal. **g.** Correlation matrix of input to transplanted SST interneurons. Size and color, correlation coefficient. *$P < 0.05$; two-sided Pearson's correlation. Scale bars, 100 µm (a, g), 1 mm (b, c).

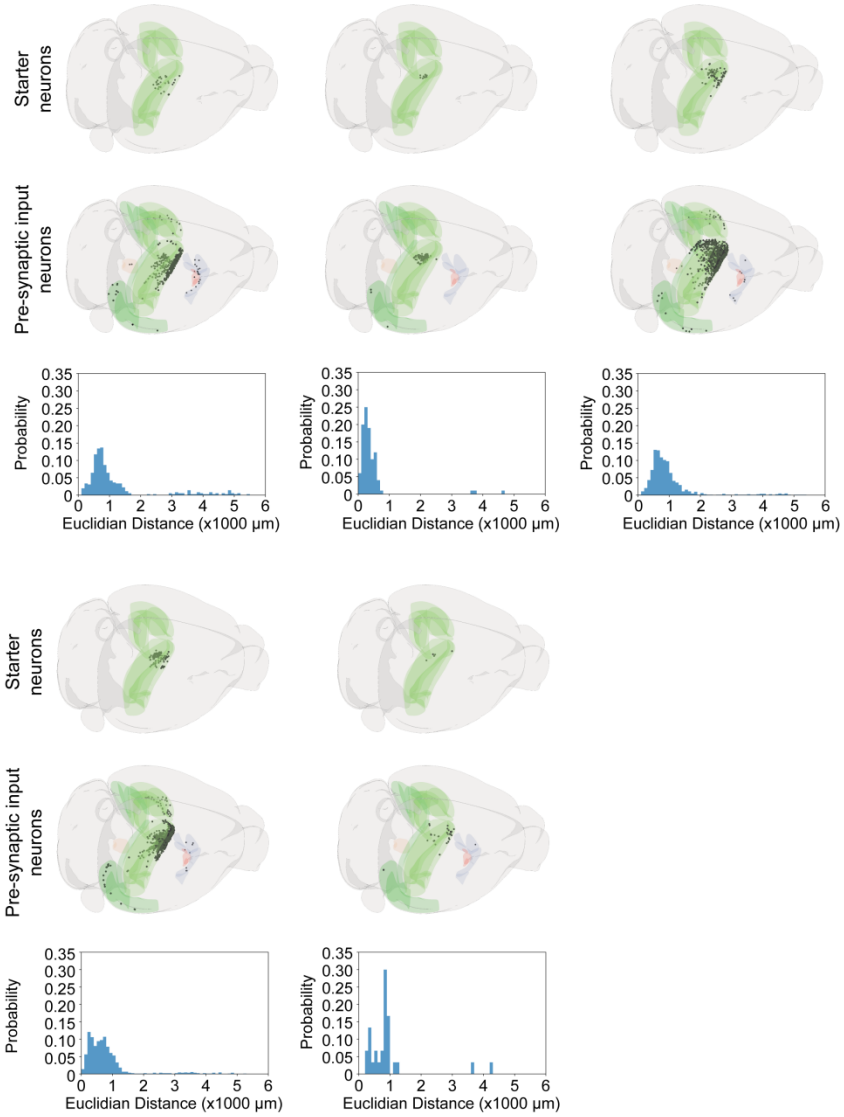


Figure 3.24: Individual animal plots of input to transplanted SST interneurons. Top: whole-brain plots of starter cells and pre-synaptic input neurons annotated in standardized atlas space. Bottom: histograms showing Euclidian distances at 100 µm bins. Black dots represent individual cells registered in standardized atlas space. Shading indicates hippocampal formation (green), pallial regions (blue) and hypothalamus (red).

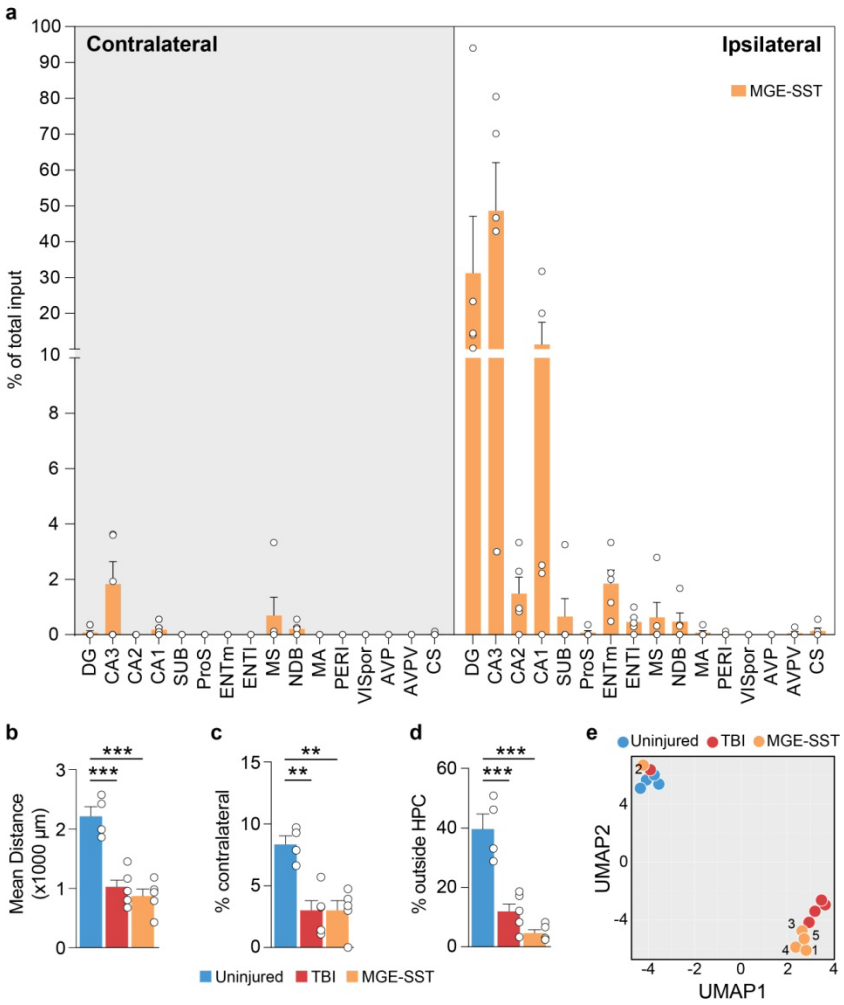


Figure 3.25: Input to transplanted interneurons. a. Proportion of input neurons to transplanted SST interneurons found in each discrete brain area. *n* = 4 MGE-SST mice. **b.** Quantification of average Euclidian distance between transplanted starter cell centroid and input neuron positions. Uninjured: 2214.1 ± 169.9 µm, TBI: 1012.4 ± 136.7 µm, MGE-SST: 865.0 ± 125.9 µm; ***P = 3.07E-04, uninjured versus TBI; ***P = 1.13E-04, uninjured versus MGE-SST; P = 7.35E-01, TBI versus MGE-SST; one-way ANOVA with Tukey's post-hoc test, n = 4 uninjured, 5 TBI, and 5 MGE-SST mice. **c.** Proportion of input neurons found in contralateral hemisphere. Uninjured: 8.4 ± 0.7 %, TBI: 3.0 ± 0.8 %, MGE-SST: 3.0 ± 0.8 %; **P = 1.83E-03, uninjured versus TBI; **P = 1.91E-03, uninjured versus MGE-SST, P = 9.99E-01, TBI versus MGE-SST; one-way ANOVA with Tukey's post-hoc test, n = 4 uninjured, 5 TBI, and 5 MGE-SST mice. **d.** Proportion of input neurons found outside hippocampus. Uninjured: 39.6 ± 5.2 %, TBI: 11.8 ± 2.8 %, MGE-SST: 4.6 ± 1.1%; **P = 2.0E-04, uninjured versus TBI; ***P = 2.45E-05, uninjured versus MGE-SST; P = 0.25, TBI versus MGE-SST; one-way ANOVA with Tukey's post-hoc test, n = 4 uninjured, 5 TBI, and 5 MGE-SST mice. **e.** Uniform Manifold Approximation and Projection (UMAP) clustering by % input neurons. Error bars, s.e.m.

Discussion

Using a mouse model of focal TBI, we report a systematic assessment of large-scale circuit reorganization in a damaged brain. We mapped the brain-wide input to a single cell type with high therapeutic relevance, SST interneurons, in uninjured controls, after brain injury and after

transplantation into brain-injured animals. Our data demonstrate that surviving SST interneurons gain new local input after TBI, but they are largely disconnected from distant brain regions. This occurred at two spatially distinct but interacting brain areas: the injury site in the hippocampus and far away from the injury in PFC, which was not directly damaged by TBI. Our observation of circuit reorganization far away from the injury was unexpected, because PFC was not directly damaged by TBI and results from silver staining experiments suggest interhemisphere projections do not degenerate (Hall et al., 2008). Thus, post-traumatic circuit rewiring is not restricted only to damaged areas, but occurs broadly throughout the brain in response to focal injury. We further show that the diminished long-range connections did not result from cell loss in distant brain areas or a general reduction in axon collaterals projecting into the damaged hippocampus. Transplanted SST interneurons integrated robustly into brain-injured hippocampus and received local and long-range host input that resembled the connections of native-born interneurons. This is consistent with previous ex vivo functional studies documenting robust excitatory drive onto transplanted interneurons from the host brain (Hunt et al., 2013; Zhu et al., 2019; Larimer et al., 2016), although the source of these inputs was previously unknown.

TBI produces major structural and functional alterations in neural circuitry, resulting from progressive brain damage and secondary neuroplasticity responses, which develop over time (Povlishock and Katz, 2005; Hunt et al., 2013a). Until recently, our understanding of how TBI damages the brain's wiring diagram has been limited to standard neuroanatomy and slice electrophysiology approaches. These studies show principal neurons undergo initial deafferentation after TBI, possibly due to loss of input neurons (Povlishock and Katz, 2005; Hunt et al., 2013a; Scheff et al., 2005; Ribak and Reiffenstein 1982). This is followed by a progressive increase in the number of synaptic contacts and the formation of new excitatory circuits within injured areas of the brain (Hunt et al., 2013a; Purpura and Housepian, 1961; Santhakumar et al., 2000; Kharatishvili et al., 2006; Kharatishvili et al., 2007; Hunt et al., 2009, 2010). Excitatory drive

onto hippocampal SST interneurons, which normally receive sparse input from local principal neurons, is also increased after brain injury (Hunt et al., 2011). However, slice recordings are limited to resolving functional connections of a few neurons within local circuits, because they are surgically isolated from long-range afferent input. By comprehensively mapping brain-wide inputs to SST interneurons at cellular resolution, we found a significant enhancement of local input neurons to hilar SST interneurons after TBI, in agreement with prior slice electrophysiology studies. We additionally identified previously unknown sources of input in controls, such as a back-projection pathway from CA1 to hilar SST interneurons which is enhanced after TBI. Notably, CA1 interneurons are also capable of projecting to dentate gyrus in temporal lobe epilepsy models (Peng et al., 2013), but these cells primarily innervate granule cells.

Previous functional connectivity studies assume that TBI shifts the brain away from a small-world architecture, defined as densely connected local networks linked by sparse long-range input that connects discrete brain areas (Sharp et al., 2014). In line with this concept, interhemispheric resting-state fMRI connectivity is reduced after TBI (Marquez de de la Plata et al., 2011), possibly a result of diffuse axonal injury (Sharp et al., 2014), and there is a temporary increase in hyper-connectivity of local networks that generally weakens over time (Harris et al., 2016). While these methods are useful for general hypotheses about brain connectivity, they are unable to identify a precise structural basis for circuit dysfunction in TBI and are likely disproportionately influenced by excitatory neurons. Our circuit mapping data are not entirely consistent with this idea at the cell type level. In both hippocampus and PFC, we found the most prominent sources of long-range input to SST interneurons, including input from the contralateral hemisphere, were diminished after focal TBI, but local connections are chronically increased. Thus, TBI may permanently enhance small worldness of inhibitory circuits by increasing local network connections and making long-range input more sparse. There is support for this idea from human functional connectivity studies (Nakamura et al., 2009).

There is obvious axon damage after CCI (Hall et al., 2008), and this likely affects long-range input to the hippocampus. We cannot exclude the possibility that some of the structural reorganization we observed after TBI is influenced by damage to white matter tracts. However, axon damage alone cannot fully explain the long-range circuit changes we observed in brain-injured animals. In hippocampus, we found ~4-fold reduction in long-range input to SST interneurons that was not accompanied by cell loss in distant brain regions or their projections in the hippocampus (e.g., CHAT+ afferents). This suggests input regions are not disconnected from SST interneurons by a general loss of input neurons or axotomy. Rather, inputs may be added or removed in a cell-type-specific manner. It is possible that long-range afferents are selectively damaged by CCI but remain otherwise intact. For example, it is well known that TBI disrupts axonal transport mechanisms (Johnson et al., 2013), and this could disproportionately affect retrograde transport of rabies into long-range pre-synaptic input neurons. However, our finding that transplanted interneurons are capable of establishing long-distance connections at all suggests that the potential for re-growing these diminished inputs was retained in all brain-injured animals. We found similar increases in local input and decreases in long-range input to SST interneurons in PFC. Unlike hippocampus, these projections are not directly damaged and do not degenerate after CCI (Hall et al., 2008). Of particular interest is the anteromedial thalamus, which was the only thalamic area with altered input neurons after TBI. Anterior thalamus (ATN, comprised of anteromedial, anteroventral and anterodorsal subdivisions) provides a subcortical circuit supporting memory and spatial navigation (Jankowski et al., 2013), behaviors that are profoundly affected in rodent models of TBI. It is possible that excessive activity in damaged hippocampus could lead to downstream changes in PFC (e.g., via the hippocampus-ATN-PFC circuit). Alternatively, seizures are well documented in this injury model and could lead to circuit reorganization across the entire brain. Nevertheless, our results suggest that focal TBI leads to

widespread remapping of inputs to SST interneurons across the brain regardless of whether there was direct injury or cell loss.

With far fewer inhibitory neurons in the damaged hippocampus, TBI puts extraordinary demands on surviving interneurons. There are three physiological features of SST interneurons that might explain why a loss of long-range input could reflect a compensatory response to damage. First, SST interneurons receive strongly facilitating excitatory synaptic input and have other membrane properties that allow these cells to be activated by a high-frequency burst from just one pre-synaptic neuron (Kapfer et al., 2007; Silberberg and Markram, 2007). In hippocampus, gaining input from local principal neurons and losing ENTm input may help stabilize local network activity after TBI (Cholvin et al., 2021). Second, muscarinic-mediated depolarization can produce prolonged spiking in SST interneurons (Kawaguchi, 1997). Given the rich local innervations after TBI, the loss of CHAT input from basal forebrain could reflect a strategy to balance the excitatory drive to this important cell type in the injured brain. Third, even a single dendrite-targeting interneuron can control spike generation in cortical principal neurons (Larkum et al., 1999). Thus, a shift from feed-forward to feedback inhibition to dendrites – through the loss of long-range input and enhanced local back-projections – may reflect a potential strategy to gate input integration and maintain the sparse activation of dentate granule cells that enables memory and prevents seizures (Kahn et al., 2019; Pignatelli et al., 2019). Alternatively, increased local input may synchronize SST interneurons, support patterns of pathological activity or impede the coordination between discrete brain areas. Further work combining in vivo neurophysiology with selective manipulation of hippocampal cell types will be required to clarify these possibilities.

The ability of transplanted SST interneurons to incorporate structurally into the damaged hippocampus was striking given the dramatic reorganization of inhibitory circuits across the injured brain. Although host-donor cell connectivity has been broadly documented (Doerr et al.,

2017; Tornero et al., 2017), the precise anatomical input to individual neuron types has not. Cell-type specificity is an important consideration, especially for understanding the circuit basis of disease. Despite massive reactive plasticity in the damaged brain, we found that transplanted interneurons receive highly orthotopic input that is cell-type-specific rather than region-specific. We propose that the beneficial effects of interneuron transplantation seen in various preclinical disease models are driven by the precise integration of interneuron precursors into host brain circuits. This view is supported by a large body of evidence reporting the general structure and function of transplanted interneurons closely resemble their native-born counterparts (Hunt et al., 2013a, Zhu et al., 2019; Larimer et al., 2016; Alvarez-Dolado et al., 2006; Braz et al., 2012; Etlin et al., 2016) as well as recent DREADD-inactivation and VGAT loss-of-function studies demonstrating that therapeutic effects are linked to the electrophysiological integration of the transplanted interneurons (Zhu et al., 2019; Priya et al., 2019). An alternate view suggests interneuron precursors form only weak contacts with the host brain (Southwell et al., 2010) and work indirectly by releasing rejuvenation factors that modify host brain circuits (Zheng et al., 2021). Yet detailed electrophysiological studies consistently report strong synaptic connections (Zhu et al., 2019; Larimer et al., 2016; Hsieh and Baraban, 2017; Howard and Baraban, 2016) and direct evidence for a circuit rejuvenator remains to be identified. In the current study, we were unable to directly test synaptic connections among transplanted interneurons, because it was not possible to distinguish starter cells from AAV-labeled SST neurons that received rabies via retrograde transport. However, the large majority of local input neurons were putative principal neurons, not inhibitory neurons (based on morphology and laminar location). This is consistent with a robust literature on MGE transplantation using EM ultrastructural analysis, neuroanatomy, and patch-clamp electrophysiology that demonstrates most synaptic connections are with principal cells of the host brain (Zhu et al., 2019; Larimer et al., 2016; Alvarez-Dolado et al., 2006; Southwell et al., 2010; Zheng et al., 2021; Hsieh and Baraban, 2017; Howard and Baraban, 2016; Baraban et al., 2009).

The pattern of synaptic circuit rewiring after TBI is complex. Our results suggest that focal brain damage reorganizes inhibitory circuits on a global scale. We expect this experimental approach will serve as a useful framework for considering whole-brain analyses of network dysfunction in TBI and related brain disorders.

CHAPTER FOUR

Brain injury degrades the precision of hippocampal spatial representations

Abstract

Traumatic brain injury (TBI) disrupts spatial memory, but the circuit mechanisms are unknown. Here we used in vivo endoscopic calcium imaging to record CA1 activity dynamics in freely behaving mice with TBI. Spontaneous CA1 neuron activity was broadly preserved three months after brain injury. However, chronic TBI reorganizes hippocampal spatial representations by increasing the fraction of spatially unresponsive neurons, broadening place fields among spatially tuned neurons and diminishing the persistence of spatial representations across sessions. These circuit alterations are accompanied by impaired discrimination of a novel spatial environment. Thus, TBI reorganizes the cellular structure and precision of hippocampal spatial representations despite preserved overall CA1 activity, revealing a dissociation between neuronal activity and network function that may underlie persistent cognitive dysfunction.

Introduction

The hippocampus generates dynamic representations of space that are essential for navigation and memory. In CA1, pyramidal neurons fire selectively at specific locations within an environment, collectively forming a neural representation of space whose precision and stability depend on coordinated interactions across local and long-range circuits (O'Keefe and Dostrovsky, 1971; O'Keefe, 1976; Bittner et al., 2015). Entorhinal inputs provide major excitatory drive into hippocampus, while local inhibitory circuits regulate network excitability and constrain the spatial tuning of CA1 neurons (Klausberger et al., 2003; Solstad et al., 2006; Brun et al., 2008; Geiller et al., 2022; Zutshi et al., 2022). Disruption of these circuits can alter the precision, information

content or stability of spatial representations in hippocampus (Morris et al., 1982; Calton et al., 2003; Hales et al., 2014; Bittner et al., 2015; Udakis et al., 2025).

Traumatic brain injury (TBI) produces extensive and persistent remodeling of hippocampal circuitry, including loss of inhibition, fewer entorhinal inputs and increased local excitatory connectivity (Toth et al., 1997; Santhakumar et al., 2000; Hunt et al., 2009, 2011; Frankowski et al., 2022). Electrophysiological studies have provided preliminary evidence of altered task-related hippocampal coding after TBI (Eakin and Miller, 2012; Broussard et al., 2020), but how hippocampal spatial representations are organized once chronic circuit remodeling has emerged is unknown. Work in other neurodegenerative disorders affecting hippocampus, such as epilepsy and Alzheimer's disease models, has applied more classic paradigms and shown that circuit remodeling can degrade spatial coding (Liu et al., 2003; Cacucci et al., 2008; Mably et al., 2017; Jun et al., 2020; Shuman et al., 2020). This raises the question of whether chronic TBI reshapes how the hippocampus represents space.

Here, we used longitudinal endoscopic calcium imaging to examine CA1 neuronal activity and spatial representations in freely behaving mice three months after TBI. We first characterized spontaneous neuronal activity, then assessed the recruitment, spatial precision and persistence of CA1 place cell representations during a linear track task. Finally, we tested the behavioral consequences of these circuit changes using a spatial novelty discrimination task. We find that chronic TBI leaves overall CA1 neuronal activity broadly preserved but disrupts its organization into spatial representations, with reduced place cell recruitment, broader place fields and diminished persistence across sessions. These circuit changes are accompanied by impaired discrimination of novel spatial environments. Together, these results identify degradation of hippocampal network precision as a circuit correlate of cognitive dysfunction after TBI.

Methods

Experimental model

All animal procedures were approved by the Institutional Animal Care and Use Committee of University of California Irvine and performed in accordance with National Institutes of Health Guidelines for the Care and Use of Laboratory Animals. Experiments were performed in adult homozygous *Camk2a-Cre* mice (JAX Stock No. 005359) of both sexes maintained under standard housing conditions on a 12 h light/dark cycle with food and water available *ad libitum* until food restriction was initiated for linear track training.

Brain injury

Controlled cortical impact (CCI) was performed in male and female mice at postnatal day 60–65 as previously described (Frankowski et al., 2022). Briefly, mice were anesthetized with 2% isoflurane and secured in a custom stereotaxic frame. Following a midline scalp incision, a 4–5 mm craniotomy was made approximately 1 mm lateral to the sagittal suture and centered between bregma and lambda. The skull cap was removed with fine forceps without disrupting the underlying dura. CCI was delivered to the neocortex using a computer-controlled, pneumatically driven impactor fitted with a 3 mm diameter beveled stainless-steel tip (Precision Systems and Instrumentation, TBI-0310) at a depth of 1.0 mm, velocity of 3.5 m/s, and dwell time of 500 ms. The incision was sutured without replacing the skull cap, which was retained for subsequent lens implantation. Animals recovered on a heating pad. Buprenorphine hydrochloride (Buprenex; 0.05 mg/kg, intraperitoneally) was administered at the time of surgery and 12 h later.

Virus injection

AAV1-syn-FLEX-jGCAMP8m-WPRE (Addgene, plasmid no. 162378; 1.0 × 10^13 genome copies/mL) was diluted 1:10 in sterile PBS immediately before injection. Virus was loaded into beveled glass micropipettes (50μm tip diameter; Wiretrol 5 μm, Drummond Scientific), and 100

nL was injected at ~15 nL/min. The micropipette was left in place for 10 min before withdrawal. Viral injections targeting dorsal CA1 were performed 5–8 weeks after CCI. Injection coordinates were established in preliminary experiments to optimize targeting of dorsal CA1 and to determine viral titer and injection volume for pyramidal cell specificity (**Figure 4.1**). Coordinates for control mice were anteroposterior (AP) −2.1 mm, mediolateral (ML) 1.5 mm, and dorsoventral (DV) −1.2 mm; coordinates for CCI mice were AP −1.9 mm, ML 1.5 mm, and DV −0.65 mm.

GRIN lens implantation

Three weeks after viral injection, a ~1 mm craniotomy was made above the injection site. In CCI mice, the skull cap was replaced at this time. Cortical tissue was carefully aspirated using 27- and 30-gauge blunt needles connected to a vacuum pump until the alveus overlying CA1 was visible. Cold sterile saline was continuously applied during aspiration. Surgifoam (Ethicon) was used to control bleeding and establish a clear optical window. A GRIN lens (1 mm diameter, 4 mm length; Inscopix, 1050-004595) was slowly lowered to the target region using a stereotaxic arm (DV −1.2 mm for control mice; −0.85 mm for brain injured mice to account for hippocampal herniation). The lens was secured to the skull using cyanoacrylate glue and dental cement. Kwik-Sil (World Precision Instruments) was applied to the exposed lens surface to protect the optical interface. One week later, mice were briefly anesthetized with isoflurane and a miniscope mounted on a baseplate was positioned over the GRIN lens. The miniscope was adjusted to identify an optimal field of view (FOV) containing in-focus jGCaMP8m-expressing cells. The baseplate was secured using cyanoacrylate glue and dental cement. The miniscope was removed and replaced with a protective plastic cap between recording sessions.

Linear track

One week after lens implantation, mice were food restricted to approximately 85% of their initial body weight. Body weight and general health were monitored daily, and food was provided if signs

of fatigue or distress were observed. Mice were handled for at least 5 min/day for 2 weeks before behavioral testing. To habituate mice to the weight of the miniscope, a dummy scope (OpenEphys, OEPS-7409) was worn for progressively increasing periods beginning 1 week before experiments, until mice could comfortably tolerate the scope for 15 min/day. The linear track consisted of a 200 × 6 × 12 cm white acrylic track with black visual cues on the walls (**Figure 4.2**). Room illumination was maintained at 20 lux. Before each recording session, the miniscope was attached to the baseplate and the FOV was confirmed. Home-cage recordings were obtained on the first day of linear track training immediately before the first track session. Mice were placed at one end of the track and trained to run back and forth for a food reward (sugar pellet; Bio-Serv, F0023) after completion of each lap. Each imaging session consisted of at least 15 laps, with four sessions per day separated by 10 min home-cage rest periods. Training was conducted for 7 days, and data from day 7 were used for spatial analyses. The track was cleaned with 70% ethanol between trials.

Calcium imaging

Calcium imaging was performed using UCLA Miniscope v4 systems (http://miniscope.org) connected to a data acquisition system through a flexible coaxial cable (OpenEphys, OEPS-5503). The acquisition system was connected to a computer through USB 3.0 (**Figure 4.3**). The focal plane and excitation intensity were adjusted before each recording session. Miniscope acquisition was controlled using a Bonsai workflow (Lopes et al., 2015), and images were acquired at 20 frames/s.

Position and speed tracking

Behavior was recorded using an overhead camera (acA2040-90um, Basler) at 30 frames/s and synchronized to miniscope imaging frames using hardware timestamps in a custom Bonsai workflow (**Figure 4.3**). The animal's position was tracked offline using the miniscope-mounted

LED and DeepLabCut (Mathis et al., 2018). Tracking output was visually inspected, and erroneous coordinates were corrected manually. Position data were smoothed using a Gaussian filter (σ = 150 ms), and running speed was calculated from the smoothed position data.

Calcium imaging pre-processing

Calcium imaging data were processed using MIN1PIPE for background subtraction, motion correction, calcium trace extraction, and spatial footprint extraction (Lu et al., 2018). Calcium events were inferred from fluorescence traces using MLspike (Deneux et al., 2016) and converted to firing rates. Traces with high noise levels (σ > 0.1; σ defined as the root-mean-square of fluorescence signals between 3 and 20 Hz) were excluded. Mice in which >30% of extracted cells were excluded were removed from subsequent analyses (**Figure 4.4**). Spatial footprints generated by MIN1PIPE were used to register cells across sessions using CellReg (Sheintuch et al., 2017). Automated cell extraction, spike inference, and cell registration were manually inspected for accuracy.

Place cell analysis

For linear track analyses, only periods during which mice were running >5 cm/s were included. Rightward and leftward traversals were analyzed separately. Position was divided into 2 cm spatial bins, and firing rate was calculated for each bin as the number of inferred calcium events divided by occupancy time. Rate maps were smoothed using a Gaussian kernel (σ = 2 cm). Spatial information was calculated for each neuron using the method of Skaggs et al. (1993):

$$Spatial\ information = \sum_i p_i \frac{\lambda_i}{\lambda} \log_2 \frac{\lambda_i}{\lambda}$$

where λ_i is the mean firing rate in spatial bin i, λ is the overall mean firing rate, and p_i is the probability of occupancy of spatial bin i.

Place cells were identified using a circular-shuffling procedure (Diehl et al., 2017). For each cell, spike times were circularly shifted by a single randomly selected temporal offset, thereby dissociating spike timing from animal position while preserving the temporal structure of the spike train. Spike times exceeding the session duration were wrapped to the beginning of the session. Spatial information was calculated for 1,000 shuffled datasets per cell. A neuron was classified as a potential place cell when its observed spatial information exceeded the 95th percentile of its shuffled distribution. Place fields were further defined as contiguous regions ≥12 cm and ≤70 cm in length in which firing rate exceeded 20% of the peak firing rate. Cells with a peak firing rate <1 Hz were excluded from place field analysis. Recorded neurons were considered to be a place cell if they met the following criteria: i) information score ≥ 95th percentile, ii) place field size ≥12 cm and ≤ 70 cm, and iii) peak firing rate > 1Hz. Within-session spatial stability was assessed by calculating the Pearson correlation coefficient between rate maps generated from odd and even numbered laps.

Y-maze

Novelty discrimination was assessed using a three-arm Y-maze (Panlab, LE847) consisting of three identical enclosed arms (30 × 6 × 15 cm) arranged at 120° angles. Visual cues were positioned above and outside the maze. Room illumination was maintained at 20 lux. The maze orientation and entry arm were held constant across trials, while the identities of the familiar and novel arms were counterbalanced across animals. The test consisted of two trials separated by 60 min. During the exposure trial, mice were placed at the end of the entry arm and allowed to explore for 10 min with one arm inaccessible. Mice were then returned to their home-cage for 60 min. During the test trial, all three arms were accessible and mice were allowed to explore for 5 min. The maze was cleaned with 70% ethanol between trials. Behavior was recorded by video and tracked using DeepLabCut. Time spent in each arm was quantified using custom Python scripts. Novelty discrimination was quantified as a discrimination index (DI): DI

$= [t_{novel} - t_{entry}]/[t_{novel} + t_{entry}] \times 100)$ or $DI = [t_{novel} - t_{familiar}]/[t_{novel} + t_{familiar}] \times 100)$ where t represents time spent in the indicated arm. Total distance traveled and mean running speed were calculated from smoothed x,y coordinates using a Gaussian filter (σ = 150 ms).

Immunohistochemistry

Mice were transcardially perfused with 0.1 M PBS followed by 4% paraformaldehyde (PFA) in 0.1 M PBS, and brains were post-fixed overnight in 4% PFA. Coronal sections (50 µm, 300 µm apart) were prepared using a vibratome and processed using standard immunohistochemical procedures (Tierno et al., 2026). Primary antibodies included chicken anti-GFP (1:1,000; Aves, GFP1020; RRID: AB_10000240) and rabbit anti-WFS1 (1:1,000; Proteintech, 11558-1-AP; RRID: AB_2216046). Secondary antibodies were Alexa Fluor 488-conjugated goat anti-chicken IgG (Invitrogen, A11039; RRID: AB_2534096) and Alexa Fluor 647-conjugated goat anti-rabbit IgG (Invitrogen, A21244; RRID: AB_2535812), both at 1:1,000. Sections were mounted on charged slides with Fluoromount-G containing DAPI. Images were acquired using a Leica DM6 microscope at 5 to 20x with LAS X software and quantified using FIJI (ImageJ). Brightness and contrast were adjusted manually in FIJI (ImageJ) and applied uniformly across each image. For cell count quantification, all jGCaMP8m-expressing cells were quantified in three consecutive brain sections 300 µm apart through the injection site in CA1 per animal.

Quantification and Statistical Analysis

Statistical analyses were performed using GraphPad Prism 11, Python 3.13.5 (SciPy 1.15.3), or MATLAB (MathWorks). Boxplots were generated using a seaborn boxplot function where boxes represent the interquartile range (IQR), the median indicated by a horizontal line; whiskers extend to the most extreme values within 1.5 × IQR, and individual points beyond this range are shown as outliers. Statistical tests included two-tailed Student's *t*-tests, two-way repeated-measures ANOVA with Sidak or Tukey post hoc tests, Mann-Whitney *U* tests with Bonferroni correction, and

Fisher's exact test with Bonferroni correction. Data are presented as mean ± SEM unless otherwise indicated, and significance was set at $P < 0.05$.

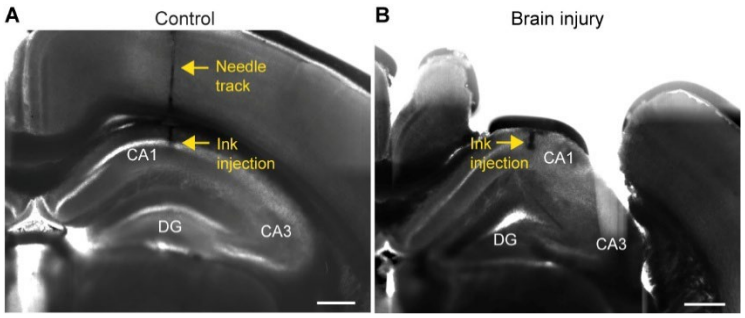


Figure 4.1: Verification of CA1 targeting and cell type specificity of jGCaMP8m expression. A. Representative coronal section from a control mouse following ink injection into the CA1 region. Yellow arrows indicate the needle track and injection site. **B.** Representative coronal section from a brain injured mouse following ink injection into the CA1 region. Yellow arrow indicates the injection site. Scale bars, 500 µm.

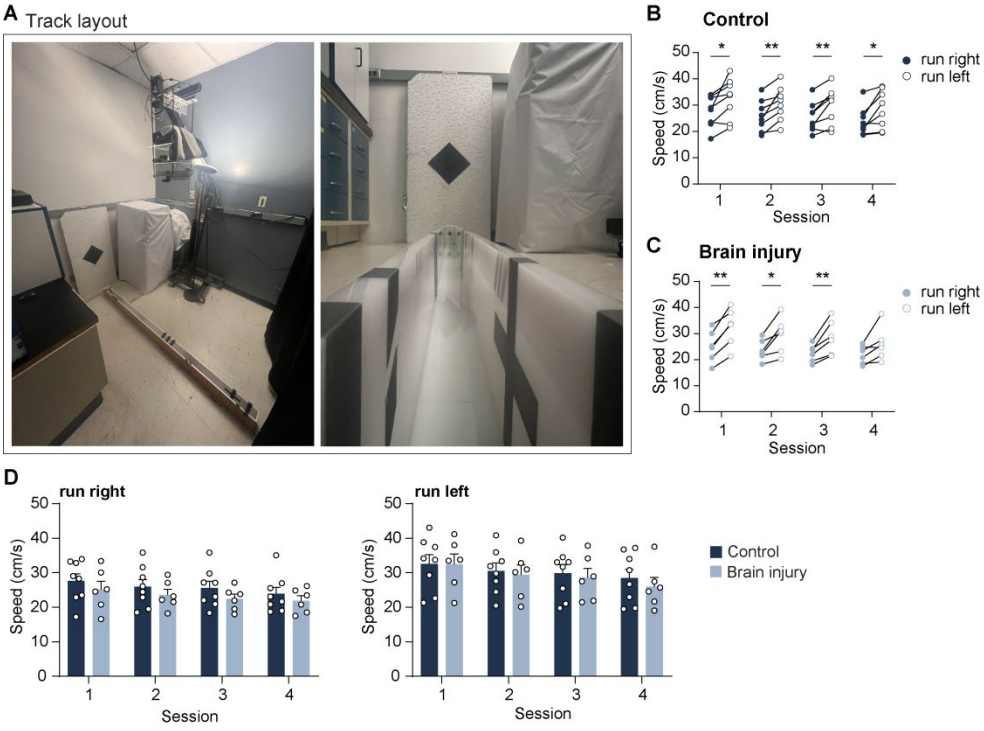


Figure 4.2: Track layout and running speed. A. Linear track apparatus and environmental cues. Mice ran between the two ends of the track, with running direction defined as rightward or leftward. **B, C.** Speed (cm/s) during rightward (closed circles) and leftward (open circles) running across four sessions in control (B) and brain injured (C) mice. *P* values indicate rightward versus leftward running within each session (control: session 1, $P = 0.02$; session 2, $P = 5E-03$; session 3, $P = 8E-03$; session 4, $P = 0.02$; brain injury: session 1, $P = 1E-03$; session 2, $P = 0.02$; session 3, $P = 8E-03$; session 4, $P = 0.06$; two-way repeated measures ANOVA with Tukey's post hoc test; $n = 8$ control and 6 brain

injured mice). **D.** Mean running speed across sessions for control and brain injured mice during rightward (left) and leftward (right) running. Data points represent individual mice. Error bars, SEM.

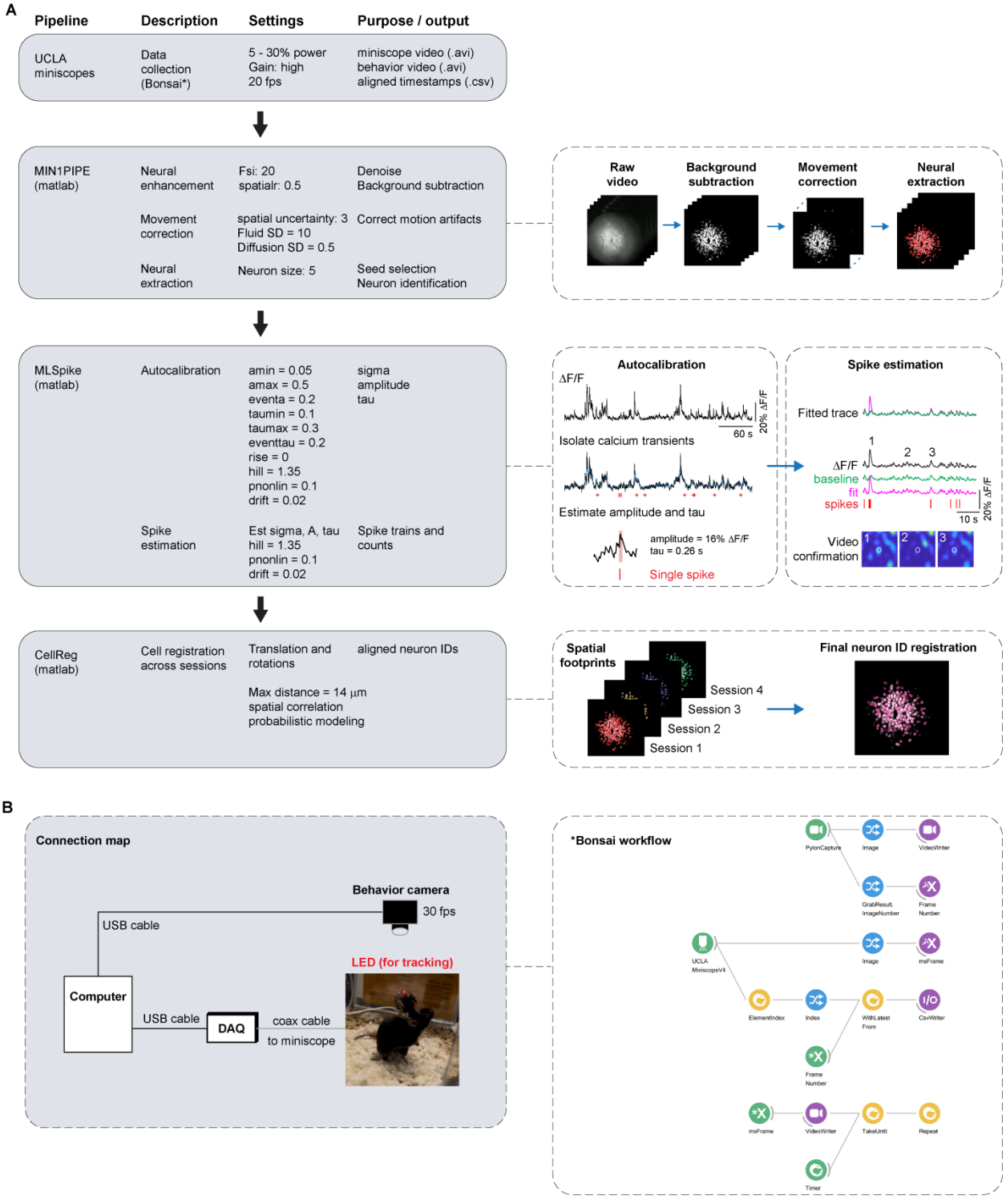


Figure 4.3: Pipeline for calcium signal extraction and analysis from miniscope recordings. A. Overview of the calcium imaging and analysis pipeline. Miniscope recordings were acquired using a UCLA Miniscope and synchronized

with behavioral video using a custom Bonsai workflow. Calcium imaging videos were processed using MIN1PIPE for background subtraction, movement correction, neural extraction, and neuron identification. Calcium traces were then processed using MLspike for spike estimation, including autocalibration of single spike amplitude and decay parameters followed by estimation of spike events across the full trace. Trace alignment was manually verified and corrected for each neuron and mouse. For longitudinal linear track recordings, neurons were registered across sessions using CellReg, and registered neuron identities were used for downstream analyses. **B.** Miniscope recording and synchronization setup. Left, connections between the computer, behavior camera, data acquisition device, and miniscope. Right, Bonsai workflow used for real-time synchronization of behavioral and calcium imaging recordings. Outputs include miniscope video (.avi), behavioral video (.avi), and aligned frame timestamps (.csv).

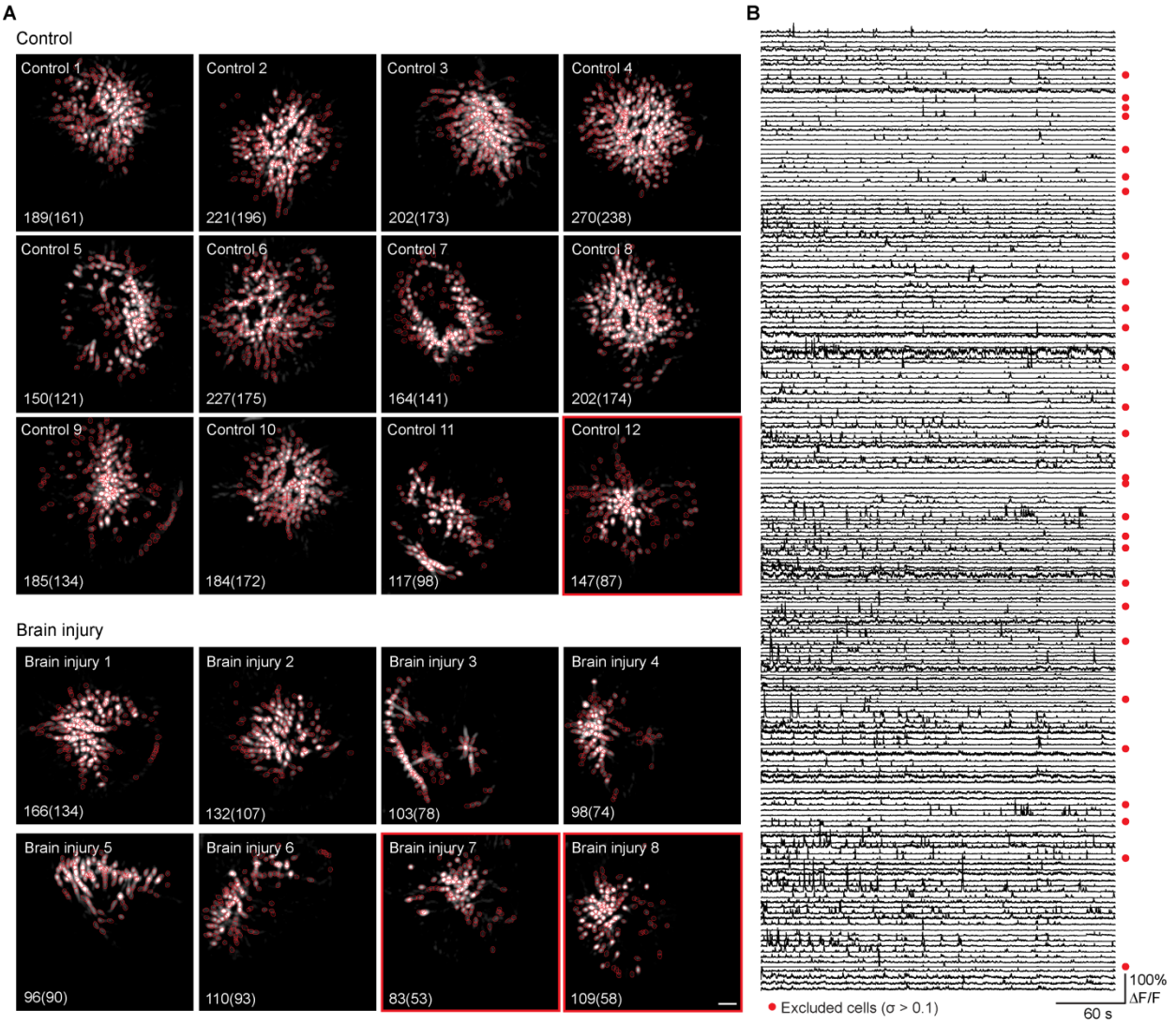


Figure 4.4: Field of view (FOV) and calcium traces from all recorded mice. A. Miniscope FOVs from all recorded mice following calcium signal extraction with MIN1PIPE. Individual neuronal contours are outlined in red. Red boxes indicate mice excluded from analysis because >30% of extracted neurons had high noise (σ > 0.1). Numbers indicate the total number of identified neurons, with the number included in subsequent analyses shown in parentheses. **B.** Calcium traces from all neurons identified in one representative control mouse during the home-cage recording. Red circles indicate neurons excluded from analysis based on the noise criterion. Scale bar, 100 μm.

Results

CA1 activity is preserved after brain injury

To determine whether chronic brain injury alters baseline CA1 network activity, we performed unilateral CCI over the somatosensory cortex of Camk2a-Cre mice at P60. Five weeks later, jGCaMP8m was expressed in dorsal CA1 of control and brain injured littermates, followed by implantation of GRIN lenses for one-photon in vivo calcium imaging (**Figure 4.5A–C**). jGCaMP8m expression was largely restricted to WFS1-positive CA1 pyramidal neurons in both groups (**Figure 4.5A,B**). Imaging was initiated 10-13 weeks after injury, and high quality neurons identified within the miniscope FOV were retained for analysis (**Figure 4.5D,E**). The number of identified neurons was reduced in brain injured mice compared with controls (control: 192 ± 12; brain injury: 118 ± 11 cells; P = 4.87E-04, two-tailed t-test), possibly related to loss of CA1 neurons after brain injury (Saatman et al., 2006), whereas the proportion of identified cells meeting quality criteria for analysis was comparable between groups (control: 84 ± 2%; brain injury: 82 ± 3%; P = 0.48, Fisher's exact test).

We then quantified CA1 neuronal activity during home-cage exploration using spike inference from calcium traces (**Figure 4.5F**). Calcium event frequency did not differ between control and brain injured mice, either overall or when analyzed by sex (**Figure 4.5K,L**). Home-cage behavior was also comparable between groups, including movement trajectories, total distance traveled and average speed (**Figure 4.5G–J**). Thus, despite a reduction in the number of neurons detected within the imaging FOV after injury, baseline CA1 neuron activity and locomotor behavior were broadly preserved during the chronic phase of TBI.

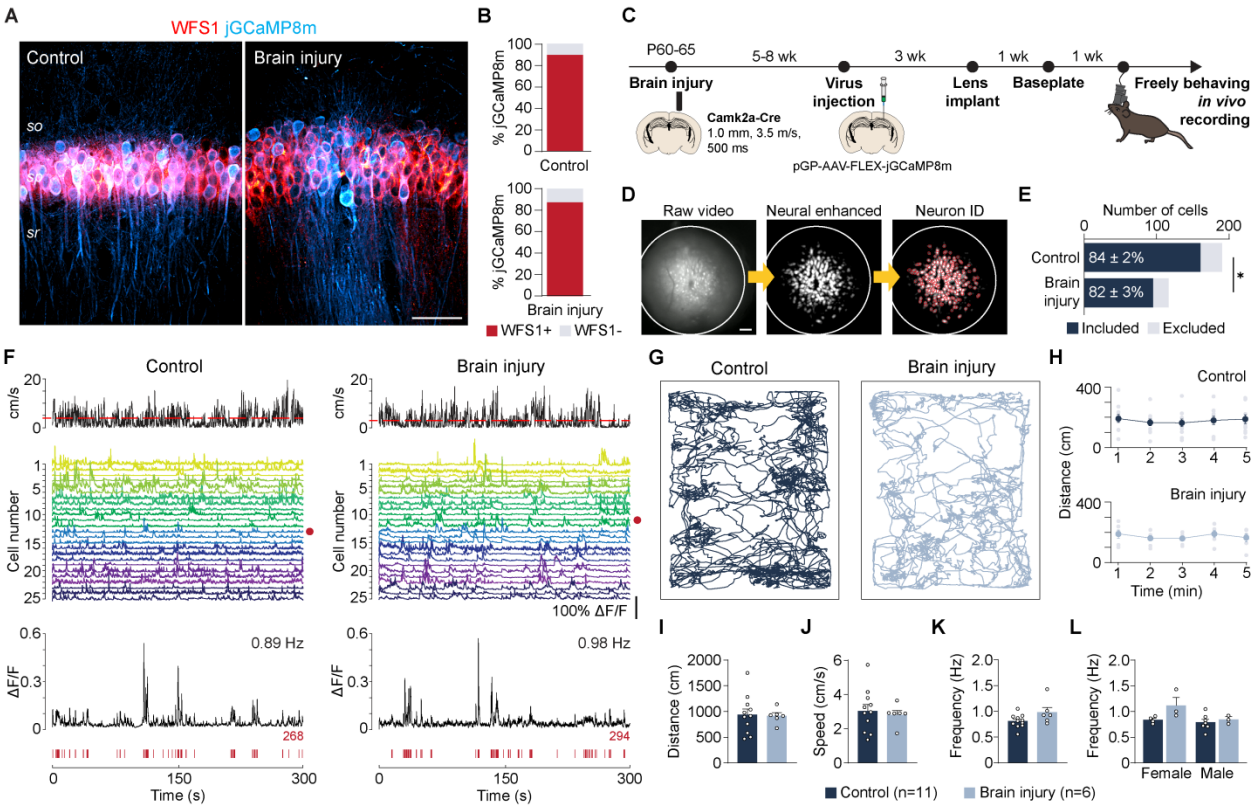


Figure 4.5: CA1 activity is preserved after brain injury. A. Representative images of CA1 from control and brain injured Camk2a-Cre mice expressing FLEX-jGCaMP8m (blue) and immunolabeled for WFS1 (red). **B.** Quantification of jGCaMP8m-expressing neurons co-labeled with WFS1 in control (top) and brain injured (bottom) mice. **C.** Experimental timeline for in vivo calcium imaging. **D.** Representative steps in calcium signal processing using MIN1PIPE. Left, raw miniscope FOV; middle, neural enhanced image; right, identified neuronal contours (red). **E.** Number of neurons identified in the miniscope FOV in control and brain injured mice (control, 192 ± 12 cells, *n* = 11 mice; brain injury, 118 ± 11 cells, *n* = 6 mice; *P* = 4.87E-04, two-tailed t-test). The percentage of identified neurons included in subsequent analyses is indicated within each bar; exclusion criteria are described in Figure 4.4. **F.** Representative home-cage recordings from control and brain injured mice. Top, locomotor speed; red dashed line indicates mean speed during the recording session. Middle, calcium traces from 25 representative neurons. Bottom, representative calcium trace and inferred spike events (red) from the neuron indicated by the red marker above. **G.** Representative home-cage trajectories from control and brain injured mice. **H.** Distance traveled over consecutive 1 min intervals during the recording session. Lines and symbols indicate group means; individual mouse values are shown in gray. **I.** Total distance traveled during the recording session. **J.** Mean locomotor speed. **K.** Mean CA1 calcium event frequency per mouse. **L.** Mean calcium event frequency separated by sex. Data are mean ± SEM. Scale bars, 50 μm (A) and 100 μm (D). SO, stratum oriens; SP, stratum pyramidale; SR, stratum radiatum.

Brain injury reduces the precision of CA1 spatial activity

Next, we asked whether chronic brain injury alters the organization of spatially responsive CA1 neurons. Mice were trained to run back and forth on a 2 m linear track for 7 days, with four sessions per day (**Figure 4.6A**). By day 7, both groups were able to complete at least 15 laps within a 10 min session (**Figure 4.6B,C**). Running speed did not differ between control and brain

injured mice across sessions, although both groups consistently ran faster in the leftward direction (**Figure 4.2**). Calcium traces were extracted and aligned to the animal's position and running direction. Spatially tuned neurons were identified in both groups and during both running directions, including neurons with directionally selective or bidirectional place fields as well as neurons without spatially tuned activity (**Figures 4.6D–G, 4.7**). Because place cell activity is directionally organized in one-dimensional environments (Muller et al., 1994), rightward and leftward running were analyzed independently. Place cells were identified using a single-cell, shuffle-based spatial information criterion (Skaggs et al., 1993; Diehl et al., 2017), with neurons classified as place cells when their spatial information exceeded the 95th percentile of their shuffled distribution (**Figure 4.6H**), field size was 12 – 70 cm and peak firing rate > 1Hz.

Although brain injured mice retained neurons that met place cell criteria, a significantly greater proportion of neurons never qualified as a place cell across the four imaging sessions, while fewer neurons were repeatedly classified as place cells (**Figure 4.6I,J**). This reduction in place cell recruitment was evident during both running directions. Thus, chronic brain injury reduces the population of CA1 neurons that participates in spatial representations across repeated experience.

We next examined the properties of neurons that did form place fields. Place fields were modestly but consistently broader in brain injured mice during both rightward and leftward running (**Figure 4.6K**). In contrast, spatial information was preserved among place cells and did not differ between groups (**Figure 4.6L**). Within-session stability was also preserved during rightward running and was modestly increased in brain injured mice during leftward running (**Figure 4.6M**). Stability increased with repeated exposure to the track in both groups and running directions (**Figure 4.8A,B**), and peak and mean firing rates of place cells were comparable between groups (**Figure 4.8C,D**). Thus, brain injury does not abolish the spatial activity of established place cells. Rather,

neurons that form place fields exhibit broader spatial tuning despite preserved spatial information and within-session stability.

Nonspatial neurons in brain injured mice had lower firing rates than controls during both running directions, and their within-session stability was also reduced (**Figure 4.8E-H**). This suggests neurons that failed to meet place cell criteria are not simply inactive; they exhibited reduced and less stable activity after injury. Together with the reduced recruitment of neurons into place cell populations, our findings indicate that chronic brain injury alters the cellular organization of hippocampal spatial activity, with fewer neurons participating in spatial representations, broader spatial tuning among recruited neurons, and reduced activity and stability among neurons that remain nonspatial.

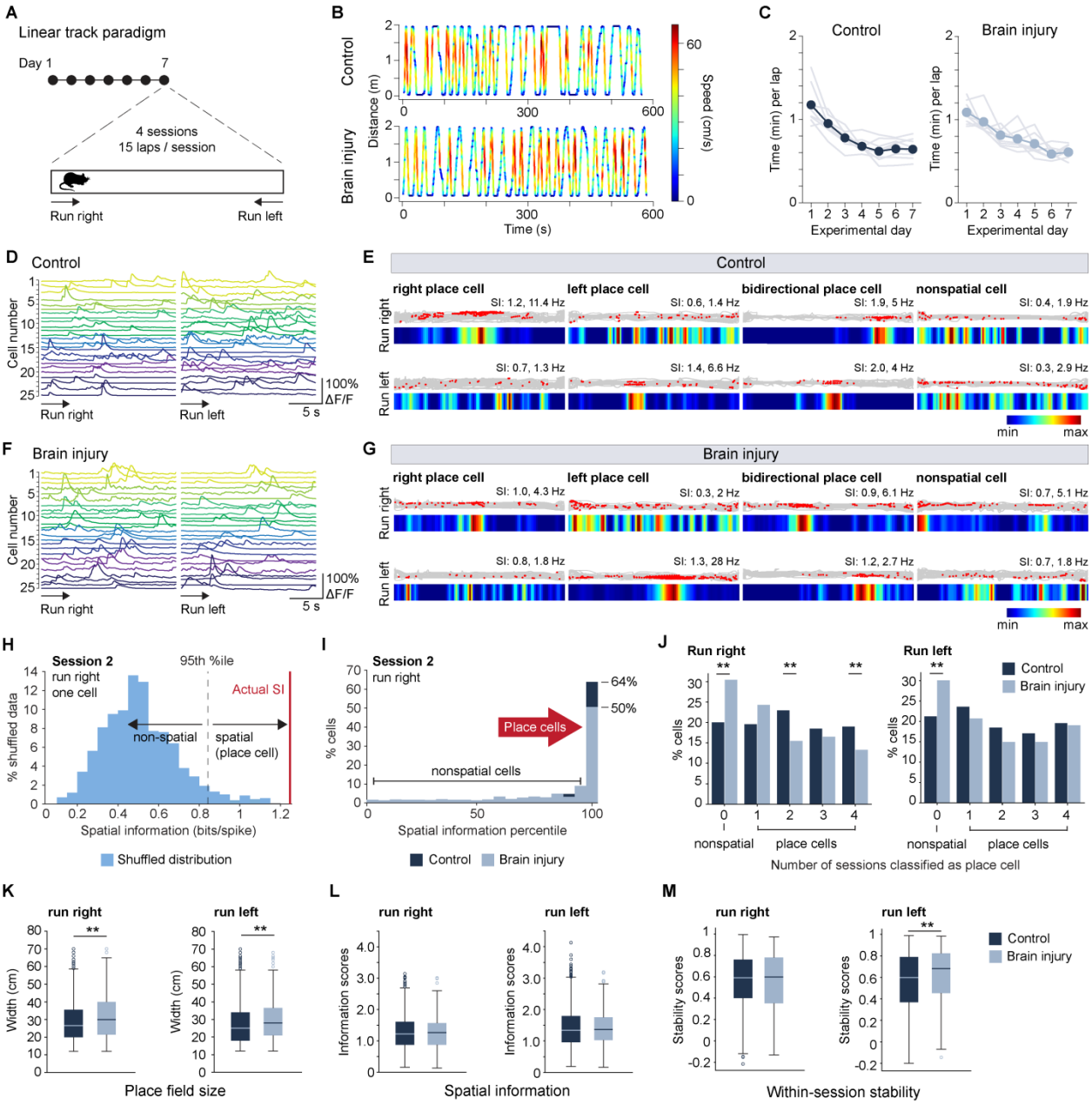


Figure 4.6: Chronic brain injury alters the recruitment and spatial precision of CA1 representations. A. Experimental design for the linear track task. **B.** Representative running trajectories and speed profiles from control and brain injured mice. **C.** Time per lap across experimental days. Gray lines indicate individual mice and colored symbols indicate group means. **D, F.** Representative calcium traces during rightward and leftward running from control (D) and brain injured (F) mice. **E, G.** Representative rightward, leftward, bidirectional, and nonspatial cells from control (E) and brain injured (G) mice. Gray trajectories indicate position and red dots indicate inferred calcium events; spatial firing rate maps, spatial information (SI), and peak event frequency are shown for each running direction. **H.** Example shuffled SI distribution used for place cell classification. **I.** Distribution of SI percentiles for all cells during one session; the 95th percentile threshold and proportion of place cells are indicated. **J.** Percentage of cells classified as place cells according to the number of sessions in which they met place cell criteria. Run right: P = 1.11E-06, 3.2E-04, and 6.27E-03 for 0, 2 and 4 sessions; run left: P = 6.9E-05 for 0 sessions; Fisher's exact test with Bonferroni correction. **K.** Place field width. Run right, P = 2.72E-04; run left, P = 4.29E-05. **L.** Mean SI per group. **M.** Within-session stability. Run left, P = 2.28E-05. Mann–Whitney U test for K–M. n = 1,205 cells from 8 control mice and 455 cells from 6 brain injured mice for K–M; n = 1,506 cells from 8 control mice and 654 cells from 6 brain injured mice for J. Box plots show median and interquartile range (IQR), with whiskers extending to 1.5 × IQR.

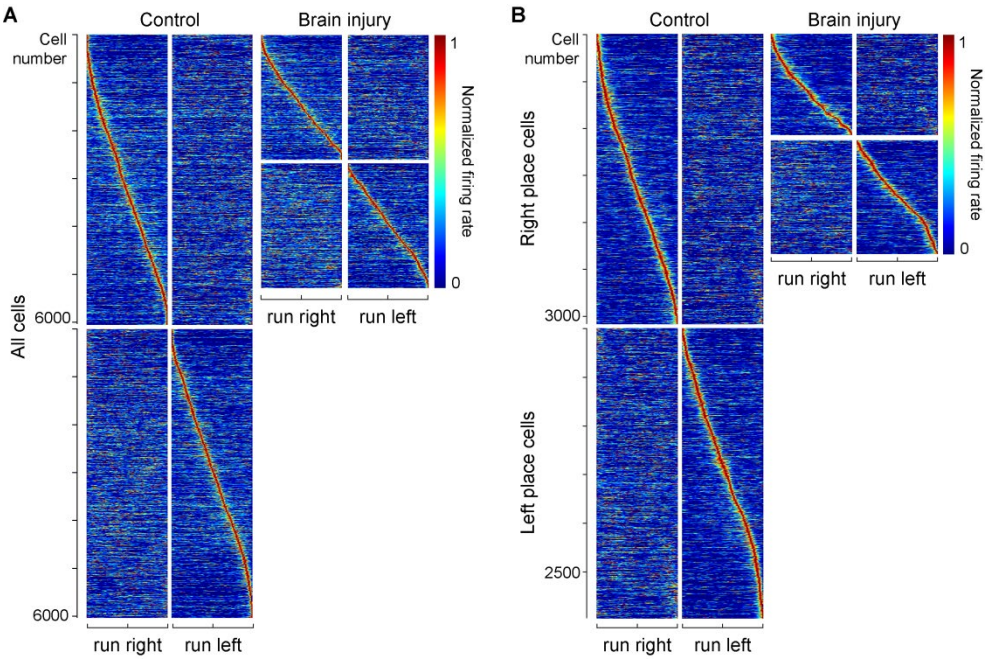


Figure 4.7: Firing rate maps of CA1 neurons. A. Spatial firing rate maps for all cells recorded across four linear track sessions during rightward and leftward running in control and brain injured mice. Maps are ordered by peak firing rate for each running direction (n = 6,024 cells from 8 control mice; n = 2,616 cells from 6 brain injured mice). **B.** Spatial firing rate maps for place cells recorded across four sessions during rightward and leftward running. Maps are ordered by peak firing rate (n = 3,078 rightward and 2,972 leftward place cells from 8 control mice; n = 1,074 rightward and 1,166 leftward place cells from 6 brain injured mice). Firing rates are normalized to the maximum firing rate of each cell.

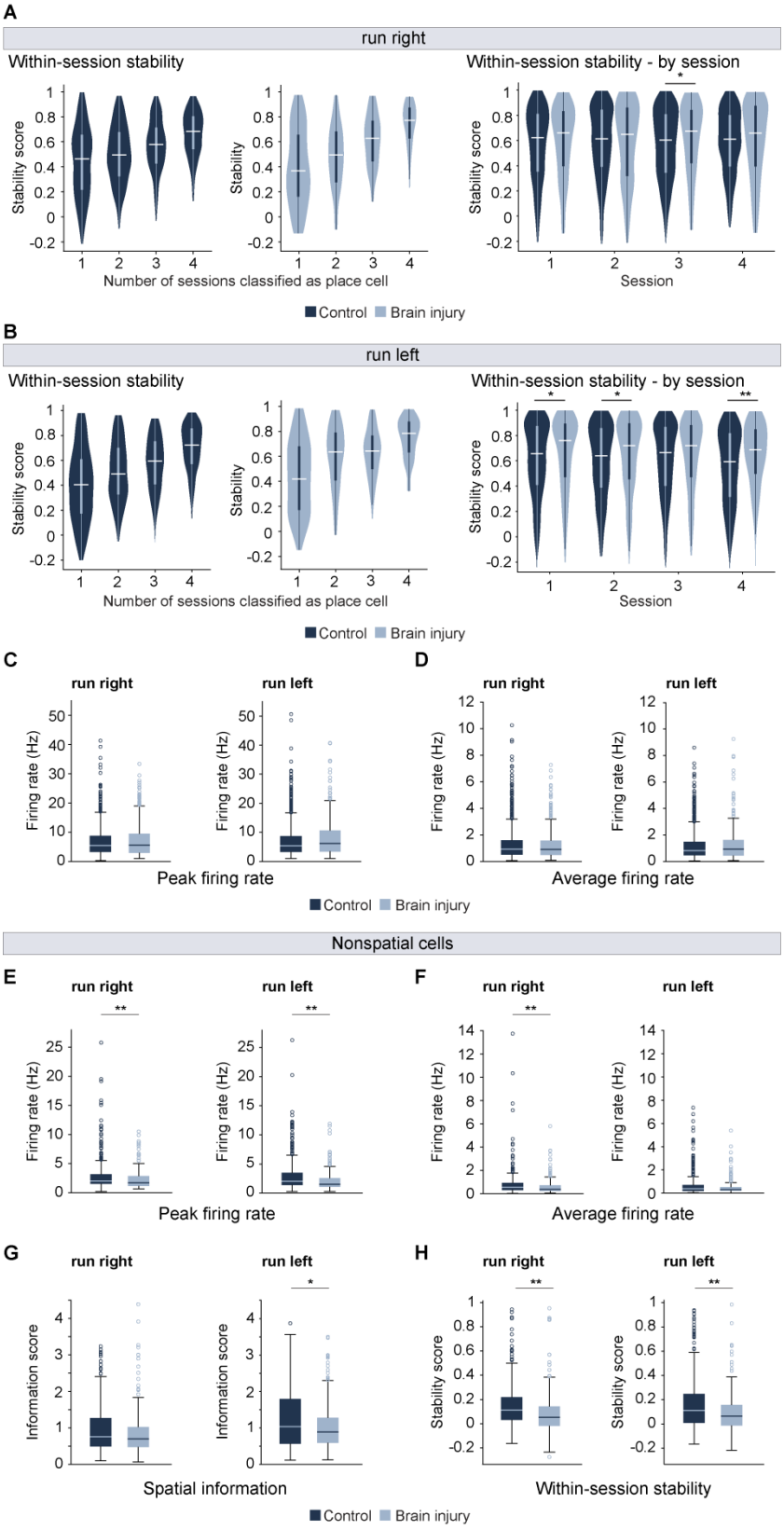

A
run right
Within-session stability
Within-session stability - by session
Stability score
Stability
Number of sessions classified as place cell
Session
Control
Brain injury
B
run left
Within-session stability
Within-session stability - by session
Stability score
Stability
Number of sessions classified as place cell
Session
Control
Brain injury
C
run right
run left
Firing rate (Hz)
Peak firing rate
D
run right
run left
Firing rate (Hz)
Average firing rate
Control
Brain injury
Nonspatial cells
E
run right
run left
Firing rate (Hz)
Peak firing rate
F
run right
run left
Firing rate (Hz)
Average firing rate
G
run right
run left
Information score
Spatial information
H
run right
run left
Stability score
Within-session stability
Control
Brain injury

Figure 4.8: Place cell stability, firing rates and nonspatial cell properties. A. Within-session stability of place cells during rightward running as a function of the number of sessions in which cells were classified as place cells (left) and by session number (right) in control and brain injured mice (session 3, $P = 0.02$; Mann–Whitney U test with Bonferroni correction). **B.** Same as **A** for leftward running (session 1, $P = 0.04$; session 2, $P = 0.016$; session 4, $P = 7.3E-05$; Mann–Whitney U test with Bonferroni correction). For A, B, $n = 3,078$ rightward place cells from 8 control mice and 1,074 from 6 brain injured mice; $n = 2,972$ leftward place cells from 8 control mice and 1,166 from 6 brain injured mice. Violin plots show the distribution of stability values; white lines indicate medians and boxes indicate interquartile ranges (IQR). **C.** Peak firing rates of place cells during rightward and leftward running. **D.** Mean firing rates of place cells during rightward and leftward running. For C, D, $n = 1,205$ cells from 8 control mice and 455 cells from 6 brain injured mice. **E.** Spatial information of nonspatial cells, defined as cells that were not classified as place cells in any session, during rightward and leftward running (leftward, $P = 1.55E-02$). **F.** Within-session stability of nonspatial cells (rightward, $P = 5.52E-06$; leftward, $P = 6.41E-04$). **G.** Peak firing rate of nonspatial cells (rightward, $P = 4.45E-04$; leftward, $P = 3.36E-07$). **H.** Mean firing rate of nonspatial cells (rightward, $P = 1.82E-04$). Mann–Whitney U test was used for E–H. For nonspatial cells, $n = 301$ control and 199 brain injured cells for rightward running and 320 control and 197 brain injured cells for leftward running. Box plots show median, IQR, and whiskers extending to 1.5 × IQR.

Brain injury impairs spatial novelty discrimination

To determine whether altered organization of CA1 spatial activity was accompanied by impaired spatial memory, we tested the same mice in a Y-maze novelty discrimination task (**Figure 4.9A**). Mice were initially restricted to two arms of the maze and, following a 1 h rest period in the home-cage, were allowed to explore all three arms. During the test phase, control mice preferentially explored the novel arm, spending more time there than brain injured mice, which showed no preference among the three arms (**Figure 4.9B**). To quantify novelty discrimination, we calculated discrimination indices comparing time spent in the novel arm with time spent in either the entry or familiar arm (**Figure 4.9C**). Control mice exhibited significantly greater discrimination indices for both comparisons than brain injured mice, consistent with increased preference for the novel arm. These differences were not attributable to altered locomotor behavior, as total distance traveled and running speed were comparable between groups (**Figure 4.9D,E**). Thus, chronic brain injury impairs discrimination of a novel spatial environment despite preserved locomotor performance.

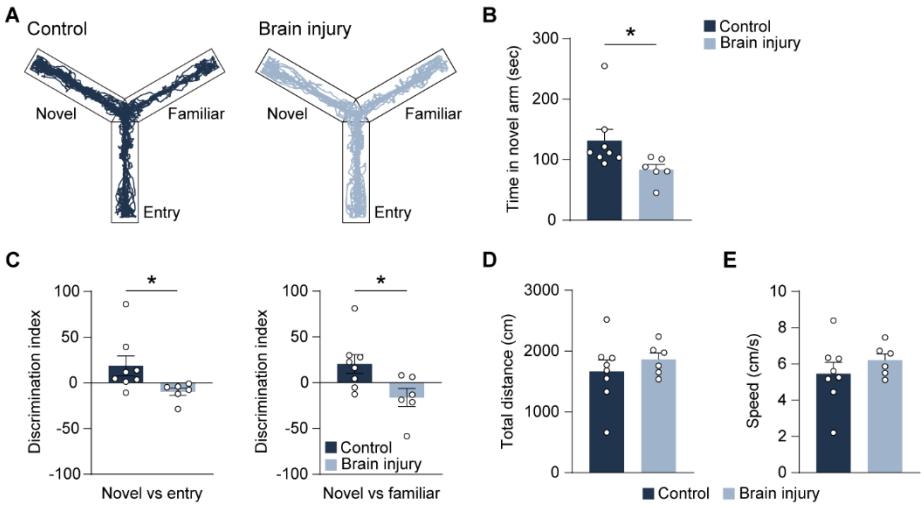


Figure 4.9: Novelty discrimination is impaired after brain injury. A. Representative tracking plots from control (left) and brain injured (right) mice during the test phase of the Y-maze task. **B.** Time spent in the novel arm during the test phase in control and brain injured mice (control, 131.4 ± 18.6 s; Brain injury, 83.4 ± 8.6 s; *P = 0.04, two-tailed t-test). **C.** Discrimination index for the novel arm relative to the entry arm (left) or familiar arm (right) (novel vs. entry: control, 18.8 ± 10.9; brain injury, −9.7 ± 4.1; P = 0.04; novel vs. familiar: control, 20.5 ± 10.2; brain injury, −16.1 ± 9.8; P = 0.02; two-tailed t-test, n = 8 control and 6 brain injured mice). **D.** Total distance traveled during the test phase in control and brain injured mice (control, 1663 ± 187.9 cm; brain injury, 1862 ± 106.7 cm). **E.** Mean locomotor speed during the test phase (control, 5.5 ± 0.6 cm/s; brain injury, 6.2 ± 0.4 cm/s). Data are mean ± SEM.

Discussion

TBI produces substantial remodeling of hippocampal excitatory and inhibitory networks, with changes predicted to alter CA1 excitability in opposing directions. Loss of inhibition and the emergence of aberrant recurrent glutamatergic circuits could promote elevated excitability (Toth et al., 1997; Santhakumar et al., 2000; Hunt et al., 2009, 2011), whereas overall synapse loss and reductions in long-range afferent inputs could constrain neuronal activity (Scheff et al., 2005; Frankowski et al., 2022). Despite these competing influences, we found CA1 firing was broadly preserved three months after injury, a finding that has been consistently reported in models of TBI (Eakin and Miller, 2012; Koch et al., 2020; Ulyanova et al., 2023; Adam et al., 2026). Thus, post-traumatic circuit remodeling does not produce a simple change in the overall level of CA1 activity or excitation–inhibition balance, but rather alters how that activity is organized across neuronal populations. The spatial representation of the environment provides a particularly clear example of this reorganization. TBI increases the fraction of neurons that remain spatially

unresponsive, broadens the place fields of neurons that do form spatial representations and alters the activity and stability of the nonspatial population.

Despite these changes, several properties of established place cell representations remain intact. Spatial information and within-session stability were preserved among neurons that formed place fields, indicating that chronic TBI does not abolish the capacity of CA1 neurons to encode space. This may represent a degree of functional compensation that preserves fundamental hippocampal processing without restoring the fidelity required for normal memory. Several features of post-traumatic circuit remodeling could contribute to this incomplete compensation. Local inhibition constrains the formation and spatial tuning of CA1 place fields (Royer et al., 2012; Dudok et al., 2021; Geiller et al., 2022) and is prominently disrupted after TBI (Hunt et al., 2011; Ulyanova et al., 2023), potentially broadening spatial tuning and impairing the recruitment of neurons into spatial representations. TBI also disrupts long-range inputs from entorhinal cortex (Frankowski et al., 2022), which could reduce the spatial information available to CA1. Consistent with this possibility, disruption of medial entorhinal input produces broader and less precise CA1 place fields (Hales et al., 2014). The reduced firing and stability of nonspatial neurons further suggest that altered inhibitory or afferent inputs may affect both the formation of spatial representations and the precision of established place fields. Intriguingly, transplantation of inhibitory neurons into the hippocampus improves memory after TBI (Zhu et al., 2019), while transplanted neurons also receive new entorhinal inputs (Frankowski et al., 2022), providing evidence that restoration of local inhibition and afferent connectivity may improve hippocampal function after TBI. At the same time, post-traumatic circuit remodeling may carry pathological consequences, as loss of inhibition, enhanced excitatory connectivity and aberrant recurrent circuit formation can promote network hyperexcitability and post-traumatic epilepsy (Hunt et al., 2009). Although epilepsy was not assessed in this study, no seizures were observed during experimentation.

The spatial phenotype we observed after chronic TBI also differs from epilepsy and Alzheimer's disease models. In epilepsy, place cell representations show reductions in the number of spatially tuned neurons, spatial information and stability, with pronounced disruption of the temporal organization of place cell firing (Liu et al., 2003; Shuman et al., 2020). Alzheimer's disease models similarly exhibit reduced recruitment and spatial information without a change in field size (Mably et al., 2017; Jun et al., 2020). Thus, whereas these models show a broader degradation of established spatial representations, chronic TBI produces a more selective reorganization of the cellular composition and spatial tuning of CA1 representations. These differences may reflect the more restricted spatial extent of CCI pathology compared with the widespread CNS pathology produced by status epilepticus or the distributed cortical–hippocampal pathology of Alzheimer's disease models. Although CCI can induce secondary circuit remodeling beyond the primary lesion (Holden et al., 2019; Frankowski et al., 2022), the relative preservation of spatial representations may reflect this more focal pattern of injury. Thus, chronic post-traumatic remodeling may preserve fundamental aspects of hippocampal network function while compromising the fidelity with which they are implemented.

Together, our findings support a model in which TBI preserves overall CA1 activity while reorganizing the cellular and spatial structure of hippocampal representations. This dissociation between neuronal activity and network function provides a circuit-level framework for understanding how persistent post-traumatic remodeling can preserve basic hippocampal activity while compromising the precision required for spatial memory.

CONCLUSIONS

Traumatic brain injury initiates a cascade of cellular and circuit-level changes that extend far beyond the tissue directly damaged by the initial mechanical insult. Structural consequences of injury have been extensively characterized in a variety of animal and injury models; yet, less is understood about how neural circuits respond to injury, both in early and late phases of injury. Moreover, how these responses ultimately alter the computation required for higher-order cognition is not well understood. The three studies presented in this dissertation address this question by examining 1. neural activity, 2. anatomical connectivity, and 3. hippocampal population dynamics, that span the spatial and temporal timescales of injury. Together, these findings demonstrate that focal brain injury should not be viewed solely as a localized insult, but rather as an event that initiates widespread and persistent changes in the organization and function of neural circuits.

Summary of my findings

Three major findings emerge from my work. First, using the TRAP2 transgenic mouse model, I show that shortly after injury there is widespread neuronal activation that extends beyond the glial and astrocytic responses. Ai14+ neurons are present mainly on the ipsilateral side of the injury across the neocortex, hippocampus, and subcortical regions, with areas of the contralateral hippocampus also labeled. Next, I demonstrate that the effects of injury persist chronically at the circuit-level. Brain injury results in profound neural reorganization, altering the long-range and local connections of inhibitory interneurons in areas directly and not directly damaged by the initial insult. Finally, at this chronic timepoint after injury, the precision of hippocampal spatial representations are altered, despite relatively normal hippocampal neuron activity. These results show the progression of injury, from widespread neuronal activation to circuit reorganization, and ultimately a degradation of neural representations associated with cognitive dysfunction.

Focal injury has widespread consequences

Although the initial mechanical insult of CCI is spatially restricted, with the impactor centered over a certain brain region, subsequent pathology can extend beyond the lesion and affect anatomically connected regions. Neurons within a region of the brain do not act alone; they are embedded into networks that can have extensive crosstalk. Therefore, defining the lesion based only on structural damage can be misleading and underestimates the full extent of damage. Chapter 1 provides evidence for this through the early activation of neuronal populations widespread throughout the brain.

The spatial distribution of TRAPed neurons is extensive, both anterior and posterior to the site of impact, but also extending into contralateral brain regions. The glial and astrocytic response is restricted to the injury site, a response extensively shown in CCI models (Smith et al., 1995; Susarla et al., 2014; Frankowski et al., 2019; Zhu et al., 2019). Much of the ipsilateral neocortex is labeled by Ai14, extending into the hippocampus and subcortical areas. This dissociation between the activation patterns of TRAPed neurons and GFAP/IBA1 labeling suggests that those neurons that were initially activated potentially participate in the organization of neural networks after injury. An important question raised by these findings is whether widespread neuronal activation is restricted to the acute phase of injury or whether this activation sets up circuit reorganization mechanism during the chronic phase of injury. Indeed, this acute activation may mark sites of future circuit remodeling (Harris et al., 2016). Chapter 2 demonstrates that chronic TBI reorganizes brain circuits in a very specific way. Surviving interneurons lose long-range inputs and gain local inputs in a cell-type manner, and more importantly, this pattern is present in areas not directly damaged by the injury. This establishes that during chronic TBI, the effects of the initial insult are not restricted to the area of direct damage. Structurally spared tissue can indeed be incorporated into the post-injury circuit in the later stages of TBI.

At the functional level, the injured network can retain activity, evident by specific behavioral phenotypes that are preserved versus disrupted, as previously described after CCI (Zhu et al., 2019). However, retention of activity may not always be enough. The hippocampus provides an excellent example of this, shown through survival and preservation of normal activity patterns, yet not sufficient for precision of the network. Results from Chapter 4 describe that three months after injury, hippocampal neurons demonstrate no altered patterns of firing rates at baseline levels in home-cage experiments. Yet, when you challenge the network in a task that involves computations of space and the surrounding environment, less neurons are able to participate in spatial coding, and animals display novelty discrimination deficits. The absence of gross abnormalities may not be indicative of a lack of functional deficits. Understanding post-traumatic circuit changes requires a comprehensive analysis of not only cell loss or tissue damage, but how surviving neurons function and integrate into the injured network.

Early neuronal activation to chronic network rewiring

The widespread pattern of Ai14+ cells present shortly after TBI may not only represent a transient upregulation of IEG, but a potential substrate for subsequent activity-dependent remodeling of the network. Circuit remodeling occurs over the course of days to even years after injury but the way early responses shape these events is elusive. Cell death, early inflammation, axonal degeneration, and synaptic loss contribute to the dynamically changing environment in the brain after insult (Hunt et al., 2013a). The findings from Chapter 2 and 3 suggest that neuronal activation may link the acute response to injury with the subsequent chronic circuit changes.

Immediate early gene (IEG) expression is often used as a neural correlate for active cell populations in an attempt to link brain function to behavior (Guzowski et al, 2005; DeNardo and Luo, 2017). Some of the first models to study this were injury or disease models, such as epilepsy (Dragunow and Robertson, 1987; Lauterborn et al.,1996), ischemia (Kiessling and Gass, 1993)

and brain injury (Dragunow and Robertson, 1988; Raghupathi et al., 1995b). Apart from bring a useful marker of activity, many IEGs may play a role regulating synaptic plasticity (Guzowski et al., 2000; Chowdhury et al., 2006). This brings into light why certain neurons are TRAPed versus not. Although the labeling of neurons through TRAP does not directly mean that these neurons are primed for participation in post-traumatic circuits, it does raise the possibility that early post-traumatic activity might contribute to cellular and synaptic plasticity.

One idea is that the neurons recruited during the time of injury may be a part of an “injury-related ensemble.” Their subsequent connectivity and recruitment into the injured circuit may differ from those that are not a part of the ensemble. This ensemble might not necessarily be separated into labeled versus unlabeled (Ai14+) populations but rather an ensemble that encompasses a combination of both. Several possibilities arise from this idea. Neurons labeled at the time of injury could be preferentially retained/lost, with their inputs more prone for synaptic remodeling (Scheff et al., 2005). Similarly, these neurons might be preferentially incorporated into the recurrent circuitry commonly seen after TBI (Hunt et al., 2009, 2011). At the functional level, the injured ensemble could be more or less likely to participate in memory representations, such as spatial learning and navigation. If these labeled neurons are later recruited, it is possible that their firing properties upon reactivation lead to aberrant behaviors. My current set of experiments did not directly establish the link between neurons acutely activated after injury and their preferential circuit remodeling. However, there is sufficient evidence to suggest that the connectivity of surviving neuron populations is highly plastic, even at chronic timepoints after injury. While one timepoint was looked at in the current study, it would be interesting to perform a more detailed time course of neuronal activation. This could be done by using 4-OHT rather than tamoxifen at defined periods covering immediate, early and chronic injury.

The reorganization patterns observed in Chapter 3 may be maladaptive or compensatory. Chronic injury altered the inputs onto interneurons, both their local and long-range connectivity. Temporal lobe epilepsy can also reorganize inhibitory circuits such that there is increased excitatory drive onto these cells and they are capable of projecting to areas they typically do not occupy (Hunt et al., 2011; Peng et al., 2013). In TBI, surviving SST interneurons form back-projections from CA1 to the hilus, a previously unknown input. This increase in local connectivity could be compensatory due to the deafferentation caused by TBI (Ribak and Reiffenstein, 1982; Scheff et al., 2005). Thus, post-traumatic plasticity may attempt to maintain network activity without restoring the original organization of the network.

Chapter 4 demonstrates this preservation of network activity. CA1 neuron firing rates remain broadly comparable between control and TBI mice. However, this preservation is accompanied by a change in their recruitment during spatial navigation. Brain injured mice display a larger proportion of neurons that never qualify as place cells. The post-traumatic remodeling in hippocampus fails to preserve the organization necessary for precise spatial representations. This means that surviving neural circuits are not simply less active after injury; rather, the information encoded by these populations is fundamentally altered.

Preserved neuronal activity does not mean preserved network function

Neural circuit dysfunction following a brain injury is often associated with hyperexcitability. Higher order behaviors, like cognition, require active neurons in addition to precise timing of specific inputs across neuronal populations. In that way, using CA1, a well-studied circuit with defined inputs and outputs, allows us to study how CA1 neurons change their function, especially during spatial tasks. This is where the differences in CA1 function started to emerge.

Place cells in the context of injury have been understudied and Chapter 4 attempts to shed light as to how CCI affects their dynamics. In a fluid percussion model of injury, the proportion of place cells is reduced, along with their information content and stability (Broussard et al., 2020). This contrasts with my results which suggest a more subtle phenotype after CCI. Spatial coding showed a selective degradation after injury. Place cells exist in similar proportions to uninjured controls. Their properties such as spatial information, peak firing rate, mean firing rate and within-session stability are largely preserved after TBI. CA1 neurons are capable of creating place fields, but with broader widths. In addition, a larger proportion of neurons never qualified as place cells in the TBI mice. The nonspatial population of neurons is particularly interesting given their reduced firing rates and stability scores. These findings raise the possibility that TBI reduces the capacity for CA1 to recruit neurons into stable spatial representations, especially across repeated experiences. Chronic TBI therefore does not eliminate spatial coding but changes the precision with which these populations of neurons represent space.

The fundamental properties of the remaining place cells are retained in the injured mice. Place cells in the injured hippocampus carry similar information content and do not differ in their stability scores, suggesting that the circuit retains a substantial computational capacity, even at chronic time points. However, the reorganized network is not functional enough to reproduce the precision and organization of the intact circuit. Together, this suggests that measures of overall activity are not enough to view the full extent of circuit dysfunction after TBI. Rather a circuit-level mechanism is most likely playing a role in disrupting the organization, specificity and precision by which CA1 encodes spatial memory.

Circuit mechanisms underlying altered hippocampal spatial representations

The formation of place fields in CA1 does not rely solely on pyramidal neurons in isolation. Spatial tuning reflects the integration of long-range inputs in conjunction with local excitatory and

inhibitory inputs (Ahmed and Mehta, 2009). TBI can disrupt the processing of these inputs at a circuit-level. A loss of long-range inputs, from entorhinal cortex for example, was observed in hilar interneurons and could be a possibility in CA1 pyramidal neurons as well. A sharp decline in synapse numbers is present shortly after injury, with a ~70% recovery of synapses compared to original levels (Scheff et al., 2005). The location of these inputs is not known but potential hypothesis could be that a loss of inhibition is driving at least some of the spatial deficits observed. Altered inhibition is a good candidate for why place fields are broadening after TBI. Local inhibition constrains when and where CA1 neurons fire, generating robust firing patterns during spatial behaviors (Jeong and Singer, 2022). Thus, disrupting the inhibitory organization in the hippocampus could potentially reduce the spatial specificity of pyramidal neuron activity. Place cells can remain spatially informative while reducing the precision of their spatial tuning. The role of inhibition on place cell dynamics has been well documented. Dendritic and somatic inhibition play different roles in controlling inhibition; where PV interneurons control spike timing, SST interneurons regulate the bursting of place field firing (Royer et al., 2012). Broader place fields after injury could also be explained by CA1 interneuron dysfunction. Suppressing the firing of inhibitory neurons causes pyramidal cells to fire in areas outside of their original place fields, thus suggesting inhibition sharpens the spatial response of CA1 neurons (Grienberger et al., 2017). The precise timing of these inhibitory inputs onto CA1 neurons is equally as important (Valero et al., 2022) and may be critical in the context of injury where selective loss of inhibitory neurons and their circuits is observed (Frankowski et al., 2019).

Another mechanism by which spatial precision and recruitment is disrupted after TBI is the potential loss of entorhinal cortex input. Indeed, hilar interneurons have reduced input from the entorhinal cortex. We show that the neurons in the entorhinal cortex are still present, yet they are contacting less hilar interneurons in injured mice. Although we do not directly show that CA1 neurons become disconnected from entorhinal cortex, the data suggests that a disruption to this

input could produce broader, less precise CA1 place fields. Altered afferent input may influence which neurons are recruited for spatial coding of the environments, whereas local inhibition may influence the precision which recruited neurons represent space. My experiments did not mechanistically test this theory but suggest that a combination of these two hypotheses could be at play.

Both excitatory and inhibitory synapses onto pyramidal neurons serve as modulators of firing rates and subsequently spatial representations. For example, dendritic and somatic inhibition of CA1 neurons lead to different types of plasticity that change the way CA3 and entorhinal cortex inputs converge (Udakis et al., 2020). Stabilization of place cells is important for remembering a familiar environment, but the network must also be flexible to create a different representation in a novel environment. The ability to adapt to a changing environment depends on the balance between CA3 and entorhinal cortex inputs, allowing for remapping (Udakis et al., 2020). In addition, input from the medial septum plays an important role in generating theta rhythms in hippocampus (Rawlins et al. 1979; Freund and Antal, 1988; Unal et al., 2015). When this input is silenced, the activity of interneurons is significantly reduced in CA1, yet no loss in spatial selectivity of pyramidal neurons is observed (Mizumori et al., 1989). Afte injury, we show that hilar interneurons receive less medial septal inputs while CA1 neurons retain their firing properties and their ability to create spatial representations is preserved. This further suggests that the filtering of inputs is critical in creating an accurate cognitive map. The convergence of inputs from the extrahippocampal regions and local networks within the hippocampus, excitatory and inhibitory, provide a circuit-level explanation for how CA1 neuronal activity can remain intact, yet spatial precision is degraded following brain injury.

Future directions

My results provide evidence for widespread effects of focal brain injury, rewiring of surviving circuits, and functional plasticity of hippocampal spatial representations. However, certain questions remain that could be expanded upon with further experiments. An experiment that could tie together the c-fos expression patterns seen in Chapter 2 with activity, in terms of action potentials, would be patch-clamp electrophysiology in regions labeled by Ai14 during the early phase of injury. Additionally, because the TRAP technique permanently labels the neurons, the possibility of recording firing properties across all injury timepoints is available.

An interesting experiment that brings together the data supporting results from Chapter 2 and 3 would be to look at whether inhibitory neurons are activated immediately after injury. Observations of the morphology and location of Ai14-labeled neurons suggest a small subset of these neurons could be inhibitory neurons. Furthermore, TRAP labeling of CA1 neurons at the time of injury and later observing their firing properties while mice perform a spatial task would provide a direct link between early activation and spatial processing deterioration. This could also answer whether cells that are activated early are preferentially recruited to participate in spatial representations chronically.

It is unknown whether other interneuron types in the hippocampus are rewired in the same way that hilar SST interneurons are after brain injury. Taking advantage of other interneuron Cre-driver mouse lines (PV-and VIP-cre, for example) would allow us to test whether different interneuron types display similar patterns of circuit reorganization. More specifically, tracing the inputs (and outputs) of CA1 interneurons is critical for the understanding of how pyramidal neurons are dynamically processing information about space after injury. Furthermore, transplantation of interneuron progenitors into the brain has been shown to suppress seizures and improve memory (Hunt et al., 2013b; Zhu et al., 2019). We have shown that these interneurons are capable of

integrating into the injured brain; thus, we could test whether interneuron transplantation rescues the degradation of precise spatial representations *in vivo*.

Relatedly, *in vivo* imaging of interneurons would be a good complement to the place cell experiments described in Chapter 4. Using the SST-cre mouse line combined with the FLEX-jGCAMP8m virus, we could look at the activity of inhibitory neurons in the same linear track task. This would help us draw better conclusions as to the function of inhibition in the post-traumatic hippocampal circuit, given the broadening of place fields and degradation of precision.

The use of miniscopes allowed us to test neuronal activity in freely behaving mice. This opens up the possibility for testing other naturalistic behaviors after injury. Given the generalized fear response seen in CCI mice (Zhu et al., 2019), recording neuronal activity in both shock and no-shock contexts would elucidate how these neurons are processing changes in the environment. We did not test the remapping ability of CA1 neurons after TBI. In Alzheimer's models, place cells display similar patterns of activity when placed in two different linear tracks, demonstrating disrupted remapping ability (Jun et al., 2020). Thus, testing TBI mice on a novel linear track would allow us to test whether the population of nonspatial cells is recruited in the novel environment. Finally, because miniscopes allow longitudinal tracking of the same neuronal populations over time, imaging CA1 neurons at an early timepoint could would allow us to observe initial deterioration of the spatial code, followed by the progression of precision deterioration. However, due to the constraints of the CCI surgery and viral injection and expression, the earliest plausible timepoint given our current experimental paradigm would be 3 weeks after injury.

The spatial resolution of one-photon endoscopic imaging is restricted to cell bodies that are within 200 μm of the GRIN lens. Use of a multi-photon imaging technique in freely behaving mice (Zong et al., 2022) would allow further investigation as to how dendritic inputs are integrating in CA1

pyramidal neurons. Of particular interest, performing dendritic recordings of CA1 neurons following transplantation of interneurons after TBI would capture the integration of interneuron inputs *in vivo* and possibly test whether certain behaviors change CA1 firing properties.

Taken together, the results in this dissertation encompass the temporal and spatial dynamics of TBI through varying levels of complexity, from brain-wide to circuit-level mapping and functional assays. The anatomical boundaries of the injury are not indicative of the functional consequences of TBI. Therefore, studying the effects of injury using only the focal and structural damage of the initial insult underestimates the true extent of TBI.

REFERENCES

Aboghazleh, R., Parker, E., Yang, L. T., Kaufer, D., Dreier, J. P., Friedman, A., & van Hameren, G. (2021). Brainstem and Cortical Spreading Depolarization in a Closed Head Injury Rat Model. *International Journal of Molecular Sciences*, *22*(21), 11642. https://doi.org/10.3390/ijms222111642

Abrous, D. N., Rodriguez, J., le Moal, M., Moser, P. C., & Barnéoud, P. (1999). Effects of mild traumatic brain injury on immunoreactivity for the inducible transcription factors c-Fos, c-Jun, JunB, and Krox-24 in cerebral regions associated with conditioned fear responding. *Brain Research*, *826*(2), 181–192. https://doi.org/10.1016/S0006-8993(99)01259-7

Adam, C. D., Mirzakhalili, E., Gagnon, K. G., Cottone, C., Arena, J. D., Ulyanova, A., Johnson, V. E., & Wolf, J. A. (2026). Disrupted hippocampal theta-gamma coupling and spike-field coherence following experimental traumatic brain injury. *eLife*, *13*, RP100642. https://doi.org/10.7554/eLife.100642

Agrawal, A., Timothy, J., Pandit, L., & Manju, M. (2006). Post-traumatic epilepsy: An overview. *Clinical Neurology and Neurosurgery*, *108*(5), 433–439. https://doi.org/10.1016/j.clineuro.2005.09.001

Ahmed, O. J., & Mehta, M. R. (2009). The hippocampal rate code: Anatomy, physiology and theory. *Trends in Neurosciences*, *32*(6), 329–338. https://doi.org/10.1016/j.tins.2009.01.009

Ährlund-Richter, S., Xuan, Y., van Lunteren, J. A., Kim, H., Ortiz, C., Pollak Dorocic, I., Meletis, K., & Carlén, M. (2019). A whole-brain atlas of monosynaptic input targeting four different cell types in the medial prefrontal cortex of the mouse. *Nature Neuroscience*, *22*(4), 657–668. https://doi.org/10.1038/s41593-019-0354-y

Alessandri, B., Heimann, A., Filippi, R., Kopacz, L., & Kempski, O. (2003). Moderate Controlled Cortical Contusion in Pigs: Effects on Multi-Parametric Neuromonitoring and Clinical Relevance. *Journal of Neurotrauma*, *20*(12), 1293–1305. https://doi.org/10.1089/089771503322686094

Almeida-Suhett, C. P., Prager, E. M., Pidoplichko, V., Figueiredo, T. H., Marini, A. M., Li, Z., Eiden, L. E., & Braga, M. F. M. (2015). GABAergic interneuronal loss and reduced inhibitory synaptic transmission in the hippocampal CA1 region after mild traumatic brain injury. *Experimental Neurology*, *273*, 11–23. https://doi.org/10.1016/j.expneurol.2015.07.028

Alvarez-Dolado, M., Calcagnotto, M. E., Karkar, K. M., Southwell, D. G., Jones-Davis, D. M., Estrada, R. C., Rubenstein, J. L. R., Alvarez-Buylla, A., & Baraban, S. C. (2006). Cortical Inhibition Modified by Embryonic Neural Precursors Grafted into the Postnatal Brain. *Journal of Neuroscience*, *26*(28), 7380–7389. https://doi.org/10.1523/JNEUROSCI.1540-06.2006

Amaral, D. G., Dolorfo, C., & Alvarez-Royo, P. (1991). Organization of CA1 projections to the subiculum: A PHA-L analysis in the rat. *Hippocampus*, *1*(4), 415–435. https://doi.org/10.1002/hipo.450010410

Amaral, D. G., & Witter, M. P. (1989). The three-dimensional organization of the hippocampal formation: A review of anatomical data. *Neuroscience*, *31*(3), 571–591.

https://doi.org/10.1016/0306-4522(89)90424-7

Anderson, K. J., Miller, K. M., Fugaccia, I., & Scheff, S. W. (2005). Regional distribution of Fluoro-Jade B staining in the hippocampus following traumatic brain injury. *Experimental Neurology, Including Abstracts of the Twelfth Annual Conference of the American Society for Neural Transplantation and Repair*, *193*(1), 125–130. https://doi.org/10.1016/j.expneurol.2004.11.025

Anderson, S. A., Marín, O., Horn, C., Jennings, K., & Rubenstein, J. L. R. (2001). Distinct cortical migrations from the medial and lateral ganglionic eminences. *Development*, *128*(3), 353–363. https://doi.org/10.1242/dev.128.3.353

Annegers, J. F., Hauser, W. A., Coan, S. P., & Rocca, W. A. (1998). A Population-Based Study of Seizures after Traumatic Brain Injuries. *New England Journal of Medicine*, *338*(1), 20–24. https://doi.org/10.1056/NEJM199801013380104

Antonoudiou, P., Stone, B. T., Colmers, P. L. W., Evans-Strong, A., Teboul, E., Walton, N. L., Weiss, G. L., & Maguire, J. (2024). Experience-dependent information routing through the basolateral amygdala shapes behavioral outcomes. *Cell Reports*, *43*(7). https://doi.org/10.1016/j.celrep.2024.114489

Ariza, M., Serra-Grabulosa, J. M., Junqué, C., Ramírez, B., Mataró, M., Poca, A., Bargalló, N., & Sahuquillo, J. (2006). Hippocampal head atrophy after traumatic brain injury. *Neuropsychologia*, *44*(10), 1956–1961. https://doi.org/10.1016/j.neuropsychologia.2005.11.007

Ascoli, G. A., Alonso-Nanclares, L., Anderson, S. A., Barrionuevo, G., Benavides-Piccione, R., Burkhalter, A., Buzsáki, G., Cauli, B., DeFelipe, J., Fairén, A., Feldmeyer, D., Fishell, G., Fregnac, Y., Freund, T. F., Gardner, D., Gardner, E. P., Goldberg, J. H., Helmstaedter, M., Hestrin, S., … The Petilla Interneuron Nomenclature Group (PING). (2008). Petilla terminology: Nomenclature of features of GABAergic interneurons of the cerebral cortex. *Nature Reviews Neuroscience*, *9*(7), 557–568. https://doi.org/10.1038/nrn2402

Baldwin, S. A., Gibson, T., Callihan, C. T., Sullivan, P. G., Palmer, E., & Scheff, S. W. (1997). Neuronal Cell Loss in the CA3 Subfield of the Hippocampus Following Cortical Contusion Utilizing the Optical Disector Method for Cell Counting. *Journal of Neurotrauma*, *14*(6), 385–398. https://doi.org/10.1089/neu.1997.14.385

Baraban, S. C., Southwell, D. G., Estrada, R. C., Jones, D. L., Sebe, J. Y., Alfaro-Cervello, C., García-Verdugo, J. M., Rubenstein, J. L. R., & Alvarez-Buylla, A. (2009). Reduction of seizures by transplantation of cortical GABAergic interneuron precursors into Kv1.1 mutant mice. *Proceedings of the National Academy of Sciences*, *106*(36), 15472–15477. https://doi.org/10.1073/pnas.0900141106

Beal, M. F., Mazurek, M. F., Svendsen, C. N., Bird, E. D., & Martin, J. B. (1986). Widespread reduction of somatostatin-like immunoreactivity in the cerebral cortex in Alzheimer's disease. *Annals of Neurology*, *20*(4), 489–495. https://doi.org/10.1002/ana.410200408

Becerra, A. P., Logsdon, A. F., Banks, W. A., & Ransom, C. B. (2021). Traumatic Brain Injury Broadly Affects GABAergic Signaling in Dentate Gyrus Granule Cells. *eNeuro*, *8*(3). https://doi.org/10.1523/ENEURO.0055-20.2021

Belluardo, N., Mudò, G., Dell'albani, P., Hang, X. H., & Condorelli, D. F. (1995). NMDA receptor-

dependent and -independent immediate early gene expression induced by focal mechanical brain injury. *Neurochemistry International*, *26*(5), 443–453. https://doi.org/10.1016/0197-0186(94)00155-N

Bigler, E. D., Andersob, C. V., & Blatter, D. D. (2002). Temporal Lobe Morphology in Normal Aging and Traumatic Brain Injury. *American Journal of Neuroradiology*, *23*(2), 255–266.

Bittner, K. C., Grienberger, C., Vaidya, S. P., Milstein, A. D., Macklin, J. J., Suh, J., Tonegawa, S., & Magee, J. C. (2015). Conjunctive input processing drives feature selectivity in hippocampal CA1 neurons. *Nature Neuroscience*, *18*(8), 1133–1142. https://doi.org/10.1038/nn.4062

Bolkvadze, T., & Pitkänen, A. (2012). Development of Post-Traumatic Epilepsy after Controlled Cortical Impact and Lateral Fluid-Percussion-Induced Brain Injury in the Mouse. *Journal of Neurotrauma*, *29*(5), 789–812. https://doi.org/10.1089/neu.2011.1954

Bráz, J. M., Sharif-Naeini, R., Vogt, D., Kriegstein, A., Alvarez-Buylla, A., Rubenstein, J. L., & Basbaum, A. I. (2012). Forebrain GABAergic Neuron Precursors Integrate into Adult Spinal Cord and Reduce Injury-Induced Neuropathic Pain. *Neuron*, *74*(4), 663–675. https://doi.org/10.1016/j.neuron.2012.02.033

Brodovskaya, A., Shiono, S., & Kapur, J. (2021). Activation of the basal ganglia and indirect pathway neurons during frontal lobe seizures. *Brain*, *144*(7), 2074–2091. https://doi.org/10.1093/brain/awab119

Brodovskaya, A., Shiono, S., Sun, C., Perez-Reyes, E., & Kapur, J. (2025). Preferential superficial cortical layer activation during seizure propagation. *Epilepsia*, *66*(3), 929–941. https://doi.org/10.1111/epi.18239

Broussard, J. I., Redell, J. B., Zhao, J., Maynard, M. E., Kobori, N., Perez, A., Hood, K. N., Zhang, X. O., Moore, A. N., & Dash, P. K. (2020). Mild Traumatic Brain Injury Decreases Spatial Information Content and Reduces Place Field Stability of Hippocampal CA1 Neurons. *Journal of Neurotrauma*, *37*(2), 227–235. https://doi.org/10.1089/neu.2019.6766

Brown, E. V., Malik, A. F., Moese, E. R., McElroy, A. F., & Lepore, A. C. (2022). Differential Activation of Pain Circuitry Neuron Populations in a Mouse Model of Spinal Cord Injury-Induced Neuropathic Pain. *Journal of Neuroscience*, *42*(15), 3271–3289. https://doi.org/10.1523/JNEUROSCI.1596-21.2022

Brun, V. H., Leutgeb, S., Wu, H.-Q., Schwarcz, R., Witter, M. P., Moser, E. I., & Moser, M.-B. (2008). Impaired Spatial Representation in CA1 after Lesion of Direct Input from Entorhinal Cortex. *Neuron*, *57*(2), 290–302. https://doi.org/10.1016/j.neuron.2007.11.034

Buriticá, E., Villamil, L., Guzmán, F., Escobar, M. I., García-Cairasco, N., & Pimienta, H. J. (2009). Changes in Calcium-Binding Protein Expression in Human Cortical Contusion Tissue. *Journal of Neurotrauma*, *26*(12), 2145–2155. https://doi.org/10.1089/neu.2009.0894

Butler, C. R., Boychuk, J. A., & Smith, B. N. (2015). Effects of Rapamycin Treatment on Neurogenesis and Synaptic Reorganization in the Dentate Gyrus after Controlled Cortical Impact Injury in Mice. *Frontiers in Systems Neuroscience*, *9*. https://doi.org/10.3389/fnsys.2015.00163

Butler, C. R., Boychuk, J. A., & Smith, B. N. (2016). Differential effects of rapamycin treatment on

tonic and phasic GABAergic inhibition in dentate granule cells after focal brain injury in mice. *Experimental Neurology*, *280*, 30–40. https://doi.org/10.1016/j.expneurol.2016.03.022

Butt, S. J. B., Fuccillo, M., Nery, S., Noctor, S., Kriegstein, A., Corbin, J. G., & Fishell, G. (2005). The Temporal and Spatial Origins of Cortical Interneurons Predict Their Physiological Subtype. *Neuron*, *48*(4), 591–604. https://doi.org/10.1016/j.neuron.2005.09.034

Cacucci, F., Yi, M., Wills, T. J., Chapman, P., & O'Keefe, J. (2008). Place cell firing correlates with memory deficits and amyloid plaque burden in Tg2576 Alzheimer mouse model. *Proceedings of the National Academy of Sciences*, *105*(22), 7863–7868. https://doi.org/10.1073/pnas.0802908105

Cai, D. J., Aharoni, D., Shuman, T., Shobe, J., Biane, J., Song, W., Wei, B., Veshkini, M., La-Vu, M., Lou, J., Flores, S. E., Kim, I., Sano, Y., Zhou, M., Baumgaertel, K., Lavi, A., Kamata, M., Tuszynski, M., Mayford, M., … Silva, A. J. (2016). A shared neural ensemble links distinct contextual memories encoded close in time. *Nature*, *534*(7605), 115–118. https://doi.org/10.1038/nature17955

Calton, J. L., Stackman, R. W., Goodridge, J. P., Archey, W. B., Dudchenko, P. A., & Taube, J. S. (2003). Hippocampal Place Cell Instability after Lesions of the Head Direction Cell Network. *Journal of Neuroscience*, *23*(30), 9719–9731. https://doi.org/10.1523/JNEUROSCI.23-30-09719.2003

Cantu, D., Walker, K., Andresen, L., Taylor-Weiner, A., Hampton, D., Tesco, G., & Dulla, C. G. (2015). Traumatic Brain Injury Increases Cortical Glutamate Network Activity by Compromising GABAergic Control. *Cerebral Cortex*, *25*(8), 2306–2320. https://doi.org/10.1093/cercor/bhu041

CDC. (2025, August 4). *Facts About TBI*. Traumatic Brain Injury & Concussion. https://www.cdc.gov/traumatic-brain-injury/data-research/facts-stats/index.html

Chapman, D. P., Power, S. D., Vicini, S., Ryan, T. J., & Burns, M. P. (2024). Amnesia after Repeated Head Impact Is Caused by Impaired Synaptic Plasticity in the Memory Engram. *Journal of Neuroscience*, *44*(8). https://doi.org/10.1523/JNEUROSCI.1560-23.2024

Cheng, J., Gu, J., Ma, Y., Yang, T., Kuang, Y., Li, B., & Kang, J. (2010). Development of a rat model for studying blast-induced traumatic brain injury. *Journal of the Neurological Sciences*, *294*(1), 23–28. https://doi.org/10.1016/j.jns.2010.04.010

Chevaleyre, V., & Siegelbaum, S. A. (2010). Strong CA2 Pyramidal Neuron Synapses Define a Powerful Disynaptic Cortico-Hippocampal Loop. *Neuron*, *66*(4), 560–572. https://doi.org/10.1016/j.neuron.2010.04.013

Cholvin, T., Hainmueller, T., & Bartos, M. (2021). The hippocampus converts dynamic entorhinal inputs into stable spatial maps. *Neuron*, *109*(19), 3135-3148.e7. https://doi.org/10.1016/j.neuron.2021.09.019

Chowdhury, S., Shepherd, J. D., Okuno, H., Lyford, G., Petralia, R. S., Plath, N., Kuhl, D., Huganir, R. L., & Worley, P. F. (2006). Arc/Arg3.1 Interacts with the Endocytic Machinery to Regulate AMPA Receptor Trafficking. *Neuron*, *52*(3), 445–459. https://doi.org/10.1016/j.neuron.2006.08.033

Christodoulou, C., DeLuca, J., Ricker, J. H., Madigan, N. K., Bly, B. M., Lange, G., Kalnin, A. J., Liu, W.-C., Steffener, J., Diamond, B. J., & Ni, A. C. (2001). Functional magnetic resonance imaging of working memory impairment after traumatic brain injury. *Journal of Neurology, Neurosurgery & Psychiatry*, *71*(2), 161–168. https://doi.org/10.1136/jnnp.71.2.161

Claudi, F., Tyson, A. L., Petrucco, L., Margrie, T. W., Portugues, R., & Branco, T. (2021). Visualizing anatomically registered data with brainrender. *eLife*, *10*, e65751. https://doi.org/10.7554/eLife.65751

Corrigan, J. D., & Hammond, F. M. (2013). Traumatic Brain Injury as a Chronic Health Condition. *Archives of Physical Medicine and Rehabilitation*, *94*(6), 1199–1201. https://doi.org/10.1016/j.apmr.2013.01.023

Cronin, J., & Dudek, F. E. (1988). Chronic seizures and collateral sprouting of dentate mossy fibers after kainic acid treatment in rats. *Brain Research*, *474*(1), 181–184. https://doi.org/10.1016/0006-8993(88)90681-6

Cummings, K. A., & Clem, R. L. (2020). Prefrontal somatostatin interneurons encode fear memory. *Nature Neuroscience*, *23*(1), 61–74. https://doi.org/10.1038/s41593-019-0552-7

Curran, T., & Morgan, J. I. (1985). Superinduction of c-fos by Nerve Growth Factor in the Presence of Peripherally Active Benzodiazepines. *Science*, *229*(4719), 1265–1268. https://doi.org/10.1126/science.4035354

Curran, T., & Teich, N. M. (1982). Identification of a 39,000-dalton protein in cells transformed by the FBJ murine osteosarcoma virus. *Virology*, *116*(1), 221–235. https://doi.org/10.1016/0042-6822(82)90415-9

de Lanerolle, N. C., Kim, J. H., Robbins, R. J., & Spencer, D. D. (1989). Hippocampal interneuron loss and plasticity in human temporal lobe epilepsy. *Brain Research*, *495*(2), 387–395. https://doi.org/10.1016/0006-8993(89)90234-5

de Sousa, A. F., Zeidler, Z. E., Almeida-Filho, D. G., Shen, Y., Luchetti, A., Simanian, S., Mardini, M., DeNardo, L. A., & Silva, A. J. (2026). The prefrontal cortex controls memory organization in the hippocampus. *Nature Neuroscience*, *29*(5), 1191–1202. https://doi.org/10.1038/s41593-026-02231-1

DeNardo, L. A., Liu, C. D., Allen, W. E., Adams, E. L., Friedmann, D., Fu, L., Guenthner, C. J., Tessier-Lavigne, M., & Luo, L. (2019). Temporal evolution of cortical ensembles promoting remote memory retrieval. *Nature Neuroscience*, *22*(3), 460–469. https://doi.org/10.1038/s41593-018-0318-7

DeNardo, L., & Luo, L. (2017). Genetic strategies to access activated neurons. *Current Opinion in Neurobiology, Molecular Neuroscience*, *45*, 121–129. https://doi.org/10.1016/j.conb.2017.05.014

Deneux, T., Kaszas, A., Szalay, G., Katona, G., Lakner, T., Grinvald, A., Rózsa, B., & Vanzetta, I. (2016). Accurate spike estimation from noisy calcium signals for ultrafast three-dimensional imaging of large neuronal populations in vivo. *Nature Communications*, *7*(1), 12190. https://doi.org/10.1038/ncomms12190

Denk, W., Strickler, J. H., & Webb, W. W. (1990). Two-Photon Laser Scanning Fluorescence Microscopy. *Science*, *248*(4951), 73–76. https://doi.org/10.1126/science.2321027

Didier, M., Roux, P., Piechaczyk, M., Verrier, B., Bockaert, J., & Pin, J.-P. (1989). Cerebellar granule cell survival and maturation induced by K+ and NMDA correlate with c-*fos* proto-oncogene expression. *Neuroscience Letters*, *107*(1), 55–62. https://doi.org/10.1016/0304-3940(89)90790-8

Diehl, G. W., Hon, O. J., Leutgeb, S., & Leutgeb, J. K. (2017). Grid and Nongrid Cells in Medial Entorhinal Cortex Represent Spatial Location and Environmental Features with Complementary Coding Schemes. *Neuron*, *94*(1), 83-92.e6. https://doi.org/10.1016/j.neuron.2017.03.004

Dikmen, S. S., Corrigan, J. D., Levin, H. S., Machamer, J., Stiers, W., & Weisskopf, M. G. (2009). Cognitive outcome following traumatic brain injury. *The Journal of Head Trauma Rehabilitation*, *24*(6), 430–438. https://doi.org/10.1097/HTR.0b013e3181c133e9

Dixon, C. E., Lyeth, B. G., Povlishock, J. T., Findling, R. L., Hamm, R. J., Marmarou, A., Young, H. F., & Hayes, R. L. (1987). *A fluid percussion model of experimental brain injury in the rat*. https://doi.org/10.3171/jns.1987.67.1.0110

Do, J. P., Xu, M., Lee, S.-H., Chang, W.-C., Zhang, S., Chung, S., Yung, T. J., Fan, J. L., Miyamichi, K., Luo, L., & Dan, Y. (2016). Cell type-specific long-range connections of basal forebrain circuit. *eLife*, *5*, e13214. https://doi.org/10.7554/eLife.13214

Doerr, J., Schwarz, M. K., Wiedermann, D., Leinhaas, A., Jakobs, A., Schloen, F., Schwarz, I., Diedenhofen, M., Braun, N. C., Koch, P., Peterson, D. A., Kubitscheck, U., Hoehn, M., & Brüstle, O. (2017). Whole-brain 3D mapping of human neural transplant innervation. *Nature Communications*, *8*(1), 14162. https://doi.org/10.1038/ncomms14162

Dragunow, M., de Castro, D., & Faull, R. L. M. (1990). Induction of Fos in glia-like cells after focal brain injury but not during wallerian degeneration. *Brain Research*, *527*(1), 41–54. https://doi.org/10.1016/0006-8993(90)91058-O

Dragunow, M., & Robertson, H. A. (1987). Kindling stimulation induces c-fos protein(s) in granule cells of the rat dentate gyrus. *Nature*, *329*(6138), 441–442. https://doi.org/10.1038/329441a0

Dragunow, M., & Robertson, H. A. (1988). Brain injury induces c-fos protein(s) in nerve and glial-like cells in adult mammalian brain. *Brain Research*, *455*(2), 295–299. https://doi.org/10.1016/0006-8993(88)90088-1

Dudok, B., Szoboszlay, M., Paul, A., Klein, P. M., Liao, Z., Hwaun, E., Szabo, G. G., Geiller, T., Vancura, B., Wang, B.-S., McKenzie, S., Homidan, J., Klaver, L. M. F., English, D. F., Huang, Z. J., Buzsáki, G., Losonczy, A., & Soltesz, I. (2021). Recruitment and inhibitory action of hippocampal axo-axonic cells during behavior. *Neuron*, *109*(23), 3838-3850.e8. https://doi.org/10.1016/j.neuron.2021.09.033

Dutcher, S. A., Underwood, B. D., Walker, P. D., Diaz, F. G., & Michael, D. B. (1999). Patterns of immediate early gene mRNA expression following rodent and human traumatic brain injury. *Neurological Research*, *21*(3), 234–242. https://doi.org/10.1080/01616412.1999.11740924

Eakin, K., & Miller, J. P. (2012). Mild Traumatic Brain Injury Is Associated with Impaired

Hippocampal Spatiotemporal Representation in the Absence of Histological Changes. *Journal of Neurotrauma*, *29*(6), 1180–1187. https://doi.org/10.1089/neu.2011.2192

Edward Dixon, C., Clifton, G. L., Lighthall, J. W., Yaghmai, A. A., & Hayes, R. L. (1991). A controlled cortical impact model of traumatic brain injury in the rat. *Journal of Neuroscience Methods*, *39*(3), 253–262. https://doi.org/10.1016/0165-0270(91)90104-8

Erlander, M. G., Tillakaratne, N. J. K., Feldblum, S., Patel, N., & Tobin, A. J. (1991). Two genes encode distinct glutamate decarboxylases. *Neuron*, *7*(1), 91–100. https://doi.org/10.1016/0896-6273(91)90077-D

Etlin, A., Bráz, J. M., Kuhn, J. A., Wang, X., Hamel, K. A., Llewellyn-Smith, I. J., & Basbaum, A. I. (2016). Functional Synaptic Integration of Forebrain GABAergic Precursors into the Adult Spinal Cord. *Journal of Neuroscience*, *36*(46), 11634–11645. https://doi.org/10.1523/JNEUROSCI.2301-16.2016

Faber, D. J., Mik, E. G., Aalders, M. C. G., & Leeuwen, T. G. van. (2003). Light absorption of (oxy-)hemoglobin assessed by spectroscopic optical coherence tomography. *Optics Letters*, *28*(16), 1436–1438. https://doi.org/10.1364/OL.28.001436

Farbota, K. D., Bendlin, B. B., Alexander, A. L., Rowley, H. A., Dempsey, R. J., & Johnson, S. C. (2012). Longitudinal diffusion tensor imaging and neuropsychological correlates in traumatic brain injury patients. *Frontiers in Human Neuroscience*, *6*. https://doi.org/10.3389/fnhum.2012.00160

Feeney, D. M., Boyeson, M. G., Linn, R. T., Murray, H. M., & Dail, W. G. (1981). Responses to cortical injury: I. Methodology and local effects of contusions in the rat. *Brain Research*, *211*(1), 67–77. https://doi.org/10.1016/0006-8993(81)90067-6

Ferguson, P. L., Smith, G. M., Wannamaker, B. B., Thurman, D. J., Pickelsimer, E. E., & Selassie, A. W. (2010). A population-based study of risk of epilepsy after hospitalization for traumatic brain injury. *Epilepsia*, *51*(5), 891–898. https://doi.org/10.1111/j.1528-1167.2009.02384.x

Förstner, P., & Knöll, B. (2020). Interference of neuronal activity-mediated gene expression through serum response factor deletion enhances mortality and hyperactivity after traumatic brain injury. *The FASEB Journal*, *34*(3), 3855–3873. https://doi.org/10.1096/fj.201902257RR

Frankowski, J. C., Foik, A. T., Tierno, A., Machhor, J. R., Lyon, D. C., & Hunt, R. F. (2021). Traumatic brain injury to primary visual cortex produces long-lasting circuit dysfunction. *Communications Biology*, *4*(1), 1297. https://doi.org/10.1038/s42003-021-02808-5

Frankowski, J. C., Kim, Y. J., & Hunt, R. F. (2019). Selective vulnerability of hippocampal interneurons to graded traumatic brain injury. *Neurobiology of Disease*, *129*, 208–216. https://doi.org/10.1016/j.nbd.2018.07.022

Frankowski, J. C., Tierno, A., Pavani, S., Cao, Q., Lyon, D. C., & Hunt, R. F. (2022). Brain-wide reconstruction of inhibitory circuits after traumatic brain injury. *Nature Communications*, *13*(1), 3417. https://doi.org/10.1038/s41467-022-31072-2

Freund, T. F., & Antal, M. (1988). GABA-containing neurons in the septum control inhibitory interneurons in the hippocampus. *Nature*, *336*(6195), 170–173. https://doi.org/10.1038/336170a0

Freund, T. f., & Buzsáki, G. (1996). Interneurons of the hippocampus. *Hippocampus*, *6*(4), 347–470. https://doi.org/10.1002/(SICI)1098-1063(1996)6:4%253C347::AID-HIPO1%253E3.0.CO;2-I

Frey, L. C. (2003). Epidemiology of Posttraumatic Epilepsy: A Critical Review. *Epilepsia*, *44*(s10), 11–17. https://doi.org/10.1046/j.1528-1157.44.s10.4.x

Geiller, T., Sadeh, S., Rolotti, S. V., Blockus, H., Vancura, B., Negrean, A., Murray, A. J., Rózsa, B., Polleux, F., Clopath, C., & Losonczy, A. (2022). Local circuit amplification of spatial selectivity in the hippocampus. *Nature*, *601*(7891), 105–109. https://doi.org/10.1038/s41586-021-04169-9

Ghosh, K. K., Burns, L. D., Cocker, E. D., Nimmerjahn, A., Ziv, Y., Gamal, A. E., & Schnitzer, M. J. (2011). Miniaturized integration of a fluorescence microscope. *Nature Methods*, *8*(10), 871–878. https://doi.org/10.1038/nmeth.1694

Gissel, C., Doutheil, J., & Paschen, W. (1997). Temporal Analysis of Changes in Neuronal c-fos mRNA Levels Induced by Depletion of Endoplasmic Reticulum Calcium Stores: Effect of Clamping Cytoplasmic Calcium Activity at Resting Levels. *Journal of Neurochemistry*, *69*(6), 2538–2545. https://doi.org/10.1046/j.1471-4159.1997.69062538.x

Graham, D. I., Raghupathi, R., Saatman, K. E., Meaney, D., & McIntosh, T. K. (2000). Tissue tears in the white matter after lateral fluid percussion brain injury in the rat: Relevance to human brain injury. *Acta Neuropathologica*, *99*(2), 117–124. https://doi.org/10.1007/PL00007414

Greenberg, M. E., & Ziff, E. B. (1984). Stimulation of 3T3 cells induces transcription of the c-fos proto-oncogene. *Nature*, *311*(5985), 433–438. https://doi.org/10.1038/311433a0

Greenberg, M. E., Ziff, E. B., & Greene, L. A. (1986). Stimulation of Neuronal Acetylcholine Receptors Induces Rapid Gene Transcription. *Science*, *234*(4772), 80–83. https://doi.org/10.1126/science.3749894

Grienberger, C., Milstein, A. D., Bittner, K. C., Romani, S., & Magee, J. C. (2017). Inhibitory suppression of heterogeneously tuned excitation enhances spatial coding in CA1 place cells. *Nature Neuroscience*, *20*(3), 417–426. https://doi.org/10.1038/nn.4486

Guardamagna, M., Chadney, O., Stella, F., Zhang, Q., Kentros, C., & Battaglia, F. P. (2025). Direct entorhinal control of CA1 temporal coding. *Nature Communications*, *16*(1), 6430. https://doi.org/10.1038/s41467-025-61453-2

Guenthner, C. J., Miyamichi, K., Yang, H. H., Heller, H. C., & Luo, L. (2013). Permanent Genetic Access to Transiently Active Neurons via TRAP: Targeted Recombination in Active Populations. *Neuron*, *78*(5), 773–784. https://doi.org/10.1016/j.neuron.2013.03.025

Guo, C., Blair, G. J., Sehgal, M., Sangiuliano Jimka, F. N., Bellafard, A., Silva, A. J., Golshani, P., Basso, M. A., Blair, H. T., & Aharoni, D. (2023). Miniscope-LFOV: A large-field-of-view, single-cell-resolution, miniature microscope for wired and wire-free imaging of neural dynamics in freely behaving animals. *Science Advances*, *9*(16), eadg3918. https://doi.org/10.1126/sciadv.adg3918

Gupta, P. K., Sayed, N., Ding, K., Agostini, M. A., Van Ness, P. C., Yablon, S., Madden, C., Mickey, B., D'Ambrosio, R., & Diaz-Arrastia, R. (2014). Subtypes of Post-Traumatic Epilepsy: Clinical, Electrophysiological, and Imaging Features. *Journal of Neurotrauma*, *31*(16), 1439–1443. https://doi.org/10.1089/neu.2013.3221

Guzowski, J. F., Lyford, G. L., Stevenson, G. D., Houston, F. P., McGaugh, J. L., Worley, P. F., & Barnes, C. A. (2000). Inhibition of Activity-Dependent Arc Protein Expression in the Rat Hippocampus Impairs the Maintenance of Long-Term Potentiation and the Consolidation of Long-Term Memory. *Journal of Neuroscience*, *20*(11), 3993–4001. https://doi.org/10.1523/JNEUROSCI.20-11-03993.2000

Guzowski, J. F., Timlin, J. A., Roysam, B., McNaughton, B. L., Worley, P. F., & Barnes, C. A. (2005). Mapping behaviorally relevant neural circuits with immediate-early gene expression. *Current Opinion in Neurobiology, Neuronal and Glial Cell Biology / New Technologies*, *15*(5), 599–606. https://doi.org/10.1016/j.conb.2005.08.018

Halabisky, B., Parada, I., Buckmaster, P. S., & Prince, D. A. (2010). Excitatory Input Onto Hilar Somatostatin Interneurons Is Increased in a Chronic Model of Epilepsy. *Journal of Neurophysiology*, *104*(4), 2214–2223. https://doi.org/10.1152/jn.00147.2010

Hales, J. B., Schlesiger, M. I., Leutgeb, J. K., Squire, L. R., Leutgeb, S., & Clark, R. E. (2014). Medial Entorhinal Cortex Lesions Only Partially Disrupt Hippocampal Place Cells and Hippocampus-Dependent Place Memory. *Cell Reports*, *9*(3), 893–901. https://doi.org/10.1016/j.celrep.2014.10.009

Hall, E. D., Bryant, Y. D., Cho, W., & Sullivan, P. G. (2008). Evolution of Post-Traumatic Neurodegeneration after Controlled Cortical Impact Traumatic Brain Injury in Mice and Rats as Assessed by the De Olmos Silver and Fluorojade Staining Methods. *Journal of Neurotrauma*, *25*(3), 235–247. https://doi.org/10.1089/neu.2007.0383

Hall, E. D., Sullivan, P. G., Gibson, T. R., Pavel, K. M., Thompson, B. M., & Scheff, S. W. (2005). Spatial and Temporal Characteristics of Neurodegeneration after Controlled Cortical Impact in Mice: More than a Focal Brain Injury. *Journal of Neurotrauma*, *22*(2), 252–265. https://doi.org/10.1089/neu.2005.22.252

Hamm, R. J., Dixon, C. E., Gbadebo, D. M., Singha, A. K., Jenkins, L. W., Lyeth, B. G., & Hayes, R. L. (1992). Cognitive Deficits Following Traumatic Brain Injury Produced by Controlled Cortical Impact. *Journal of Neurotrauma*, *9*(1), 11–20. https://doi.org/10.1089/neu.1992.9.11

Harris, N. G., Verley, D. R., Gutman, B. A., & Sutton, R. L. (2016). Bi-directional changes in fractional anisotropy after experiment TBI: Disorganization and reorganization? *NeuroImage*, *133*, 129–143. https://doi.org/10.1016/j.neuroimage.2016.03.012

Hartings, J. A., Bullock, M. R., Okonkwo, D. O., Murray, L. S., Murray, G. D., Fabricius, M., Maas, A. I., Woitzik, J., Sakowitz, O., Mathern, B., Roozenbeek, B., Lingsma, H., Dreier, J. P., Puccio, A. M., Shutter, L. A., Pahl, C., & Strong, A. J. (2011). Spreading depolarisations and outcome after traumatic brain injury: A prospective observational study. *The Lancet Neurology*, *10*(12), 1058–1064. https://doi.org/10.1016/S1474-4422(11)70243-5

Herrera, D. G., & Robertson, H. A. (1996). Activation of *c-fos* in the brain. *Progress in Neurobiology*, *50*(2), 83–107. https://doi.org/10.1016/S0301-0082(96)00021-4

Himanen, L., Portin, R., Isoniemi, H., Helenius, H., Kurki, T., & Tenovuo, O. (2005). Cognitive functions in relation to MRI findings 30 years after traumatic brain injury. *Brain Injury*, *19*(2), 93–100. https://doi.org/10.1080/02699050410001720031

Holden, S. S., Grandi, F. C., Aboubakr, O., Higashikubo, B., Cho, F. S., Chang, A. H., Forero, A. O., Morningstar, A. R., Mathur, V., Kuhn, L. J., Suri, P., Sankaranarayanan, S., Andrews-Zwilling, Y., Tenner, A. J., Luthi, A., Aronica, E., Corces, M. R., Yednock, T., & Paz, J. T. (2021). Complement factor C1q mediates sleep spindle loss and epileptic spikes after mild brain injury. *Science*, *373*(6560), eabj2685. https://doi.org/10.1126/science.abj2685

Hou, B., Varghese, N., Soh, H., Santaniello, S., & Tzingounis, A. V. (2021). Loss of KCNQ2 or KCNQ3 Leads to Multifocal Time-Varying Activity in the Neonatal Forebrain Ex Vivo. *eNeuro*, *8*(3). https://doi.org/10.1523/ENEURO.0024-21.2021

Hou, G., Jiang, S., Chen, G., Deng, X., Li, F., Xu, H., Chen, B., & Zhu, Y. (2023). Opioid Receptors Modulate Firing and Synaptic Transmission in the Paraventricular Nucleus of the Thalamus. *Journal of Neuroscience*, *43*(15), 2682–2695. https://doi.org/10.1523/JNEUROSCI.1766-22.2023

Howard, M. A., & Baraban, S. C. (2016). Synaptic integration of transplanted interneuron progenitor cells into native cortical networks. *Journal of Neurophysiology*, *116*(2), 472–478. https://doi.org/10.1152/jn.00321.2016

Hsieh, J.-Y., & Baraban, S. C. (2017). Medial Ganglionic Eminence Progenitors Transplanted into Hippocampus Integrate in a Functional and Subtype-Appropriate Manner. *eNeuro*, *4*(2). https://doi.org/10.1523/ENEURO.0359-16.2017

Hughes, P., Lawlor, P., & Dragunow, M. (1992). Basal expression of Fos, Fos-related, Jun, and Krox 24 proteins in rat hippocampus. *Molecular Brain Research*, *13*(4), 355–357. https://doi.org/10.1016/0169-328X(92)90219-2

Hunt, R. F., Boychuk, J. A., & Smith, B. N. (2013). Neural circuit mechanisms of post–traumatic epilepsy. *Frontiers in Cellular Neuroscience*, *7*. https://doi.org/10.3389/fncel.2013.00089

Hunt, R. F., Girskis, K. M., Rubenstein, J. L., Alvarez-Buylla, A., & Baraban, S. C. (2013). GABA progenitors grafted into the adult epileptic brain control seizures and abnormal behavior. *Nature Neuroscience*, *16*(6), 692–697. https://doi.org/10.1038/nn.3392

Hunt, R. F., Scheff, S. W., & Smith, B. N. (2009). Posttraumatic epilepsy after controlled cortical impact injury in mice. *Experimental Neurology*, *215*(2), 243–252. https://doi.org/10.1016/j.expneurol.2008.10.005

Hunt, R. F., Scheff, S. W., & Smith, B. N. (2010). Regionally Localized Recurrent Excitation in the Dentate Gyrus of a Cortical Contusion Model of Posttraumatic Epilepsy. *Journal of Neurophysiology*, *103*(3), 1490–1500. https://doi.org/10.1152/jn.00957.2009

Hunt, R. F., Scheff, S. W., & Smith, B. N. (2011). Synaptic Reorganization of Inhibitory Hilar Interneuron Circuitry after Traumatic Brain Injury in Mice. *Journal of Neuroscience*, *31*(18), 6880–6890. https://doi.org/10.1523/JNEUROSCI.0032-11.2011

Jensen, E. C. (2013). Quantitative Analysis of Histological Staining and Fluorescence Using ImageJ. *The Anatomical Record*, *296*(3), 378–381. https://doi.org/10.1002/ar.22641

Jeong, N., & Singer, A. C. (2022). Learning from inhibition: Functional roles of hippocampal CA1 inhibition in spatial learning and memory. *Current Opinion in Neurobiology*, *76*, 102604.

https://doi.org/10.1016/j.conb.2022.102604

Jin, J., & Maren, S. (2015). Prefrontal-Hippocampal Interactions in Memory and Emotion. *Frontiers in Systems Neuroscience*, *9*. https://doi.org/10.3389/fnsys.2015.00170

Johnson, V. E., Stewart, W., & Smith, D. H. (2013). Axonal pathology in traumatic brain injury. *Experimental Neurology, Special Issue: Axonal Degeneration*, *246*, 35–43. https://doi.org/10.1016/j.expneurol.2012.01.013

Jun, H., Bramian, A., Soma, S., Saito, T., Saido, T. C., & Igarashi, K. M. (2020). Disrupted Place Cell Remapping and Impaired Grid Cells in a Knockin Model of Alzheimer's Disease. *Neuron*, *107*(6), 1095-1112.e6. https://doi.org/10.1016/j.neuron.2020.06.023

Kahn, J. B., Port, R. G., Yue, C., Takano, H., & Coulter, D. A. (2019). Circuit-based interventions in the dentate gyrus rescue epilepsy-associated cognitive dysfunction. *Brain*, *142*(9), 2705–2721. https://doi.org/10.1093/brain/awz209

Kapfer, C., Glickfeld, L. L., Atallah, B. V., & Scanziani, M. (2007). Supralinear increase of recurrent inhibition during sparse activity in the somatosensory cortex. *Nature Neuroscience*, *10*(6), 743–753. https://doi.org/10.1038/nn1909

Katona, I., Acsády, L., & Freund, T. F. (1999). Postsynaptic targets of somatostatin-immunoreactive interneurons in the rat hippocampus. *Neuroscience*, *88*(1), 37–55. https://doi.org/10.1016/S0306-4522(98)00302-9

Kawaguchi, Y. (1997). Selective Cholinergic Modulation of Cortical GABAergic Cell Subtypes. *Journal of Neurophysiology*, *78*(3), 1743–1747. https://doi.org/10.1152/jn.1997.78.3.1743

Kepecs, A., & Fishell, G. (2014). Interneuron cell types are fit to function. *Nature*, *505*(7483), 318–326. https://doi.org/10.1038/nature12983

Kharatishvili, I., Immonen, R., Gröhn, O., & Pitkänen, A. (2007). Quantitative diffusion MRI of hippocampus as a surrogate marker for post-traumatic epileptogenesis. *Brain*, *130*(12), 3155–3168. https://doi.org/10.1093/brain/awm268

Kharatishvili, I., Nissinen, J. P., McIntosh, T. K., & Pitkänen, A. (2006). A model of posttraumatic epilepsy induced by lateral fluid-percussion brain injury in rats. *Neuroscience*, *140*(2), 685–697. https://doi.org/10.1016/j.neuroscience.2006.03.012

Kiessling, M., & Gass, P. (1993). Immediate Early Gene Expression in Experimental Epilepsy. *Brain Pathology*, *3*(4), 381–393. https://doi.org/10.1111/j.1750-3639.1993.tb00766.x

King, C., Robinson, T., Dixon, C. E., Rao, G. R., Larnard, D., & Nemoto, C. E. M. (2010). Brain Temperature Profiles during Epidural Cooling with the ChillerPad in a Monkey Model of Traumatic Brain Injury. *Journal of Neurotrauma*, *27*(10), 1895–1903. https://doi.org/10.1089/neu.2009.1178

Kinnunen, K. M., Greenwood, R., Powell, J. H., Leech, R., Hawkins, P. C., Bonnelle, V., Patel, M. C., Counsell, S. J., & Sharp, D. J. (2011). White matter damage and cognitive impairment after traumatic brain injury. *Brain*, *134*(2), 449–463. https://doi.org/10.1093/brain/awq347

Kirst, C., Skriabine, S., Vieites-Prado, A., Topilko, T., Bertin, P., Gerschenfeld, G., Verny, F.,

Topilko, P., Michalski, N., Tessier-Lavigne, M., & Renier, N. (2020). Mapping the Fine-Scale Organization and Plasticity of the Brain Vasculature. *Cell*, *180*(4), 780-795.e25. https://doi.org/10.1016/j.cell.2020.01.028

Klausberger, T., Magill, P. J., Márton, L. F., Roberts, J. D. B., Cobden, P. M., Buzsáki, G., & Somogyi, P. (2003). Brain-state- and cell-type-specific firing of hippocampal interneurons in vivo. *Nature*, *421*(6925), 844–848. https://doi.org/10.1038/nature01374

Klausberger, T., & Somogyi, P. (2008). Neuronal Diversity and Temporal Dynamics: The Unity of Hippocampal Circuit Operations. *Science*, *321*(5885), 53–57. https://doi.org/10.1126/science.1149381

Koch, P. F., Cottone, C., Adam, C. D., Ulyanova, A. V., Russo, R. J., Weber, M. T., Arena, J. D., Johnson, V. E., & Wolf, J. A. (2020). Traumatic Brain Injury Preserves Firing Rates But Disrupts Laminar Oscillatory Coupling and Neuronal Entrainment in Hippocampal CA1. *eNeuro*, *7*(5). https://doi.org/10.1523/ENEURO.0495-19.2020

Kumar, R., Viswanath, O., & Saadabadi, A. (2026). Buprenorphine. In *StatPearls*. StatPearls Publishing. http://www.ncbi.nlm.nih.gov/books/NBK459126/

Lanahan, A., & Worley, P. (1998). Immediate-Early Genes and Synaptic Function. *Neurobiology of Learning and Memory*, *70*(1), 37–43. https://doi.org/10.1006/nlme.1998.3836

Larimer, P., Spatazza, J., Espinosa, J. S., Tang, Y., Kaneko, M., Hasenstaub, A. R., Stryker, M. P., & Alvarez-Buylla, A. (2016). Caudal Ganglionic Eminence Precursor Transplants Disperse and Integrate as Lineage-Specific Interneurons but Do Not Induce Cortical Plasticity. *Cell Reports*, *16*(5), 1391–1404. https://doi.org/10.1016/j.celrep.2016.06.071

Larkum, M. E., Zhu, J. J., & Sakmann, B. (1999). A new cellular mechanism for coupling inputs arriving at different cortical layers. *Nature*, *398*(6725), 338–341. https://doi.org/10.1038/18686

Lauterborn, J. C., Rivera, S., Stinis, C. T., Hayes, V. Y., Isackson, P. J., & Gall, C. M. (1996). Differential Effects of Protein Synthesis Inhibition on the Activity-Dependent Expression of BDNF Transcripts: Evidence for Immediate-Early Gene Responses from Specific Promoters. *Journal of Neuroscience*, *16*(23), 7428–7436. https://doi.org/10.1523/JNEUROSCI.16-23-07428.1996

Lavin, T. K., Jin, L., Lea, N. E., & Wickersham, I. R. (2020). Monosynaptic Tracing Success Depends Critically on Helper Virus Concentrations. *Frontiers in Synaptic Neuroscience*, *12*. https://doi.org/10.3389/fnsyn.2020.00006

Le Merre, P., Ährlund-Richter, S., & Carlén, M. (2021). The mouse prefrontal cortex: Unity in diversity. *Neuron*, *109*(12), 1925–1944. https://doi.org/10.1016/j.neuron.2021.03.035

Leão, R. N., Mikulovic, S., Leão, K. E., Munguba, H., Gezelius, H., Enjin, A., Patra, K., Eriksson, A., Loew, L. M., Tort, A. B. L., & Kullander, K. (2012). OLM interneurons differentially modulate CA3 and entorhinal inputs to hippocampal CA1 neurons. *Nature Neuroscience*, *15*(11), 1524–1530. https://doi.org/10.1038/nn.3235

Lenck-Santini, P.-P., & Holmes, G. L. (2008). Altered Phase Precession and Compression of Temporal Sequences by Place Cells in Epileptic Rats. *Journal of Neuroscience*, *28*(19), 5053–5062. https://doi.org/10.1523/JNEUROSCI.5024-07.2008

Leonard, J. R., Maris, D. O., & Grady, M. S. (1994). Fluid Percussion Injury Causes Loss of Forebrain Choline Acetyltransferase and Nerve Growth Factor Receptor Immunoreactive Cells in the Rat. *Journal of Neurotrauma*, *11*(4), 379–392. https://doi.org/10.1089/neu.1994.11.379

Lesuis, S. L., Park, S., Hoorn, A., Rashid, A. J., Mocle, A. J., Salter, E. W., Vislavski, S., Gray, M. T., Torelli, A. M., DeCristofaro, A., Driever, W. P. F., Stelt, M. van der, Zweifel, L. S., Collingridge, G. L., Lefebvre, J. L., Walters, B. J., Frankland, P. W., Hill, M. N., & Josselyn, S. A. (2025). Stress disrupts engram ensembles in lateral amygdala to generalize threat memory in mice. *Cell*, *188*(1), 121-140.e20. https://doi.org/10.1016/j.cell.2024.10.034

Leutgeb, S., Leutgeb, J. K., Barnes, C. A., Moser, E. I., McNaughton, B. L., & Moser, M.-B. (2005). Independent Codes for Spatial and Episodic Memory in Hippocampal Neuronal Ensembles. *Science*, *309*(5734), 619–623. https://doi.org/10.1126/science.1114037

Li, Y., Bao, H., Luo, Y., Yoan, C., Sullivan, H. A., Quintanilla, L., Wickersham, I., Lazarus, M., Shih, Y.-Y. I., & Song, J. (2020). Supramammillary nucleus synchronizes with dentate gyrus to regulate spatial memory retrieval through glutamate release. *eLife*, *9*, e53129. https://doi.org/10.7554/eLife.53129

Lighthall, J. W. (1988). Controlled Cortical Impact: A New Experimental Brain Injury Model. *Journal of Neurotrauma*, *5*(1), 1–15. https://doi.org/10.1089/neu.1988.5.1

Liu, X., Muller, R. U., Huang, L.-T., Kubie, J. L., Rotenberg, A., Rivard, B., Cilio, M. R., & Holmes, G. L. (2003). Seizure-Induced Changes in Place Cell Physiology: Relationship to Spatial Memory. *Journal of Neuroscience*, *23*(37), 11505–11515. https://doi.org/10.1523/JNEUROSCI.23-37-11505.2003

Liu, Y.-J., Ehrengruber, M. U., Negwer, M., Shao, H.-J., Cetin, A. H., & Lyon, D. C. (2013). Tracing Inputs to Inhibitory or Excitatory Neurons of Mouse and Cat Visual Cortex with a Targeted Rabies Virus. *Current Biology*, *23*(18), 1746–1755. https://doi.org/10.1016/j.cub.2013.07.033

Lopes, G., Bonacchi, N., Frazão, J., Neto, J. P., Atallah, B. V., Soares, S., Moreira, L., Matias, S., Itskov, P. M., Correia, P. A., Medina, R. E., Calcaterra, L., Dreosti, E., Paton, J. J., & Kampff, A. R. (2015). Bonsai: An event-based framework for processing and controlling data streams. *Frontiers in Neuroinformatics*, *9*. https://doi.org/10.3389/fninf.2015.00007

Lorente De Nó, R. (1934). Studies on the structure of the cerebral cortex. II. Continuation of the study of the ammonic system. *Journal Für Psychologie Und Neurologie*, *46*, 113–177.

Lovett-Barron, M., Kaifosh, P., Kheirbek, M. A., Danielson, N., Zaremba, J. D., Reardon, T. R., Turi, G. F., Hen, R., Zemelman, B. V., & Losonczy, A. (2014). Dendritic Inhibition in the Hippocampus Supports Fear Learning. *Science*, *343*(6173), 857–863. https://doi.org/10.1126/science.1247485

Lowenstein, D. H., Thomas, M. J., Smith, D. H., & McIntosh, T. K. (1992). Selective vulnerability of dentate hilar neurons following traumatic brain injury: A potential mechanistic link between head trauma and disorders of the hippocampus. *Journal of Neuroscience*, *12*(12), 4846–4853. https://doi.org/10.1523/JNEUROSCI.12-12-04846.1992

Lu, J., Li, C., Singh-Alvarado, J., Zhou, Z. C., Fröhlich, F., Mooney, R., & Wang, F. (2018).

MIN1PIPE: A Miniscope 1-Photon-Based Calcium Imaging Signal Extraction Pipeline. *Cell Reports*, *23*(12), 3673–3684. https://doi.org/10.1016/j.celrep.2018.05.062

Maas, A. I. R., Menon, D. K., Manley, G. T., Abrams, M., Åkerlund, C., Andelic, N., Aries, M., Bashford, T., Bell, M. J., Bodien, Y. G., Brett, B. L., Büki, A., Chesnut, R. M., Citerio, G., Clark, D., Clasby, B., Cooper, D. J., Czeiter, E., Czosnyka, M., … Zemek, R. (2022). Traumatic brain injury: Progress and challenges in prevention, clinical care, and research. *The Lancet Neurology*, *21*(11), 1004–1060. https://doi.org/10.1016/S1474-4422(22)00309-X

Maas, A. I., Stocchetti, N., & Bullock, R. (2008). Moderate and severe traumatic brain injury in adults. *The Lancet Neurology*, *7*(8), 728–741. https://doi.org/10.1016/S1474-4422(08)70164-9

Mably, A. J., Gereke, B. J., Jones, D. T., & Colgin, L. L. (2017). Impairments in spatial representations and rhythmic coordination of place cells in the 3xTg mouse model of Alzheimer's disease. *Hippocampus*, *27*(4), 378–392. https://doi.org/10.1002/hipo.22697

Manley, G. T., Rosenthal, G., Lam, M., Morabito, D., Yan, D., Derugin, N., Bollen, A., Knudson, M. M., & Panter, S. S. (2006). Controlled cortical impact in swine: Pathophysiology and biomechanics. *Journal of Neurotrauma*, *23*(2), 128–139. https://doi.org/10.1089/neu.2006.23.128

Marmarou, A., Foda, M. A. A.-E., Brink, W. van den, Campbell, J., Kita, H., & Demetriadou, K. (1994). *A new model of diffuse brain injury in rats*. https://doi.org/10.3171/jns.1994.80.2.0291

Marquez de la Plata, C. D., Garces, J., Shokri Kojori, E., Grinnan, J., Krishnan, K., Pidikiti, R., Spence, J., Devous, M. D., Sr, Moore, C., McColl, R., Madden, C., & Diaz-Arrastia, R. (2011). Deficits in Functional Connectivity of Hippocampal and Frontal Lobe Circuits After Traumatic Axonal Injury. *Archives of Neurology*, *68*(1), 74–84. https://doi.org/10.1001/archneurol.2010.342

Martinez-Losa, M., Tracy, T. E., Ma, K., Verret, L., Clemente-Perez, A., Khan, A. S., Cobos, I., Ho, K., Gan, L., Mucke, L., Alvarez-Dolado, M., & Palop, J. J. (2018). Nav1.1-Overexpressing Interneuron Transplants Restore Brain Rhythms and Cognition in a Mouse Model of Alzheimer's Disease. *Neuron*, *98*(1), 75-89.e5. https://doi.org/10.1016/j.neuron.2018.02.029

Mathis, A., Mamidanna, P., Cury, K. M., Abe, T., Murthy, V. N., Mathis, M. W., & Bethge, M. (2018). DeepLabCut: Markerless pose estimation of user-defined body parts with deep learning. *Nature Neuroscience*, *21*(9), 1281–1289. https://doi.org/10.1038/s41593-018-0209-y

McAllister, T. W., Saykin, A. J., Flashman, L. A., Sparling, M. B., Johnson, S. C., Guerin, S. J., Mamourian, A. C., Weaver, J. B., & Yanofsky, N. (1999). Brain activation during working memory 1 month after mild traumatic brain injury. *Neurology*, *53*(6), 1300–1300. https://doi.org/10.1212/WNL.53.6.1300

McIntosh, T. K., Noble, L., Andrews, B., & Faden, A. I. (1987). Traumatic Brain Injury in the Rat: Characterization of a Midline Fluid-Percussion Model. *Central Nervous System Trauma*, *4*(2), 119–134. https://doi.org/10.1089/cns.1987.4.119

McIntosh, T. K., Vink, R., Noble, L., Yamakami, I., Fernyak, S., Soares, H., & Faden, A. L. (1989). Traumatic brain injury in the rat: Characterization of a lateral fluid-percussion model. *Neuroscience*, *28*(1), 233–244. https://doi.org/10.1016/0306-4522(89)90247-9

McNamara, E. H., Grillakis, A. A., Tucker, L. B., & McCabe, J. T. (2020). The closed-head impact

model of engineered rotational acceleration (CHIMERA) as an application for traumatic brain injury pre-clinical research: A status report. *Experimental Neurology*, *333*, 113409. https://doi.org/10.1016/j.expneurol.2020.113409

Menon, D. K., Schwab, K., Wright, D. W., & Maas, A. I. (2010). Position Statement: Definition of Traumatic Brain Injury. *Archives of Physical Medicine and Rehabilitation*, *91*(11), 1637–1640. https://doi.org/10.1016/j.apmr.2010.05.017

Mizumori, S. J. Y., Barnes, C. A., & McNaughton, B. L. (1989). Reversible inactivation of the medial septum: Selective effects on the spontaneous unit activity of different hippocampal cell types. *Brain Research*, *500*(1), 99–106. https://doi.org/10.1016/0006-8993(89)90303-X

Morales, C., Morici, J. F., Espinosa, N., Sacson, A., Lara-Vasquez, A., García-Pérez, M. A., Bekinschtein, P., Weisstaub, N. V., & Fuentealba, P. (2021). Dentate Gyrus Somatostatin Cells are Required for Contextual Discrimination During Episodic Memory Encoding. *Cerebral Cortex*, *31*(2), 1046–1059. https://doi.org/10.1093/cercor/bhaa273

Morgan, J. I., & Curran, T. (1986). Role of ion flux in the control of c-fos expression. *Nature*, *322*(6079), 552–555. https://doi.org/10.1038/322552a0

Morganti-Kossmann, M. C., Rancan, M., Stahel, P. F., & Kossmann, T. (2002). Inflammatory response in acute traumatic brain injury: A double-edged sword. *Current Opinion in Critical Care*, *8*(2), 101–105. https://doi.org/10.1097/00075198-200204000-00002

Morris, R. G. M., Garrud, P., Rawlins, J. N. P., & O'Keefe, J. (1982). Place navigation impaired in rats with hippocampal lesions. *Nature*, *297*(5868), 681–683. https://doi.org/10.1038/297681a0

Muller, R. U., Bostock, E., Taube, J. S., & Kubie, J. L. (1994). On the directional firing properties of hippocampal place cells. *Journal of Neuroscience*, *14*(12), 7235–7251. https://doi.org/10.1523/JNEUROSCI.14-12-07235.1994

Muller, R. U., & Kubie, J. L. (1987). The effects of changes in the environment on the spatial firing of hippocampal complex-spike cells. *Journal of Neuroscience*, *7*(7), 1951–1968. https://doi.org/10.1523/JNEUROSCI.07-07-01951.1987

Multiple Cause of Death Data on CDC WONDER. (n.d.). Retrieved September 14, 2026, from https://wonder.cdc.gov/mcd.html

Naik, A. A., Brodovskaya, A., Subedi, S., Akram, A., & Kapur, J. (2022). Extrahippocampal Seizure and Memory Circuits Overlap. *eNeuro*, *9*(4). https://doi.org/10.1523/ENEURO.0179-22.2022

Nakamura, T., Hillary, F. G., & Biswal, B. B. (2009). Resting Network Plasticity Following Brain Injury. *PLOS ONE*, *4*(12), e8220. https://doi.org/10.1371/journal.pone.0008220

Nambu, M. F., Lin, Y.-J., Reuschenbach, J., & Tanaka, K. Z. (2022). What does engram encode?: Heterogeneous memory engrams for different aspects of experience. *Current Opinion in Neurobiology*, *75*, 102568. https://doi.org/10.1016/j.conb.2022.102568

Namjoshi, D. R., Cheng, W. H., McInnes, K. A., Martens, K. M., Carr, M., Wilkinson, A., Fan, J., Robert, J., Hayat, A., Cripton, P. A., & Wellington, C. L. (2014). Merging pathology with

biomechanics using CHIMERA (Closed-Head Impact Model of Engineered Rotational Acceleration): A novel, surgery-free model of traumatic brain injury. *Molecular Neurodegeneration*, *9*(1), 55. https://doi.org/10.1186/1750-1326-9-55

Niedworok, C. J., Brown, A. P. Y., Jorge Cardoso, M., Osten, P., Ourselin, S., Modat, M., & Margrie, T. W. (2016). aMAP is a validated pipeline for registration and segmentation of high-resolution mouse brain data. *Nature Communications*, *7*(1), 11879. https://doi.org/10.1038/ncomms11879

Nilsson, B., Pontén, U., & Voigt, G. (1977). *Experimental head injury in the rat*. https://doi.org/10.3171/jns.1977.47.2.0241

Obasa, A. A., Olopade, F. E., Juliano, S. L., & Olopade, J. O. (2024). Traumatic brain injury or traumatic brain disease: A scientific commentary. *Brain Multiphysics*, *6*, 100092. https://doi.org/10.1016/j.brain.2024.100092

O'Keefe, J. (1976). Place units in the hippocampus of the freely moving rat. *Experimental Neurology*, *51*(1), 78–109. https://doi.org/10.1016/0014-4886(76)90055-8

O'Keefe, J., & Conway, D. H. (1978). Hippocampal place units in the freely moving rat: Why they fire where they fire. *Experimental Brain Research*, *31*(4), 573–590. https://doi.org/10.1007/BF00239813

O'Keefe, J., & Dostrovsky, J. (1971). The hippocampus as a spatial map. Preliminary evidence from unit activity in the freely-moving rat. *Brain Research*, *34*(1), 171–175. https://doi.org/10.1016/0006-8993(71)90358-1

Oliva, A. A., Jiang, M., Lam, T., Smith, K. L., & Swann, J. W. (2000). Novel Hippocampal Interneuronal Subtypes Identified Using Transgenic Mice That Express Green Fluorescent Protein in GABAergic Interneurons. *Journal of Neuroscience*, *20*(9), 3354–3368. https://doi.org/10.1523/JNEUROSCI.20-09-03354.2000

O'Mara, S. M. (2013). The anterior thalamus provides a subcortical circuit supporting memory and spatial navigation. *Frontiers in Systems Neuroscience*, *7*. https://doi.org/10.3389/fnsys.2013.00045

Onishi, T., Hirose, K., & Sakaba, T. (2024). Molecular tools to capture active neural circuits. *Frontiers in Neural Circuits*, *18*. https://doi.org/10.3389/fncir.2024.1449459

Paterno, R., Folweiler, K. A., & Cohen, A. S. (2017). Pathophysiology and Treatment of Memory Dysfunction After Traumatic Brain Injury. *Current Neurology and Neuroscience Reports*, *17*(7), 52. https://doi.org/10.1007/s11910-017-0762-x

Pearn, M. L., Niesman, I. R., Egawa, J., Sawada, A., Almenar-Queralt, A., Shah, S. B., Duckworth, J. L., & Head, B. P. (2017). Pathophysiology Associated with Traumatic Brain Injury: Current Treatments and Potential Novel Therapeutics. *Cellular and Molecular Neurobiology*, *37*(4), 571–585. https://doi.org/10.1007/s10571-016-0400-1

Pease, M., Gupta, K., Moshé, S. L., Correa, D. J., Galanopoulou, A. S., Okonkwo, D. O., Gonzalez-Martinez, J., Shutter, L., Diaz-Arrastia, R., & Castellano, J. F. (2024). Insights into epileptogenesis from post-traumatic epilepsy. *Nature Reviews Neurology*, *20*(5), 298–312.

https://doi.org/10.1038/s41582-024-00954-y

Pelkey, K. A., Chittajallu, R., Craig, M. T., Tricoire, L., Wester, J. C., & McBain, C. J. (2017). Hippocampal GABAergic Inhibitory Interneurons. *Physiological Reviews*, *97*(4), 1619–1747. https://doi.org/10.1152/physrev.00007.2017

Peng, Z., Zhang, N., Wei, W., Huang, C. S., Cetina, Y., Otis, T. S., & Houser, C. R. (2013). A Reorganized GABAergic Circuit in a Model of Epilepsy: Evidence from Optogenetic Labeling and Stimulation of Somatostatin Interneurons. *Journal of Neuroscience*, *33*(36), 14392–14405. https://doi.org/10.1523/JNEUROSCI.2045-13.2013

Pesold, C., Impagnatiello, F., Pisu, M. G., Uzunov, D. P., Costa, E., Guidotti, A., & Caruncho, H. J. (1998). Reelin is preferentially expressed in neurons synthesizing γ-aminobutyric acid in cortex and hippocampus of adult rats. *Proceedings of the National Academy of Sciences*, *95*(6), 3221–3226. https://doi.org/10.1073/pnas.95.6.3221

Phillips, L. L., & Belardo, E. T. (1992). Expression of c-fos in the Hippocampus Following Mild and Moderate Fluid Percussion Brain Injury. *Journal of Neurotrauma*, *9*(4), 323–333. https://doi.org/10.1089/neu.1992.9.323

Pignatelli, M., Ryan, T. J., Roy, D. S., Lovett, C., Smith, L. M., Muralidhar, S., & Tonegawa, S. (2019). Engram Cell Excitability State Determines the Efficacy of Memory Retrieval. *Neuron*, *101*(2), 274-284.e5. https://doi.org/10.1016/j.neuron.2018.11.029

Povlishock, J. T., & Katz, D. I. (2005). Update of neuropathology and neurological recovery after traumatic brain injury. *The Journal of Head Trauma Rehabilitation*, *20*(1), 76–94. https://doi.org/10.1097/00001199-200501000-00008

Priya, R., Rakela, B., Kaneko, M., Spatazza, J., Larimer, P., Hoseini, M. S., Hasenstaub, A. R., Alvarez-Buylla, A., & Stryker, M. P. (2019). Vesicular GABA Transporter Is Necessary for Transplant-Induced Critical Period Plasticity in Mouse Visual Cortex. *Journal of Neuroscience*, *39*(14), 2635–2648. https://doi.org/10.1523/JNEUROSCI.1253-18.2019

Purpura, D. P., & Housepian, E. M. (1961). Morphological and physiological properties of chronically isolated immature neocortex. *Experimental Neurology*, *4*(5), 377–401. https://doi.org/10.1016/0014-4886(61)90025-5

Raghupathi, R., McIntosh, T. K., & Smith, D. H. (1995). Cellular Responses to Experimental Brain Injury. *Brain Pathology*, *5*(4), 437–442. https://doi.org/10.1111/j.1750-3639.1995.tb00622.x

Raghupathi, R., Welsh, F. A., Lowenstein, D. H., Gennarelli, T. A., & McIntosh, T. K. (1995). Regional Induction of c-Fos and Heat Shock Protein-72 mRNA following Fluid-Percussion Brain Injury in the Rat. *Journal of Cerebral Blood Flow & Metabolism*, *15*(3), 467–473. https://doi.org/10.1038/jcbfm.1995.58

Raible, D. J., Frey, L. C., Del Angel, Y. C., Carlsen, J., Hund, D., Russek, S. J., Smith, B., & Brooks-Kayal, A. R. (2015). JAK/STAT pathway regulation of GABAA receptor expression after differing severities of experimental TBI. *Experimental Neurology*, *271*, 445–456. https://doi.org/10.1016/j.expneurol.2015.07.001

Rawlins, J. N. P., Feldon, J., & Gray, J. A. (1979). Septo-hippocampal connections and the

hippocampal theta rhythm. *Experimental Brain Research*, *37*(1), 49–63. https://doi.org/10.1007/BF01474253

Ray, S. K., Dixon, C. E., & Banik, N. L. (2002). Molecular mechanisms in the pathogenesis of traumatic brain injury. *Histology and Histopathology*, *17*(4), 1137–1152. https://doi.org/10.14670/hh-17.1137

Reneer, D. V., Hisel, R. D., Hoffman, J. M., Kryscio, R. J., Lusk, B. T., & Geddes, J. W. (2011). A Multi-Mode Shock Tube for Investigation of Blast-Induced Traumatic Brain Injury. *Journal of Neurotrauma*, *28*(1), 95–104. https://doi.org/10.1089/neu.2010.1513

Renier, N., Adams, E. L., Kirst, C., Wu, Z., Azevedo, R., Kohl, J., Autry, A. E., Kadiri, L., Umadevi Venkataraju, K., Zhou, Y., Wang, V. X., Tang, C. Y., Olsen, O., Dulac, C., Osten, P., & Tessier-Lavigne, M. (2016). Mapping of Brain Activity by Automated Volume Analysis of Immediate Early Genes. *Cell*, *165*(7), 1789–1802. https://doi.org/10.1016/j.cell.2016.05.007

Ribak, C. E., & Reiffenstein, R. J. (1982). Selective inhibitory synapse loss in chronic cortical slabs: A morphological basis for epileptic susceptibility. *Canadian Journal of Physiology and Pharmacology*, *60*(6), 864–870. https://doi.org/10.1139/y82-122

Ritter, A. C., Wagner, A. K., Szaflarski, J. P., Brooks, M. M., Zafonte, R. D., Pugh, M. J. V., Fabio, A., Hammond, F. M., Dreer, L. E., Bushnik, T., Walker, W. C., Brown, A. W., Johnson-Greene, D., Shea, T., Krellman, J. W., & Rosenthal, J. A. (2016). Prognostic models for predicting posttraumatic seizures during acute hospitalization, and at 1 and 2 years following traumatic brain injury. *Epilepsia*, *57*(9), 1503–1514. https://doi.org/10.1111/epi.13470

Roy, D. S., Park, Y.-G., Kim, M. E., Zhang, Y., Ogawa, S. K., DiNapoli, N., Gu, X., Cho, J. H., Choi, H., Kamentsky, L., Martin, J., Mosto, O., Aida, T., Chung, K., & Tonegawa, S. (2022). Brain-wide mapping reveals that engrams for a single memory are distributed across multiple brain regions. *Nature Communications*, *13*(1), 1799. https://doi.org/10.1038/s41467-022-29384-4

Royer, S., Zemelman, B. V., Losonczy, A., Kim, J., Chance, F., Magee, J. C., & Buzsáki, G. (2012). Control of timing, rate and bursts of hippocampal place cells by dendritic and somatic inhibition. *Nature Neuroscience*, *15*(5), 769–775. https://doi.org/10.1038/nn.3077

Rudy, B., Fishell, G., Lee, S., & Hjerling-Leffler, J. (2011). Three groups of interneurons account for nearly 100% of neocortical GABAergic neurons. *Developmental Neurobiology*, *71*(1), 45–61. https://doi.org/10.1002/dneu.20853

Saatman, K. E., Creed, J., & Raghupathi, R. (2010). Calpain as a Therapeutic Target in Traumatic Brain Injury. *Neurotherapeutics, Traumatic Brain Injury*, *7*(1), 31–42. https://doi.org/10.1016/j.nurt.2009.11.002

Saatman, K. E., Duhaime, A.-C., Bullock, R., Maas, A. I. R., Valadka, A., & Manley, G. T. (2008). Classification of Traumatic Brain Injury for Targeted Therapies. *Journal of Neurotrauma*, *25*(7), 719–738. https://doi.org/10.1089/neu.2008.0586

Saatman, K. E., Feeko, K. J., Pape, R. L., & Raghupathi, R. (2006). Differential Behavioral and Histopathological Responses to Graded Cortical Impact Injury in Mice. *Journal of Neurotrauma*, *23*(8), 1241–1253. https://doi.org/10.1089/neu.2006.23.1241

Sagar, S. M., Sharp, F. R., & Curran, T. (1988). Expression of c-fos Protein in Brain: Metabolic Mapping at the Cellular Level. *Science*, *240*(4857), 1328–1331. https://doi.org/10.1126/science.3131879

Santhakumar, V., Bender, R., Frotscher, M., Ross, S. T., Hollrigel, G. S., Toth, Z., & Soltesz, I. (2000). Granule cell hyperexcitability in the early post-traumatic rat dentate gyrus: The 'irritable mossy cell' hypothesis. *The Journal of Physiology*, *524*(1), 117–134. https://doi.org/10.1111/j.1469-7793.2000.00117.x

Scheff, S. W., Price, D. A., Hicks, R. R., Baldwin, S. A., Robinson, S., & Brackney, C. (2005). Synaptogenesis in the Hippocampal CA1 Field following Traumatic Brain Injury. *Journal of Neurotrauma*, *22*(7), 719–732. https://doi.org/10.1089/neu.2005.22.719

Schmidt, R. H., & Grady, M. S. (1995). *Loss of forebrain cholinergic neurons following fluid-percussion injury: Implications for cognitive impairment in closed head injury*. https://doi.org/10.3171/jns.1995.83.3.0496

Schmued, L. C., Stowers, C. C., Scallet, A. C., & Xu, L. (2005). Fluoro-Jade C results in ultra high resolution and contrast labeling of degenerating neurons. *Brain Research*, *1035*(1), 24–31. https://doi.org/10.1016/j.brainres.2004.11.054

Scoville, W. B., & Milner, B. (1957). Loss of Recent Memory After Bilateral Hippocampal Lesions. *Journal of Neurology, Neurosurgery & Psychiatry*, *20*(1), 11–21. https://doi.org/10.1136/jnnp.20.1.11

Shapira, Y., Setton, D., Artru, A. A., & Shohami, E. (1993). Blood-brain barrier permeability, cerebral edema, and neurologic function after closed head injury in rats. *Anesthesia and Analgesia*, *77*(1), 141–148. https://doi.org/10.1213/00000539-199307000-00028

Sharp, D. J., Scott, G., & Leech, R. (2014). Network dysfunction after traumatic brain injury. *Nature Reviews Neurology*, *10*(3), 156–166. https://doi.org/10.1038/nrneurol.2014.15

Sheintuch, L., Rubin, A., Brande-Eilat, N., Geva, N., Sadeh, N., Pinchasof, O., & Ziv, Y. (2017). Tracking the Same Neurons across Multiple Days in Ca2+ Imaging Data. *Cell Reports*, *21*(4), 1102–1115. https://doi.org/10.1016/j.celrep.2017.10.013

Sheng, M., & Greenberg, M. E. (1990). The regulation and function of c-*fos* and other immediate early genes in the nervous system. *Neuron*, *4*(4), 477–485. https://doi.org/10.1016/0896-6273(90)90106-P

Shuman, T., Aharoni, D., Cai, D. J., Lee, C. R., Chavlis, S., Page-Harley, L., Vetere, L. M., Feng, Y., Yang, C. Y., Mollinedo-Gajate, I., Chen, L., Pennington, Z. T., Taxidis, J., Flores, S. E., Cheng, K., Javaherian, M., Kaba, C. C., Rao, N., La-Vu, M., … Golshani, P. (2020). Breakdown of spatial coding and interneuron synchronization in epileptic mice. *Nature Neuroscience*, *23*(2), 229–238. https://doi.org/10.1038/s41593-019-0559-0

Silberberg, G., & Markram, H. (2007). Disynaptic Inhibition between Neocortical Pyramidal Cells Mediated by Martinotti Cells. *Neuron*, *53*(5), 735–746. https://doi.org/10.1016/j.neuron.2007.02.012

Skaggs, W., McNaughton, B., & Gothard, K. (1992). An Information-Theoretic Approach to

Deciphering the Hippocampal Code. *Advances in Neural Information Processing Systems*, *5*. https://proceedings.neurips.cc/paper_files/paper/1992/hash/5dd9db5e033da9c6fb5ba83c7a7ebea9-Abstract.html

Smith, D. H., Soares, H. D., Pierce, J. S., Perlman, K. G., Saatman, K. E., Meaney, D. F., Dixon, C. E., & McINTOSH, T. K. (1995). A Model of Parasagittal Controlled Cortical Impact in the Mouse: Cognitive and Histopathologic Effects. *Journal of Neurotrauma*, *12*(2), 169–178. https://doi.org/10.1089/neu.1995.12.169

Solstad, T., Moser, E. I., & Einevoll, G. T. (2006). From grid cells to place cells: A mathematical model. *Hippocampus*, *16*(12), 1026–1031. https://doi.org/10.1002/hipo.20244

Southwell, D. G., Froemke, R. C., Alvarez-Buylla, A., Stryker, M. P., & Gandhi, S. P. (2010). Cortical Plasticity Induced by Inhibitory Neuron Transplantation. *Science*, *327*(5969), 1145–1148. https://doi.org/10.1126/science.1183962

Spruston, N. (2008). Pyramidal neurons: Dendritic structure and synaptic integration. *Nature Reviews Neuroscience*, *9*(3), 206–221. https://doi.org/10.1038/nrn2286

Squire, L. R. (1992). Memory and the hippocampus: A synthesis from findings with rats, monkeys, and humans. *Psychological Review*, *99*(2), 195–231. https://doi.org/10.1037/0033-295X.99.2.195

Stefanelli, T., Bertollini, C., Lüscher, C., Muller, D., & Mendez, P. (2016). Hippocampal Somatostatin Interneurons Control the Size of Neuronal Memory Ensembles. *Neuron*, *89*(5), 1074–1085. https://doi.org/10.1016/j.neuron.2016.01.024

Stenman, J., Toresson, H., & Campbell, K. (2003). Identification of Two Distinct Progenitor Populations in the Lateral Ganglionic Eminence: Implications for Striatal and Olfactory Bulb Neurogenesis. *Journal of Neuroscience*, *23*(1), 167–174. https://doi.org/10.1523/JNEUROSCI.23-01-00167.2003

Steward, O. (1976). Topographic organization of the projections from the entorhinal area to the hippocampal formation of the rat. *Journal of Comparative Neurology*, *167*(3), 285–314. https://doi.org/10.1002/cne.901670303

Steward, O., & Scoville, S. A. (1976). Cells of origin of entorhinal cortical afferents to the hippocampus and fascia dentata of the rat. *Journal of Comparative Neurology*, *169*(3), 347–370. https://doi.org/10.1002/cne.901690306

Sun, Q., Li, X., Ren, M., Zhao, M., Zhong, Q., Ren, Y., Luo, P., Ni, H., Zhang, X., Zhang, C., Yuan, J., Li, A., Luo, M., Gong, H., & Luo, Q. (2019). A whole-brain map of long-range inputs to GABAergic interneurons in the mouse medial prefrontal cortex. *Nature Neuroscience*, *22*(8), 1357–1370. https://doi.org/10.1038/s41593-019-0429-9

Sun, Y., Nguyen, A. Q., Nguyen, J. P., Le, L., Saur, D., Choi, J., Callaway, E. M., & Xu, X. (2014). Cell-Type-Specific Circuit Connectivity of Hippocampal CA1 Revealed through Cre-Dependent Rabies Tracing. *Cell Reports*, *7*(1), 269–280. https://doi.org/10.1016/j.celrep.2014.02.030

Susarla, B. T. S., Villapol, S., Yi, J.-H., Geller, H. M., & Symes, A. J. (2014). Temporal Patterns of Cortical Proliferation of Glial Cell Populations after Traumatic Brain Injury in Mice. *ASN Neuro*, *6*(3), AN20130034. https://doi.org/10.1042/AN20130034

Swartz, B. E., Houser, C. R., Tomiyasu, U., Walsh, G. O., DeSalles, A., Rich, J. R., & Delgado-Escueta, A. (2006). Hippocampal Cell Loss in Posttraumatic Human Epilepsy. *Epilepsia*, *47*(8), 1373–1382. https://doi.org/10.1111/j.1528-1167.2006.00602.x

Taş, Y. Ç., Solaroğlu, İ., & Gürsoy-Özdemir, Y. (2019). Spreading Depolarization Waves in Neurological Diseases: A Short Review about its Pathophysiology and Clinical Relevance. *Current Neuropharmacology*, *17*(2), 151–164. https://doi.org/10.2174/1570159X15666170915160707

Teasdale, G., & Jennett, B. (1974). ASSESSMENT OF COMA AND IMPAIRED CONSCIOUSNESS: A Practical Scale. *The Lancet, Originally Published as Volume 2, Issue 7872*, *304*(7872), 81–84. https://doi.org/10.1016/S0140-6736(74)91639-0

Thompson, L. T., & Best, P. J. (1990). Long-term stability of the place-field activity of single units recorded from the dorsal hippocampus of freely behaving rats. *Brain Research*, *509*(2), 299–308. https://doi.org/10.1016/0006-8993(90)90555-P

Thornhill, S., Teasdale, G. M., Murray, G. D., McEwen, J., Roy, C. W., & Penny, K. I. (2000). Disability in young people and adults one year after head injury: Prospective cohort study. *BMJ*, *320*(7250), 1631–1635. https://doi.org/10.1136/bmj.320.7250.1631

Tian, L., Hires, S. A., Mao, T., Huber, D., Chiappe, M. E., Chalasani, S. H., Petreanu, L., Akerboom, J., McKinney, S. A., Schreiter, E. R., Bargmann, C. I., Jayaraman, V., Svoboda, K., & Looger, L. L. (2009). Imaging neural activity in worms, flies and mice with improved GCaMP calcium indicators. *Nature Methods*, *6*(12), 875–881. https://doi.org/10.1038/nmeth.1398

Tierno, A., Baraban, A., & Hunt, R. F. (2026). Cortex-Wide Neuron Activation after Traumatic Brain Injury in Mice. *eNeuro*, *13*(5). https://doi.org/10.1523/ENEURO.0020-26.2026

Tierno, A., & Hunt, R. (2026). Brain injury degrades the precision of hippocampal spatial representations. *bioRxiv*, 2026.08.28.747393. https://doi.org/10.64898/2026.08.28.747393

Tornero, D., Tsupykov, O., Granmo, M., Rodriguez, C., Grønning-Hansen, M., Thelin, J., Smozhanik, E., Laterza, C., Wattananit, S., Ge, R., Tatarishvili, J., Grealish, S., Brüstle, O., Skibo, G., Parmar, M., Schouenborg, J., Lindvall, O., & Kokaia, Z. (2017). Synaptic inputs from stroke-injured brain to grafted human stem cell-derived neurons activated by sensory stimuli. *Brain*, *140*(3), 692–706. https://doi.org/10.1093/brain/aww347

Tóth, K., Freund, T. F., & Miles, R. (1997). Disinhibition of rat hippocampal pyramidal cells by GABAergic afferents from the septum. *The Journal of Physiology*, *500*(2), 463–474. https://doi.org/10.1113/jphysiol.1997.sp022033

Tremblay, R., Lee, S., & Rudy, B. (2016). GABAergic Interneurons in the Neocortex: From Cellular Properties to Circuits. *Neuron*, *91*(2), 260–292. https://doi.org/10.1016/j.neuron.2016.06.033

Tyson, A. L., Rousseau, C. V., Niedworok, C. J., Keshavarzi, S., Tsitoura, C., Cossell, L., Strom, M., & Margrie, T. W. (2021). A deep learning algorithm for 3D cell detection in whole mouse brain image datasets. *PLOS Computational Biology*, *17*(5), e1009074. https://doi.org/10.1371/journal.pcbi.1009074

Udakis, M., Claydon, M. D. B., Zhu, H. W., Oakes, E. C., & Mellor, J. R. (2025). Hippocampal OLM interneurons regulate CA1 place cell plasticity and remapping. *Nature Communications*, *16*(1), 9912. https://doi.org/10.1038/s41467-025-64859-0

Udakis, M., Pedrosa, V., Chamberlain, S. E. L., Clopath, C., & Mellor, J. R. (2020). Interneuron-specific plasticity at parvalbumin and somatostatin inhibitory synapses onto CA1 pyramidal neurons shapes hippocampal output. *Nature Communications*, *11*(1), 4395. https://doi.org/10.1038/s41467-020-18074-8

Ueda, H. R., Dodt, H.-U., Osten, P., Economo, M. N., Chandrashekar, J., & Keller, P. J. (2020). Whole-Brain Profiling of Cells and Circuits in Mammals by Tissue Clearing and Light-Sheet Microscopy. *Neuron*, *106*(3), 369–387. https://doi.org/10.1016/j.neuron.2020.03.004

Ulyanova, A. V., Adam, C. D., Cottone, C., Maheshwari, N., Grovola, M. R., Fruchet, O. E., Alamar, J., Koch, P. F., Johnson, V. E., Cullen, D. K., & Wolf, J. A. (2023). Hippocampal interneuronal dysfunction and hyperexcitability in a porcine model of concussion. *Communications Biology*, *6*(1), 1136. https://doi.org/10.1038/s42003-023-05491-w

Unal, G., Joshi, A., Viney, T. J., Kis, V., & Somogyi, P. (2015). Synaptic Targets of Medial Septal Projections in the Hippocampus and Extrahippocampal Cortices of the Mouse. *Journal of Neuroscience*, *35*(48), 15812–15826. https://doi.org/10.1523/JNEUROSCI.2639-15.2015

Vakil, E. (2005). The Effect of Moderate to Severe Traumatic Brain Injury (TBI) on Different Aspects of Memory:A Selective Review. *Journal of Clinical and Experimental Neuropsychology*, *27*(8), 977–1021. https://doi.org/10.1080/13803390490919245

Valero, M., Navas-Olive, A., Prida, L. M. de la, & Buzsáki, G. (2022). Inhibitory conductance controls place field dynamics in the hippocampus. *Cell Reports*, *40*(8). https://doi.org/10.1016/j.celrep.2022.111232

Varga, C., Lee, S. Y., & Soltesz, I. (2010). Target-selective GABAergic control of entorhinal cortex output. *Nature Neuroscience*, *13*(7), 822–824. https://doi.org/10.1038/nn.2570

Vivar, C., Potter, M. C., Choi, J., Lee, J., Stringer, T. P., Callaway, E. M., Gage, F. H., Suh, H., & van Praag, H. (2012). Monosynaptic inputs to new neurons in the dentate gyrus. *Nature Communications*, *3*(1), 1107. https://doi.org/10.1038/ncomms2101

Wang, Q., Ding, S.-L., Li, Y., Royall, J., Feng, D., Lesnar, P., Graddis, N., Naeemi, M., Facer, B., Ho, A., Dolbeare, T., Blanchard, B., Dee, N., Wakeman, W., Hirokawa, K. E., Szafer, A., Sunkin, S. M., Oh, S. W., Bernard, A., … Ng, L. (2020). The Allen Mouse Brain Common Coordinate Framework: A 3D Reference Atlas. *Cell*, *181*(4), 936-953.e20. https://doi.org/10.1016/j.cell.2020.04.007

Werner, C., & Engelhard, K. (2007). Pathophysiology of traumatic brain injury. *BJA: British Journal of Anaesthesia*, *99*(1), 4–9. https://doi.org/10.1093/bja/aem131

Wichterle, H., Garcia-Verdugo, J. M., Herrera, D. G., & Alvarez-Buylla, A. (1999). Young neurons from medial ganglionic eminence disperse in adult and embryonic brain. *Nature Neuroscience*, *2*(5), 461–466. https://doi.org/10.1038/8131

Wickersham, I. R., Lyon, D. C., Barnard, R. J. O., Mori, T., Finke, S., Conzelmann, K.-K., Young,

J. A. T., & Callaway, E. M. (2007). Monosynaptic Restriction of Transsynaptic Tracing from Single, Genetically Targeted Neurons. *Neuron*, *53*(5), 639–647. https://doi.org/10.1016/j.neuron.2007.01.033

Wilson, M. A., & McNaughton, B. L. (1993). Dynamics of the Hippocampal Ensemble Code for Space. *Science*, *261*(5124), 1055–1058. https://doi.org/10.1126/science.8351520

Wittner, L., Henze, D. A., Záborszky, L., & Buzsáki, G. (2006). Hippocampal CA3 pyramidal cells selectively innervate aspiny interneurons. *European Journal of Neuroscience*, *24*(5), 1286–1298. https://doi.org/10.1111/j.1460-9568.2006.04992.x

Wolf, J. A., Stys, P. K., Lusardi, T., Meaney, D., & Smith, D. H. (2001). Traumatic Axonal Injury Induces Calcium Influx Modulated by Tetrodotoxin-Sensitive Sodium Channels. *Journal of Neuroscience*, *21*(6), 1923–1930. https://doi.org/10.1523/JNEUROSCI.21-06-01923.2001

Wonders, C. P., & Anderson, S. A. (2006). The origin and specification of cortical interneurons. *Nature Reviews Neuroscience*, *7*(9), 687–696. https://doi.org/10.1038/nrn1954

Xiong, Y., Mahmood, A., & Chopp, M. (2013). Animal models of traumatic brain injury. *Nature Reviews Neuroscience*, *14*(2), 128–142. https://doi.org/10.1038/nrn3407

Xu, Y., Zhao, M., Han, Y., & Zhang, H. (2020). GABAergic Inhibitory Interneuron Deficits in Alzheimer's Disease: Implications for Treatment. *Frontiers in Neuroscience*, *14*. https://doi.org/10.3389/fnins.2020.00660

Yang, K., Mu, X. S., Xue, J. J., Perez-Polo, J. R., & Hayes, R. L. (1995). Regional and temporal profiles of c-fos and nerve growth factor mRNA expression in rat brain after lateral cortical impact injury. *Journal of Neuroscience Research*, *42*(4), 571–578. https://doi.org/10.1002/jnr.490420415

Yang, K., Mu, X. S., Xue, J. J., Whitson, J., Salminen, A., Dixon, C. E., Liu, P. K., & Hayes, R. L. (1994). Increased expression of c-*fos* mRNA and AP-1 transcription factors after cortical impact injury in rats. *Brain Research*, *664*(1), 141–147. https://doi.org/10.1016/0006-8993(94)91964-X

Yuan, M., Meyer, T., Benkowitz, C., Savanthrapadian, S., Ansel-Bollepalli, L., Foggetti, A., Wulff, P., Alcami, P., Elgueta, C., & Bartos, M. (2017). Somatostatin-positive interneurons in the dentate gyrus of mice provide local- and long-range septal synaptic inhibition. *eLife*, *6*, e21105. https://doi.org/10.7554/eLife.21105

Zhang, W., Yamawaki, R., Wen, X., Uhl, J., Diaz, J., Prince, D. A., & Buckmaster, P. S. (2009). Surviving Hilar Somatostatin Interneurons Enlarge, Sprout Axons, and Form New Synapses with Granule Cells in a Mouse Model of Temporal Lobe Epilepsy. *Journal of Neuroscience*, *29*(45), 14247–14256. https://doi.org/10.1523/JNEUROSCI.3842-09.2009

Zhang, Y., Rózsa, M., Liang, Y., Bushey, D., Wei, Z., Zheng, J., Reep, D., Broussard, G. J., Tsang, A., Tsegaye, G., Narayan, S., Obara, C. J., Lim, J.-X., Patel, R., Zhang, R., Ahrens, M. B., Turner, G. C., Wang, S. S.-H., Korff, W. L., … Looger, L. L. (2023). Fast and sensitive GCaMP calcium indicators for imaging neural populations. *Nature*, *615*(7954), 884–891. https://doi.org/10.1038/s41586-023-05828-9

Zhao, R., Fowler, S. W., Chiang, A. C. A., Ji, D., & Jankowsky, J. L. (2014). Impairments in experience-dependent scaling and stability of hippocampal place fields limit spatial learning in a

mouse model of Alzheimer's disease. *Hippocampus*, *24*(8), 963–978. https://doi.org/10.1002/hipo.22283

Zhao, S., Todorov, M. I., Cai, R., -Maskari, R. A., Steinke, H., Kemter, E., Mai, H., Rong, Z., Warmer, M., Stanic, K., Schoppe, O., Paetzold, J. C., Gesierich, B., Wong, M. N., Huber, T. B., Duering, M., Bruns, O. T., Menze, B., Lipfert, J., … Ertürk, A. (2020). Cellular and Molecular Probing of Intact Human Organs. *Cell*, *180*(4), 796-812.e19. https://doi.org/10.1016/j.cell.2020.01.030

Zheng, X., Salinas, K. J., Velez, D. X. F., Nakayama, T., Lin, X., Banerjee, D., Xu, X., & Gandhi, S. P. (2021). Host interneurons mediate plasticity reactivated by embryonic inhibitory cell transplantation in mouse visual cortex. *Nature Communications*, *12*(1), 862. https://doi.org/10.1038/s41467-021-21097-4

Zhong, J., Lan, Y., Sun, L., Zhao, Z., Liu, X., Shi, J., Ren, L., Zuo, Q., Wei, X., & Dou, X. (2025). Global prevalence of post-traumatic epilepsy in traumatic brain injury patients: A systematic review and meta-analysis (1997–2024). *Neuroscience*, *584*, 180–189. https://doi.org/10.1016/j.neuroscience.2025.07.008

Zhu, B., Eom, J., & Hunt, R. F. (2019). Transplanted interneurons improve memory precision after traumatic brain injury. *Nature Communications*, *10*(1), 5156. https://doi.org/10.1038/s41467-019-13170-w

Ziv, Y., Burns, L. D., Cocker, E. D., Hamel, E. O., Ghosh, K. K., Kitch, L. J., Gamal, A. E., & Schnitzer, M. J. (2013). Long-term dynamics of CA1 hippocampal place codes. *Nature Neuroscience*, *16*(3), 264–266. https://doi.org/10.1038/nn.3329

Zong, W., Obenhaus, H. A., Skytøen, E. R., Eneqvist, H., Jong, N. L. de, Vale, R., Jorge, M. R., Moser, M.-B., & Moser, E. I. (2022). Large-scale two-photon calcium imaging in freely moving mice. *Cell*, *185*(7), 1240-1256.e30. https://doi.org/10.1016/j.cell.2022.02.017

Zutshi, I., Valero, M., Fernández-Ruiz, A., & Buzsáki, G. (2022). Extrinsic control and intrinsic computation in the hippocampal CA1 circuit. *Neuron*, *110*(4), 658-673.e5. https://doi.org/10.1016/j.neuron.2021.11.015

APPENDIX A

Miniscope surgery protocol

The miniscope surgery is split into 3 separate surgeries: virus injection, lens implantation and baseplating. Modifications for mice that have undergone CCI are noted in ***bold italics***.

Virus injection

Materials:

- Sterile (or autoclaved) 0.6 mL tubes
- Sterile, filtered pipette tips
- Sterile PBS (for dilution of virus, if necessary)
- Virus (AAV1-FLEX-jGCAMP8m; Addgene cat no: 162378-AAV1)
- Ice
- Beveled needle (50µm diameter tip; Wiretol 5µm, Drummond Scientific)
- Ideal micro drill (Cellpoint Scientific cat no: 67-1200A)
- Drill bit (0.8 mm for burr hole)
- ***For TBI mice: #11 scalpel (Fine Science Tools cat no. 10011-00)***
- MO-10 injector (Narishige)

Methods:

1. Before stereotactic injection of the virus, dilute virus with sterile PBS (use sterile tubes, pipette tips, and perform dilution in hood)
    a. Optimize concentration and virus volume to brain region and target cell type
        i. For CA1 injection using AAV1-FLEX-GCAMP8m into *Camk2a*-cre mice, a titer of ~$1x10^{12}$ genome copies/mL works well (typically a 1:10 dilution from Addgene stock)

ii. Volume used for CA1: 100 nL

b. For best results, make the dilution the day of virus injection and avoid >2 freeze/thaw cycles for diluted virus aliquots.

c. Remaining aliquots should be stored in -80°C.

2. Store and transport on ice until time of virus injection

3. Perform stereotactic injections.

a. Coordinates for dCA1: anteroposterior (AP) −2.1 mm, mediolateral (ML) 1.5 mm, and dorsoventral (DV) −1.2 mm

***Notes for TBI mice:**

b. Weeks after injury, dura will become tough to puncture with needle alone

c. Prior to needle insertion, zero out surface of brain at dura

d. Coordinates for dCA1 in CCI mice: AP −1.9 mm, ML 1.5 mm, and DV −0.65 mm.

e. Make a very small durotomy using a #11 scalpel, large enough for needle to be inserted.

i. Extreme care should be taken as to not damage underlying tissue; Little to no bleeding should occur during this step.

f. After delivery of the virus, wait at least 10 min before removing needle from brain to prevent virus from leaking into cavity

4. Allow at least 3 weeks for sufficient virus expression to occur

Lens implantation

Materials:

- Ideal micro drill (Cellpoint Scientific cat no: 67-1200A)
- Burrs for microdrill: 0.5 mm drill bit (Fine Science Tools cat no: 19007-05)
- Fine forceps (Fine Science Tools cat no: 11203-23)

- GRIN lens (1.0mm diameter, 4mm length; Inscopix cat no: 1050-004595)
- Cannula holder + stereotactic arm (Thorlabs cat no: XCL and XC7)
- Cotton tip applicators
- Surgifoam (Ethicon)
- 27g blunt needles (1 inch length, Luer lock)
- 30g blunt needles (1 inch length, Luer lock)
- Vacuum aspiration system (Cole-Parmer cat no: UX-13050-50)
- 0.9% saline solution (Teknova cat no. S5825)
    - Use 18g blunt needle attached to 1mL syringe to apply saline during aspiration step
    - Note: keep on ice until time of use
- Dental cement (Teets 'Cold Cure' Dental cement works *best* for this surgery but any dental cement will adhere)
    - Liquid (A-M Systems; cat no. 526000)
    - Powder (A-M Systems; cat no. 525000)
- Black powder (for mixing with dental cement mixture)
- #11 scalpel (FST cat no. 10011-00)
- Kwik-Sil and mixing tips (World Precision Instruments cat no. KWIK-SIL)
- Krazy glue
- cyanoacrylate glue accelerator
- Eye ointment
- Buprenorphine hydrochloride
- Lens paper
- Kimwipes
- 70% ethanol (v/v)

- Betadine surgical scrub (Fisher Scientific cat no: 50-305-7193)
- Ultra fine tip black ink marker (Sharpie)
- Heating pad (for recovery after surgery)

Methods:

1. Anesthetize mouse in isoflurane (2% in induction chamber)
2. Inject buprenorphine (0.05 mg/kg i.p.) at the start of the surgery (and 12hr post-op)
3. Apply eye ointment to eyes to prevent drying out during surgery
4. Stabilize mouse's skull in stereotactic device using ear bars
5. Shave hair off mouse head
    a. Optional: to ensure complete removal of hair, use hair removal cream (Nair): apply with a cotton tip applicator, leave on for 1 min, and completely clean off using water and cotton applicator
6. Clean the surgical site using 3 alternating scrubs of alcohol and Betadine
7. Make an incision along sagittal suture of the skull and expose the skull, enough to see bregma and lambda landmarks
8. Clean off surface of skull using cotton-tip applicator, removing all connective tissue / fascia

    For TBI mice: Take extreme care when clearing skull especially near the injury site and craniotomy
9. Ensure skull is flat in both dorsal/ventral direction and medial/lateral direction
    a. Adjust dorsal-ventral position of the head such that the difference in height between lambda and bregma is within 0.05 mm
    b. Same applies for medial/lateral leveling of the head
10. Score the skull using a #11 scalpel blade

a. This ensures that lens and baseplate do not become loose during recording sessions and are securely glued onto the skull

For TBI mice: Take extreme care when scoring the skull especially near injury

For craniotomy:

11. Zero out at bregma using a needle attached to the stereotactic arm.
12. Move needle to the appropriate x,y coordinates where the lens will be implanted and mark the spot with ultra fine tip marker
13. Perform ~1mm diameter craniotomy centered in this region, slowly etching away the skull using a drill bit attached to the microdrill. Cranial window should be just large enough that lens will fit and be stabilized with minimal movement

***** For TBI mice, follow steps below before performing craniotomy*****

a. Clear off any overlying tissue near craniotomy and ensure there is no bleeding.

b. Replace skull cap that was removed during TBI surgery craniotomy. Glue skull cap onto skull using Krazy glue, being careful not to apply any glue to the dura itself. Glue should only be applied to the edges where the cap meets the skull. Wait for glue to completely dry before moving on to next step.

c. Zero out at bregma again to ensure correct x,y coordinates

d. Then, perform ~1mm craniotomy as explained above

14. Carefully remove skull cap and ensure edges around the window are smooth by clearing out any bone fragments that remain
15. Irrigate exposed tissue with cold sterile saline
    a. Maintain saline solution cold by keeping on ice for duration of surgery

b. Apply saline using 18g blunt needle attached to 1mL syringe for easier control

16. Perform a durotomy to remove the overlying dura and carefully peel it away from the brain
    a. Bleeding is likely to occur; use a small piece of surgifoam and apply it over the brain while irrigating with cold saline to reduce bleeding
    b. Note: Surgifoam should always be used in combination with saline to prevent foam from adhering to brain tissue and causing unwanted damage

    ***** For TBI mice: Dura will be firmer than in control mice, so it is important to take extreme care when performing durotomy as to not damage underlying tissue***

17. Using a 27-gauge blunt needle attached to the vacuum pump, begin to aspirate cortical tissue, continuously applying saline during aspiration.
    a. Before beginning aspiration process, bend the needle to a 45-degree angle to allow for better access and control.
    b. Bleeding is normal during this step, therefore continuous application of saline should be applied throughout the entire process to maintain a clear view of the tissue and prevent the formation of blood clots
    c. Slower aspiration is better to prevent further tissue damage

    ***** For TBI mice, follow these steps instead:***

    d. Clear out any bleeding that occurred after durotomy

    e. 1.0mm CCI injuries will extend through neocortex; the overlaying cortex over hippocampus might not be present and it is possible to see fiber tracks after clearing out blood, without any further tissue aspiration needed. If corpus callosum fibers are not present, slowly and gently

aspirate using <u>30-gauge blunt needle</u> (with continuous saline application) until you can see the fibers

18. Once corpus callosum fiber are visible (horizontal fibers), switch to a 30-gauge needle and carefully peel back fibers
    a. For CA1 pyramidal cell imaging, aspiration should be stopped when alveous fibers are present (vertical fibers)

       ***** For TBI mice: Extreme care should be taken when aspirating as tissue is more delicate and prone to bleeding***
19. Ensure bleeding has *completely* stopped before implanting
    a. Use surgifoam and constant saline irrigation to prevent blood clots and drying out of exposed brain tissue

<u>For implantation:</u>

20. Clean lens using 70% ethanol and lens paper and GENTLY take off any debris
21. Attach lens to cannula holder and attach to stereotactic arm
22. Carefully lower and zero the lens at bregma
23. Visually inspect the craniotomy to ensure there is still no bleeding
    a. If bleeding present, clean using saline and suction. Bleeding occludes FOV and it will be difficult to see cells under miniscope
24. *SLOWLY*, lower lens into craniotomy until desired depth is reached
    a. Lens should be lowered in 10-20 µm increments
    b. For CA1 imaging, lens is lowered to DV = -1.2mm

       *****For TBI mice: lens is lowered to DV = -0.85mm***
25. Apply Krazy glue around the lens using a thin applicator
    a. Careful not to get glue into the cannula

26. Once glue is dry, carefully unscrew the lens holder and raise the cannula using the stereotactic arm
    a. Make notes of any bubbles, blood clots, vasculature or abnormalities you see through the top of the lens. Although not ideal, bubbles typically clear out by one week and small blood clots can also disappear 1-2 weeks post-op.
27. Apply a layer of Krazy glue on the surface of the skull, starting from the lens and moving outward, then add a drop of accelerator
    a. Caution: accelerator is very irritating to the animal so ensure it is only applied to areas where super glue is present
28. Begin applying dental cement in layers (wait until each layer is dry) until dental cement comes up to level of lens.
    a. Take care to avoid getting dental cement on the top of the lens as this can cause scratches and debris in your FOV
    b. Optional: to prevent light (other than LED) from entering miniscope recordings, add a small amount of black powder to the dental cement mixture when building the last layer of dental cement.

       *****Note for TBI mice: lens will stick out above skull more than in control mice so more dental cement will be required to build up to top of lens***
29. Build an additional layer of dental cement that goes above the lens, to protect the sides of the lens, keeping dental cement off the top of the lens
    a. If dental cement does get on the lens, *gently* clean off using a kimwipe
30. Apply Kwik-Sil to the top of the lens
    a. Ensure this is completely dry before putting mice in their recovery cage; Kwik-sil tends to come off easily
31. Place mouse in recovery cage on a heating pad and monitor until mouse is awake and walking around

32. Inject buprenorphine (0.05 mg/kg, i.p.) within 12 hours of surgery and note in post-op records
33. Mice should be singly housed from this point onward

Baseplate

Materials:

- UCLA miniscope v4
- Miniscope DAQ (OpenEphys OEPS-7431)
- USB3 type A to USB type micro-B cable (OpenEphys OEPS-5110)
- Coaxial cable (OpenEphys OEPS-5503)
- Laptop (any computer that can run Bonsai will work)
    - Bonsai workflow for baseplating
- Miniscope V4 Baseplate Variant 2 with cover (OpenEphys OEPS-7415)
- Miniscope V4 Stereotax Holder (OpenEphys OEPS-7424)
    - The one we have was made in lab
- Dental cement (liquid + powder)
- Black powder
- Loctite Gel super glue
- cyanoacrylate glue accelerator
- T-2 screwdriver (Moody tools; cat no: 2089 T-2)
- Lens paper
- 70% ethanol
- Eye ointment
- Plastic dispensing pipette (with 20uL pipette tip attached)

Methods

1. Connect miniscope to DAQ using coaxial cable

2. Connect DAQ to laptop using USB cord
3. Attach miniscope to the stereotactic arm and screw baseplate onto the miniscope
    a. Note: Take care not to misplace the black protective cap
    b. Note: ensure the baseplate is flush with the miniscope to prevent different FOVs
4. Open Bonsai workflow and set miniscope settings to:
    a. LED: 1
    b. Gain: Med
        i. Start at Medium, increase to High if necessary
    c. EWL: 0
        i. Note: Baseplating when zoom is at 0 gives you +/- 200 μm to focus your FOV during recordings
    d. Ensure miniscope turns on, then set aside
5. Anesthetize mouse in isoflurane (2% in induction chamber)
6. Stabilize mouse's skull in stereotactic device using ear bars and lower isoflurane to 1%
7. Apply eye ointment to eyes
8. Using fine forceps, remove the Kwik-sil from top of lens
9. Clean the top of the lens using 70% ethanol and lens paper
    a. Use plastic pipette to blow away any debris on top of the lens
10. Adjust the mouse head so that the top of the lens is flat
11. Lower miniscope to about 1 cm above the lens and ensure miniscope objective is level with the top of the implanted lens
12. Turn LED on in Bonsai
13. Slowly, raise/lower the stereotactic arm until you can see vasculature and GFP+ cells in the FOV (~ 2mm above lens usually works)
    a. Adjust miniscope to get maximal coverage of all the cells in FOV

    b. FOV should be even (ie the edges of the lens should be visible all the way around)

14. Adjust LED brightness and gain until cells are visible
    a. If vasculature present but no cells, try pinching tail/toe to get a response. If still nothing, either wait at least 4 weeks after virus injection or perfuse animal
    b. If FOV black and no cells are visible, do not baseplate and perfuse animal to see what the issue was (injection target, virus expression, lens depth etc)
15. Once preferred FOV is obtained, apply a small amount of Loctite glue to the four prongs of the baseplate, then add a small drop of accelerator to solidify glue
    a. Observe the FOV in Bonsai throughout this process to ensure that FOV does not move as glue might shrink once it dries
    b. Take care that glue and accelerator do NOT go on top of the lens
    c. Ensure to use Loctite *gel* glue because it is more viscous and easier to mold/build
16. *Very* carefully, unscrew the miniscope and raise the stereotactic arm to remove the miniscope from the baseplate
    a. Ensure glue is completely dry before removal to prevent detachment of baseplate from skull
17. At this point, miniscope can be turned off and set aside
18. Apply Loctite glue all around the baseplate to further secure it to the skull
19. Apply black dental cement, building walls all the way around baseplate such that no light escapes from the walls
    a. Consistency of dental cement should be thick and malleable
    b. Take care not to get dental cement in the set screw threads

c. *Critical step:* improper baseplating can lead to motion artifacts during recordings so apply enough dental cement to minimize this and secure the baseplate to the skull

20. Once dental cement has dried, attach the black protective cap and secure it using the set screw
21. Remove mouse from stereotax and allow animal to recover in its cage on a heating pad
22. Allow a couple days for mouse to recover before beginning habituation to the weight of the miniscope

APPENDIX B

Calcium Imaging and Behavior Analysis

The analysis workflow extracts calcium traces, infers spiking activity, registers cells across sessions, tracks animal behavior and performs downstream analyses of spatial activity. This contains both published and custom scripts used and developed for this study. For more information, refer to Github: https://github.com/roberthuntlab/calciumimaginganalysis

Analysis pipeline overview

The overall workflow is:

1. **MIN1pipe**: extract calcium traces and spatial footprints from miniscope videos
2. **MLspike**: infer spikes from calcium traces
3. **CellReg**: register neurons across imaging sessions
4. **DeepLabCut**: track animal position during behavioral tasks
5. Custom **MATLAB** and **Python** scrips: combine calcium and behavior data and perform downstream analyses

The analyses are organized by behavioral paradigm:

- Home-cage recordings
- Linear track
- Y-maze

System Requirements

Hardware

Published pipelines have specific hardware and dependency requirements. Please refer to the original repositories and publications for installation instructions, detailed methodology, and citation information.

- **MIN1PIPE:** https://github.com/JinghaoLu/MIN1PIPE
- **MLspike:** https://github.com/thomasdeneux/spikes
- **CellReg:** https://github.com/zivlab/CellReg
- **DeepLabCut:** https://deeplabcut.github.io/DeepLabCut/README.html
- **Custom scripts**: https://github.com/roberthuntlab/calciumimaginganalysis

All custom **MATLAB** and **Python** scripts were developed to run on standard desktop hardware.

Operating system

All analyses were performed on Windows

Software

- MATLAB R2025b
- Python 3.13.5
- Spyder 6.10.0

Python dependencies

- Matplotlib 3.10.0
- Seaborn 0.13.2
- Numpy 2.1.3
- Pandas 2.2.3
- SciPy 1.15.3
- Statsmodels 0.15.0
- OpenCV (cv2) 4.13.0
- JSON 2.0.9

Note: JSON is part of the Python standard library. cv2 is provided by the OpenCV package.

Miniscope and behavior analyses

1. MIN1pipe: calcium trace extraction

Purpose: Extract calcium fluorescence traces and spatial footprints from miniscope videos

Input

- Miniscope videos in avi format
- Videos should be in **grayscale** format

Output

- msCam_data_processed.mat
- Relevant variables used in subsequent analyses include:
    - roifn: spatial footprints
    - dff: calcium fluorescence traces

---

2. MLspike: spike inference

Purpose: infer spikes from calcium fluorescence traces

Input:

- Calcium fluorescence traces (dff) in mat format

Procedure

1. Run **autocalibration** to estimate amplitude, tau, and sigma parameters
2. Run **spkest** to infer spikes using cell-specific amplitude, tau, and sigma parameters

Output:

- Spikes.mat

---

3. **CellReg: cell registration across sessions**

   Purpose: Register same neurons across imaging sessions. Used for linear track recordings

   Input:

   - spatial footprints for each imaging session
   - roifn variable from MIN1pipe must be reshaped to match CellReg input format (see CellReg Github for more information)

   Output:

   - csv file containing aligned cell IDs

---

4. **DeepLabCut: behavior tracking**

   Purpose: track animal position during behavior

   Input:

   - Raw behavior videos in avi format

   Procedure:

   - Train network using 10+ videos for each behavioral task
   - Crop videos, if necessary
   - Analyze videos
   - Manually correct erroneous tracking using napari

   Output:

   - Csv file containing x,y coordinates
   - For linear track:

- manually identify frames corresponding to beginning and end of each right and left runs
- save info as directions.csv file with 3 columns: start, end, direction columns

---

Downstream analyses: Home-cage, linear track, and Y-maze

Home-cage recordings

1. Calcium analysis_linear_track.py (Ran in **Spyder**)

   Purpose: analyze animal behavior during home-cage recordings

   Inputs:

   - DeepLabCut x,y position csv file
   - Timestamps csv file (from Bonsai acquisition)

   Outputs:

   - Trajectory plot
   - Speed plot
   - Total distance traveled
   - Average speed

Linear track recordings

1. Calcium imaging_linear_track.py (ran in **Spyder**)

   Purpose:

   - Smooth animal x,y positions
   - Calculate running speed
   - Trim position, running direction, and spike date

- Align data to beginning of track running

Inputs:

- DeepLabCut x,y position csv file
- Timestamps csv file
- Directions csv file
- Spikes.mat

Outputs:

- Directions_mini.csv
- Locs_dist_smooth_x.csv
- Spikes_binary_crop.csv
- Tracking and speed overlay plot

All outputs are in miniscope frames (20 fps) and aligned to the beginning of track running

---

2. Locs_and_dist_directions.m (ran in **MATLAB 2025b**)

   Purpose: combine information from all four linear track sessions into a single MATLAB file

   Inputs:

   - Directions_mini.csv
   - Locs_dist_smooth_x.csv
   - Spikes_binary_crop.csv

   Outputs:

   - Loaded_session.mat

---

3. analyzePC_right_by mouse.m and analyzePC_left_bymouse.m

These scripts perform place cell analyses separately for right and left running directions

Purpose:

Calculate

- spatial information
- Number and percentage of place cells
- Place field size
- Within-session stability (odd vs even laps)
- Peak firing rate
- Average firing rate

These scripts should be run separately for **each** mouse.

Input:

- Loaded_session.mat

Output:

- rightSessions.mat
- leftSessions.mat

---

4. Right_left_PCs_comparisons.m

Purpose:

- combine right and left running data
- calculate correlations between right and left running direction ratemaps (optional)

Inputs:

- rightSessions.mat
- leftSessions.mat

Output:

- dirSessions.mat

---

5. combined_groups.m

   Purpose: combine data from control and TBI groups

   Input: dirSessions.mat for each animal

   For this step, animal data should be organized into separate **Control** and **TBI folders**

   Output: combined_data.mat

---

6. Calcium analysis_PCanalysis.py

   Purpose: perform group-level comparisons between control and TBI animals

   The script analyzes:

   - Percentage of place cells
   - Place field size
   - Spatial information
   - Within-session stability
   - Nonspatial cell properties

   Input: combined_data exported as csv file

   Output: box plots, violin plots, statistical analyses results

Y-maze recordings

1. Calcium analysis_ymaze.py

Purpose: analyze behavior performance during the Y-maze task

The script calculates: percentage of time spent in each arm, total distance traveled, average speed. Animal trajectory plots can also be generated using this script.

Inputs:

- Behavior camera avi file
- DeepLabCut csv output file

Procedure: After loading the video:

- Manually draw ROI for each arm of the maze
- Indicate the frame at which the animal is placed into the maze
- Run the analysis

Output:

- Summary.csv